

UNIVERSITY OF CALIFORNIA  
RIVERSIDE

Dispersive Measurement of Superconducting Qubits

A Dissertation submitted in partial satisfaction  
of the requirements for the degree of

Doctor of Philosophy

in

Physics

by

Mostafa Khezri

June 2018

Dissertation Committee:

Professor Alexander Korotkov, Chairperson  
Professor Leonid Pryadko  
Professor Kirill Shtengel

Copyright by  
Mostafa Khezri  
2018

The Dissertation of Mostafa Khezri is approved:

---

---

---

Committee Chairperson

University of California, Riverside

## Acknowledgments

First of all, I want to thank my amazing advisor Sasha, without whose help I would not have been where I am now. I learned from you so much that I cannot adequately describe here, and I hope I can continue to learn from you. Sasha, you were always available to spend your time and answer my questions, whether they were about work or about life. You are able to understand and explain complex problems at the “high school” level, and that gives you a unique physical intuition and understanding that you always shared with us. I remember at times you would go for a hike and deeply think about physics problems, and when you came back you would share your understanding with us. Being your student was an honor for me, and I aspire to be even a fraction of the great physicist that you are.

Our group members in QCAMP were always kind to me. Justin, I learned many things from you, from computer softwares to physics, and you always helped me navigate difficult situations. Eyob, I did not have much chance to work you, but I always appreciated your calm manner and attention to details. Eric, I very much liked working with you and talking about random stuff in the office. Juan, you are an amazingly hardworking and knowledgeable person, and I enjoyed working with you. Vinay, I wish you success in grad school and beyond.

It was always my pleasure to work with our friends and collaborators at the Google/UCSB team. John, I learned from you and your team that some of the greatest theorist are experimentalists such as you. Dan, your critical view about different topics and your amazing attention to details has always fascinated me. I had some of the most amazing times in grad school getting to work with you and knowing you as a friend. Jimmy,

you brought great insight and wisdom into our discussions, and I enjoyed our collaborations very much. Alireza, Dvir, Chris, Yu, Pedram, Charles, working with you guys was an experience that I will always cherish, and getting to know you was an even better one.

I was fortunate to be surrounded by many good friends during my grad school. Irene, your friendship, kindness, wisdom, energy, and your mere presence made all these years serene. You were the best companion I could ask for to walk through this part of life, and I thank you for being there through it all. Abtin, your friendship and your presence in Riverside made me vastly happier, and I enjoyed every second of the time I spent with you. Shouby, thanks for being Shouby, and for being the glue that held us all together. Hooshang, thanks for always being there for help, and thanks for all the fun. Mohammadreza, Behnam, Ali, Navid, Kamran, thanks for your friendship and for making this city somewhere worth living.

Baba and Maman, thank you for all you kindly did for me, and for encouraging me to aim higher. And finally, thanks to all my teachers, from elementary school to graduate school, who taught me with love, and showed me the way.

The works presented in this dissertation were supported by ARO grants No. W911NF-15-1-0496, W911NF-11-1-0268, and W911NF-10-1-0334.

The text of this dissertation incorporates, in part or in full, materials presented in the following publications.

- **Qubit measurement error from coupling with a detuned neighbor in circuit QED**

*Mostafa Khezri, Justin Dressel, and Alexander N. Korotkov, [Phys. Rev. A](#) **92**, 052306 (2015)*

- **Measuring a transmon in circuit QED: dressed squeezed state**

*Mostafa Khezri, Eric Mlinar, Justin Dressel and Alexander N. Korotkov, [Phys. Rev. A](#) **94**, 012347 (2016)*

- **Measurement-Induced State Transitions in a Superconducting Qubit: Beyond the Rotating Wave Approximation**

*Daniel Sank, Zijun Chen, Mostafa Khezri, R. Barends, Y. Chen, A. Fowler, R. Graff, E. Jeffrey, J. Kelly, E. Lucero, A. Megrant, J. Mutus, P. Roushan, T. White, M. Neeley, B. Campbell, B. Chiaro, A. Dunsworth, C. Neill, P. O'Malley, C. Quintana, A. Vainsencher, J. Wenner, Alexander N. Korotkov, and John M. Martinis, [Phys. Rev. Lett.](#) **117**, 190503 (2016)*

- **Phase-space-Fock-space approach to evolution of a driven nonlinear resonator**

*Mostafa Khezri and Alexander N. Korotkov, [Phys. Rev. A](#) **96**, 043839 (2017)*

- **Two-time correlators for propagating squeezed microwave in transients**

*Juan Atalaya, Mostafa Khezri, and Alexander N. Korotkov, [arXiv:1804.08789](#)*

To all my teachers, especially Sasha

# ABSTRACT OF THE DISSERTATION

Dispersive Measurement of Superconducting Qubits

by

Mostafa Khezri

Doctor of Philosophy, Graduate Program in Physics  
University of California, Riverside, June 2018  
Professor Alexander Korotkov, Chairperson

Quantum computers have the capability to improve the efficiency and speed of many computational tasks. Among different candidates for physical implementation of quantum bits (qubits), superconducting qubits are currently one of the most promising candidates due to their accessible fabrication process and recent rapid developments. Measurement of these qubits is usually done in a circuit quantum electrodynamics (QED) setup, for which experimental and theoretical research is conducted to improve the accuracy and speed of the qubit readout. In this dissertation we study some aspects of the dispersive readout of superconducting qubits, and introduce tools and methods for studying these systems.

In Chapter 2 we show that in presence of neighboring qubits, the system is typically measured in the basis of joint eigenstates of qubits, in contrast to what is expected from the textbook collapse postulate. In such setups, the excitation can switch between the eigenstates, leading to measurement error. In Chapter 3 we study the joint state of the qubit-resonator system during the measurement, and show that the qubit-induced non-

linearity of the resonator squeezes its state, and within the rotating wave approximation (RWA) the system mostly remains in the joint eigenladder that is associated with the qubit's initial state. In Chapter 4 we show that built-in energy resonances in the qubit-resonator Jaynes-Cummings ladder occur at specific resonator populations, and the couplings between these resonant levels are provided by the usually neglected non-RWA terms. Such resonances lead to measurement deterioration by exciting the qubit out of the computational subspace. In Chapter 5 we provide a hybrid phase-space-Fock-space approach for studying the evolution and squeezing of driven nonlinear resonators within Gaussian approximation, which is numerically efficient and sufficiently accurate. In Chapter 6 we study the propagating squeezed field that leaks out of the resonator, and write evolution equations for the correlators of the measured field quadrature. These equations are easy to simulate and can describe the squeezing of the propagating field during the transient, which can be used to optimize the fidelity and speed of the quadrature measurement in the dispersive readout of superconducting qubits.

# Contents

<b>List of Figures</b>	<b>xiii</b>
<b>1 Introduction</b>	<b>1</b>
1.1 Superconducting qubits . . . . .	3
1.2 Quantum operations on transmons . . . . .	5
1.3 Dispersive measurement of superconducting qubits . . . . .	8
<b>2 Qubit measurement error from coupling with a detuned neighbor in circuit QED</b>	<b>13</b>
2.1 Introduction . . . . .	14
2.2 Considered system and its ensemble-averaged evolution . . . . .	17
2.2.1 Coherent evolution . . . . .	21
2.2.2 Incoherent evolution . . . . .	23
2.3 Eigenstates vs. bare states . . . . .	27
2.4 Quantum jumps in eigenbasis . . . . .	33
2.4.1 Switching rate . . . . .	34
2.4.2 Quantum trajectory simulations . . . . .	40
2.5 Qubit measurement error . . . . .	46
2.5.1 Error contributions . . . . .	48
2.5.2 Error minimized over time . . . . .	52
2.5.3 Optimized threshold . . . . .	53
2.5.4 Measurement error due to neighboring qubit . . . . .	56
2.6 Summary . . . . .	58
<b>3 Measuring a transmon qubit in circuit QED: dressed squeezed states</b>	<b>60</b>
3.1 Introduction . . . . .	61
3.2 Model . . . . .	65
3.2.1 Pumped resonator-transmon Hamiltonian . . . . .	65
3.2.2 Numerical simulation and diagonalization . . . . .	68
3.3 Dressed coherent state model . . . . .	71
3.3.1 Model inaccuracy contributions . . . . .	72
3.3.2 Infidelity from stray population . . . . .	73

3.3.3	Infidelity from shearing . . . . .	74
3.4	Dressed squeezed state model . . . . .	81
3.4.1	Dressed sheared Gaussian state . . . . .	81
3.4.2	Conversion into squeezed state notations . . . . .	84
3.4.3	Phase-Fock-space evolution of dressed squeezed state . . . . .	86
3.4.4	Accuracy of dressed squeezed state approximation . . . . .	89
3.5	Summary . . . . .	92
<b>4</b>	<b>Measurement-Induced State Transitions in a Superconducting Qubit</b>	<b>95</b>
4.1	Introduction . . . . .	96
4.2	Experimental procedure and observations . . . . .	97
4.3	Theory of nonRWA transitions . . . . .	101
4.3.1	Energy resonances mediated by non-RWA terms . . . . .	101
4.3.2	Effective coupling at resonance . . . . .	109
4.3.3	TLS-assisted transitions . . . . .	114
4.4	Other energy resonances in the JC ladder . . . . .	116
4.5	Summary . . . . .	118
4.6	Contributions . . . . .	118
<b>5</b>	<b>Hybrid phase-space–Fock-space approach to evolution of a driven nonlinear resonator</b>	<b>120</b>
5.1	Introduction . . . . .	121
5.2	System and problem . . . . .	127
5.3	Evolution of a linear resonator . . . . .	130
5.3.1	Brief review of Gaussian states . . . . .	130
5.3.2	Evolution equations . . . . .	137
5.4	Evolution of a weakly nonlinear resonator . . . . .	139
5.4.1	Fock-space Gaussian state . . . . .	139
5.4.2	Hybrid phase-Fock-space evolution equations . . . . .	142
5.5	Numerical accuracy . . . . .	148
5.5.1	Fidelity of the conversion . . . . .	148
5.5.2	Accuracy of the hybrid phase-Fock-space evolution equations . . . . .	155
5.6	3 dB squeezing limit and its violation in transients . . . . .	165
5.7	Summary . . . . .	172
<b>6</b>	<b>Two-time correlators for propagating squeezed microwave in transients</b>	<b>177</b>
6.1	Introduction . . . . .	178
6.2	System and Hamiltonian . . . . .	179
6.3	Semiclassical model for measured fluctuations . . . . .	182
6.4	Steady-state regime . . . . .	187
6.5	Example of transient evolution . . . . .	188
6.6	Summary . . . . .	190
<b>7</b>	<b>Conclusion</b>	<b>192</b>

<b>A</b>	<b>Perturbative treatment of transmon states and circuit QED parameters</b>	<b>196</b>
A.1	Hamiltonian . . . . .	197
A.2	Perturbative Energies . . . . .	198
A.3	Perturbative Couplings . . . . .	201
A.4	Perturbative derivation of dispersive shift . . . . .	205
<b>B</b>	<b>Transmon with addition of an inductor</b>	<b>208</b>
B.1	Derivation of Hamiltonian . . . . .	208
B.2	Perturbative Treatment . . . . .	211
B.3	Comparison with experimental observations . . . . .	214
<b>C</b>	<b>Numerical methods for studying readout of qubits</b>	<b>219</b>
C.1	Transmon . . . . .	219
C.2	JC ladder of qubit and resonator . . . . .	221
<b>D</b>	<b>Derivation of the measurement error in presence of a neighboring qubit</b>	<b>227</b>
D.1	Readout histograms . . . . .	228
D.1.1	Ground-state histogram . . . . .	229
D.1.2	Excited-state histogram . . . . .	230
D.2	Measurement error probability . . . . .	237
<b>E</b>	<b>Vanishing entanglement in dressed coherent and squeezed states</b>	<b>241</b>
<b>F</b>	<b>Rotating-frame evolution of a linear-resonator state</b>	<b>248</b>
<b>G</b>	<b>Equivalence between Gaussian and Fock-space Gaussian states</b>	<b>252</b>
<b>H</b>	<b>Steady-state squeezing and heating of a driven nonlinear resonator</b>	<b>258</b>
	<b>Bibliography</b>	<b>262</b>

# List of Figures

1.1	Transmon circuit and its energy levels . . . . .	4
1.2	Coupling qubits for two-qubit gate implementation . . . . .	6
1.3	Dispersive readout of superconducting qubits . . . . .	9
2.1	Readout schematic for a qubit in presence of its neighbor . . . . .	18
2.2	Ensemble-averaged evolution of qubit population in bare and eigenbasis . .	28
2.3	Ensemble-average evolution of single excitation subspace . . . . .	32
2.4	Switching rate vs. cavity decay rate . . . . .	37
2.5	An example of quantum jump (switching event) . . . . .	42
2.6	Histograms of the integrated quadrature signal . . . . .	47
2.7	Measurement error vs. signal integration time . . . . .	50
2.8	Simulated measurement error compared with analytics . . . . .	51
3.1	Jaynes-Cummings ladder for transmon coupled to a readout resonator . . .	66
3.2	Infidelity of coherent-state approximations during resonator ring-up . . . .	74
3.3	Evolution of the dressed Q-function in the eigenladder, and comparison with analytics . . . . .	76
3.4	Infidelity of the dressed coherent state approximation compared with simple theory . . . . .	80
3.5	Comparison between the dressed squeezed state and dressed coherent state models . . . . .	90
4.1	Experimental observation of the readout induced transitions . . . . .	99
4.2	JC ladder for transmon-resonator system . . . . .	102
4.3	Transmon ac Stark shift versus resonator photon number . . . . .	104
4.4	“Fan diagram” of eigenenergy levels within an RWA strip . . . . .	107
4.5	Comparison between theory and experiment for non-RWA transitions . . .	108
4.6	Effective coupling between resonant levels . . . . .	111
4.7	Resonance between transmon and a TLS . . . . .	115
5.1	Phase-space illustration of a Gaussian state . . . . .	132
5.2	Infidelity between the Gaussian and Fock-space Gaussian states as a function of $\beta$ . . . . .	150

5.3	Infidelity between the Gaussian and Fock-space Gaussian states as a function of the short-axis angle . . . . .	151
5.4	Infidelity between the Gaussian and Fock-space Gaussian states as a function of the long-axis variance . . . . .	152
5.5	Time dependence of the state infidelity . . . . .	157
5.6	“Squeezing factor”, “unsqueezing factor”, and state center as functions of time	159
5.7	Contour plot for the Wigner function of the resonator state . . . . .	162
5.8	Time dependence of infidelity for different stationary-state photon numbers	163
5.9	Violating 3 dB squeezing limit during the transients . . . . .	168
5.10	Time dependence of the squeezing factor . . . . .	173
6.1	Schematic of a parametrically driven resonator and its leaked field . . . . .	180
6.2	Time evolution of the correlator of the propagating squeezed field . . . . .	190
A.1	Bottom levels in the Jaynes-Cummings ladder of the qubit and the readout resonator . . . . .	206
B.1	Circuit of transmon with addition of a series inductor . . . . .	209
B.2	Anaharmonicicity of the transmon vs qubit frequency . . . . .	217
C.1	JC ladder of the qubit and the readout resonator . . . . .	223
D.1	Eigenbasis population jump and readout histogram . . . . .	233
D.2	Comparison between analytical and numerical measurement histograms . .	235
D.3	Time evolution of the integrated signal histogram . . . . .	237
E.1	infidelity of approximating the dressed coherent state with a direct-product state . . . . .	247

# Chapter 1

## Introduction

The idea to use quantum effects for computation was first proposed by Feynman in 1959 [1]. Later Manin in 1980 [2] and Feynman himself in 1982 [3] realized that simulating quantum systems with a classical computer requires exponentially large resources, while a quantum computer in principle could overcome this problem. Building on these ideas, researchers have explored computational capabilities of quantum systems in more detail. Bennet and Brassard laid the foundation of quantum cryptography [4]. Deutsch described the idea of a universal quantum computer [5] and later with Jozsa proposed a quantum algorithm to efficiently find balanced functions [6]. Shor introduced his landmark algorithm for prime factorization [7, 8] which was later extended by Kitaev [9]. Grover designed a quantum algorithm for faster search in unsorted databases [10]. Shor, Steane, and Calderbank proposed the first methods for quantum error correction [11–13]. Lloyd showed that quantum computers can be programmed to simulate quantum systems [14]. Bernstein and Vazirani studied the quantum computation from a complexity theory view

[15]. Kitaev introduced topological quantum computing using anyons [16] (see Ref. [17] for an overview of quantum algorithms and their application). Today, quantum computation and quantum information is an active field in Physics, with research being conducted both theoretically and experimentally. There are now a variety of other proposed applications for quantum computers, such as adiabatic quantum computation [18, 19] that operates differently from gate-based models, hybrid quantum-classical algorithms [20], simulation of molecular energies [21], quantum machine learning [22], etc.

The building blocks of quantum computers are qubits. There are in principle many different physical implementations of the qubits, since any two-level quantum system, or even two lowest levels of a many-level quantum system, can be used as a qubit. However, any physical implementation of a qubit requires a set of properties in order to be a viable candidate for building a quantum computer. These properties are sometimes called the DiVincenzo criteria [23], and consist of scalability, existence of a universal set of quantum gates, qubit-specific measurement capabilities, etc. Given these criteria, trapped ions [24–26] and superconducting qubits [27–30] are currently among the best candidates for physical implementation of qubits, with superconducting qubits favored mostly because they can be built using existing and well-developed fabrication processes of the semiconductor industry. We should also note that semiconductor quantum computing schemes [31–33] are rapidly advancing, with prospects for implementing traditional qubits [34] as well as topological quantum computation using non-Abelian anyons [35–37].

## 1.1 Superconducting qubits

Superconducting qubits are built somewhat similar to electrical circuits, by etching away or growing layers of different materials on a substrate to form paths for current flow, making linear elements such as capacitors and inductors, and most importantly non-linear Josephson junctions [38]. This non-linearity is the key to making quantum systems with non-equidistant levels that can be individually addressed and therefore used as a qubit. Although there are a variety of different superconducting qubits, they can be generally categorized into three types [27, 30]: charge qubit [39], flux qubit [40, 41], and phase qubit [42, 43]. The main difference between the three types of qubits is the ratio of the Josephson energy to the charging (capacitive) energy. A charge qubit consists of a Josephson junction and a capacitor in parallel, yielding a shallow cosine potential where the Josephson energy is  $\sim 10 - 100$  times smaller than the charging energy. A flux qubit has an additional parallel inductor that gives it a double-well potential, with Josephson energy  $\sim 10 - 1000$  times larger than the charging energy. A phase qubit is somewhat similar to the flux qubit, but with an additional external flux bias into its loop that tilts the double well potential, with Josephson energy tens of thousands of times larger than the charging energy. Each of these qubits is designed with a specific task in mind, and is sensitive to different types of noise. For example, flux qubits are currently mostly used in quantum annealers because they can approximately realize the transverse Ising model Hamiltonian.

Currently, the preferred superconducting qubit type for gate-based quantum computation is the transmon qubit [44], which was designed by making the charge qubit less sensitive to the charge noise by having a smaller capacitive energy. In its simplest form,

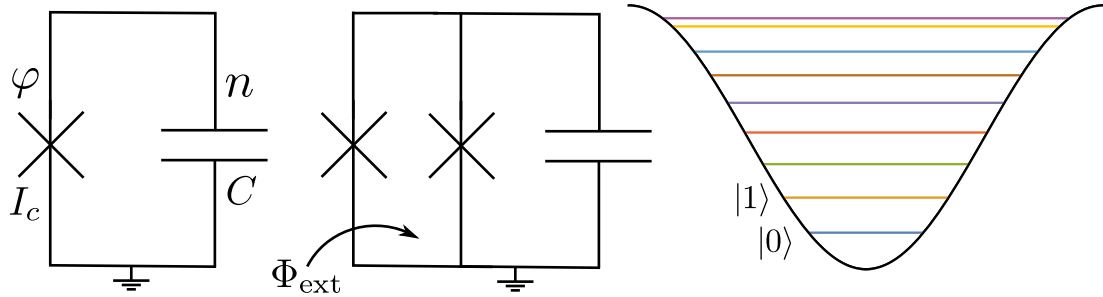


Figure 1.1: Transmon and its potential. Left: the circuit for transmon, with Josephson junction critical current of  $I_c$  and superconducting phase  $\varphi$  across it. The capacitance is  $C$ , and  $n$  is the number of Cooper pairs transferred across the junction. Middle: Frequency-tunable transmon, showing an external flux  $\Phi_{\text{ext}}$  applied into the loop consisting of two junctions. Right: Cosine potential of transmon with different energy levels, the two lowest levels of which are used as states  $|0\rangle$  and  $|1\rangle$  of the qubit.

transmon is a Josephson junction with a large capacitor in parallel (Fig. 1.1). If instead of a single junction, a loop of two junctions is used, then the qubit frequency can be tuned by applying an external magnetic flux inside that loop (see Fig. 1.1), e.g., by having a current line next to the loop (called dc flux bias). There are a variety of different flavors of transmon made with different design choices and tasks in mind [45–57].

The Hamiltonian for a transmon can be written as

$$H = 4E_C \hat{n} - E_J \cos \hat{\varphi}, \quad (1.1)$$

where  $E_C = e^2/2C$  is the charging energy,  $E_J = I_c \Phi_0/2\pi$  is the Josephson energy,  $\Phi_0 = h/2e$  is the magnetic flux quantum,  $\hat{\varphi}$  is the superconducting phase operator, and  $\hat{n}$  is its canonically conjugate operator associated with the number of Cooper pairs tunneled through the junction, such that  $[\hat{\varphi}, \hat{n}] = i$ . A transmon operates in the regime where  $E_J/E_C \sim 10^2$ –, therefore, its cosine potential acts as a slightly anharmonic oscillator, where the two lowest energy levels are used as  $|0\rangle$  and  $|1\rangle$  states of a qubit (Fig. 1.1). The

difference between  $|0\rangle \leftrightarrow |1\rangle$  transition frequency  $\omega_{10}$  and  $|1\rangle \leftrightarrow |2\rangle$  transition frequencies  $\omega_{21}$  is called the anharmonicity,  $\eta = \omega_{10} - \omega_{21} > 0$ . Higher levels of a transmon are sometimes used in practical operations, but they are more susceptible to charge noise. For more details about energy levels and states of transmon, see Appendices [A](#) and [C](#).

## 1.2 Quantum operations on transmons

Quantum gates (operations) [\[58\]](#) are applied to transmons using microwave pulses and/or fast dc flux biases, i.e., nearby current lines that induce magnetic flux into superconducting loops. To implement single qubit X and Y gates (Pauli  $\sigma_x$  and  $\sigma_y$ ), the qubit is directly driven by a microwave tone via a coupled transmission line, or sometimes via a coupled bus resonator. Naturally, if the frequency of the microwave drive is the same as the frequency of the qubit, then it induces Rabi oscillations on the qubit. By properly adjusting the envelope, amplitude, duration, and phase of these pulses, rotations around an arbitrary axis in the x-y plane are performed (see Ref. [\[59\]](#) for a short review). For Z rotations, there are a few methods that we briefly mention here. Note that these Z gates are better understood in the rotating frame of the qubit (which is usually used in practice), where the qubit does not revolve around its z-axis with frequency  $\omega_{10}$ . A simple method is to apply composite/consecutive X and Y gates to construct a Z gate, a natural property of Pauli operators. However, faster gates with better control and fidelity can be made as well. For tunable qubits, one can tune the qubit frequency away and then back to its original value, which effectively induces a rotation around the z-axis in the rotating frame of the qubit, and can be calibrated by adjusting the duration and magnitude of the frequency change [\[60\]](#).

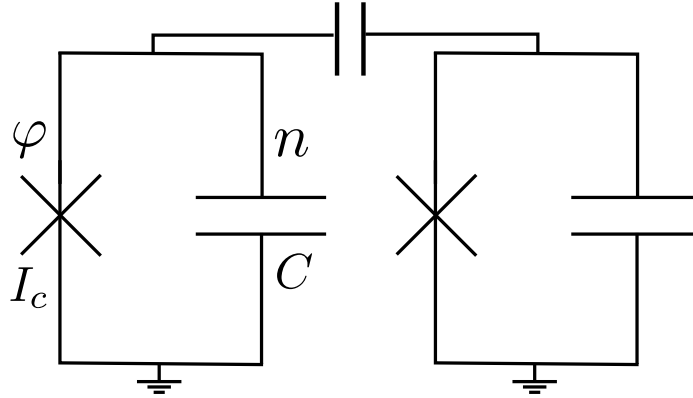


Figure 1.2: Two transmon qubits coupled directly via a capacitor. This direct coupling scheme is also referred to as capacitive or charge-charge coupling. The coupling is required for implementing two-qubit entangling gates.

Another method is to just add a phase offset in the software controlling the x-y pulse line, and redefine the rotation axis for all the subsequent  $X$  and  $Y$  rotations. This is equivalent to redefining the rotating frame whenever a z-axis rotation is needed, and is called a virtual  $Z$  gate [59, 61]. Single qubit gates are routinely implemented in superconducting qubits, and can achieve fidelities of 99.9% or more [59, 62, 63].

Two-qubit entangling gates are generally harder to master and calibrate, with a variety of methods for their implementation depending on the architecture, design choices, and trade-offs. These gates require coupling between qubits, which can either be a direct coupling (e.g., as in Fig. 1.2), or an indirect coupling through a coupler circuit. Below we briefly discuss the two main approaches for implementing entangling gates, depending on whether the qubit frequencies are tunable or not.

For frequency-tunable qubits, the main approach is to bring the  $|0\rangle \leftrightarrow |1\rangle$  transition frequency of the control qubit close to the  $|1\rangle \leftrightarrow |2\rangle$  transition of the target qubit, and after

allowing some time for interaction, tune it away to its initial frequency [64–66]. During this operation (which can be performed relatively fast and yet adiabatic [66]), the target qubit can acquire extra phase because of an avoided level crossing between  $|11\rangle$  and  $|02\rangle$  states, which is used to implement a controlled-phase (i.e., CZ) gate between the qubits <sup>1</sup>. Practical implementation of these gates have fidelities ranging from 90% [67] to more than 99% [62, 68].

The other widely-used type of entangling gate is used for frequency-fixed qubits, and is called cross-resonance (CR) gate [69], where the control qubit is driven at the frequency of the target qubit. Such a cross resonant drive rotates the target qubit along the x-axis with a rate that depends on the state of the control qubit. Simply speaking, this happens because of the eigenstate formation between the two qubits, and may be thought of as a quantum (and unavoidably classical) crosstalk effect [70]. With addition of single-qubit gates on the target qubit, the CR interaction is turned into common two-qubit gates such as CNOT, implemented with fidelities reaching 99% [71].

Besides the two main types of entangling gates mentioned above, there are other methods for implementing two-qubit gates, some of which require flux tunability of the qubits [72, 73], and some use direct microwave pulses to activate desired coupling between the qubits [74–77].

---

<sup>1</sup>With addition of some single-qubit gates, other two-qubit gates can be implemented as well.

### 1.3 Dispersive measurement of superconducting qubits

The measurement of the state of the transmon is done in a circuit QED (cQED) setup [78] as outlined below. The transmon is coupled to a detuned readout resonator (i.e., a quantum harmonic oscillator), where the resonator can be pumped and its leaked field can be amplified and measured [see Fig. 1.3(a)]. Because of the eigenstate formation between the qubit and the resonator, the frequency of the resonator will depend on the state of the qubit [Fig. 1.3(b)]. To distinguish the slightly different resonator frequencies (associated with different qubit states), the resonator is pumped, and its leaked output field is measured. This output field will have distinct amplitude and phase shift depending on the resonator frequency [Fig. 1.3(c)], which is then used to infer the state of the qubit.

More formally, when the coupling between the qubit and resonator is much smaller than the detuning between them, one can approximately calculate eigenenergies of the system to approximately write the interaction between the qubit and the resonator as

$$H_I \approx \chi \sigma_z a^\dagger a, \quad (1.2)$$

where  $\sigma_z = |0\rangle\langle 0| - |1\rangle\langle 1|$  is the qubit Pauli Z operator, and  $a$  ( $a^\dagger$ ) is the resonator lowering (raising) operators. We can see from Eq. (1.2) that the dispersive coupling changes the resonator frequency by  $2\chi$  when the qubit goes from the excited to the ground state [see Fig. 1.3(b)]. The total dispersive shift of the resonator frequency is (see Appendix A)

$$2\chi \approx 2 \frac{g^2}{\Delta} \frac{\eta}{\Delta + \eta} \frac{\omega_r}{\omega_q}, \quad (1.3)$$

where  $g$  is the coupling between the qubit and the resonator,  $\omega_r$  and  $\omega_q$  are bare frequencies of the resonator and the qubit respectively,  $\Delta = \omega_r - \omega_q$  is the detuning between the two,

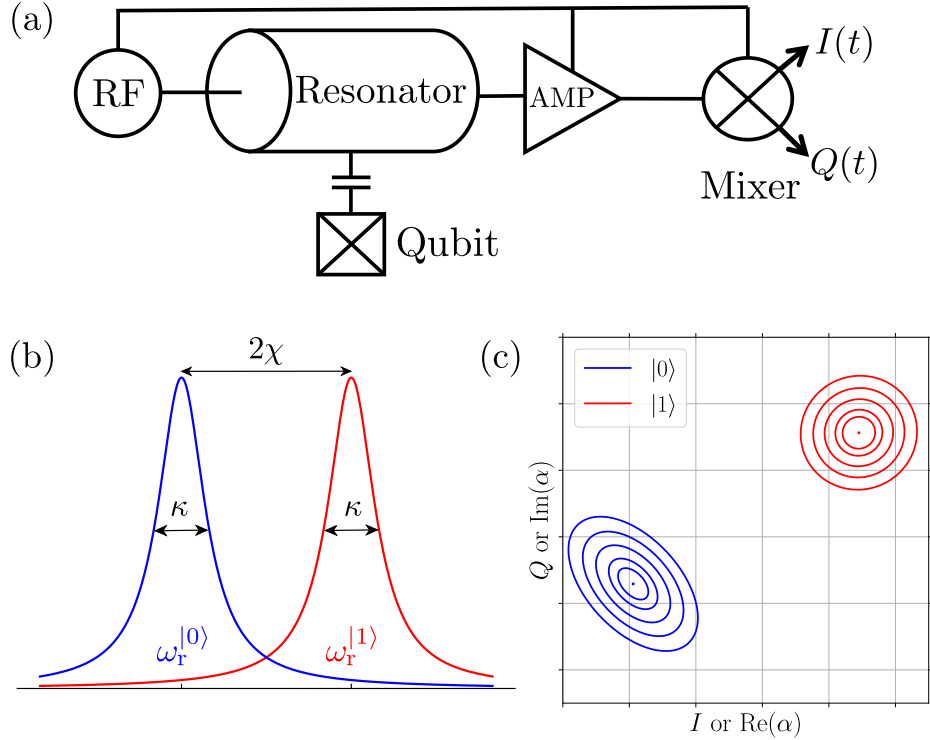


Figure 1.3: (a) Schematic of the dispersive readout, where the qubit is coupled to a readout resonator, the resonator is pumped with a coherent drive (RF), and the leaked field of resonator is amplified (AMP) and passed through a mixer. (b) Schematic of the transmission spectrum of the resonator. The two Lorentzians are centered around the resonator frequency when the qubit is in the ground ( $\omega_r^{(0)}$ ) or excited ( $\omega_r^{(1)}$ ) state, with width of  $\kappa$  (resonator energy decay rate). The total dispersive shift is  $2\chi$ . (c) Example of the intracavity state of the resonator in the I-Q plane. The two blobs correspond to different qubit states. The state becomes significantly squeezed for relatively large number of photons in the resonator.

and  $\eta > 0$  is the anharmonicity of the qubit. When the readout resonator is pumped with a coherent tone, we can write the approximate classical evolution equation (i.e., coherent state evolution) for the resonator state [78]

$$\dot{\alpha} = -i \left( \omega_r^{(q)} - \omega_d \right) \alpha - \frac{\kappa}{2} \alpha - i\varepsilon, \quad (1.4)$$

where  $\omega_r^{(q)}$  is the resonator frequency when the qubit is in state  $|q\rangle$ ,  $\omega_d$  is the drive frequency,  $\kappa$  is the energy decay rate of the resonator, and  $\varepsilon$  is the drive amplitude. The coherent

state approximation becomes inaccurate for sufficiently strong drive tones [79, 80], when squeezing develops as shown in Fig. 1.3(c). The resonator field is then leaked, amplified, and measured, which can be done in two ways. One approach is to use a phase-sensitive amplifier, which amplifies only one quadrature of the signal, and then the amplified quadrature  $I$  is measured. The other approach is to use a phase-preserving amplifier, which amplifies both quadratures  $I$  and  $Q$ , then both quadratures are measured at the same time. Fig. 1.3(c) depicts the phase-space representation of the intracavity resonator field, where the blobs show the uncertainty in the measurement of  $\alpha$ . In both amplification schemes, the signal for when qubit is in the ground state is discriminated from the signal when the qubit is in the excited state. Amplifiers are essential to the measurement of superconducting qubits, and their development played an important role in achieving high-fidelity single-shot readout [81–87]. The theoretical details of phase-preserving (heterodyne) or phase-sensitive (homodyne) quadrature measurements are discussed in Refs. [88–90], and are out of the scope of this chapter.

We note that in practice, the readout signal can be transmitted through the resonator, as depicted in Fig. 1.3(a), or it can be reflected from the resonator. The main difference between these two schemes is that the reflected signal contains directly-reflected pump microwave; nevertheless, both methods are the same from the perspective of the theory of dispersive measurement. Also note that by coupling the qubit to the resonator, we are indirectly coupling it to the environment, which unavoidably leads to energy decay in the qubit, called Purcell decay [91]. Moreover, faster measurement requires stronger coupling to the environment, which comes at the price of degrading the qubit lifetime. This

problem can be mitigated by adding a Purcell filter [92–96] to the measurement chain, which essentially prevents the photons at the qubit frequency from leaking to the environment, but allows for the measurement signal at resonator frequency to pass, therefore increasing qubit lifetime without sacrificing readout speed.

Practical quantum computation requires fast and accurate measurement of the qubits [58], a task which is specifically important for the repetitive syndrome measurement schemes of the error-corrected systems [97–99]. Consequently, dispersive cQED measurement of superconducting qubits has been studied and improved in different aspects over the years. Purcell filters are now used to suppress the qubit relaxation through the readout resonator [93, 95], the resonator leftover photon population can be actively emptied for the next measurement [100, 101], and machine learning techniques can be utilized to discriminate the qubit states in the I-Q plane [102] to name a few. The qubit readout fidelities are now reaching 99% in under 100 ns [103], and the effort to increase the fidelities and decrease the readout time still continues.

In this dissertation, we explore the dispersive measurement of the qubits, investigate some mechanisms that can deteriorate measurement of the superconducting qubits, and introduce tools and methods for studying these systems. In Chapter 2 and briefly in Chapter 4, we investigate how the presence of neighboring qubits affects the measurement of the superconducting qubits. Such analysis is important since practical quantum computers require an array of qubits to interact with each other, and at the same time they require individual readout capability for each qubit. Chapter 3 studies the Jaynes-Cummings ladder of the qubit-resonator system to provide an approximate yet accurate model for the

joint system in its eigenbasis. This chapter emphasizes the importance of the eigenbasis picture when studying the dispersive readout. In Chapter 4 we go beyond the usual approximations made in the modeling of the dispersive readout, find the underlying reason for mysterious readout deterioration at large photon numbers, and confirm our theory with experimental observations. Such large photon-number regimes are essential for fast measurement of qubits, and studying them helps us to understand the limitations of the dispersive measurement and design more clever readout schemes. In Chapter 5 we study the evolution of the pumped readout resonator and provide a simple yet accurate model for the resonator field that is extremely efficient in numerical simulations. Chapter 6 extends this model to study the propagating field that leaks out of the resonator. Such models can be used to minimize the uncertainty (maximize SNR) in the phase-sensitive and/or phase-preserving measurements, and can also be used for studying squeezed light. We conclude in Chapter 7.

## Chapter 2

# Qubit measurement error from coupling with a detuned neighbor in circuit QED

In modern circuit QED architectures, superconducting transmon qubits are measured via the state-dependent phase and amplitude shift of a microwave field leaking from a coupled resonator. Determining this shift requires integrating the field quadratures for a nonzero duration, which can permit unwanted concurrent evolution. In this chapter we investigate such dynamical degradation of the measurement fidelity caused by a detuned neighboring qubit. We find that in realistic parameter regimes, where the qubit ensemble-dephasing rate is slower than the qubit-qubit detuning, the joint qubit-qubit eigenstates are better discriminated by measurement than the bare states. Furthermore, we show that when the resonator decays much more slowly than the qubit-qubit detuning, the measure-

ment tracks the joint eigenstates nearly adiabatically. However, the measurement process also causes rare quantum jumps between the eigenstates. The rate of these jumps becomes significant if the resonator decay is comparable to or faster than the qubit-qubit detuning, thus significantly degrading the measurement fidelity in a manner reminiscent of energy relaxation processes.

## 2.1 Introduction

Recent years have witnessed the rapid evolution of superconducting circuit QED technology for quantum computation [49, 68, 72, 78, 104–108] (reviewed in [28, 109, 110]). The most recent developments have converged on charge-insensitive designs, based on transmons [44], which can be dispersively measured with coupled microwave resonators. Multi-qubit chips based on these designs have recently demonstrated high-fidelity entangling gates [49, 68], which are now nearing the gate fidelity thresholds necessary for implementing practical quantum error correction protocols [58, 98, 111]. Indeed, several groups have recently demonstrated bit-flip error correction in such multi-qubit superconducting processors [50, 62, 112, 113]. With the gate fidelity reaching such unprecedented levels, it is now interesting to identify and address more subtle sources of error that can arise in such a multi-qubit environment, such as the effect of non-tunable qubit-qubit or qubit-bus coupling [114] on the dispersive measurement fidelity.

Unlike the textbook projective measurements usually assumed in the quantum computing literature [58], which involve instantaneous state collapse, realistic measurements occur over a nonzero duration of time. In the transmon-based circuits we consider

here, each qubit is dispersively coupled to a pumped microwave resonator such that the leaked field is phase-shifted (and, in general, amplitude-shifted) by a qubit-state-dependent amount [78]. The leaked field is then passed through an amplifier and mixed with a local oscillator to produce a noisy homodyne signal. This signal needs to be integrated until the signal-to-noise ratio exceeds an acceptable discrimination threshold (more advanced signal processing techniques can moderately increase the measurement fidelity [115]). For an isolated qubit, the increase of the signal-to-noise ratio by longer integration is limited by the energy relaxation (and excitation) processes. However, in circuits intended for quantum computation, the qubits will also be coupled to frequency-detuned neighbors, which may permit unwanted dynamics to additionally degrade the measurement fidelity. We wish to better understand the detailed dynamics of a realistic transmon qubit measurement, and minimize the dynamical measurement error that will arise from the coupling to a neighboring qubit (or bus, which plays a similar role).

In this chapter, we demonstrate that in typical experimental parameter regimes, where the qubit ensemble-dephasing rate due to measurement is slower than the qubit-qubit detuning, dynamical measurement error always exists when distinguishing the bare energy states of coupled qubits. However, this measurement error can be decreased by distinguishing not the bare energy states, but instead the qubit-qubit *eigenstates* that are stationary under the effect of the qubit-qubit coupling and detuning (similarly to the measurement of coupled phase qubits analyzed in [114]). Despite the fact that only the main qubit is being measured, the relatively slow measurement process allows the two-qubit system to collapse to these stationary eigenstates, in contrast to what may be naively expected from textbook

projective measurements. Notably, these eigenstates have also been shown to be a natural choice for the logical encoding of high-fidelity multi-qubit gates [114] (for similar reasons), which makes multi-qubit eigenstates an unambiguously optimal choice for logical encoding in realistic parameter regimes.

We further demonstrate for coupled transmon measurement that, in addition to the ensemble-dephasing rate and the qubit-qubit detuning, the measurement fidelity depends on a third important parameter: the readout resonator energy decay rate due to leakage into a transmission line. For decay rates much slower than the qubit-qubit detuning (as is typical in experiments, e.g., [50, 62, 113]), the leaked resonator field nearly adiabatically follows the qubit-qubit eigenstate to produce little error. However, for decay rates that are comparable to or larger than the qubit-qubit detuning, the resonator decays more rapidly than it can equilibrate with the qubit-qubit eigenstates, causing frustrated dynamics during the measurement. Such rapid resonator decay will primarily couple the leaked field to the bare energy states, while the fast inter-qubit oscillations (compared to the measurement rate) will relate the output signal to the joint qubit-qubit eigenstates. This frustrated dynamics leads to random quantum jumps between the eigenstates. We derive the rate of these quantum jumps (which we call a switching rate) using a model based on fluctuations of the photon number in the resonator, which perturb the two-qubit eigenstates. We show that the switching can be significant for rapid resonator decay, but becomes almost negligible for realistically slow resonator decay. We also derive the measurement error probability resulting from these quantum jumps, and show that it accumulates almost linearly with integration time in an analogous way to the error from energy-decay ( $T_1$ ) processes.

This chapter is organized as follows. In Section 2.2, we introduce the considered system, formulate the problem, and discuss how to model the ensemble-averaged dynamics. In Section 2.3, we identify three qualitatively distinct parameter regimes in the ensemble-averaged dynamics: textbook, adiabatic, and frustrated. In Section 2.4, we study the transition between the adiabatic and frustrated regimes as the resonator decay is varied, by introducing a simple model of a semiclassically fluctuating field in the resonator that produces random quantum jumps between the eigenstates. We derive the average switching rate for these jumps, and numerically confirm this jump behavior by simulating quantum trajectories in the fast resonator decay regime. In Section 2.5, we demonstrate that the contribution of these jumps to the measurement error is nearly linearly increasing with integration time, and find the error minimized over the integration time. We conclude in Section 2.6.

## 2.2 Considered system and its ensemble-averaged evolution

The archetypal circuit QED system we consider here is shown in Fig. 2.1. A superconducting transmon (main qubit) with frequency  $\omega_q$  (which includes the ac Stark shift) is capacitively coupled to a driven readout resonator with bare frequency  $\omega_r$ , and is also capacitively coupled to another transmon (neighboring qubit) with a detuned bare frequency  $\omega_n$ , such that the qubit-qubit detuning  $\Delta \equiv \omega_q - \omega_n$  is much larger than the qubit-qubit coupling  $g$ ,  $|\Delta| \gg g$ . (The role of the neighboring qubit can be played by a bus resonator; we consider a qubit for definiteness.) We assume that the Purcell decay [91, 116, 117] of the main qubit through the resonator has been suppressed by a filter

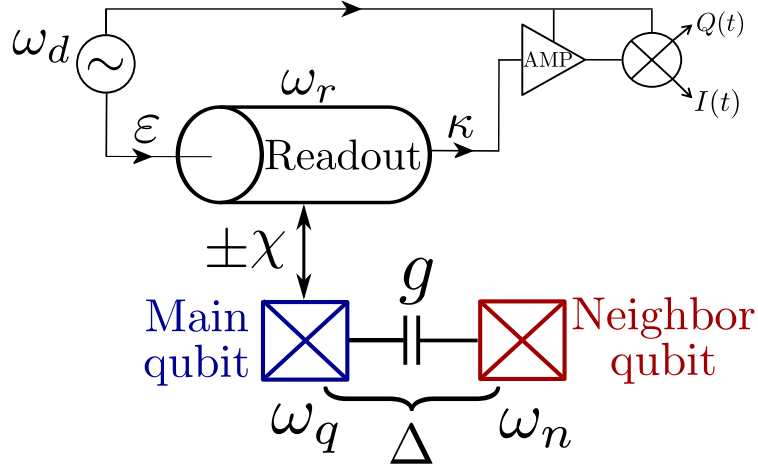


Figure 2.1: Analyzed system. A measured (main) transmon qubit (blue) with frequency  $\omega_q$  has capacitive coupling  $g$  to a detuned neighboring qubit (red) with a frequency  $\omega_n$  such that  $g \ll |\Delta|$ , where  $\Delta \equiv \omega_q - \omega_n$  ( $\omega_q$  includes the ac Stark shift). A readout resonator with frequency  $\omega_r$  is dispersively coupled to the main qubit, and thus is frequency-shifted by  $\pm\chi$  depending on the main qubit state. During measurement, this resonator is driven with a coherent microwave  $\varepsilon$  at a frequency  $\omega_d$ . The field leaks from the resonator (with the energy decay rate  $\kappa$ ) to a transmission line, where it is amplified and mixed with a local oscillator to measure the quadrature  $I(t)$  that is sensitive to the qubit-state-dependent phase and amplitude shift. The coupling of the main qubit with the neighboring qubit contributes to the qubit measurement error.

[92, 93, 95], and that the resonator and main qubit are sufficiently detuned to treat their coupling as effectively dispersive (implying the rotating wave approximation) [78, 118]. We also assume that the transmon energy levels outside of the qubit subspace are taken into account through renormalization of the state-dependent dispersive shift  $\pm\chi$  of the resonator frequency. The readout resonator is additionally driven by a coherent field  $\varepsilon$  at a microwave frequency  $\omega_d$ , which then leaks to a transmission line at an energy-decay rate  $\kappa$  (the setup can be either in transmission or in reflection). The leaked field is passed through an amplifier and mixed with a local oscillator to perform a homodyne measurement, which isolates the qubit-state-dependent phase and amplitude shift caused by the dispersive coupling; the

information-carrying quadrature is denoted as  $I(t)$  in Fig. 2.1.

While this measurement procedure is largely understood for a single qubit coupled to the readout resonator [78, 118–120], we investigate here how the addition of the neighboring qubit will contribute to the measurement error. Specifically, we wish to find out whether the wavefunction “tail” probability  $(g/\Delta)^2$  contributes to the measurement error or not. In this chapter we focus on discriminating the bare states  $|10\rangle$  and  $|00\rangle$  (with qubit ordering convention  $|\text{main, neighbor}\rangle$ ) or the states  $|\overline{10}\rangle$  and  $|00\rangle$ , where  $|\overline{10}\rangle$  is the eigenstate that accounts for the qubit-qubit interaction. We assume the logic state of zero for the neighboring qubit for simplicity, without significant loss of generality, because the discrimination of the states  $|11\rangle$  and  $|01\rangle$  (or  $|11\rangle$  and  $|\overline{01}\rangle$ ) is a very similar problem. Also, the discrimination of all four states in the case when both qubits are measured is a simple generalization of our basic problem. Note that we do not consider another important question: deterioration of a superposition  $\alpha|00\rangle + \beta|01\rangle$  (or  $\alpha|00\rangle + \beta|\overline{01}\rangle$ ) after the main qubit measurement; however, the mechanism of this deterioration is similar to what we consider. Also note that in an architecture [114, 121], in which the zero state of the neighboring qubit is used as a resource to decrease crosstalk, our assumption of discriminating  $|10\rangle$  and  $|00\rangle$  (or  $|\overline{10}\rangle$  and  $|00\rangle$ ) is naturally satisfied. We will refer to the pair of states to be discriminated as logical 1 and 0.

The logical states are discriminated by integrating the fluctuating output signal  $I(t)$  over time and then comparing the result with a threshold. Therefore, the discrimination error  $P_{\text{err}}$  (discussed in more detail in Sec. 2.5) can be calculated from the “overlap” of the probability distributions of the integrated result for the two logical states. The error

depends on the chosen threshold (in Sec. 2.5 we will consider the symmetric and optimal thresholds) and on the integration time. As will be discussed later, the measurement error  $P_{\text{err}}$  has a minimum as a function of the integration time, which is determined by the rate of “switching” (quantum jumps) between the qubit states, resembling the energy relaxation events.

Our final goal is to find such optimized measurement error for distinguishing the bare-basis states  $|10\rangle$  and  $|00\rangle$ , and for distinguishing the eigenbasis states  $|\overline{10}\rangle$  and  $|00\rangle$ , thus finding which encoding basis is preferable in the circuit QED measurement. The analysis of a similar question for the measurement of phase qubits showed [114] that using the eigenbasis is preferable. In this chapter we will obtain a similar result for the parameter regime of typical circuit QED measurements [50, 62, 113], even though the measurement dynamics is significantly more complicated than for phase qubits. In particular, we will show that in contrast to what is expected for a textbook projective measurement, the bare-basis error exceeds  $(g/\Delta)^2/2$ , while there is no such limitation for discriminating the eigenstates. For the eigenbasis the limitation comes from the quantum jumps between the eigenstates  $|\overline{10}\rangle$  and  $|\overline{01}\rangle$ ; however, for typical experimental parameters this limitation is almost negligible.

To obtain these results, we first discuss how to model both the coherent and incoherent aspects of the evolution for the ensemble-averaged case. This ensemble-averaged dynamics will be sufficient to identify broad parameter regimes of interest for the coupled-qubit measurement, and to identify which qubit-qubit bases are preserved by the measurement in these regimes, but will be insufficient for understanding and quantifying the measurement error for specific realizations. In Section 2.4, we will generalize the ensemble-averaged ap-

proach to model the individual quantum trajectories, which will allow us to understand and derive the measurement error induced by the qubit-qubit coupling. Note that we consider only one neighboring qubit, while in practical architectures (e.g., in surface codes) there are several neighbors; however, the generalization of our theory to several neighboring qubits is rather straightforward.

### 2.2.1 Coherent evolution

The total resonator-qubit-qubit Hamiltonian can be split into five terms,

$$H = H_r + H_q + H_d + H_{qr} + H_{qq}. \quad (2.1)$$

The bare-energy contributions ( $\hbar = 1$ ) are

$$H_r = \omega_r a^\dagger a, \quad H_q = \frac{\omega_q^b}{2} \sigma_z^{(1)} + \frac{\omega_n}{2} \sigma_z^{(2)}, \quad (2.2)$$

where  $\sigma_z^{(j)} \equiv |1\rangle\langle 1|_j - |0\rangle\langle 0|_j$  are the Pauli  $z$  operators for each qubit ( $j = 1, 2$ ),  $a^\dagger$  ( $a$ ) are the raising (lowering) operators of the coupled resonator mode that satisfy  $[a, a^\dagger] = 1$ , and  $\omega_q^b$ ,  $\omega_n$ , and  $\omega_r$  are the bare frequencies of the main qubit, neighboring qubit, and resonator.

The resonator drive contribution has the form

$$H_d(t) = \varepsilon e^{-i\omega_a t} a^\dagger + \varepsilon^* e^{i\omega_a t} a. \quad (2.3)$$

The bare energies are modified by the dispersive qubit-resonator coupling

$$H_{qr} = \chi \sigma_z^{(1)} a^\dagger a, \quad (2.4)$$

which shifts the resonator frequency by  $\pm\chi$  depending on the qubit state or, alternatively, shifts the qubit frequency,

$$\omega_q = \omega_q^b + \delta\omega_q, \quad (2.5)$$

by the ac Stark shift  $\delta\omega_q$ , depending on the number of photons in the resonator (we include the Lamb shift [78, 122, 123] into  $\omega_q^b$ ). The qubit-qubit coupling Hamiltonian (assuming the rotating wave approximation) is

$$H_{\text{qq}} = g (|01\rangle\langle 10| + |10\rangle\langle 01|), \quad (2.6)$$

and we are interested in the case of strongly detuned qubits,  $g \ll |\omega_q - \omega_n|$  (for simplicity we assume  $g > 0$ ).

Note that the qubit-qubit coupling in Eq. (2.6) coherently mixes the single-excitation subspace  $\{|01\rangle, |10\rangle\}$  and produces the eigenstates of the qubit-qubit Hamiltonian  $H_q + H_{\text{qq}}$  that are rotated from the bare states by an angle  $\theta = \frac{1}{2} \arctan(2g/\Delta)$ ,

$$\begin{aligned} |\bar{10}\rangle &= \cos\theta|10\rangle + \sin\theta|01\rangle \approx \sqrt{1 - \left(\frac{g}{\Delta}\right)^2} |10\rangle + \frac{g}{\Delta} |01\rangle, \\ |\bar{01}\rangle &= \cos\theta|01\rangle - \sin\theta|10\rangle \approx \sqrt{1 - \left(\frac{g}{\Delta}\right)^2} |01\rangle - \frac{g}{\Delta} |10\rangle, \end{aligned} \quad (2.7)$$

where

$$\Delta \equiv \omega_q - \omega_n \quad (2.8)$$

is the (ac Stark-shifted) qubit-qubit detuning and the approximation is to lowest order in  $g/|\Delta| \ll 1$ . If the measurement process occurs effectively in this eigenbasis, then an initially bare state  $|10\rangle$  will collapse into the incorrect eigenstate  $|\bar{01}\rangle$  with an error probability  $(g/\Delta)^2$ , resulting in additional measurement error. In Section 2.3 we will clarify which parameter regimes of the measurement naturally select the eigenstates of Eq. (2.7) in this manner. Note that for brevity of notations, in inequalities describing the parameter regimes we will use  $\Delta$  instead of  $|\Delta|$ .

### 2.2.2 Incoherent evolution

In addition to the coherent evolution given by the Hamiltonian in Eq. (2.1), the energy in the resonator incoherently decays to a transmission line at the rate  $\kappa$ . Assuming that all leaked photons may not later return to the resonator, we can model the ensemble-averaged Markovian evolution of the joint qubit-qubit-resonator state with a master equation [122]

$$d\rho = -i[H, \rho]dt + (\kappa dt) a\rho a^\dagger - \frac{\kappa dt}{2} (a^\dagger a\rho + \rho a^\dagger a). \quad (2.9)$$

Physically, we can interpret this equation as stating that in a small interval  $dt$  the system does not only coherently evolve with the usual evolution operator

$$U = \exp(-iHdt),$$

but additionally has one of two distinct incoherent processes happen (e.g., Ref. [124]):

- (a) Each of  $N$  photons in the resonator may escape with probability  $\kappa dt$ , which modifies the resonator state with the decay operator

$$M_{\text{decay}} = \sqrt{\kappa dt} a.$$

- (b) All  $N$  photons stay in the resonator with probability  $1 - \kappa dt N$ , which modifies the resonator state with the null result (no decay) operator

$$M_{\text{null}} = \sqrt{\mathbb{1} - \kappa dt a^\dagger a}.$$

These measurement (Kraus) operators for the incoherent part of the evolution satisfy the usual completeness condition  $M_{\text{decay}}^\dagger M_{\text{decay}} + M_{\text{null}}^\dagger M_{\text{null}} = \mathbb{1}$ , indicating that the probabilities for each possibility to occur are correctly normalized [58]. Mixing together both

possibilities (i.e., discarding any record of whether the decay happened or not) produces the updated mixed state

$$\begin{aligned}\rho' &= M_{\text{decay}}\rho M_{\text{decay}}^\dagger + M_{\text{null}}\rho M_{\text{null}}^\dagger, \\ &= \kappa dt a\rho a^\dagger + \sqrt{\mathbb{1} - \kappa dt a^\dagger a} \rho \sqrt{\mathbb{1} - \kappa dt a^\dagger a},\end{aligned}\tag{2.10}$$

that describes the ensemble-averaged evolution for a duration  $dt$ . The Hamiltonian evolution is then interleaved between these incoherent updates:  $\rho' \mapsto U\rho'U^\dagger$ . Expanding the full increment  $d\rho \equiv U\rho'U^\dagger - \rho$  to linear order in  $dt$  produces the standard master equation form of Eq. (2.9). We note, however, that the update in Eq. (2.10) is not only conceptually transparent, but (as we checked) is more numerically stable for simulation purposes and in some regimes is faster than solving Eq. (2.9).

If additional decay channels are present, they can be added phenomenologically to the incoherent sum in Eq. (2.10). For example, qubit energy-decay with rate  $1/T_1$  and environmental qubit dephasing with rate  $\Gamma_e$  have the forms

$$\begin{aligned}M_{T_1} &= \sqrt{dt/T_1^{(1)}} \sigma_-^{(1)} + \sqrt{dt/T_1^{(2)}} \sigma_-^{(2)}, \\ M_{\text{dephase}} &= \sqrt{\Gamma_e^{(1)} dt} \sigma_z^{(1)} + \sqrt{\Gamma_e^{(2)} dt} \sigma_z^{(2)},\end{aligned}$$

which will modify the null result operator accordingly to include all decay channels  $M_k$

$$M_{\text{null}} = \sqrt{\mathbb{1} - \sum_k M_k^\dagger M_k}.$$

These additional decay channels correspondingly modify the linear increment in Eq. (2.9) in the standard way. For simplicity, we will neglect such additional decay channels in most of what follows, in order to focus solely upon the effects of the neighboring qubit on the

measurement fidelity. When we do add these effects, we will assume that  $T_1^{(1)} = T_1^{(2)} \equiv T_1$  and  $\Gamma_e^{(1)} = \Gamma_e^{(2)} \equiv \Gamma_e$ .

Now let us briefly review some results for measurement of a *single* qubit [78, 118–120], which we will use as a starting point and to introduce notations. For the qubit in the state  $|1\rangle$  or  $|0\rangle$ , the effective frequency of the resonator is  $\omega_r \pm \chi$  (the upper sign is for the state  $|1\rangle$ ). Then the evolution of the resonator coherent state  $|\alpha_\pm\rangle = e^{-|\alpha_\pm|^2/2} \sum_n \alpha_\pm^n (n!)^{-1/2} e^{-in\omega_{at}} |n\rangle$  (we use the rotating frame  $e^{-i\omega_{at}}$ ) is

$$\dot{\alpha}_\pm = -i(\Delta_r \pm \chi) \alpha_\pm - \frac{\kappa}{2} \alpha_\pm - i\varepsilon, \quad (2.11)$$

where  $\Delta_r \equiv \omega_r - \omega_d$  is the bare resonator-drive detuning. The steady-state solution of this equation is

$$\alpha_\pm = \frac{-i\varepsilon}{\kappa/2 + i(\Delta_r \pm \chi)}, \quad (2.12)$$

and the corresponding mean photon number is

$$\bar{n}_\pm = |\alpha_\pm|^2 = \bar{n}_{\max} \frac{\kappa^2}{\kappa^2 + 4(\Delta_r \pm \chi)^2}, \quad (2.13)$$

which we expressed via the photon number at exact resonance,  $\bar{n}_{\max} = 4|\varepsilon|^2/\kappa^2$ . The ac Stark shift is then [118]

$$\delta\omega_q = 2\chi \operatorname{Re}(\alpha_+^* \alpha_-), \quad (2.14)$$

and the measurement-induced ensemble dephasing rate is [118]

$$\Gamma_m = 2\chi \operatorname{Im}(\alpha_+^* \alpha_-) = \kappa \frac{|\alpha_+ - \alpha_-|^2}{2}. \quad (2.15)$$

These results can be expressed in terms of  $\bar{n}_\pm$  and  $\bar{n}_{\max}$  as

$$\delta\omega_q = 2\chi \frac{\bar{n}_+ \bar{n}_-}{\bar{n}_{\max}} \left[ 1 + \frac{4(\Delta_r^2 - \chi^2)}{\kappa^2} \right], \quad (2.16)$$

$$\Gamma_m = \frac{8\chi^2}{\kappa} \frac{\bar{n}_+ \bar{n}_-}{\bar{n}_{\max}}, \quad (2.17)$$

which reduce to the simple formulas [78, 118]  $\delta\omega_q \approx 2\chi\bar{n}$ ,  $\Gamma_m \approx 8\chi^2\bar{n}/\kappa$  when  $\bar{n}_+ \approx \bar{n}_- \approx \bar{n}_{\max}$ . One of the ways to interpret the measurement-induced dephasing process is as being caused by fluctuations of the ac Stark shift that arise from the fluctuating photon number. The total ensemble-dephasing rate  $\Gamma = \Gamma_m + \Gamma_e$  generally includes additional environmental dephasing  $\Gamma_e$ , but we will mostly neglect  $\Gamma_e$  for simplicity. The measurement-induced ensemble dephasing is related to the *distinguishability time* (sometimes called the “measurement time”)

$$\tau \equiv (2\eta\Gamma_m)^{-1}, \quad (2.18)$$

needed for achieving unit signal-to-noise ratio in the quadrature output, where  $\eta \in [0, 1]$  is the quantum efficiency of the detection circuit.

We emphasise that these standard results for  $\delta\omega_q$  and  $\Gamma_m$  are for the measurement of a single qubit; moreover, they implicitly assume the “bad cavity limit” in the sense that the qubit evolution is much slower than  $\kappa$  (in this case it is sufficient to consider only coherent states in the resonator, entangled with the qubit, which leads to relatively simple formulas). Therefore, we should not expect that these results are directly applicable to our problem, which focuses on evolution involving the neighboring qubit. In particular, when the qubit-qubit detuning  $\Delta$  is larger than  $\kappa$ , the relatively slow fluctuations of the photon number in the resonator will not produce the same dephasing  $\Gamma_m$  between the states [10]

and  $|01\rangle$  (as would be expected for infinitely fast fluctuations). Similarly, for  $\Delta \gg \kappa$  the ac Stark shift contribution to  $\Delta$  is supposed to be governed mainly by  $\bar{n}_+$  (or  $\bar{n}_-$  if the main state is  $|01\rangle$ ) rather than given by Eq. (2.16). Even though  $\Gamma_m$  in Eq. (2.17) does not in general describe the ensemble dephasing between  $|10\rangle$  and  $|01\rangle$ , in this chapter we will extensively use  $\Gamma_m$  defined in Eq. (2.17) as a notation.

### 2.3 Eigenstates vs. bare states

A master equation is incapable of describing the fidelity of the qubit measurement, even in principle, so we will be forced to consider the individual quantum trajectories in Section 2.4. Nevertheless, even without a more detailed trajectory description we can already answer the most basic question about the qubit measurement: does the ensemble-averaged evolution faithfully preserve a logical qubit basis?

To answer this question, we simulate the full master equation in Eq. (2.9) [equivalently, Eq. (2.10) can be iterated] starting in either a bare state  $|10\rangle$ , or an eigenstate  $|\overline{10}\rangle$ , with the resonator in an initial ground state for simplicity (the simulation starting in the state  $|00\rangle$  is trivial). When starting in  $|10\rangle$ , we calculate the evolution of the bare state population  $P_{10}$ , and when starting in  $|\overline{10}\rangle$ , we calculate the eigenstate population  $P_{\overline{10}}$  (see the left and right panels in Fig. 2.2). If one of these populations remains very close to 1, then we infer that the corresponding basis is faithfully preserved by the measurement dynamics.

As shown in Fig. 2.2, from these simulations we identify three parameter regimes that have qualitatively different behaviors (using  $g \ll \Delta$  and  $\Gamma_e = 0$ ):

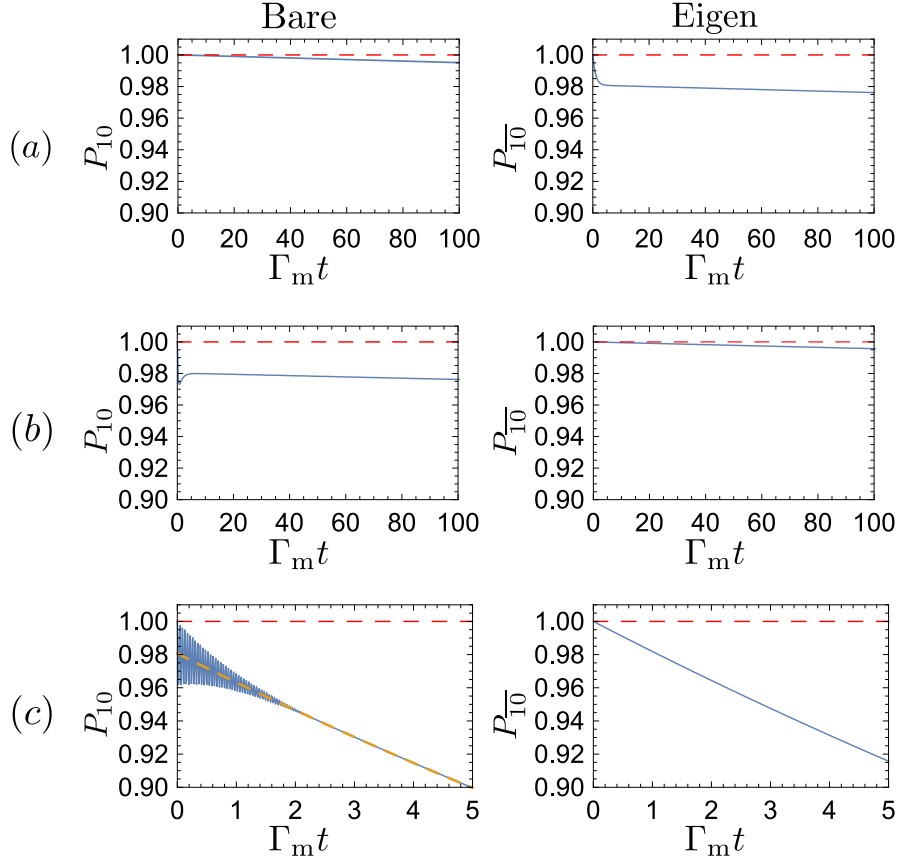


Figure 2.2: Blue lines: ensemble-averaged evolution of the population  $P_{10}$  of the bare-basis state  $|10\rangle$  when the evolution starts in this state (left panels) and the population  $P_{\bar{10}}$  of the eigenstate  $|\bar{10}\rangle$  when starting in this state (right panels). The dashed red lines show the initial value 1 of all blue lines for reference. The time is normalized by the ensemble-dephasing rate  $\Gamma_m$  due to measurement; we assume fixed qubit-qubit coupling and detuning with  $g/\Delta = 1/10$  for all regimes. (a) Textbook regime with  $\Delta \ll \Gamma_m \ll \kappa$ , using directly applied qubit-dephasing of  $\Gamma_m/\Delta = 20$  for simplicity (i.e., assuming  $\kappa \rightarrow \infty$ ). The bare state  $|10\rangle$  is best preserved by the evolution, but slowly decays at the rate  $2g^2/\Gamma_m$ , while the eigenstate population  $P_{\bar{10}}$  additionally drops by approximately  $2(g/\Delta)^2$ . (b) Adiabatic (experimental) regime with  $(\Gamma_m, \kappa) \ll \Delta$ , using  $\kappa/\Delta = 10^{-1}$  and  $\Gamma_m/\Delta = 10^{-2}$ , set by assuming a weak response  $\chi/\kappa = 3.5 \times 10^{-2}$  and a resonator drive  $\omega_d = \omega_r$  with power tuned to produce the steady-state photon number  $\bar{n} = 10$ . The eigenstate  $|\bar{10}\rangle$  is best preserved by the evolution, but slowly decays (analogously to the textbook regime for  $P_{10}$ ), while the bare population  $P_{10}$  additionally drops by  $2(g/\Delta)^2$ . (c) Frustrated regime with  $\Gamma_m \ll \Delta \ll \kappa$ , using  $\kappa/\Delta = 10$  and  $\Gamma_m/\Delta = 10^{-4}$ , keeping the same  $\chi/\Delta$  and  $\bar{n}$  as in the adiabatic regime. The bare state population  $P_{10}$  drops by  $2(g/\Delta)^2$  compared to the eigenstate population  $P_{\bar{10}}$ , and both populations show rapid decay. The decay rate seen in regimes (b) and (c) matches the analytical results for averaged incoherent quantum jumps between the eigenstates (see Fig. 2.4), an example of which is shown here in the bare (c) plot as the overlaid dashed yellow curve.

- (a)  $\Delta \ll (\Gamma_m, \kappa)$  : textbook — *almost stable bare state*,
- (b)  $(\Gamma_m, \kappa) \ll \Delta$  : adiabatic — *almost stable eigenstate*,
- (c)  $\Gamma_m \ll \Delta \ll \kappa$  : frustrated — *unstable eigenstate*.

The parameters used for each of these regimes are detailed in the caption for Fig. 2.2. As expected from the similar analysis for measurement of phase qubits [114], for  $\Gamma_m \ll \Delta$  the measurement effectively occurs in the eigenbasis, while the traditional (textbook) bare-basis measurement requires  $\Gamma_m \gg \Delta$ . However, transmon qubits have an additional important parameter that has no analogue in phase qubits: the resonator energy-decay rate  $\kappa$ . As we will see, the relative magnitudes of  $\kappa$  and  $\Delta$  determine the “stability” of the eigenbasis.

In the regime (a), the resonator empties and the system dephases much faster than the qubit-qubit evolution, so the *bare states*  $|10\rangle$  and  $|00\rangle$  are preserved as the optimal logical basis, just as we would expect from a textbook projective measurement. That is, our numerical simulation in Fig. 2.2(a) shows that the bare state population  $P_{10}$  is preserved practically at 1, while the eigenstate population  $P_{\overline{10}}$  (when starting with  $|\overline{10}\rangle$ ) drops by roughly  $2(g/\Delta)^2$  during the transient (collapse) evolution. [Here one factor of  $(g/\Delta)^2$  stems from the physical collapse of the eigenstate to an incoherent mixture of the single-excitation bare states  $|10\rangle$  and  $|01\rangle$ , while the second factor  $(g/\Delta)^2$  comes from plotting the eigenstate population.] At a much longer time scale the bare-basis population gradually decreases because non-zero  $g$  makes the measurement not fully projective, leading to rare transitions (jumps) between the states  $|10\rangle$  and  $|01\rangle$ . Note that for numerical simplicity in the regime (a) we simulated the evolution assuming  $\kappa \gg \Gamma_m$ , so that the qubits and resonator remain effectively disentangled (qubit entanglement with the emitted field is not important for the

master equation approach). With this approximation, we can simplify Eq. (2.9) by reducing it to a two-qubit Hilbert space and taking into account the interaction with the resonator by applying the dephasing with the rate  $\Gamma_m$  to the measured qubit. In this case the transient evolution occurs on the time scale  $\Gamma_m^{-1}$  and the population  $P_{10}$  decays with the rate  $2g^2/\Gamma_m$ . The textbook regime (a) is most easy to understand and analyze. However, we emphasize that this regime is not realized in realistic experiments with transmons, in which typically  $\Delta \gg \Gamma_m$ .

In the adiabatic regime (b), which more closely describes recent experiments [50, 62, 113], the resonator empties and the system dephases more slowly than the qubit-qubit evolution, so the *eigenstates*  $|\overline{10}\rangle$  and  $|00\rangle$  are preserved as the optimal logical basis. That is, our numerical simulation in Fig. 2.2(b) shows that the eigenstate population  $P_{\overline{10}}$  is preserved at almost 1, in contrast to the textbook regime, while the bare state population  $P_{10}$  (when initially 1) drops by roughly  $2(g/\Delta)^2$  within the collapse timescale (this timescale is  $\Gamma_m^{-1}$  if  $\kappa \gg \Gamma_m$ , while for  $\kappa \ll \Gamma_m$  everything is determined by transients). Again, in this drop one factor of  $(g/\Delta)^2$  comes from the collapse into an incoherent mixture of single-excitation eigenstates  $|\overline{10}\rangle$  and  $|\overline{01}\rangle$ , while the second factor comes from plotting the bare state population. At longer time scales, we also observe in Fig. 2.2(b) that the eigenstate population  $P_{\overline{10}}$  decays exponentially at a very slow rate. This occurs because of rare transitions (jumps) between the eigenstates  $|\overline{10}\rangle$  and  $|\overline{01}\rangle$ , discussed in more detail later.

The frustrated regime (c) differs from the adiabatic regime (b) only by the relative magnitude of the resonator decay  $\kappa$  and the qubit-qubit detuning  $\Delta$ ,  $\kappa \gg \Delta$ . Nevertheless,

this regime dramatically amplifies the exponential decay process observed at long times in the adiabatic regime (b). The rapid decay seen in Fig. 2.2(c) occurs for both bare and eigenstates, so that neither of these bases is good for preserving a logical state. This occurs because fast oscillations  $\Delta$  (compared to dephasing  $\Gamma_m$ ) favor the eigenbasis, while even faster decay  $\kappa$  makes the outgoing photons sensitive to the bare basis.

In both regimes (b) and (c), the system collapses to the *eigenstates*, after which the state may jump between the eigenstates. This behavior is evidenced in Fig. 2.3, showing the ensemble-averaged evolution in the Bloch sphere representation of the qubit-qubit single-excitation subspace. The ratio  $\kappa/\Delta = 1$  is chosen in between the regimes (b) and (c). The initially bare state rapidly oscillates around the eigenstate axis as it spirals into this axis on average, indicating that the initially bare state collapses to an incoherent mixture of the eigenstates. After that the exponential decay occurs along the eigenstate axis of the Bloch sphere, indicating that it arises solely from a *classical mixing* process that scrambles those eigenstates.

The physical origin of the exponential decay seen in regimes (b) and (c) is not apparent from examining the ensemble-averaged behavior of the master equation alone, but we shall see that this decay can be interpreted as arising from averaging random quantum jumps between the eigenstates that occur during the continuous measurement process. For the remainder of this chapter we will mostly focus on understanding the transition between the adiabatic regime (b) and the frustrated regime (c) as  $\kappa$  is varied with respect to  $\Delta$ .

We also briefly note that in principle there is a fourth parameter regime: (d)  $\kappa \ll \Delta \ll \Gamma_m$ . We do not consider this regime here, since in this case it is difficult to

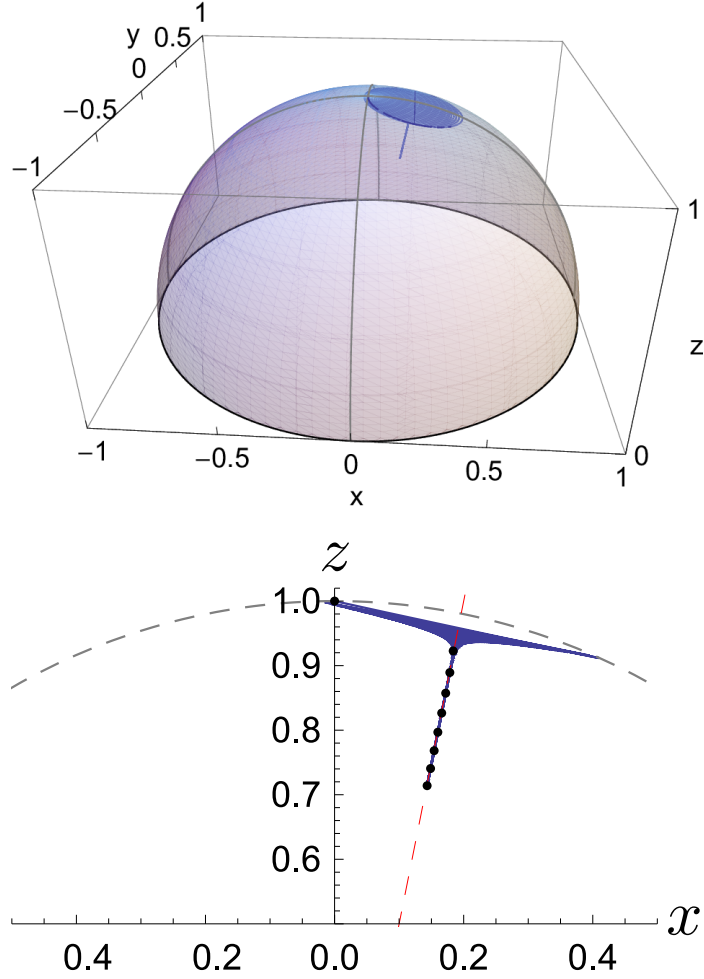


Figure 2.3: Qubit-qubit single-excitation ensemble-averaged evolution, using bare Bloch sphere coordinates defined by  $x = |10\rangle\langle 01| + |01\rangle\langle 10|$ ,  $y = -i(|10\rangle\langle 01| - |01\rangle\langle 10|)$  and  $z = |10\rangle\langle 10| - |01\rangle\langle 01|$ , and parameters  $g/\Delta = 1/10$ ,  $\kappa/\Delta = 1$ , and  $\Gamma_m/\Delta = 1/100$  (with  $\bar{n} = 2$  and correspondingly  $\chi/\kappa = 1/40$ ). An initially bare state  $|10\rangle \equiv (0, 0, 1)$  oscillates rapidly around the tilted axis corresponding to the eigenbasis  $\{|\bar{1}0\rangle, |\bar{0}1\rangle\}$ , and approaches this axis, indicating the gradual collapse, which produces an incoherent mixture of the eigenstates. At longer times, the ensemble averaged state continues moving along the eigenstate axis at a slow rate, indicating an additional classical mixing process. (top) 3D plot of  $(x, y, z)$  evolution, showing the spiraling evolution to the eigenstate axis and then along the axis, simulated for  $\Gamma_m t \in [0, 40]$ . (bottom) Slice of x-z plane, with sphere surface shown as the dashed gray curve and the eigenstate axis shown as the dashed red line tilted from the bare  $z$  axis by the angle  $2\theta = \arctan(2g/\Delta)$ . Black dots show time intervals of  $\Gamma_m t = 5$ .

clearly pose the problem of finding a preferable measurement basis without focusing solely on the ring up evolution for the resonator, and since this regime is not relevant to actual experiments.

## 2.4 Quantum jumps in eigenbasis

In this section we focus on understanding the exponential decay at long times in Figs. 2.2 and 2.3 for the adiabatic and frustrated regimes (b) and (c). The ensemble-averaged simulation suggests that after an initial state collapses to one of the two eigenstates  $\{|\overline{10}\rangle, |\overline{01}\rangle\}$ , these eigenstates then become further mixed at a rate that depends on the relative magnitude of the resonator decay  $\kappa$  and the qubit-qubit detuning  $\Delta$ . As we will soon see using quantum trajectory simulations, this mixing process can be identified as stochastic quantum jumps between otherwise stabilized eigenstates.

Treating these jumps semiclassically as telegraph noise, we surmise there must exist two unidirectional *switching rates*  $\Gamma_{\text{sw}}^{\pm}$  for randomly transitioning from the state  $|\overline{10}\rangle$  to  $|\overline{01}\rangle$  (-) or vice versa (+). The eigenstate population therefore should obey the simple ensemble-averaged rate equation

$$\dot{P}_{\overline{10}} = -\Gamma_{\text{sw}}^{-} P_{\overline{10}} + \Gamma_{\text{sw}}^{+} (1 - P_{\overline{10}}), \quad (2.19)$$

where we used  $P_{\overline{10}} + P_{\overline{01}} = 1$ . In particular, the solution of this equation starting with  $P_{\overline{10}}(0) = 1$  is

$$P_{\overline{10}}(t) = \frac{\Gamma_{\text{sw}}^{+}}{\Gamma_{\text{sw}}^{+} + \Gamma_{\text{sw}}^{-}} + \frac{\Gamma_{\text{sw}}^{-}}{\Gamma_{\text{sw}}^{+} + \Gamma_{\text{sw}}^{-}} e^{-(\Gamma_{\text{sw}}^{+} + \Gamma_{\text{sw}}^{-})t}, \quad (2.20)$$

it eventually saturates at the population  $\Gamma_{\text{sw}}^{+}/(\Gamma_{\text{sw}}^{+} + \Gamma_{\text{sw}}^{-})$ , and has an initial decay slope

of  $\Gamma_{\text{sw}}^-$ . If the switching rates are equal, the solution will eventually reach the maximally mixed eigenpopulation of  $1/2$  (i.e., the center of the Bloch sphere in Fig. 2.3). We derive the switching rates for this model in the next section, after which we will describe how to simulate the quantum trajectories that show this switching behavior explicitly.

### 2.4.1 Switching rate

In order to calculate the rates  $\Gamma_{\text{sw}}^\pm$  of jumps between the eigenstates  $|\overline{10}\rangle$  and  $|\overline{01}\rangle$  in the slow dephasing regime  $\Gamma_{\text{m}} \ll \Delta$  of Fig. 2.2(b,c), we will take literally the interpretation of the ensemble dephasing  $\Gamma_{\text{m}}$  in Eq. (2.17) as being due to a fluctuating number of photons in the resonator, causing a fluctuating ac Stark shift. Moreover, we will treat the fluctuating photon numbers  $n_\pm(t) = \bar{n}_\pm + \delta n_\pm(t)$  as classical variables, with the means  $\bar{n}_\pm$  given in Eq. (2.13) and fluctuations  $\delta n_\pm(t)$  having temporal correlations [78, 90]

$$\langle \delta n_\pm(t) \delta n_\pm(0) \rangle = \bar{n}_\pm e^{-\kappa|t|/2}. \quad (2.21)$$

Here the upper sign corresponds to the state  $|\overline{10}\rangle$ , for which the main qubit is practically in the state  $|1\rangle$ , while the lower sign is for  $|\overline{01}\rangle$ . We will be mostly interested in the switching rate  $\Gamma_{\text{sw}}^-$  for the process  $|\overline{10}\rangle \rightarrow |\overline{01}\rangle$ , which is caused by fluctuations of  $n_+(t)$ ; however, for completeness we calculate both switching rates (the upper sign in all equations below is sufficient to find  $\Gamma_{\text{sw}}^-$ ). Note that the decay rate of  $\kappa/2$  in Eq. (2.21) is consistent with the decay of classical energy fluctuations in a pumped resonator (in contrast to the energy decay  $\kappa$  in an unpumped resonator). Also note that here we neglected the oscillations of the correlator with frequency  $\Delta_{\text{r}} \pm \chi$  (discussed later).

The fluctuating number of photons  $n_\pm(t)$  causes a fluctuating ac Stark shift  $2\chi n_\pm(t)$

[as follows from the dispersive coupling of Eq. (2.4)], which leads to a fluctuating qubit-qubit detuning  $\Delta + \delta\Delta$ , with  $\delta\Delta(t) = 2\chi \delta n_{\pm}(t)$ . This in turn produces a fluctuating effective coupling  $\tilde{g}(t)$  between the stationary eigenstates  $|\bar{10}\rangle$  and  $|\bar{01}\rangle$ , since they are no longer true eigenstates for the detuning  $\Delta + \delta\Delta$ . The fluctuations  $\delta n_{+}(t)$  for the state  $|\bar{10}\rangle$  produce the coupling

$$\tilde{g}_{+}(t) = \langle \bar{01} | \delta H | \bar{10} \rangle = -\frac{g}{\Omega} \delta\Delta(t) = -2\frac{g}{\Omega} \chi \delta n_{+}(t), \quad (2.22)$$

while for the state  $|\bar{01}\rangle$  the fluctuations  $\delta n_{-}(t)$  are somewhat different, producing

$$\tilde{g}_{-}(t) = \langle \bar{10} | \delta H | \bar{01} \rangle = -2\frac{g}{\Omega} \chi \delta n_{-}(t), \quad (2.23)$$

where in the single-excitation subspace  $\delta H = (\delta\Delta/2) (|10\rangle\langle 10| - |01\rangle\langle 01|)$  and

$$\Omega = \Delta \sqrt{1 + (2g/\Delta)^2} \approx \Delta \quad (2.24)$$

is energy difference between  $|\bar{10}\rangle$  and  $|\bar{01}\rangle$  (we omit the subscripts in  $\Delta_{\pm}$ ,  $\Omega_{\pm}$  and  $\delta\Delta_{\pm}$  for brevity). The derivation of Eq. (2.22) is very simple when  $g \ll \Delta$ . Then the true eigenstates should correspond to the rotation angle  $\theta \approx g/(\Delta + \delta\Delta)$  from the bare basis instead of the angle  $\theta \approx g/\Delta$  for  $|\bar{10}\rangle$  and  $|\bar{01}\rangle$ . The additional angle,  $\delta\theta \approx -g\delta\Delta/\Delta^2$ , is the rotation  $\tilde{g}/\Delta$  between the true and stationary eigenbases. Thus we obtain  $\tilde{g} = -(g/\Delta)\delta\Delta$ , which is Eq. (2.22) with  $\Omega \approx \Delta$ . In the exact derivation we can use  $\theta = \arctan(2g/\Delta)/2$ , then the derivative is  $d\theta/d\Delta = -g/\Omega^2$ , which should be equal to  $(\tilde{g}/\Omega)/\delta\Delta$ ; this gives Eq. (2.22).

The fluctuating effective coupling  $\tilde{g}$  between the eigenstates  $|\bar{10}\rangle$  and  $|\bar{01}\rangle$  leads to a gradual mixing between them, which corresponds to random jumps between the eigenstates in the approach of quantum trajectories. We can find the rate  $\Gamma_{\text{sw}}$  of these jumps by starting with one of the eigenstates and equating  $\Gamma_{\text{sw}}t$  with the population of the other eigenstate,

which follows from the solution of the Schrödinger equation with the coupling  $\tilde{g}$ . Thus, to lowest order in  $\tilde{g}$  we find the switching rate

$$\Gamma_{\text{sw}}^{\mp} = \left\langle \frac{1}{t} \left| \int_0^t \tilde{g}_{\pm}(t') e^{\pm i\Omega(t-t')} dt' \right|^2 \right\rangle, \quad (2.25)$$

where the brackets mean averaging over the random realizations of  $\tilde{g}(t)$ . This equation formally depends on time  $t$ ; however, there is actually no time dependence for sufficiently long  $t$ , for which the evolution can be physically described by a switching rate. This can be seen by expressing the square of the windowed Fourier transform in Eq. (2.25) via the (two-sided) spectral density  $S_{\tilde{g}_{\pm}}(\omega)$  of  $\tilde{g}_{\pm}(t)$ :  $\Gamma_{\text{sw}}^{\mp} = \int_{-\infty}^{\infty} S_{\tilde{g}_{\pm}}(\pm\Omega + \omega) [1 - \cos(\omega t)] (\pi t \omega^2)^{-1} d\omega$ . Therefore, at sufficiently long times  $\Gamma_{\text{sw}}^{\mp} = S_{\tilde{g}_{\pm}}(\pm\Omega)$ , which does not depend on time. Because of the linear relations (2.22) and (2.23) between  $\tilde{g}_{\pm}(t)$  and  $\delta n_{\pm}(t)$ , their spectral densities are related as  $S_{\tilde{g}_{\pm}}(\Omega) = (2\chi g/\Omega)^2 S_{\delta n_{\pm}}(\Omega)$ , therefore

$$\Gamma_{\text{sw}}^{\mp} = (2\chi g/\Omega)^2 S_{\delta n_{\pm}}(\pm\Omega). \quad (2.26)$$

[Note that for classical fluctuations  $\delta n_{\pm}(t)$  the spectral density is symmetric,  $S_{\delta n_{\pm}}(-\Omega) = S_{\delta n_{\pm}}(\Omega)$ ; however, we keep the sign of  $\Omega$  in Eq. (2.26) to discuss the asymmetric case later.]

The (two-sided) spectral density  $S_{\delta n_{\pm}}$  can be found via the Wiener-Khinchin theorem [125]

$S_{\delta n_{\pm}}(\Omega) = \int_{-\infty}^{\infty} \langle \delta n_{\pm}(t) \delta n_{\pm}(0) \rangle e^{-i\Omega t} dt$ , so that using Eq. (2.21) we obtain the switching rate

$$\Gamma_{\text{sw}}^{\mp} = \frac{2g^2}{\Omega^2} \frac{8\chi^2 \bar{n}_{\pm}}{\kappa} \frac{\kappa^2}{\kappa^2 + 4\Omega^2}. \quad (2.27)$$

This result obviously assumes  $\Gamma_{\text{sw}}^{\mp} \ll |\Omega|$  and is not applicable during the initial transient evolution due to collapse.

Note that the term  $8\chi^2 \bar{n}_{\pm}/\kappa$  in Eq. (2.27) is similar to the measurement-induced dephasing  $\Gamma_{\text{m}}$  given by Eq. (2.17), but it depends on  $\bar{n}_{+}$  for  $\Gamma_{\text{sw}}^{-}$  (or on  $\bar{n}_{-}$  for  $\Gamma_{\text{sw}}^{+}$ ) rather

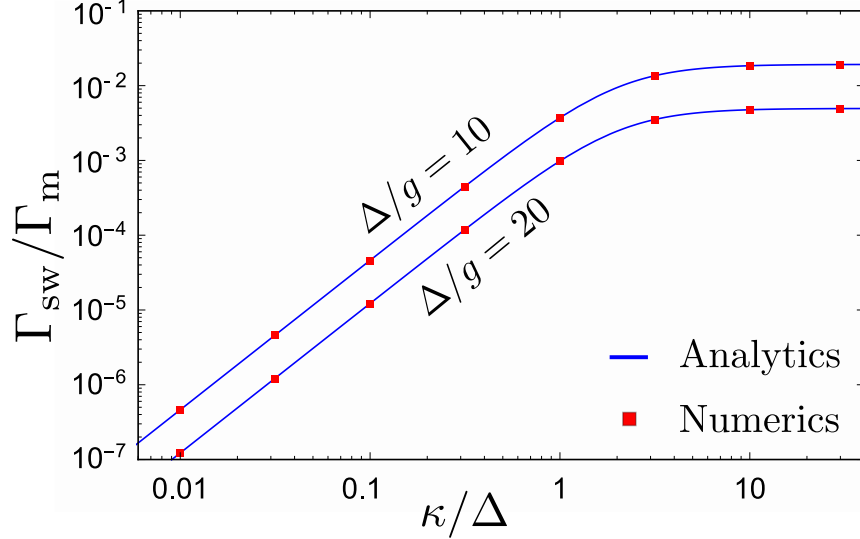


Figure 2.4: Switching rate vs. cavity decay rate. Blue solid line: switching rate analytics  $\Gamma_{\text{sw}}/\Gamma_{\text{m}} = 2(g/\Omega)^2/[1 + (2\Omega/\kappa)^2]$  as a function of the ratio  $\kappa/\Delta$ . Red boxes: numerical switching rate obtained from solving the master equation and extracting the decay rate  $\Gamma_{\text{sw}}$  from fitting  $P_{10}(t)$  [as shown in the right panels of Figs. 2.2(b,c)] with Eq. (2.20), assuming  $\Gamma_{\text{sw}}^+ = \Gamma_{\text{sw}}^-$ . A typical relative difference between the numerical and analytical results is about  $10^{-3}$ , which is comparable to an inaccuracy from the fitting procedure. The used parameters are:  $g/\Delta = 1/10$  and  $1/20$ ,  $\bar{n} = 10$ ,  $\Delta_{\text{r}} = 0$ , and  $\chi/\Delta = 10^{-3}$ .

than the combination  $\bar{n}_+ \bar{n}_- / \bar{n}_{\text{max}}$  in Eq. (2.17). In the case when  $\bar{n}_+ \approx \bar{n}_- \approx \bar{n}_{\text{max}}$  (which occurs when  $|\Delta_{\text{r}} \pm \chi| \ll \kappa$ ) we obtain  $\Gamma_{\text{sw}}^+ \approx \Gamma_{\text{sw}}^- \equiv \Gamma_{\text{sw}}$  with

$$\Gamma_{\text{sw}} \approx 2\Gamma_{\text{m}} \frac{g^2}{\Delta^2} \frac{\kappa^2}{\kappa^2 + 4\Delta^2}, \quad (2.28)$$

where we also used  $\Omega \approx \Delta$  since  $g \ll \Delta$ . Note that in the regime  $\kappa \gg \Delta$  [as in Fig. 2.2(c)] the last factor in Eq. (2.28) is close to 1, and the switching rate is rather large,  $\Gamma_{\text{sw}} \approx 2\Gamma_{\text{m}}(g/\Delta)^2$ , while in the regime  $\kappa \ll \Delta$  [as in Fig. 2.2(b)] the switching rate is additionally suppressed by the factor  $(\kappa/2\Delta)^2$ .

We have numerically verified Eq. (2.27) for the switching rates by comparing the telegraph noise solution of Eq. (2.20) to the ensemble-averaged population decay obtained

from simulating the full master equation (2.9) for a range of  $\kappa/\Delta$ . The comparison is plotted in Fig. 2.4, showing excellent agreement. A typical mismatch between the analytics and numerics is on the order of 0.1%, which is comparable to the inaccuracy from the numerical fitting procedure. Most importantly, in Fig. 2.4 we see a strong suppression of the switching rate at  $\kappa/\Delta \ll 1$ .

Solution of Eq. (2.19) with the switching rates given by Eq. (2.27) is sufficient to describe the ensemble-averaged evolution when the initial state is an eigenstate. If this is not the case, we need to include collapse of the initial state into the eigenbasis. In particular, for the bare initial state  $|10\rangle$ , the evolution in Eq. (2.19) effectively starts with  $P_{10}(0) = \cos^2 \theta$ . As an example, the yellow line in the left panel of Fig. 2.2(c) shows such evolution, which is then converted back into the bare basis. While this simple approach does not describe the transient (collapse) dynamics, it accurately describes the evolution after that.

Our derivation for the switching rates  $\Gamma_{\text{sw}}^{\mp}$  in this section has been based on treating fluctuations  $\delta n_{\pm}(t)$  as classical fluctuations. The quantum nature of these fluctuations leads to an asymmetric spectral density [90]  $S_{\delta n_{\pm}}(\Omega) = \bar{n}_{\pm} \kappa / [(\kappa/2)^2 + (\Omega - \Delta_r \mp \chi)^2]$ . Inserting this formula into Eq. (2.26), we obtain  $\Gamma_{\text{sw}}^{\mp} = 2(g/\Omega)^2 (8\chi^2 \bar{n}_{\pm} / \kappa) \kappa^2 / [\kappa^2 + 4(\pm\Omega - \Delta_r \mp \chi)^2]$ , which introduces a slight correction compared to Eq. (2.27). Physically, this formula says that if the extra photon energy  $-\Delta_r \mp \chi$  is positive, this helps the switching process with increase of energy, and vice versa. Even though this correction is very minor in the typical case, our numerical results using the master equation confirm the presence of this correction. However, our numerical results are more consistent with the combination  $\kappa^2 + 4(\pm\Omega - \Delta_r \pm \chi)^2$  in the denominator of the equation. This combination means that the

process depends on the extra photon energy  $-\Delta_r \pm \chi$  after the switching (which changes the resonator frequency by  $\pm 2\chi$ ) instead of the extra energy  $-\Delta_r \mp \chi$  before the switching. Note that the logic of our derivation cannot correctly take into account the change of the resonator frequency during switching. Also, numerical results for some parameters are not consistent with the combination  $-\Delta_r \pm \chi$  as well (indicating a possible presence of a parameter-dependent coefficient in front of  $\pm\chi$ ). Therefore, we are confident only in the correction of Eq. (2.27) due to  $\Delta_r$ ,

$$\Gamma_{\text{sw}}^{\mp} = \frac{2g^2}{\Omega^2} \frac{8\chi^2 \bar{n}_{\pm}}{\kappa} \frac{\kappa^2}{\kappa^2 + 4(\pm\Omega - \Delta_r)^2}, \quad (2.29)$$

omitting the dependence on  $\chi$  in the denominator.

Note that if additional environmental dephasing  $\Gamma_e$  is included in the master equation, it will contribute a similar term of  $(2\Gamma_e)(g/\Omega)^2$  to both the up and down switching rates equally. Environmental energy-decay will also effectively contribute a term  $(1/T_1)$  to only the down switching rate  $\Gamma_{\text{sw}}^-$ . However, while such energy decay may be qualitatively similar in its effect on the excited population  $P_{\overline{10}}$ , it is intrinsically different from the eigenstate switching behavior derived here since it transfers the excitation to the ground state  $|00\rangle$  outside the single-excitation subspace, instead of switching to  $|\overline{01}\rangle$ .

We also note that the mechanism discussed here of switching between the eigenstates  $|\overline{10}\rangle$  and  $|\overline{01}\rangle$  is physically similar to the mechanism of “dressed dephasing” [126, 127], in which the role of the two-qubit coupling is played by the Jaynes-Cummings coupling between the qubit and resonator.

### 2.4.2 Quantum trajectory simulations

In order to justify our understanding of the exponential decay in Fig. 2.2(b,c) as resulting from quantum jumps, we must go beyond the master equation in Eq. (2.9) and consider more detailed *quantum trajectories* [119, 128–131] (which have been confirmed experimentally with superconducting qubits [132–135]). In this approach we simulate individual realizations of the evolution due to measurement, rather than ensemble-averaged dynamics. In particular, in this case there is no measurement-induced *dephasing* (i.e., a change of the qubit phase); instead, the gradually-acquired information obtained from measurement causes continuous stochastic “attraction” to the states  $|0\rangle$  and  $|1\rangle$  of the measured qubit (random motion along the meridians on the Bloch sphere). After ensemble averaging, these two evolutions produce the same effect, but in each individual measurement the effects are drastically different. Most importantly, using the approach of trajectories we simulate actual experimental realizations, which is impossible using the master equation.

Since the full quantum trajectory simulation [119, 129] of our system is very difficult computationally, we performed the simulation only in the regimes of Figs. 2.2(a) and 2.2(c), i.e., assuming the “bad cavity limit”,  $\kappa \gg (\Delta, \Gamma)$ . In this case the full simulation can be replaced with the simple quantum Bayesian approach [120, 130]. For further simplification we assumed that the resonator is driven practically on resonance,  $|\Delta_r \pm \chi| \ll \kappa$ , and the setup in Fig. 2.1 uses a phase-sensitive amplifier, which amplifies and outputs the optimal quadrature  $I(t)$ , carrying information about the qubit state (the use of a phase-preserving amplifier can be described by introducing a limited quantum efficiency,  $\eta \leq 1/2$ ).

The simulations have been performed in the standard quantum Bayesian way

[106, 120, 130, 132, 136], restricted to the two-qubit single-excitation subspace, i.e., we simulate evolution of the density matrix with elements  $\rho_{10,10}$ ,  $\rho_{01,01}$ , and  $\rho_{10,01}$ , using the bare basis. In brief, at each (small) time step  $dt$ , the unitary evolution due to the two-qubit Hamiltonian  $H_q + H_{q\text{q}}$  [see Eqs. (2.2) and (2.6)] is interleaved with the evolution due to measurement, calculated in the following way. First, the value of the output signal  $I(t)$  (averaged over the duration  $dt$ ) is picked randomly from the probability distribution

$$p(I) = \rho_{10,10}(t) \frac{e^{-(I-I_1)^2/2D}}{(2\pi D)^{1/2}} + \rho_{01,01}(t) \frac{e^{-(I-I_0)^2/2D}}{(2\pi D)^{1/2}}, \quad (2.30)$$

where  $I_1 = 1$  and  $I_0 = -1$  correspond to the bare qubit states  $|10\rangle$  and  $|01\rangle$ , and the variance of the Gaussians is  $D = \tau/dt$  with the distinguishability time  $\tau = (2\eta\Gamma_m)^{-1}$  defined in Eq. (2.18). After picking a random value of  $I$ , the density matrix is updated using the relations

$$\begin{aligned} \frac{\rho_{10,10}(t+dt)}{\rho_{01,01}(t+dt)} &= \frac{\rho_{10,10}(t) \exp[-(I-I_1)dt/2\tau]}{\rho_{01,01}(t) \exp[-(I-I_0)dt/2\tau]}, \\ \frac{\rho_{10,01}(t+dt)}{\sqrt{\rho_{10,10}(t+dt)\rho_{01,01}(t+dt)}} &= \frac{\rho_{10,01}(t) e^{-(\Gamma-\eta\Gamma_m)dt}}{\sqrt{\rho_{10,10}(t)\rho_{01,01}(t)}}, \end{aligned} \quad (2.31)$$

where  $\rho_{10,10} + \rho_{01,01} = 1$  and  $\Gamma = \Gamma_m + \Gamma_e$  may include additional environmental dephasing  $\Gamma_e$ . For clarity, in what follows we assume  $\eta = 1$  and  $\Gamma = \Gamma_m$ . For a sufficiently small  $dt$ , this random sampling and state update procedure approximates continuous stochastic trajectories for the two-qubit state  $\rho(t)$ , as well as for the normalized readout  $I(t) = z(t) + \xi(t)$  that tracks the bare population difference  $z(t) = \rho_{10,10}(t) - \rho_{01,01}(t)$ , up to additive white noise  $\xi(t)$  with a constant (two-sided) spectral density  $S = \tau$ . While the simulations are performed in the bare basis, the resulting density matrix  $\rho$  can be easily converted into the eigenbasis. In particular, we are interested in tracking the eigenbasis populations  $P_{10} =$

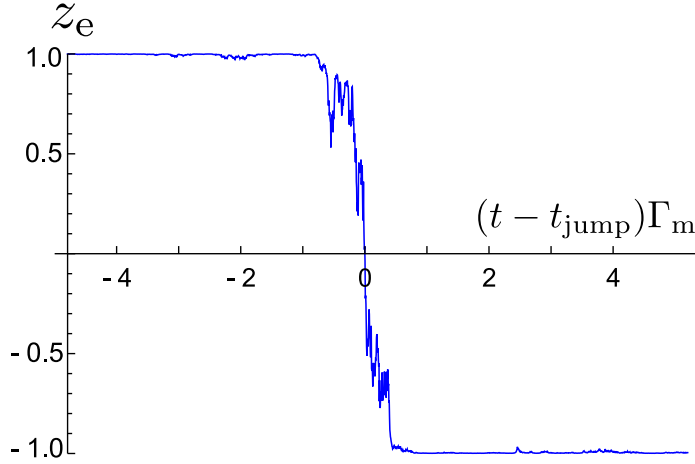


Figure 2.5: An example of quantum jump (switching event) between eigenstates  $|\overline{10}\rangle$  and  $|\overline{01}\rangle$ , obtained in the quantum trajectory simulation for  $g/\Delta = 1/20$ ,  $\Gamma_m/\Delta = 2.5 \times 10^{-4}$  and  $\kappa \gg \Delta$  (bad cavity regime). The eigenstate Bloch coordinate  $z_e = P_{\overline{10}} - P_{\overline{01}}$  noisily hovers near  $\pm 1$ , except when it rapidly jumps between the eigenstates on the timescale of  $\Gamma_m^{-1}$ . Averaging these random jumps produces the decay observed in Fig. 2.2(b,c). The physical picture of these jumps is used later to calculate the measurement error.

$\rho_{\overline{10},\overline{10}}$  and  $P_{\overline{01}} = \rho_{\overline{01},\overline{01}}$  besides the bare basis populations  $P_{10} = \rho_{10,10}$  and  $P_{01} = \rho_{01,01}$ .

With these simulations, we can analyze transition between the regimes of Fig. 2.2(a) and 2.2(c), discussed in Sec. 2.3. In the textbook regime (a),  $\Gamma_m \gg \Delta$ , we observe that an initial state (in the single-excitation subspace) gradually collapses to either the bare state  $|10\rangle$  or  $|01\rangle$  within the time scale of (few times)  $\Gamma_m^{-1}$ , with rare transitions between the bare states at long time (note that  $\eta = 1$  and  $\kappa \gg \Delta, \Gamma_m$ ). In contrast, in the regime (c),  $\Gamma_m \ll \Delta$ , we find from the simulations that the individual trajectories indeed collapse to the eigenstates  $|\overline{10}\rangle$  and  $|\overline{01}\rangle$  at the same time scale  $\Gamma_m^{-1}$ , as expected from the master equation simulations. We also observe the expected random *quantum jumps* between these eigenstates at longer time scales. An example of such a quantum jump obtained from the simulations is presented in Fig. 2.5, showing the eigenpopulation difference  $z_e = P_{\overline{10}} - P_{\overline{01}}$

switching from 1 to  $-1$ . The typical “width” of the jump is comparable to  $\Gamma_m^{-1}$ , though its central part can be significantly shorter. In between these random jumps the states remain close to eigenstates (though sometimes with “attempts” of jumps), confirming the assumptions made in the telegraph noise model of the switching.

Ensemble averaging of the jumps produces the gradual decay of the population shown in Fig. 2.2(c). We have checked numerically that the averaging of the quantum trajectory results coincides with the master equation results, thus also confirming the formula (2.28) for the switching rate in the regime  $\kappa \gg \Delta$ . Note that in our trajectory simulations  $\Gamma_{\text{sw}}^+ = \Gamma_{\text{sw}}^-$ , so the switching can be characterized by a single rate  $\Gamma_{\text{sw}}$ .

We thus numerically confirm our intuitive understanding of the collapse to the eigenstates and rare switching between them when  $\Gamma_m \ll \Delta$ . Note that in the simulated regime when also  $\Delta \ll \kappa$ , the switching rate is relatively large,  $\Gamma_{\text{sw}} \approx 2\Gamma_m(g/\Delta)^2$ , as follows from Eq. (2.28). This can be understood as because the fast resonator decay  $\kappa$  allows each pump photon to probe only the *bare states* of the first qubit before escaping to be collected. In other words, the “incremental” measurement information is still sensitive to the bare basis, even though the relatively fast interqubit dynamics,  $\Delta \gg \Gamma_m$ , causes the collapse to occur in the eigenbasis (this is because by the time “significant” information is collected, the eigenbasis emerges as more relevant physically). The tension between the different bases for the measurement in this “frustrated” regime leads to a relatively large switching rate. In contrast, when  $\kappa \ll \Delta$  (and still  $\Gamma_m \ll \Delta$ ), each photon in the resonator has sufficient time to feel the two-qubit dynamics averaged over the fast oscillations  $\Delta$ . Therefore, even the “incremental” information in the measurement is sensitive to the eigenbasis, thus making

it very stable and correspondingly reducing the switching rate  $\Gamma_{\text{sw}}$ . This is a qualitative physical interpretation of the reduction factor  $\kappa^2/(\kappa^2 + 4\Delta^2)$  in Eq. (2.28) from the point of view of quantum trajectories.

Note that this interpretation is very different from the physical picture used in our derivation of  $\Gamma_{\text{sw}}$  in Sec. 2.4.1, in which the reduction factor  $\kappa^2/(\kappa^2 + 4\Delta^2)$  came from non-zero correlation time of the fluctuations  $\delta n(t)$ . Actually, that picture was based on “fake” trajectories for  $\delta n(t)$  and was not capable of producing collapse and switching. However, it was capable of describing the ensemble-averaged dynamics, from which we derived  $\Gamma_{\text{sw}}$  indirectly, by *associating* the ensemble-averaged dynamics with the physically correct picture of quantum jumps. The difference between the two pictures is that quantum trajectories in this section describe actual homodyne measurement, while in Sec. 2.4.1 we implicitly assumed a power (photon number) measurement right after the resonator. The two pictures produce the same ensemble-averaged dynamics because of the causality principle, but describe very different evolutions in individual realizations of the measurement.

Since the causality principle is not entirely trivial, let us discuss it in a little more detail. Classical causality requires that an experimenter’s action at the present time cannot affect anything in the past. More specifically, the choice of a particular action cannot affect the past. For example, such a choice cannot affect the evolution of an object that has interacted in the past with another object, which is now accessible to the experimenter. However, as we know from the Einstein-Podolsky-Rosen-Bell paradox, this classical causality principle does not work in quantum mechanics, leading in particular to subtle “delayed choice” experiments. As a recent example, for a qubit continuously measured in a circuit

QED setup, the choice of a measured microwave quadrature (selected with a phase-sensitive amplifier) can dictate the qubit evolution either along meridians or along parallels of the Bloch sphere [120], even though this choice affects the microwave only after its interaction with the qubit (this prediction has been confirmed experimentally [132]). Thus, an experimenter's choice in the present may affect the past. However, such passing of information into the past cannot be “useful”, in the sense that another experimenter in the past cannot extract information about the later choice (otherwise it would be possible to send classical information to yourself in the past; this requirement is often called “no signaling”). Technically, this limitation is caused by necessarily random results of the measurement: randomness saves causality. In the above example, we can force the qubit retroactively to move along meridians or along parallels, but we cannot control whether the qubit will move right or left (up or down), making it impossible to distinguish the two cases (without using additional information about the microwave measurement result). Because of the no signaling requirement, the choice of the measurement cannot affect the ensemble-averaged evolution in the past (i.e., averaged over the random measurement result in the present), because otherwise it would be possible to extract classical information about the choice. (A similar argument leads to the no-cloning theorem [137, 138].) Thus, the causality principle in quantum mechanics does not forbid an experimenter to affect evolution in the past; however, the ensemble-averaged evolution in the past (averaged over randomness) cannot be affected by an experimenter's choice (see also [120]).

## 2.5 Qubit measurement error

The switching events (quantum jumps) contribute to the measurement error, which we discuss in this section. Here we consider only the realistic case  $\Gamma_m \ll \Delta$ , when the eigenbasis is preferred for logical encoding over the bare basis. The goal of this section is to find the minimum error, determined by the switching rate  $\Gamma_{sw}^-$  (the analysis is very similar to the error limited by the energy relaxation time  $T_1$ ). For simplicity we do not consider transients, assuming that the measurement occurs in the steady state.

We assume that for the readout the information-carrying quadrature  $I(t)$  of the output signal is integrated over the measurement duration  $t$ , producing the averaged output

$$\bar{I}(t) = \frac{1}{t} \int_0^t I(t') dt', \quad (2.32)$$

and then this value is compared with the threshold  $I_{th}$  to produce a binary readout of “0” or “1.” (More advanced signal processing of  $I(t)$  can moderately improve the measurement fidelity [102, 115]; we consider the straightforward integration (2.32) for simplicity.) If our goal is to distinguish the states  $|\bar{10}\rangle$  and  $|00\rangle$ , then the probabilities of misidentifying these states are

$$P_{err}^{(1)} = \int_{-\infty}^{I_{th}} P(\bar{I} | \bar{10}) d\bar{I}, \quad P_{err}^{(0)} = \int_{I_{th}}^{\infty} P(\bar{I} | 00) d\bar{I}, \quad (2.33)$$

respectively, where  $P(\bar{I} | \bar{10})$  is the probability density of obtaining the result  $\bar{I}$  when the initial state is  $|\bar{10}\rangle$  and  $P(\bar{I} | 00)$  is the analogous probability for the initial state  $|00\rangle$ . The total measurement error is the average of the two errors,

$$P_{err} = \frac{1}{2} [P_{err}^{(1)} + P_{err}^{(0)}]. \quad (2.34)$$

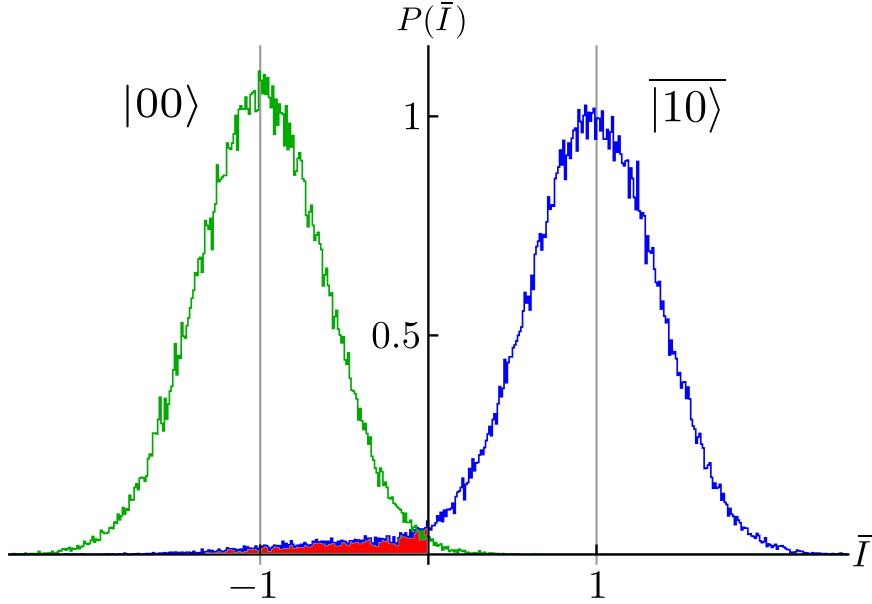


Figure 2.6: Signal histograms  $P(\bar{I} | 00)$  and  $P(\bar{I} | \overline{10})$  for the integrated quadrature  $\bar{I}$ , given the initial logical eigenstates  $|00\rangle$  and  $|\overline{10}\rangle$ . Shown are the binned readouts for 100,000 trajectories simulated as in Fig. 2.5 for duration  $t/\tau = 7$ , with  $g/\Delta = 1/10$ ,  $\Gamma_m/\Delta = 10^{-3}$ , and  $\eta = 1$ . Note that  $P(\bar{I} | 00)$  is a Gaussian centered at  $I_0 = -1$ , but  $P(\bar{I} | \overline{10})$  is a slightly shifted Gaussian [centered at  $1 - 2(g/\Delta)^2$  instead of  $I_1 = 1$ ], with a significant extended “tail” (red shaded region) caused by quantum jumps. The overlap of the two Gaussians decreases with integration time  $t$ , but the histogram overlap due to the tail increases with  $t$ , thus preventing perfect discrimination.

Figure 2.6 shows example histograms for  $P(\bar{I} | 00)$  and  $P(\bar{I} | \overline{10})$ , obtained by simulating 100,000 quantum trajectories, as discussed in the previous section for  $t/\tau = 7$ ,  $g/\Delta = 1/10$ ,  $\Gamma_m/\Delta = 10^{-3}$ , and  $\eta = 1$  (in this case  $\Gamma_{\text{sw}}\tau = 9.6 \times 10^{-3}$ ). As in the previous section, we use the normalization in which an ideal single-qubit measurement corresponds to  $\bar{I} = I_1 = 1$  for the state  $|1\rangle$  and  $\bar{I} = I_0 = -1$  for the state  $|0\rangle$ . As seen from Fig. 2.6, the probability distribution  $P(\bar{I} | 00)$  is a Gaussian centered at  $\bar{I} = -1$ , while  $P(\bar{I} | \overline{10})$  has a significant “tail” (red shaded region), caused by switching events. Also, the Gaussian part of  $P(\bar{I} | \overline{10})$  is centered at a value slightly smaller than 1 (this shift is practically not visible)

because the eigenstate  $|\overline{10}\rangle$  has a small contribution from  $|01\rangle$ . The shape of the histograms is discussed in Appendix D.

The errors  $P_{\text{err}}^{(1)}$ ,  $P_{\text{err}}^{(0)}$ , and  $P_{\text{err}}$  depend on the choice of the threshold  $I_{\text{th}}$ . Obviously, the total error  $P_{\text{err}}$  is minimized when the threshold is set such that  $P(I_{\text{th}} | \overline{10}) = P(I_{\text{th}} | 00)$ . However, in most of this section we will assume the symmetric threshold,  $I_{\text{th}} = 0$ . This is done for simplicity and also because, as we will see later, the use of the optimal threshold decreases the error insignificantly (with a typical relative improvement of  $\lesssim 3\%$ ). Also note that we will discuss the error for distinguishing the eigenstates  $|\overline{10}\rangle$  and  $|00\rangle$  as optimal for logical encoding; the corresponding error for distinguishing the bare states  $|10\rangle$  and  $|00\rangle$  has an additional contribution,

$$P_{\text{err,bare}}^{(1)} \approx P_{\text{err}}^{(1)} + (g/\Delta)^2, \quad (2.35)$$

because of the initial collapse of the bare state  $|10\rangle$  into either the eigenstate  $|\overline{10}\rangle$  or  $|\overline{01}\rangle$ .

### 2.5.1 Error contributions

In the absence of switching,  $\Gamma_{\text{sw}}^- = 0$ , the error steadily decreases with integration time because the variance  $\sigma^2 = \tau/t$  of the Gaussians in Fig. 2.6 decreases with time  $t$  [the distinguishability time  $\tau$  is given by Eq. (2.18)]. In particular, for  $I_{\text{th}} = 0$  this “separation” error is

$$P_{\text{err,sep}}^{(0)} = \frac{1}{2} \left[ 1 - \text{erf}(\sqrt{t/2\tau}) \right], \quad (2.36)$$

$$P_{\text{err,sep}}^{(1)} = \frac{1}{2} \left[ 1 - \text{erf}(\cos(2\theta)\sqrt{t/2\tau}) \right], \quad (2.37)$$

where  $\cos(2\theta) \approx 1 - 2(g/\Delta)^2$  comes from the difference between the eigenbasis and the bare basis. (For the optimal threshold both errors will contain  $\text{erf}[\sqrt{t/2\tau}(1 + \cos 2\theta)/2]$ .) For a

small  $g/\Delta$  this correction is small, and we will neglect it below.

The separation error rapidly becomes very small:  $10^{-2}$  for  $t = 5.4\tau$ ,  $10^{-3}$  for  $t = 9.5\tau$ , and  $10^{-4}$  for  $t = 13.8\tau$ . However, the switching process  $|\overline{10}\rangle \rightarrow |\overline{01}\rangle$ , occurring with the rate  $\Gamma_{\text{sw}}^-$ , adds a contribution to the error  $P_{\text{err}}^{(1)}$  that increases in time nearly linearly,

$$P_{\text{err}}^{(1)} \approx P_{\text{err,sep}}^{(1)} + \frac{1}{2} \Gamma_{\text{sw}}^- t, \quad (2.38)$$

so that the total error becomes

$$P_{\text{err}} \approx \frac{1 - \text{erf}(\sqrt{t/2\tau})}{2} + \frac{1}{4} \Gamma_{\text{sw}}^- t, \quad (2.39)$$

where we used  $\cos(2\theta) \approx 1$ ,  $I_{\text{th}} = 0$ , and  $(\Gamma_{\text{sw}}^- + \Gamma_{\text{sw}}^+)t \ll 1$ . More accurate calculations (in particular, taking into account double-switching trajectories, proper convolution of switching and noise, and effects of  $\theta$ ) are presented in Appendix D. Note that it is easy to understand the factor  $1/2$  in Eq. (2.38) by saying that the initial state  $|\overline{10}\rangle$  will be misidentified only if the switching event occurs before the middle of the integration time, so that the erroneous state is integrated for a longer time than the correct state. (A better interpretation of this factor via symmetry of the convolution is discussed in Appendix D.) We also note that Eqs. (2.38) and (2.39) can also describe the error for a single-qubit measurement that accounts for energy relaxation, with  $\Gamma_{\text{sw}}^-$  replaced by  $T_1^{-1}$ .

In Fig. 2.7 we illustrate the decomposition of the eigenbasis measurement error  $P_{\text{err}}$  of Eq. (2.39) into its two parts for  $\Gamma_{\text{sw}}^- \tau = 10^{-3}$ . The orange dashed line shows the error contribution from the integrated white noise (separation error), which monotonically decreases with integration time. The green dashed line shows the error from switching events, which linearly increases with integration time. The combination of these two op-

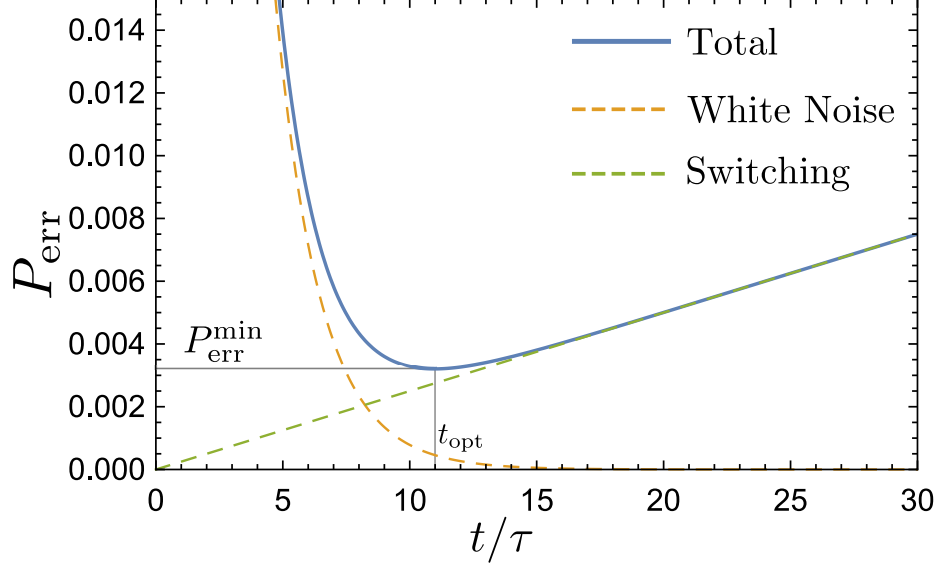


Figure 2.7: Simple analytics for the measurement error  $P_{\text{err}}$  as a function of an integration duration  $t$ , normalized by the distinguishability time  $\tau$ . Orange dashed line shows the monotonically decreasing separation error from integrated white noise. Green dashed line shows the linearly increasing error  $\Gamma_{\text{sw}}^- t/4$  from switching events, for which we choose  $\Gamma_{\text{sw}}^- \tau = 10^{-3}$ . The blue solid line shows the total measurement error, which has a minimum of  $P_{\text{err}}^{\text{min}} \approx (\Gamma_{\text{sw}}^- \tau/2) \ln(0.6/\Gamma_{\text{sw}}^- \tau)$  at the optimum time  $t_{\text{opt}}/\tau \approx 2 \ln(1/4\Gamma_{\text{sw}}^- \tau)$ .

posing effects in the total measurement error (blue solid line) produces a minimum error  $P_{\text{err}}^{\text{min}}$  at an optimum time  $t_{\text{opt}}$ , which we discuss in the following section.

To verify that this simple approach adequately models the measurement error, Fig. 2.8 shows a comparison of the measurement error  $P_{\text{err}}^{(1)}$  for the initial state  $|\overline{10}\rangle$  calculated in three ways: using quantum trajectories, using the simplified description (2.38), and using the more accurate analytics discussed in appendix D. The quantum trajectory method has used  $M = 1,500,000$  individual trajectories initialized in the eigenstate  $|\overline{10}\rangle$  for  $g/\Delta = 1/20$ ,  $\Delta/\Gamma_m = 2000$ , and  $\eta = 1$ . Each trajectory consists of  $2 \times 10^5$  time steps of size  $dt/\tau = 10^{-4}$ . For each trajectory we calculate  $\bar{I}(t)$  via Eq. (2.32) and compare it with the threshold

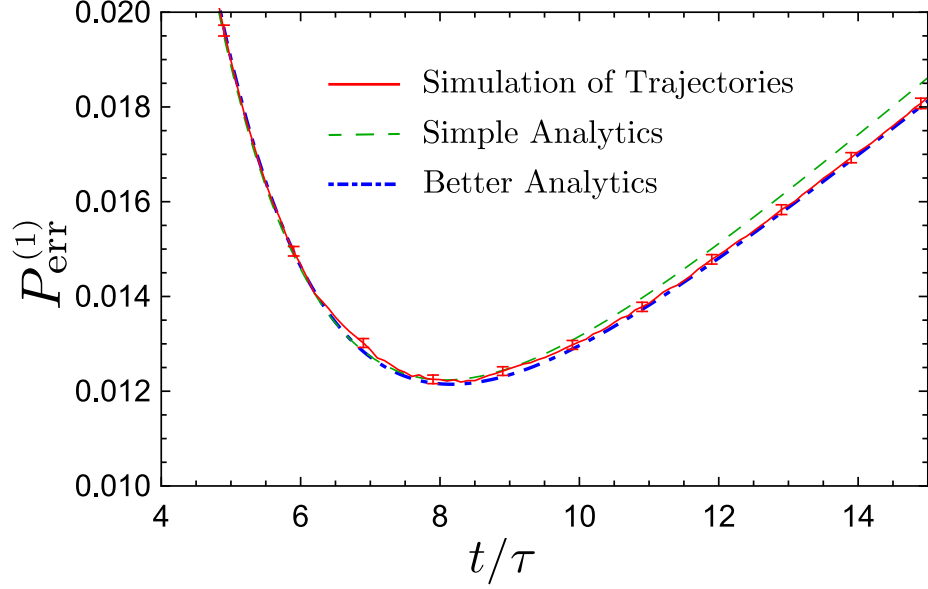


Figure 2.8: Simulated measurement error  $P_{\text{err}}^{(1)}$  for misidentifying the initial state  $|\overline{10}\rangle$ , using the discrimination threshold of  $I_{\text{th}} = 0$ . Red solid line: measurement error obtained by binning the integrated readouts for  $M = 1,500,000$  individual quantum trajectories, with  $g/\Delta = 1/20$ ,  $\Delta/\Gamma_m = 2000$ , and  $\eta = 1$ , in the bad cavity regime ( $\kappa \gg \Delta$ ). Error bars show the standard deviation of  $[P_{\text{err}}^{(1)}(1 - P_{\text{err}}^{(1)})/M]^{1/2}$ . Green dashed line: simple analytics that includes only single quantum jumps, Eq. (2.38). Blue dot-dashed line: refined analytics that includes single and double quantum jump events (see Appendix D).

$I_{\text{th}} = 0$ . The error  $P_{\text{err}}^{(1)}$  is then the fraction of trajectories with  $\bar{I} < I_{\text{th}}$ , which is shown by the solid red line in Fig. 2.8. Error bars show the standard deviation  $[P_{\text{err}}^{(1)}(1 - P_{\text{err}}^{(1)})/M]^{1/2}$  for a few representative points. For comparison, the dashed green line shows the simple analytics (2.38) with  $\Gamma_{\text{sw}}^- = 2\Gamma_m(g/\Omega)^2$  [see Eqs. (2.27) and (2.28)], so that  $\Gamma_{\text{sw}}^-\tau = 1/404$ . The dot-dashed blue line shows the more refined analytics described in Appendix D that include double switching events, as well as the proper offset of the Gaussian by  $\cos(2\theta)$ . This offset slightly shifts the curve up at times before and near the minimum, while the more accurate account of jumps noticeably shifts the curve down at times after the minimum. [Most of the difference between the green and blue lines at the times after the minimum

can be obtained by simply replacing  $\Gamma_{\text{sw}}^- t$  in Eq. (2.38) with  $1 - \exp(-\Gamma_{\text{sw}}^- t)$ ; the remaining difference is mainly due to double switching events.] As we see, the analytics of Appendix D is closer to the numerical results than the simple analytics, but the difference is minor. This difference becomes even smaller for smaller ratios  $\Gamma_{\text{sw}}^-/\Gamma_{\text{m}}$ .

### 2.5.2 Error minimized over time

The simplified model (2.39) for the measurement error has a first contribution that is rapidly decreasing in time, and a second contribution that is slowly increasing in time (Fig. 2.7). Therefore, it has a minimum that is reached at an optimal time  $t_{\text{opt}}$ . The minimum error  $P_{\text{err}}^{\text{min}}$  at this optimal time should be determined by the product  $\Gamma_{\text{sw}}^- \tau$ , since this is the only dimensionless parameter in the model. The optimal measurement duration can be found via the equation  $dP_{\text{err}}/dt = 0$ , whose solution is a product-log function, which has the recursive form

$$t_{\text{opt}} = \tau \ln \frac{2/\pi}{(\Gamma_{\text{sw}}^- \tau)^2 (t_{\text{opt}}/\tau)}. \quad (2.40)$$

The corresponding minimum error is

$$P_{\text{err}}^{\text{min}} \approx \frac{\Gamma_{\text{sw}}^- \tau}{2} + \frac{\Gamma_{\text{sw}}^- t_{\text{opt}}}{4} \approx \frac{\Gamma_{\text{sw}}^- \tau}{2} \ln \frac{C}{\Gamma_{\text{sw}}^- \tau}, \quad C \simeq 0.6, \quad (2.41)$$

where  $C \approx e\sqrt{2/\pi}\sqrt{\tau/t_{\text{opt}}}$  actually depends on  $\Gamma_{\text{sw}}^- \tau$ , but sufficiently weakly:  $C \in [0.43, 0.74]$  for  $\tau\Gamma_{\text{sw}}^- \in [10^{-6}, 10^{-2}]$ . In deriving the first relation in Eq. (2.41) we used the approximation

$$\frac{1 - \text{erf}(x)}{2} \approx \frac{\exp(-x^2)}{2\sqrt{\pi}x}, \quad x \gg 1. \quad (2.42)$$

Note that in the usual case  $\tau\Gamma_{\text{sw}}^- \ll 1$ , the main contribution to  $P_{\text{err}}^{\text{min}}$  comes from the second term in Eq. (2.39), with the relative contribution from the first term being  $2\tau/t_{\text{opt}}$ . The

ratio  $t_{\text{opt}}/\tau$  can be estimated as  $t_{\text{opt}}/\tau \approx 2 \ln(C/e\Gamma_{\text{sw}}^-\tau) \approx 2 \ln(1/4\Gamma_{\text{sw}}^-\tau)$ .

Note that at very long times,  $t \gtrsim (\Gamma_{\text{sw}}^- + \Gamma_{\text{sw}}^+)^{-1}$ , the simplified model in Eq. (2.39) becomes inapplicable. Moreover, the reverse switching events with the rate  $\Gamma_{\text{sw}}^+$  will eventually produce the integrated output signal  $\bar{I} \rightarrow (\Gamma_{\text{sw}}^+ - \Gamma_{\text{sw}}^-)/(\Gamma_{\text{sw}}^+ + \Gamma_{\text{sw}}^-)$  for the initial state  $|\bar{10}\rangle$ , which thus can be distinguished with certainty from the initial state  $|00\rangle$  (a similar situation was discussed for the measurement of phase qubits in Ref. [114]). However, such long integration times,  $t \gg 1/(\Gamma_{\text{sw}}^+ + \Gamma_{\text{sw}}^-)$ , are impractical even if we assume the absence of the energy relaxation, so we do not consider  $P_{\text{err}}(t)$  for these long times.

### 2.5.3 Optimized threshold

Let us augment the simplified model (2.39) by introducing an arbitrary threshold  $I_{\text{th}}$ ; then the error becomes

$$P_{\text{err}} \approx \frac{1 - \text{erf}[(1 + I_{\text{th}})\sqrt{t/2\tau}]}{4} + \frac{1 - \text{erf}[(1 - I_{\text{th}})\sqrt{t/2\tau}]}{4} + \frac{1 + I_{\text{th}}}{4} \Gamma_{\text{sw}}^- t. \quad (2.43)$$

Choosing a slightly negative  $I_{\text{th}}$  decreases the error because of the contribution from the last term (this is also obvious from Fig. 2.6 since the histogram for the initial state  $|\bar{10}\rangle$  has a long tail). The optimal threshold  $I_{\text{th}}^{\text{opt}}$  and optimal time  $t_{\text{opt}}$  can now be found from the system of equations,  $dP_{\text{err}}/dI_{\text{th}} = 0$  and  $dP_{\text{err}}/dt = 0$ . These equations are rather lengthy, but in the case  $t_{\text{opt}}/\tau \gg 1$  lead to a simple relation  $\exp(-I_{\text{th}}t_{\text{opt}}/\tau) = \sqrt{3}$ . Therefore, the optimal threshold is only slightly different from zero

$$I_{\text{th}}^{\text{opt}} \approx -\frac{\ln 3}{2} \frac{\tau}{t_{\text{opt}}} \approx -0.55 \frac{\tau}{t_{\text{opt}}}, \quad (2.44)$$

while the optimal time  $t_{\text{opt}}$  does not change significantly compared with Eq. (2.40).

The optimal threshold  $I_{\text{th}}^{\text{opt}}$  can also be obtained in the following crude way. Using Eq. (2.43), let us calculate the first and second derivatives of  $P_{\text{err}}$  over  $I_{\text{th}}$  at the point  $I_{\text{th}} = 0$ . This is simple and gives  $dP_{\text{err}}/dI_{\text{th}} = \Gamma_{\text{sw}}^- t/4$ ,  $d^2P_{\text{err}}/dI_{\text{th}}^2 = (2\pi)^{-1/2}(t/\tau)^{3/2} \exp(-t/2\tau)$ . Then, assuming a parabolic dependence  $P_{\text{err}}(I_{\text{th}})$ , we find the optimal threshold as  $I_{\text{th}}^{\text{opt}} = -(dP_{\text{err}}/dI_{\text{th}})/(d^2P_{\text{err}}/dI_{\text{th}}^2)$ , which, also using Eq. (2.40), gives  $I_{\text{th}}^{\text{opt}} = -\tau/2t_{\text{opt}}$ . Therefore, this crude derivation does not reproduce the result (2.44) exactly, but is still quite accurate. The error decrease due to optimization of  $I_{\text{th}}$  can then be found from the same parabolic approximation as  $\delta P_{\text{err}}^{\text{min}} = (dP_{\text{err}}/dI_{\text{th}})I_{\text{th}}^{\text{opt}}/2$ , which gives

$$P_{\text{err}}^{\text{min}}(I_{\text{th}} = I_{\text{th}}^{\text{opt}}) - P_{\text{err}}^{\text{min}}(I_{\text{th}} = 0) \approx -\frac{\Gamma_{\text{sw}}^- \tau}{16}. \quad (2.45)$$

Since we do not expect a significant change of  $P_{\text{err}}$  due to a slight shift of  $t_{\text{opt}}$  in this double-optimization procedure, we can simply replace the term  $(1/2)\Gamma_{\text{sw}}^- \tau$  in Eq. (2.41) with  $(7/16)\Gamma_{\text{sw}}^- \tau$ . Therefore, in this crude derivation the error  $P_{\text{err}}^{\text{min}}$  optimized over both time and threshold is still given by Eq. (2.41) with a modified value of  $C$ ,

$$C_{\text{opt}} = e^{-1/8}C \approx 0.88C \simeq 0.5. \quad (2.46)$$

The relative decrease of  $P_{\text{err}}^{\text{min}}$  due to the threshold optimization is approximately  $[8 \ln(C/\Gamma_{\text{sw}}^- \tau)]^{-1}$ , which is about 3% for  $\Gamma_{\text{sw}}^- \tau = 10^{-2}$  and smaller for smaller values of  $\Gamma_{\text{sw}}^- \tau$ .

By solving the optimization problem numerically over a wide parameter range  $\Gamma_{\text{sw}}^- \tau \in [10^{-6}, 10^{-2}]$ , we have confirmed that the threshold optimization changes  $C$  [defined via Eq. (2.41)] by a nearly constant factor  $C_{\text{opt}}/C \approx 0.88$ , producing the range  $C_{\text{opt}} \in [0.37, 0.65]$ . Correspondingly, this produces a nearly insignificant relative correction of [1.0%, 3.2%] in the minimum error  $P_{\text{err}}^{\text{min}}$  over this parameter range. The denominator 16 in

Eq. (2.45) in numerical results is found to be close to 15. Similarly, we confirmed that Eq. (2.44) is satisfied quite well: instead of the factor 0.55, we numerically find 0.55–0.58. This leads to the numerically optimal threshold  $I_{\text{th}}$  varying only within  $[-0.023, -0.081]$  over this same parameter range.

Besides using Eq. (2.43) for the numerical optimization, we also used a modified equation, in which the second term is multiplied by  $\exp(-\Gamma_{\text{sw}}^- t)$ , and in the third term  $\Gamma_{\text{sw}}^- t$  is replaced with  $1 - \exp(-\Gamma_{\text{sw}}^- t)$ . This practically does not change the above mentioned results, except that it slightly lowers  $C$ : for the same parameter range  $\Gamma_{\text{sw}}^- \tau \in [10^{-6}, 10^{-2}]$  it is  $C \in [0.43, 0.64]$  and correspondingly  $C_{\text{opt}} \in [0.37, 0.57]$ . Note that the factor 4 in the mentioned above approximation  $t_{\text{opt}}/\tau \approx 2 \ln(1/4\Gamma_{\text{sw}}^- \tau)$  varies within the range  $[6.1, 3.1]$  for zero threshold and the same parameter range, and within  $[5.3, 2.7]$  for the optimal threshold, increasing  $t_{\text{opt}}$  by about  $0.3\tau$  compared with the zero-threshold case.

We emphasize that the main result of our analysis of the threshold optimization is that the optimal threshold  $I_{\text{th}}^{\text{opt}}$  is close to the symmetric point  $I_{\text{th}} = 0$  and that the benefit of the optimization in decreasing the measurement error is insignificant. This justifies the use of  $I_{\text{th}} = 0$  in the analysis. This also shows that it is meaningful not to perform the threshold optimization in an experiment and instead use the symmetric point. Note that this conclusion also applies to the case of qubit energy relaxation, which is analyzed in the same way.

### 2.5.4 Measurement error due to neighboring qubit

As discussed above, the minimized measurement error can be approximated as

$$P_{\text{err}}^{\text{min}} \approx \frac{\Gamma_{\text{sw}}^- \tau}{2} \ln \frac{C}{\Gamma_{\text{sw}}^- \tau}, \quad (2.47)$$

where  $C \simeq 0.6$  for the symmetric threshold or  $\simeq 0.5$  for the optimal threshold,  $\tau = (2\eta\Gamma_{\text{m}})^{-1}$  is the distinguishability time, and

$$\Gamma_{\text{sw}}^- \approx \frac{1}{T_1} + \frac{2g^2}{\Delta^2 + 4g^2} \frac{8\chi^2 \bar{n}_+}{\kappa} \frac{\kappa^2}{\kappa^2 + 4\Delta^2 + 16g^2} \quad (2.48)$$

is the switching rate [see Eq. (2.27)]. Since in this chapter we are interested in the effect of the neighboring qubit, let us neglect the energy relaxation rate  $1/T_1$ . Also, let us use  $|g/\Delta| \ll 1$  and assume  $|\Delta_{\text{r}} \pm \chi| \lesssim \kappa$ , so that  $8\chi^2 \bar{n}_+/\kappa \approx \Gamma_{\text{m}}$ . In this case  $\Gamma_{\text{sw}}^-$  is given by Eq. (2.28) and the measurement error is

$$P_{\text{err}}^{\text{min}} \approx \frac{1}{2\eta} \left(\frac{g}{\Delta}\right)^2 \frac{\kappa^2}{\kappa^2 + 4\Delta^2} \ln \left[ C\eta \frac{\kappa^2 + 4\Delta^2}{\kappa^2 (g/\Delta)^2} \right]. \quad (2.49)$$

Note that this is the error for distinguishing the states  $|\bar{1}0\rangle$  and  $|00\rangle$ , while the error for distinguishing the bare-basis states  $|10\rangle$  and  $|00\rangle$  is larger because of the collapse occurring in the eigenbasis when  $|\Delta| \gg \Gamma_{\text{m}}$ ,

$$P_{\text{err,bare}}^{\text{min}} \approx \frac{1}{2} \left(\frac{g}{\Delta}\right)^2 + P_{\text{err}}^{\text{min}}. \quad (2.50)$$

As we see, in the “bad cavity limit”,  $\kappa \gg |\Delta|$ , the eigenbasis error,  $P_{\text{err}}^{\text{min}} \approx (1/2\eta)(g/\Delta)^2 \ln(C\eta\Delta^2/g^2)$ , is quite large, for example, for  $g/\Delta = 1/10$  and  $\eta = 0.2$  we obtain  $P_{\text{err}}^{\text{min}} \approx 6\%$ . The bare-basis error  $P_{\text{err,bare}}^{\text{min}}$  is bigger by 0.5%, which is not significant because  $P_{\text{err}}^{\text{min}}$  is so big.

This may look dangerous for the quantum processors based on superconducting qubits with “always-on” interaction between the neighbors. Fortunately, typical experimental systems do not operate in this bad cavity limit; in more realistic parameter regimes the switching process is strongly suppressed and therefore the measurement error due to the presence of a neighboring qubit is relatively small. For example, for  $\kappa^{-1} = 20$  ns and  $\Delta/2\pi = 0.5$  GHz, the switching rate is approximately  $10^{-4} \Gamma_m (g/\Delta)^2$ , so that for  $g/\Delta = 1/10$  and  $\eta = 0.2$  we obtain a very small measurement error from the neighboring qubit,  $P_{\text{err}}^{\text{min}} \approx 2 \times 10^{-5}$ . However, the bare-basis error is still significant,  $P_{\text{err,bare}}^{\text{min}} \approx 0.5\%$ , which means that the bare basis is inappropriate for encoding the logical information. Since the eigenbasis is also beneficial for logic operations and idling [114], this makes it an unambiguously optimal choice for encoding quantum information.

Note that since the switching processes are strongly suppressed in the regime when  $\kappa \ll |\Delta|$ , the qubit measurement remains accurate even when a neighboring qubit is detuned only moderately,  $|\Delta/g| \simeq 3$ , as long as the eigenstates are used for encoding. This fact may simplify the design of quantum processors in which “frequency crowding” may present a problem.

The switching between the eigenstates  $|\overline{10}\rangle$  and  $|\overline{01}\rangle$  can be observed experimentally. (For this purpose it is better to use the jumps  $|\overline{01}\rangle \rightarrow |\overline{10}\rangle$ , which can be easily distinguished from energy relaxation events.) For example, for  $\kappa^{-1} = 10$  ns,  $g/2\pi = 30$  MHz,  $\Delta/2\pi = 100$  MHz, and  $\Gamma_m/2\pi = 20$  MHz (corresponding to  $|\chi|/2\pi = 2$  MHz and  $\bar{n} = 10$ ), the expected switching time is about  $\Gamma_{\text{sw}}^{-1} \simeq 10 \mu\text{s}$ .

## 2.6 Summary

In this chapter we have investigated the measurement error of a superconducting transmon qubit in a circuit QED setup caused by the coupling  $g$  to a detuned neighboring qubit (or a bus resonator), focusing on the effects of the corresponding “tail” population  $(g/\Delta)^2$ . When the ensemble-dephasing rate due to measurement is much faster than the qubit-qubit detuning, the system collapses to the bare energy states as one would expect for a textbook projective measurement. However, in the more physically relevant regime with the ensemble-dephasing rate much slower than the detuning, the system instead collapses to the joint qubit-qubit *eigenstates*, which are also favorable for quantum operations and idling. As such, these qubit-qubit eigenstates are the most appropriate states for high-fidelity logical encoding in realistic parameter regimes.

We have shown that in regime where joint eigenstates are preferred, the excitation can randomly jump between these eigenstates while the qubit is being measured. In between these random jumps, the two-qubit state is practically pinned to one of the eigenstates. We have derived the rate of the jumps by using a semiclassical model of fluctuating ac Stark shift. The obtained analytical result for the switching rate has been confirmed by comparison with numerical solution of the master equation, for which the ensemble-averaged jumps lead to a gradual decay of the initial eigenstate population. The random jumps produce a contribution to the measurement error probability that increases almost linearly with integration time in a way qualitatively similar to the error from energy-decay processes.

The switching rate for these random jumps depends on the relative magnitude of the resonator decay and the qubit-qubit detuning. For quickly decaying resonators, the

switching rate is significant and produces the measurement error exceeding  $(g/\Delta)^2$  by several multiples. However, for more slowly decaying resonators, as is more typical experimentally, the minimized measurement error becomes essentially negligible for eigenstate encoding, while the error for bare basis encoding is still significant and exceeds  $\frac{1}{2}(g/\Delta)^2$ .

For the purposes of this study, we have used a static threshold for digitizing the continuous quadrature readout. We note that more sophisticated discrimination schemes may be able to take advantage of the additional information contained in the continuous readout to partially correct for the switching contribution to the measurement error. Generalizing our analysis to multiple neighboring qubits with simultaneous multi-qubit measurement may also be interesting for future research. Another possible generalization is the analysis of decoherence for multiqubit states that involve the neighboring qubit, which are not supposed to be affected by the measurement, but are actually influenced by the switching dynamics. We emphasize that the quantum jumps between the eigenstates predicted in this chapter could be measured experimentally using existing superconducting qubit technology.

A Python implementation of the quantum Bayesian approach to cQED measurement with moderate bandwidth [139] is available at <https://github.com/MostafaKhezri/Bayesian-cQED>.

## Chapter 3

# Measuring a transmon qubit in circuit QED: dressed squeezed states

In this chapter, we consider the circuit QED measurement of a superconducting transmon qubit via a coupled microwave resonator. For an ideal dispersive coupling, ringing up the resonator produces coherent states with frequencies matched to transmon energy states. Realistic coupling is not ideally dispersive, however, so transmon-resonator energy levels hybridize into joint eigenstate ladders of the Jaynes-Cummings type. Previous work has shown that ringing up the resonator approximately respects this ladder structure to produce a coherent state in the eigenbasis (a dressed coherent state). We numerically investigate the validity of this coherent state approximation to find two primary deviations. First, resonator ring-up leaks small stray populations into eigenstate ladders corresponding

to different transmon states. Second, within an eigenstate ladder the transmon nonlinearity shears the coherent state as it evolves. We then show that the next natural approximation for this sheared state in the eigenbasis is a dressed squeezed state, and derive simple evolution equations for such states using a hybrid phase-Fock-space description. Note that Sections 3.1-3.3.2 have been previously discussed in the Ph.D. dissertation of Eric Mlinar, UCR (2017) [140].

### 3.1 Introduction

Qubit technology using superconducting circuit quantum electrodynamics (QED) [78, 104] has rapidly developed over the past decade to become a leading contender for realizing a scalable quantum computer. Most recent qubit designs favor variations of the transmon [44, 46, 132, 141–144] due to its charge-noise insensitivity, which permits long coherence times while also enabling high-fidelity quantum gates [49, 68, 145] and high-fidelity dispersive qubit readout [85, 93, 146] via coupled microwave resonators. Transmon-based circuit operation fidelities are now near the threshold for quantum error correction protocols, some versions of which have been realized [50, 62, 112, 113].

The quantized energy states of a transmon are measured in circuit QED by coupling them to a detuned microwave resonator. For low numbers of photons populating the readout resonator, the coupling is well-studied [44, 78, 118] and approximates an idealized dispersive quantum non-demolition (QND) measurement [147]. Each transmon energy level dispersively shifts the frequency of the coupled resonator by a distinct amount, allowing the transmon state to be determined by measurement of the microwave field transmitted

through or reflected from the resonator. However, nondispersive effects become important when the number of resonator photons becomes comparable to a characteristic (“critical”) number set by the detuning and coupling strength [78, 126, 148]; present-day experiments often operate in this nondispersive (or nonlinear dispersive) regime [93, 149–151].

In this chapter, we analyze and model the nondispersive effects that occur during the ring-up of a readout resonator coupled to a transmon. These effects arise from the hybridization of the resonator and transmon states into joint resonator-transmon eigenstates. While ringing up the resonator from its ground state, the joint state remains largely confined to a single Jaynes-Cummings eigenstate ladder that corresponds to the initial transmon state. As pointed out in Refs. [152–154], this joint state can be approximated by a coherent state in the eigenbasis (recently named a dressed coherent state [154]). Here we refine this initial approximation and provide a more accurate model for the hybridized resonator-transmon state.

We numerically simulate the ring-up process for a resonator coupled to a transmon, then use this simulation to develop and verify our analytical model. We find two dominant deviations from a dressed coherent state. First, we show that the ring-up process allows a small population to leak from an initial transmon state into neighboring eigenstate ladders, and find simple expressions that quantify this stray population. Second, we show that the transmon-induced nonlinearity of the resonator distorts the dressed coherent state remaining in the correct eigenstate ladder with a shearing effect as it evolves, and show that this effect closely approximates self-squeezing of the dressed field at higher photon numbers. We then use a hybrid phase-Fock-space method to find equations of motion for the parameters of an

effective *dressed squeezed state* that is formed during the ring-up process. Our improved model is satisfyingly simple yet quite accurate.

To simplify our analysis and isolate the hybridization effects of interest, we restrict our attention to a transmon (modeled as a seven-level nonlinear oscillator) coupled to a coherently pumped but non-leaking resonator (using the rotating wave approximation). The simplification of no resonator leakage may seem artificial, but it is still a reasonable approximation during the resonator ring-up and it is also relevant for at least two known protocols. First, the catch-disperse-release protocol [152] encodes qubit information into resonator states with minimal initial leakage, then rapidly releases the resonator field to a transmission line. Second, a recently proposed readout protocol [155] similarly encodes qubit information into bright and dark resonator states with minimal leakage, then rapidly distinguishes them destructively using Josephson photomultipliers [156]. Our dressed squeezed state model should describe the ring-up process of these and similar protocols reasonably well. Additional effects arising from a more realistic treatment of the resonator decay will be considered in future work.

Our assumption of negligible resonator damping automatically eliminates qubit relaxation (and excitation) due to the Purcell effect [116, 117, 126, 153], which in the present-day experiments is often strongly suppressed by Purcell filters [92, 93, 95]. We also neglect energy relaxation and dephasing of the qubit (thus also eliminating dressed dephasing [126, 127]).

We note that squeezing of the resonator field may significantly affect fidelity of the qubit measurement [157, 158], which can be either increased or decreased, depending on the

squeezing axis direction. A significant improvement of the fidelity due to self-developing quadrature squeezing was predicted for the catch-disperse-release protocol [152]. (An extreme regime of the self-developing squeezing, with revival and formation of “cat” states was experimentally observed in [159].) The use of a squeezed input microwave for the qubit measurement was analyzed in [160]. A Heisenberg-limited scaling for the qubit readout was predicted for the two-resonator measurement scheme based on two-mode squeezed microwave in [161]. The significant current interest in various uses of squeezed microwave states [160–163] is supported by a natural way of producing them with Josephson parametric amplifiers [81–83, 164–166]. All this motivates the importance of studying squeezed microwave fields in superconducting circuits containing qubits.

This chapter is organized as follows. In Sec. 3.2 we describe the resonator-transmon system and how the numerical simulations are performed. In Sec. 3.3 we discuss the dressed coherent state model and focus on analyzing the inaccuracy of this model relative to numerical simulation. We quantify two deviations from the dressed coherent state model: stray population leakage to incorrect eigenstate ladders (Sec. 3.3.2), and distortion of the remaining dressed state during evolution into a dressed sheared state (Sec. 3.3.3). In Sec. 3.4, we prove that a dressed sheared state approximates a dressed squeezed state and then derive hybrid phase-Fock-space evolution equations for such states. Comparison with the simulation results shows that the accuracy of the dressed squeezed state approximation is much better than accuracy of the dressed coherent state approximation. We conclude in Sec. 3.5. In Appendix E we show that, somewhat unexpectedly, dressed coherent states and dressed squeezed states are practically unentangled despite the strong entanglement of the dressed

Fock states from which they are composed.

## 3.2 Model

Following the circuit QED paradigm of measurement [78], we consider a transmon coupled to a detuned readout resonator (Fig. 3.1). We do not simplify the transmon to a 2-level qubit, but instead include the lowest 7 energy levels confined by the cosine potential of the transmon. Though the transmon eigenstates may be written explicitly as Mathieu functions [27, 44], we have checked that a perturbative treatment of the transmon as an approximate oscillator with quartic anharmonicity [44] is sufficiently accurate for our purposes. We assume a transmon-resonator coupling of Jaynes-Cummings type [167], using the rotating wave approximation (RWA) for simplicity. (Notably, this approximation fails at very high photon numbers, leading to important effects [151].)

### 3.2.1 Pumped resonator-transmon Hamiltonian

In our model the resonator Hamiltonian is

$$H_r = \omega_r a^\dagger a = \sum_{n,k} n \omega_r |n, k\rangle \langle n, k|, \quad (3.1)$$

with  $\hbar = 1$ , bare resonator frequency  $\omega_r$ , lowering (raising) operator  $a$  ( $a^\dagger$ ) for the resonator mode satisfying  $[a, a^\dagger] = 1$ , and resonator index  $n = 0, 1, \dots$  for successive energy levels. For completeness we included the transmon index  $k = 0, 1, \dots, 6$  for the 7 lowest levels to emphasize the matrix representation in terms of the joint product states  $|n, k\rangle \equiv |n\rangle_r \otimes |k\rangle_q$  for the bare energy states.



Similarly, the transmon Hamiltonian has the form

$$H_q = \sum_{n,k} E_k |n, k\rangle\langle n, k|, \quad (3.2)$$

$$E_k = E_0 + \omega_q k - \eta \frac{k(k-1)}{2}. \quad (3.3)$$

The dominant effect of the nonlinearity of the cosine potential for the transmon is the quartic anharmonicity  $\eta \equiv \omega_{10} - \omega_{21} > 0$  of the upper level frequency spacings relative to the qubit frequency  $\omega_q \equiv \omega_{10}$ , where each frequency  $\omega_{k\ell} \equiv E_k - E_\ell$  denotes an energy difference. At this level of approximation, the transmon has the structure of a Duffing oscillator with a linearly accumulating anharmonicity  $\omega_{(k+1)k} = \omega_q - k\eta$ . [This approximation is sometimes extended to an infinite number of levels,  $H_q = E_0 + \omega_q b^\dagger b - (\eta/2) b^\dagger b (b^\dagger b - 1)$  [77], with an effective oscillator lowering (raising) operator  $b$  ( $b^\dagger$ ) satisfying  $[b, b^\dagger] = 1$ , but we explicitly keep only the 7 lowest levels here.]

The excitation-preserving interaction (within RWA) is

$$H_I = \sum_{n,k} g \sqrt{n(k+1)} |n-1, k+1\rangle\langle n, k| + \text{H.c.}, \quad (3.4)$$

where  $g$  is the coupling strength between levels  $|0, 1\rangle$  and  $|1, 0\rangle$ . As in Ref. [44], we neglect the effects of the anharmonicity  $\eta$  in the coupling for simplicity. [Extending this coupling to an infinite number of transmon levels yields  $H_I = g(ab^\dagger + a^\dagger b)$ .]

Finally, the Hamiltonian for coherently pumping the resonator with a classical field  $\varepsilon(t) e^{-i\omega_d t}$  is (within RWA)

$$\begin{aligned} H_d &= \varepsilon(t) e^{-i\omega_d t} a^\dagger + \varepsilon^*(t) e^{i\omega_d t} a \\ &= \varepsilon(t) e^{-i\omega_d t} \sum_{n,k} \sqrt{n+1} |n+1, k\rangle\langle n, k| + \text{H.c.}, \end{aligned} \quad (3.5)$$

where  $\varepsilon(t)$  is a complex envelope for the drive.

Combining Eqs. (3.1)–(3.5) into the total Hamiltonian  $H = H_r + H_q + H_I + H_d$ , and rewriting it in the rotating frame of the drive frequency  $\omega_d$  yields

$$\begin{aligned}
H_{\text{rot}} = \sum_{n,k} \{ & [n(\omega_r - \omega_d) + (E_k - k\omega_d)] |n, k\rangle\langle n, k| \\
& + g\sqrt{n(k+1)} |n-1, k+1\rangle\langle n, k| + \text{H.c.} \\
& + \varepsilon(t)\sqrt{n+1} |n+1, k\rangle\langle n, k| + \text{H.c.} \}. \tag{3.6}
\end{aligned}$$

This simplified Hamiltonian will be sufficient in what follows to observe the dominant non-dispersive effects that affect the resonator ring-up. Note that we use the rotating frame in numerical simulations, but physics related to Jaynes-Cummings ladders of states is easier to understand in the lab frame, so we will often imply the lab frame for clarity in the discussions below.

### 3.2.2 Numerical simulation and diagonalization

For numerical simulation, the Hamiltonian in Eq. (3.6) is represented by a  $7N \times 7N$  matrix using the bare energy basis  $|n, k\rangle$ , where  $N = 200\text{--}800$  is the maximum number of simulated levels for the resonator. We choose experimentally relevant resonator and transmon parameters, which in most simulations are  $\omega_r/2\pi = 6\text{ GHz}$ ,  $\omega_q/2\pi = 5\text{ GHz}$ ,  $\eta/2\pi = 200\text{ MHz}$ , and  $g/2\pi = 100\text{ MHz}$ . For the drive, we change the frequency  $\omega_d$  to be resonant with specific eigenstate transition frequencies of interest (detailed later) and use drive amplitudes typically in the range  $\varepsilon/2\pi = 10\text{--}60\text{ MHz}$ .

The hybridization of the joint eigenstates [see Fig. 3.1(b)] is significant when the number of photons  $n$  in the resonator is comparable to or larger than the so-called critical

photon number [78, 126, 148],

$$n_c = \frac{(\omega_r - \omega_q)^2}{4g^2}. \quad (3.7)$$

For the above parameters  $n_c = 25$ . This defines the scale at which we expect significant deviations from the ideal dispersive model.

We use the following numerical procedure for identifying the joint hybridized eigenstates  $\overline{|n, k\rangle}$  of Eq. (3.6) without a drive—we will distinguish dressed (eigen) states (and operators) from bare states by an overline throughout. After setting  $\varepsilon = 0$  to eliminate the drive, the matrix representation of Eq. (3.6) is numerically diagonalized to obtain an initially unsorted list of matched eigenenergy/eigenstate pairs  $\{\overline{E}_{n,k}, \overline{|n, k\rangle}\}$  for the qubit-resonator system. The one-to-one correspondence between these pairs and the bare energy/state pairs  $\{E_{n,k}, |n, k\rangle\}$  may be found by examining the structure of the RWA interaction Hamiltonian in Eq. (3.4): Since excitation number is preserved, there exist closed subspaces  $\{|n, k\rangle : (n + k) = n_\Sigma\}$  with constant excitation number  $n_\Sigma = 0, 1, \dots$ , which we name *RWA strips* [151] [see Fig. 3.1(b)]. Crucially, since energy levels repel during interaction and avoid crossing, the order of the eigenenergies within a strip is the same as for bare energies. Thus, for each strip with  $n_\Sigma$  excitations we first identify the eigenstates  $\overline{|n, k\rangle}$  that lie within the span of that strip; next, we order the eigenenergies  $\overline{E}_{n,k}$  to match the bare energies  $E_{n,k}$ , which uniquely identifies each hybridized eigenenergy/eigenstate pair. We then set the overall sign of each eigenstate such that it does not flip with changing  $n$ . After performing this identification, we construct a basis-change matrix

$$U \equiv \sum_{n,k} \overline{|n, k\rangle} \langle n, k| \quad (3.8)$$

to easily switch between representations numerically. Note that without proper identification (sorting) of the eigenstates, the numerical analysis at large photon numbers is practically impossible.

The eigenstates  $\overline{|n, k\rangle}$  form the Jaynes-Cummings ladders of effective resonator levels that correspond to a fixed nominal qubit level  $k$ . For brevity we will call them *eigenladders* of dressed resonator Fock states. Each eigenladder behaves like a nonlinear resonator, with an  $n$ -dependent frequency

$$\omega_r^{(k)}(n) = \overline{E}_{n+1,k} - \overline{E}_{n,k}. \quad (3.9)$$

Note that in this formula both sides are numerically calculated in the rotating frame; however, the equation in the lab frame is the same. Conversion to the lab frame involves adding the drive frequency:  $\omega_d + \omega_r^{(k)}(n)$  for the resonator frequency and  $(n+k)\omega_d + \overline{E}_{n,k}$  for energy.

At large photon numbers,  $n \gtrsim n_c$ , each  $\overline{|n, k\rangle}$  spans a significant fraction of all bare transmon levels. Nevertheless, as we will see, ringing up the resonator from its ground state with an initial transmon level  $k$  will primarily excite the states within the eigenladder corresponding to  $k$ . This behavior closely mimics that of the ideal dispersive case, where a pump excites the bare resonator states  $|n\rangle_r$  while keeping the transmon state  $|k\rangle_q$  unperturbed. However, we will also show that there are small but important dynamical differences between our RWA Jaynes-Cummings model and ideal dispersive coupling in the eigenbasis.

### 3.3 Dressed coherent state model

We now define an ideal coherent state in the eigenbasis [152–154] (a dressed coherent state) corresponding to a nominal transmon state  $k$  as

$$|\alpha\rangle_k = e^{-|\alpha|^2/2} \sum_n \frac{\alpha^n}{\sqrt{n!}} |n, k\rangle, \quad (3.10)$$

so that the only difference from the standard coherent state of the resonator is that we use eigenstates instead of the bare states. Perhaps surprisingly given the eigenstate hybridization, such a dressed coherent state is practically unentangled even for  $|\alpha|^2 \gg n_c$ , in contrast to what one might initially guess [154]—see Appendix E.

A dressed coherent state is not an eigenstate of the bare lowering operator  $a$  of the resonator. Instead, it is an eigenstate of the *dressed* lowering operator [127, 153]

$$\bar{a} \equiv UaU^\dagger = \sum_{n,k} \sqrt{n+1} |n, k\rangle \langle n+1, k| \quad (3.11)$$

that removes a collective excitation within the same eigenladder. The parameter  $\alpha$  is the expectation value of the dressed lowering operator,  $\alpha = {}_k\langle \alpha | \bar{a} | \alpha \rangle_k$ , which will be useful in what follows.

Note that for a dressed coherent state  $|\alpha\rangle_k$ ,  $|\alpha|^2$  is not exactly equal to the average number  $\bar{n}$  of photons in the resonator. (Instead,  $|\alpha|^2 = {}_k\langle \alpha | \bar{a}^\dagger \bar{a} | \alpha \rangle_k$  is the average dressed excitation number within eigenladder  $k$ .) However, the difference is very small and will be mostly neglected below, so that we will use  $\bar{n} = |\alpha|^2$ . In the cases when the difference may be important, we will specify the meaning of  $\bar{n}$  explicitly.

### 3.3.1 Model inaccuracy contributions

During resonator ring-up, we expect the joint qubit-resonator state to approximate such a dressed coherent state, rather than a bare coherent state as is usually assumed with ideal dispersive coupling. As such, we quantify the fidelity of a numerically simulated state  $|\psi\rangle$  compared to a dressed coherent state  $|\alpha\rangle_k$  as the overlap

$$F = |\langle\psi|\alpha\rangle_k|^2, \quad (3.12)$$

where the parameter  $\alpha$  is chosen to maximize the fidelity. In practice, we find that an initial guess of  $\alpha = \langle\psi|\bar{a}|\psi\rangle$  is very close to the optimal  $\alpha$ , producing nearly indistinguishable fidelity.

Note that we can expand a numerically calculated state  $|\psi\rangle = \sum_{n,\ell} c_{n,\ell} \overline{|n,\ell\rangle}$  as

$$|\psi\rangle = \sqrt{1 - P_{\text{stray}}} |\psi\rangle_k + \sqrt{P_{\text{stray}}} |\psi\rangle_{\perp}, \quad (3.13)$$

splitting it into a part  $|\psi\rangle_k \propto \sum_n c_{n,k} \overline{|n,k\rangle}$  within the “correct” eigenladder  $k$ , and a part  $|\psi\rangle_{\perp} \propto \sum_{n,\ell \neq k} c_{n,\ell} \overline{|n,\ell\rangle}$  orthogonal to that eigenladder, where  $P_{\text{stray}} = \sum_{n,\ell \neq k} |c_{n,\ell}|^2$  is the stray population that leaked out of the eigenladder  $k$ , and both  $|\psi\rangle_k$  and  $|\psi\rangle_{\perp}$  are normalized. As such, if we define the overlap fidelity within the correct eigenladder  $F_c = |{}_k\langle\alpha|\psi\rangle_k|^2$ , then we can write the total fidelity as  $F = (1 - P_{\text{stray}}) F_c$ , and thus decompose the infidelity

$$1 - F = P_{\text{stray}} + (1 - P_{\text{stray}})(1 - F_c) \quad (3.14)$$

into two distinct sources: (i) the stray population  $P_{\text{stray}}$  outside the correct eigenladder, and (ii) the infidelity  $1 - F_c$  compared with a coherent state within the correct eigenladder.

To test the infidelity of the dressed coherent state model, we numerically simulate the resonator ring-up with a (sudden) constant drive amplitude  $\varepsilon/2\pi = 10$  MHz, and then calculate the infidelity according to Eq. (3.14) as a function of time, yielding the results presented in Fig. 3.2. First, we confirm that the infidelity  $1 - F$  for a dressed coherent state (black dashed line) is typically orders of magnitude better than the infidelity  $1 - F_b$  for a bare coherent state (red dotted line); as expected,  $1 - F_b$  becomes very significant at  $n \gtrsim n_c$ . Second, we can clearly separate the effects of the stray population leakage  $P_{\text{stray}}$  (thin solid blue line) from the infidelity  $1 - F_c$  of the renormalized state within the correct eigenladder (thick solid orange line). At short times, the dominant effect is a small ( $\sim 10^{-5}$ ) stray population leakage that rapidly oscillates and then stays approximately constant. (For clarity we do not show oscillations for the black dashed line, showing only the maxima.) However, at longer times the contribution  $1 - F_c$  becomes the dominant source of infidelity (eventually reaching  $\sim 10^{-1}$ ). In the next two subsections, we quantify these two sources of infidelity in more detail.

### 3.3.2 Infidelity from stray population

A dressed coherent state is naturally produced by a drive which is acting in the eigenbasis, while the drive term in Eq. (3.6) acts on the bare basis of the system. This mismatch between the bare and eigenstates in the drive is crudely proportional to  $g/\Delta$ , and leads to the stray population outside of the correct eigenladder. For typical experimental parameters this leakage is quite small, particularly in comparison with qubit energy relaxation, dressed dephasing, Purcell relaxation, and non-RWA effects. For a more detailed

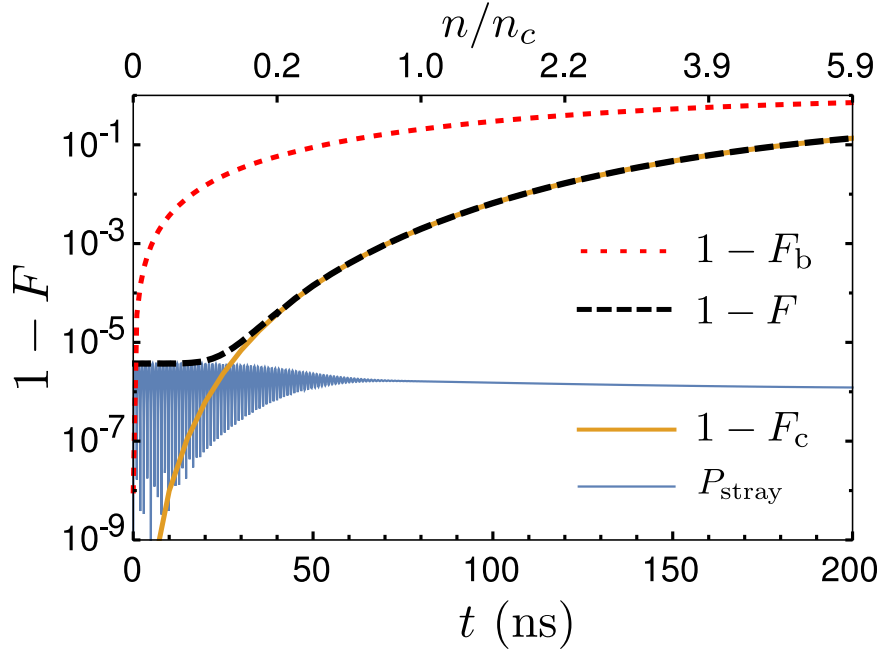


Figure 3.2: Infidelity of coherent-state approximations during resonator ring-up [140]. The infidelity  $1 - F_b$  of a bare coherent state (dotted red line) is compared with the infidelity  $1 - F$  of a dressed coherent state (dashed black line). The latter displays two distinct effects: at short time (and small photon number  $\bar{n}$ ) the dominant effect is the leakage of a stray population  $P_{\text{stray}}$  (thin solid blue line) out of the correct eigenladder; however, at longer time (and larger  $\bar{n}$ ) the infidelity  $1 - F_c$  of the renormalized state within the correct eigenladder (thick solid orange line) significantly increases during evolution. Here the system, with parameters  $\omega_r/2\pi = 6$  GHz,  $\omega_q/2\pi = 5$  GHz,  $\eta/2\pi = 200$  MHz,  $g/2\pi = 100$  MHz, is resonantly pumped from its ground state  $|0, 0\rangle$  with a constant drive envelope  $\varepsilon/2\pi = 10$  MHz.

analysis of this stray population, including a phenomenological model and comparison with numerical simulations, see Refs. [79] and [140].

### 3.3.3 Infidelity from shearing

The second contribution to the infidelity of the dressed coherent state approximation in Eq. (3.14) is due to infidelity  $1 - F_c$  within the correct eigenladder. As seen in Fig. 3.2, it becomes increasingly important at longer evolution times, when the number

of photons  $\bar{n}$  becomes large. As discussed below, this infidelity arises from the effective nonlinearity of the resonator due to its interaction with the transmon. This nonlinearity produces a shearing effect on the evolution of the dressed coherent state that squeezes the state.

Numerically, this distortion is clearly seen by plotting the Husimi Q-function of the renormalized state  $|\psi\rangle_k$  [defined as in Eq. (3.13)] that remains within the correct eigenladder,

$$Q_\psi(\alpha) = \frac{1}{\pi} |{}_k\langle\alpha|\psi\rangle_k|^2, \quad (3.15)$$

where  $|\alpha\rangle_k$  is a dressed coherent state as in Eq. (3.10). The contour plots of  $Q_\psi(\alpha)$  in the complex plane of  $\alpha$  are shown in Fig. 3.3(a) for a numerically simulated ring-up evolution, starting with the state  $|0, 0\rangle$  (there are five snapshots at time moments separated by 50 ns). If the state  $|\psi\rangle_k$  were a perfect dressed coherent state  $|\psi\rangle_k = |\beta\rangle_k$  centered at  $\beta = {}_k\langle\psi|\bar{a}|\psi\rangle_k$ , it would have a Q-function  $Q_\psi(\alpha) = e^{-|\alpha-\beta|^2}/\pi$  with circular contours. However, Fig. 3.3(a) clearly shows a progressive distortion of the initial circular profile into a squeezed ellipse as the average photon number increases. We will prove later that  $|\psi\rangle_k$  is indeed a close approximation of a (minimum-uncertainty) squeezed state in the eigenbasis  $|\overline{n, k}\rangle$  – see Fig. 3.3(b).

The squeezing distortion in Fig. 3.3 is similar to the self-developing quadrature squeezing discussed in Ref. [152] for the catch-disperse-release measurement protocol (e.g., compare Fig. 3.3 with the figures in the Supplemental Material of [152]). In that protocol, the squeezing was shown to significantly decrease the measurement error. In general, the self-developing squeezing can either increase or decrease the measurement error depending on the angle of the squeezing axis, and the analysis is clearly important for practical qubit

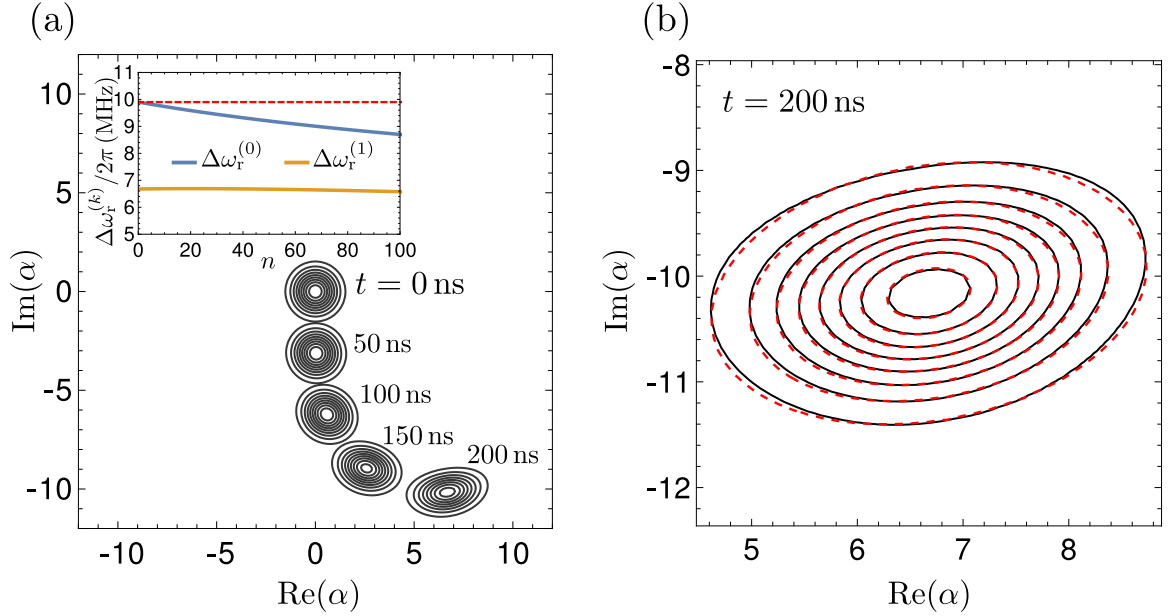


Figure 3.3: (a) Numerically simulated evolution of the dressed Husimi Q-function for the state remaining in the correct eigenladder, given an initial state of  $|0,0\rangle$  and a resonant drive. Snapshots taken at 50 ns intervals show the progressive shearing of the state caused by resonator nonlinearity. Inset:  $n$ -dependence of the difference  $\Delta\omega_r^{(k)} = \omega_r^{(k)} - \omega_r$  between the effective and bare resonator frequencies. The solid blue (upper) line shows  $\Delta\omega_r^{(0)}(n)$  for the ground-state eigenladder, the solid orange (lower) line shows  $\Delta\omega_r^{(1)}(n)$  for the excited-state eigenladder, and the red dashed line indicates the applied drive frequency. (b) Detail of the Q-function at 200 ns. The analytical result for a *dressed squeezed state* (dashed red) shows good agreement with the numerically simulated state (solid black). The agreement is significantly better for earlier times (not shown). Parameters are:  $\omega_r/2\pi = 6$  GHz,  $\omega_q/2\pi = 5$  GHz,  $\eta/2\pi = 200$  MHz,  $g/2\pi = 100$  MHz, and  $\varepsilon/2\pi = 10$  MHz. The contours of the Q-function are drawn at the levels of  $0.1/\pi, 0.2/\pi, \dots, 0.8/\pi$ .

measurements. A strong self-developing squeezing has been observed experimentally in Ref. [159].

The reason for the self-developing squeezing is the nonlinearity of the transmon, which makes the effective resonator frequency  $\omega_r^{(k)}(n)$  dependent on the number of photons  $n$  – see Eq. (3.9) and the inset of Fig. 3.3(a). Qualitatively, this  $n$ -dependence causes parts of the circles in Fig. 3.3(a) with different distances  $|\alpha|$  from the origin to rotate with slightly

different angular velocities, thus shearing the circular profile of an initially coherent state as it evolves. Note that in the case of a constant derivative  $d\omega_r^{(k)}(n)/dn$ , the shearing rate should grow with  $|\alpha|$  because  $dn = 2|\alpha|d|\alpha|$ ; thus, the effect becomes more important for larger photon numbers. Also note that the drift of the resonator detuning from the drive with  $n$  could be compensated for by changing the drive frequency (chirping); however, this does not affect the shearing, since it originates from the frequency variation within the photon number uncertainty  $\bar{n} \pm \sqrt{\bar{n}}$ .

It is easy to analyze the shearing effect in the absence of the drive. If at  $t = 0$  we have a dressed coherent state given by Eq. (3.10) (with notation  $\alpha$  replaced by  $\beta$ ), then it obviously evolves as

$$|\psi(t)\rangle_k = e^{-|\beta|^2/2} \sum_n \frac{\beta^n}{\sqrt{n!}} e^{-i\bar{E}_{n,k}t} \overline{|n, k\rangle}, \quad (3.16)$$

where the eigenenergies  $\bar{E}_{n,k}$  are in the rotating frame  $\omega_d$ , i.e., with subtracted terms  $(n+k)\omega_d$ . Let us expand these energies up to the second order in the vicinity of  $\bar{n} = |\beta|^2$  as  $\bar{E}_{n,k} \approx \bar{E}_{\bar{n},k} + \omega_r^{(k)}(\bar{n})(n - \bar{n}) + \frac{1}{2}(d\omega_r^{(k)}/dn)|_{\bar{n}}(n - \bar{n})^2$ , where the resonator frequencies  $\omega_r^{(k)}(n)$  are also in the rotating frame (i.e., with subtracted  $\omega_d$ ) and we neglect discreteness of  $n$  by assuming  $\bar{n} \gg 1$  and sufficiently small nonlinearity. This gives

$$|\psi(t)\rangle_k \approx e^{-|\beta|^2/2} \sum_n \frac{[\beta(t)]^n}{\sqrt{n!}} e^{-iq(n-\bar{n})^2} \overline{|n, k\rangle}, \quad (3.17)$$

$$\dot{\beta} = -i\omega_r^{(k)}(\bar{n})\beta, \quad \dot{q} = \frac{1}{2}(d\omega_r^{(k)}/dn)|_{\bar{n}}, \quad (3.18)$$

where we neglected the overall phase of  $|\psi(t)\rangle_k$ . Thus, to leading order in  $|n - \bar{n}|$ , the effect is an appearance of the quadratic phase factor  $e^{-iq(n-\bar{n})^2}$  and an obvious rotation of  $\beta(t)$  when the effective resonator frequency  $\omega_r^{(k)}(\bar{n})$  is not exactly on resonance with the drive. The presence of the growing quadratic-term coefficient  $q$  in the phase factor leads

to a deviation from the dressed coherent state, for which  $q = 0$ . (We restrict our attention to the case  $q \ll 1$ ; very interesting effects beyond this regime, including state revival and formation of “cat” states, have been observed in [159].)

It is easy to see that the infidelity of the sheared state (3.17) compared with the dressed coherent state  $|\beta\rangle_k$  is

$$1 - F_c \approx q^2 \overline{(n - \bar{n})^4} \approx 3(q|\beta|^2)^2, \quad (3.19)$$

assuming  $1 - F_c \ll 1$  and  $\bar{n} \gg 1$ . This infidelity grows in time because of the  $q$ -evolution (3.18) due to the nonlinearity. However, the state evolution due to drive (in a locally linear system) should preserve  $1 - F_c$  because both states ( $|\psi\rangle_k$  and  $|\beta\rangle_k$ ) are equally displaced within the complex plane of  $\alpha$  (mathematically, because the standard displacement operator is unitary). Therefore, if the state remains in the form (3.17), then

$$\frac{d}{dt}(q|\beta|^2) = \dot{q}|\beta|^2 = \frac{\bar{n}}{2} (d\omega_r^{(k)}/dn)|_{\bar{n}}. \quad (3.20)$$

In particular, if  $\bar{n} \approx (\varepsilon t)^2$  for a resonant drive and the derivative  $d\omega_r^{(k)}/dn$  does not significantly depend on  $n$  [see inset in Fig. 3.3(a)], then  $q\bar{n} \simeq (d\omega_r^{(k)}/dn) \varepsilon^2 t^3/6$ , and the infidelity is

$$1 - F_c \simeq \frac{1}{12} [\varepsilon^2 t^3 (d\omega_r^{(k)}/dn)]^2. \quad (3.21)$$

This is a very crude estimate because  $d\omega_r^{(k)}/dn$  depends on  $n$ , the approximation  $\bar{n} \approx (\varepsilon t)^2$  works only at small  $t$  and, most importantly, the state during the evolution does not remain in the form (3.17), as discussed in the next section. [The form (3.17) is no longer applicable when the motion of the Q-function center shown in Fig. 3.3(a) deviates from a straight line.] Nevertheless, comparison with numerical results in Fig. 3.4 shows that Eq.

(3.21) gives a reasonable estimate of the infidelity. The blue (upper) solid line in Fig. 3.4 is identical to the orange line in Fig. 3.2 and shows the numerically calculated  $1 - F_c$  for the evolution starting with  $|0, 0\rangle$ . The blue (upper) dashed line is obtained using Eq. (3.21) with  $d\omega_r^{(0)}/dn$  calculated at  $n = 0$ . It fits the solid line well at short times, and then deviates up, mostly because  $|d\omega_r^{(0)}/dn|$  decreases with  $n$  [see inset in Fig. 3.3(a)] while analytics still uses the value at  $n = 0$ . The red (lower) solid line in Fig. 3.4 shows  $1 - F_c$  for the evolution starting with  $|\overline{0, 1}\rangle$ . This infidelity is crudely two orders of magnitude less than for the blue (upper) line because the derivative  $|d\omega_r^{(1)}/dn|$  within the excited-state eigenladder is much smaller than that for the ground state [see inset in Fig. 3.3(a)]. The infidelity  $1 - F_c$  shows a dip near 100 ns. This is because  $\omega_r^{(1)}(n)$  increases for  $n < 20$  and decreases for  $n > 20$ ; therefore  $q|\beta|^2$  in Eq. (3.20) first increases and then decreases, passing through zero. At the point of passing zero we expect  $1 - F_c = 0$ , thus producing the dip; numerically it is not zero because the form (3.17) is only an approximation. Since  $d\omega_r^{(1)}/dn$  depends on  $n$  very significantly (even changing the sign), we cannot use Eq. (3.21), so instead we have integrated Eq. (3.20) to obtain the red (lower) dashed line in Fig. 3.4. As we see, it agrees well with the solid line. If the integration of Eq. (3.20) is also done for the evolution starting with  $|0, 0\rangle$ , then the result is significantly closer to the blue solid line than the blue dashed line.

Note that the states with a quadratic phase factor as in Eq. (3.17) have been discussed in optics long ago [168–171]. It was shown that these states are squeezed in the broad sense that variance of a quadrature operator can be smaller than that for a coherent state. However, to the best of our knowledge, it was never shown that such states with

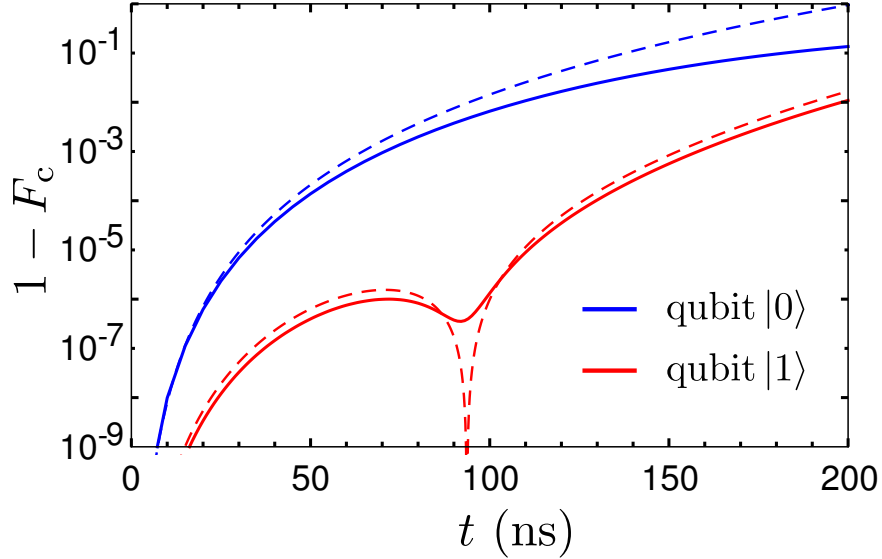


Figure 3.4: Infidelity  $1 - F_c$  of the dressed coherent state approximation within the initial eigenladder, starting with  $|0, 0\rangle$  (upper lines, blue) or  $|0, 1\rangle$  (lower lines, red). Parameters are the same as for Fig. 3.2. The solid lines show numerical results, upper (blue) dashed line is calculated via Eq. (3.21) with the frequency derivative taken at  $n = 0$ , and the lower (red) dashed line is calculated by integrating Eq. (3.20).

large  $\bar{n}$  can be represented as squeezed states in the narrow sense, i.e., they are close to satisfying the minimum-uncertainty condition. Moreover, it was often emphasized that the states described by Eq. (3.17) are not the minimum-uncertainty states, because for sufficiently large  $q$  they have crescent-like shape of the Q-function instead of the elliptical shape, and for even larger  $q$  the shape becomes a ring-like one (see experiment [159]). In contrast, in the next section we will show that in the practically interesting regime these states are quite close to the squeezed states in the narrow sense. This is because for large  $\bar{n}$  the squeezing factor is determined by  $q|\beta|^2$ , while significant deviation from a minimum-uncertainty squeezed state starts at  $|q\beta| \gtrsim 0.1$ ; therefore the squeezing becomes significant already for such values of  $q$ , for which the deviation (crescent-like shape) is still quite small – see Fig. 3.3(b). In the next section we will also derive simple evolution equations for these

squeezed states.

### 3.4 Dressed squeezed state model

As discussed in the previous section, transmon-induced nonlinearity of the resonator (i.e., frequency dependence on the number of photons) evolves a dressed coherent state into a sheared state of the form (3.17) with quadratic phase factor. Unfortunately, it is not easy to describe evolution of this sheared state due to drive. In some sense this is because an evolution due to drive is naturally described in the phase space (which is almost always used in optics), while the sheared state representation requires Fock space. We will be able to solve this dilemma by showing that the sheared state (3.17) is actually close to a (minimum-uncertainty) squeezed state in the eigenbasis, which we call a dressed squeezed state. Evolution of a squeezed state due to drive can be easily described in the phase space, while its evolution due to nonlinearity can be easily described in the Fock space. Thus, if we have a reasonably simple conversion between the Fock and phase spaces for squeezed states, we can describe the state evolution due to both nonlinearity and drive. This simple conversion is possible only for large  $\bar{n}$ , which is an important assumption for our derivation below (in practice, it is still well applicable for the dynamics starting with the vacuum state).

#### 3.4.1 Dressed sheared Gaussian state

In this section we prove that for sufficiently large number of photons, the (dressed) sheared state is approximately equivalent to a (dressed) minimum-uncertainty squeezed

state.

For  $|\beta|^2 \gg 1$  we can use a Gaussian approximation for the wavefunction (3.17) in the Fock space. Let us introduce a more general (dressed) sheared Gaussian state as

$$|\beta, K, W\rangle_k = \sum_n \frac{1}{(2\pi W|\beta|^2)^{1/4}} \exp\left[-\frac{(n - |\beta|^2)^2}{4W|\beta|^2}\right] \times \exp[in \arg(\beta)] \exp\left[-i\frac{K(n - |\beta|^2)^2}{|\beta|^2}\right] |n, k\rangle, \quad (3.22)$$

in which we used the new notation  $K = q|\beta|^2$  and also introduced a new parameter  $W = \sigma_n^2/\sigma_{n,\text{cs}}^2$ , which is the variance  $\sigma_n^2$  of the Gaussian  $n$ -distribution compared with the variance  $\sigma_{n,\text{cs}}^2 = |\beta|^2$  of a dressed coherent state, so that  $w = \sqrt{W}$  is the relative width of the  $n$ -distribution. Thus, the sheared Gaussian state is characterized by 4 parameters:  $\beta$  has the standard optical meaning,  $K$  characterizes the shearing,  $W$  characterizes the relative width of photon number distribution, and  $k$  labels the eigenladder. We assume that  $K$  and  $W$  are on the order of 1, while  $|\beta|^2 \gg 1$ . Note that the term  $in \arg(\beta)$  can be replaced with  $i(n - |\beta|^2) \arg(\beta)$ ; this changes only the unimportant overall phase of the state, but clarifies the role of  $\arg(\beta)$  as the linear-order part of the phase expansion in  $n$  around the mean  $|\beta|^2$ .

We call the form (3.22) a hybrid phase-Fock representation, because  $\beta$  is borrowed from optical phase space, while  $K$  and  $W$  are the Fock-space parameters. Note that the state (3.22) is not exactly normalized, but the difference from perfect normalization is less than  $10^{-5}$  if  $|\beta|^2 > \max(20W, 1/W)$ . With a similar accuracy,  $\bar{n} = |\beta|^2$  for the average number of photons (excitations in the eigenladder).

The average value of the dressed lowering operator for the state (3.22) is

$$\langle \bar{a} \rangle \approx \beta + \frac{2 - W - 1/W}{8\beta^*} - i\frac{KW}{\beta^*} - \frac{2K^2W}{\beta^*} \approx \beta, \quad (3.23)$$

where in the second equality we neglected the terms scaling as  $|\beta|^{-1}$ . Similarly, neglecting  $|\beta|^{-1}$ -terms, we find

$$\langle \bar{a}^2 \rangle \approx \beta^2 + \frac{\beta^2}{|\beta|^2} \left( \frac{1}{2} - \frac{1}{2W} - 4iKW - 8K^2W \right). \quad (3.24)$$

Now let us define (dressed) quadrature operators,

$$X_\varphi = \frac{1}{2} \left( e^{-i\varphi} \bar{a} + e^{i\varphi} \bar{a}^\dagger \right), \quad (3.25)$$

for which  $\varphi$  is the quadrature angle (note that notation  $\varphi$  was briefly used for a different quantity in Sec. 3.3.2). Using Eqs. (3.23) and (3.24) we find the variance  $\sigma_{X_\varphi}^2 = \langle X_\varphi^2 \rangle - \langle X_\varphi \rangle^2$ ,

$$\begin{aligned} \sigma_{X_\varphi}^2 &= \frac{W + 1/W}{8} + 2K^2W + KW \sin[2 \arg(\beta) - 2\varphi] \\ &+ \left( \frac{W - 1/W}{8} - 2K^2W \right) \cos[2 \arg(\beta) - 2\varphi]. \end{aligned} \quad (3.26)$$

It is easy to check that the  $\varphi$ -dependence of this variance is exactly what would be expected for a minimum-uncertainty squeezed state. In particular, the product of the minimum and maximum values of  $\sigma_{X_\varphi}^2$  is the same as for a coherent state,

$$\sigma_{X_\varphi, \min}^2 \sigma_{X_\varphi, \max}^2 = 1/16, \quad (3.27)$$

with

$$\sigma_{X_\varphi, \min}^2 = \left[ 1 + S - \sqrt{(1 + S)^2 - 1} \right] / 4, \quad (3.28)$$

$$S = 8K^2W + (W + 1/W - 2)/2, \quad (3.29)$$

and  $\sigma_{X_\varphi, \max}^2 = [1 + S + \sqrt{(1 + S)^2 - 1}] / 4$ . We see that the degree of squeezing is determined by the parameter  $S$ , so that  $S = 0$  corresponds to a (dressed) coherent state. The minimum

quadrature variance  $\sigma_{X\varphi,\min}^2$  is achieved at the angle  $\varphi_{\min} = \theta/2$ , where

$$\begin{aligned} \theta = 2 \arg(\beta) + \arctan\left(\frac{8KW}{16K^2W - W + 1/W}\right) \\ + \frac{\pi}{2} [1 - \text{sgn}(16K^2W - W + 1/W)], \end{aligned} \quad (3.30)$$

and the factor of 2 between  $\theta$  and  $\varphi_{\min}$  is to conform with the standard optical definition of the squeezing parameter discussed later.

Thus, we have proven that for sufficiently large  $|\beta|^2$  the (dressed) sheared Gaussian state (3.22) is close to a (dressed) minimum-uncertainty squeezed state (despite this is not true for small  $|\beta|^2$  [159, 170, 171]). Note that the ‘‘conservation of area’’ criterion (3.27) for a minimum-uncertainty squeezed state is valid for quadratures, but is not valid for the Husimi Q-function shown in Fig. 3.3, because the Q-function involves convolution with a coherent state, and therefore the width of the short axis can be at most a factor of  $\sqrt{2}$  shorter than that of a coherent state.

### 3.4.2 Conversion into squeezed state notations

Using the standard optical definition [172, 173], a dressed squeezed state should be defined as

$$|\beta, \xi\rangle_k = \exp[\beta\bar{a}^\dagger - \beta^*\bar{a}] \exp\left[\xi^*\frac{\bar{a}^2}{2} - \xi\frac{\bar{a}^\dagger}{2}\right] \overline{|0, k\rangle}, \quad (3.31)$$

where  $\xi \equiv re^{i\theta}$  is the squeezing parameter, while  $\beta$  is a displacement in the phase space. The smallest standard deviation  $\sigma_{X\varphi,\min}$  for the quadrature  $X_\varphi$  should then be achieved [172, 173] at the angle  $\varphi_{\min} = \theta/2$  [thus corresponding to our notation in Eq. (3.30)], and its value should be  $\sigma_{X\varphi,\min} = e^{-r}\sigma_{X\varphi,\text{cs}}$  compared with the standard deviation  $\sigma_{X\varphi,\text{cs}}$  for a coherent state. The longest axis is  $\sigma_{X\varphi,\max} = e^r\sigma_{X\varphi,\text{cs}}$  at the angle  $\varphi_{\max} = \theta/2 \pm \pi/2$ .

Comparing these standard optical definitions with our approximate results (3.27), (3.28), and (3.30) for large  $|\beta|^2$ , we obtain the conversion

$$r = \frac{1}{2} \operatorname{arccosh}(S + 1), \quad (3.32)$$

where  $S$  is given by Eq. (3.29), while  $\theta$  is given by Eq. (3.30).

It is easy to check that the case  $K = 0$ ,  $W = 1$  corresponds to the dressed coherent state,  $\xi = 0$ . In the absence of shearing,  $K = 0$ , we have a dressed amplitude-squeezed state for  $W < 1$  [as is obvious from Eq. (3.22)] and a dressed phase-squeezed state for  $W > 1$  – see Eq. (3.30), from which  $\theta/2 = \arg(\beta)$  for  $W < 1$  and  $\theta/2 = \arg(\beta) \pm \pi/2$  for  $W > 1$ . As shown in Appendix E, the dressed squeezed state is practically unentangled for large  $|\beta|^2$ , in spite of a significant entanglement of the qubit-resonator eigenstates.

Using Eqs. (3.30) and (3.32) we can convert a sheared Gaussian state (3.22) with sufficiently large  $|\beta|^2$  into a (minimum-uncertainty) squeezed state (3.31). Similarly, we can convert any (minimum-uncertainty) squeezed state with sufficiently large  $|\beta|^2$  into a sheared Gaussian state. Most importantly, we know that a squeezed state is simply displaced in the phase space by an action of a drive  $\varepsilon(t)$ . This means that a sheared Gaussian state (3.22) remains a sheared Gaussian state under an action of the drive (assuming large  $|\beta|^2$ ). Since it also keeps the form (3.22) under the evolution due to nonlinearity, this form is always preserved (approximately), and therefore it is sufficient for us to characterize the evolution of the state by evolution of only three parameters:  $\beta$ ,  $K$ , and  $W$ . We emphasize that this simplicity is possible only for large  $|\beta|^2$  or, in other words, for a sufficiently small nonlinearity. In general, the simultaneous evolution due to nonlinearity and drive creates states that cannot be described as (minimum-uncertainty) squeezed states or sheared states.

Nevertheless, this approximation works quite well for our system.

### 3.4.3 Phase-Fock-space evolution of dressed squeezed state

Now let us derive evolution equations for the parameters  $K$ ,  $W$ , and  $\beta$  of the dressed sheared/squeezed state. We will first consider the evolution in the absence of the drive, then the evolution only due to the drive, and then add up the terms from these evolutions.

Evolution of the dressed sheared state (3.22) due to nonlinearity of the resonator is given by Eq. (3.18), which leads to

$$\dot{K} = \frac{1}{2} |\beta|^2 (d\omega_r^{(k)}/dn) \Big|_{n=|\beta|^2}. \quad (3.33)$$

Note that we do not need to take a derivative of  $|\beta|^2$  because this type of evolution does not change  $|\beta|^2$ . In the absence of the drive, the parameter  $\beta$  evolves only due to the resonator frequency detuning from the rotating frame,

$$\dot{\beta} = -i\omega_r^{(k)}(n) \Big|_{n=|\beta|^2} \beta. \quad (3.34)$$

To derive formulas for the evolution of  $\beta$ ,  $K$ , and  $W$  due to drive  $\varepsilon(t)$ , we use the fact [173] that for a squeezed state (3.31) the parameter  $\xi$  remains constant, while  $\beta$  changes as  $\dot{\beta} = -i\varepsilon$ . Therefore, the parameters  $S$  and  $\theta$  given by Eqs. (3.29) and (3.30) should remain constant with changing  $\beta$ . The corresponding evolution  $\dot{K}$  and  $\dot{W}$  can be found from the system of equations

$$\frac{\partial S}{\partial K} \dot{K} + \frac{\partial S}{\partial W} \dot{W} = 0, \quad \frac{\partial \theta}{\partial K} \dot{K} + \frac{\partial \theta}{\partial W} \dot{W} + \frac{\partial \theta}{\partial \beta} \dot{\beta} = 0, \quad (3.35)$$

which has the following solution:

$$\dot{W} = 8KW\text{Re}(\varepsilon/\beta), \quad \dot{K} = \left( \frac{1-W^2}{4W^2} - 4K^2 \right) \text{Re}(\varepsilon/\beta), \quad (3.36)$$

where we took into account the equation  $\dot{\beta} = -i\varepsilon$ . Note that here we should not include evolution of  $\beta$  due to detuning, Eq. (3.34), because otherwise the angle  $\theta$  would not be constant. Also note that in the term  $(\partial\theta/\partial\beta)\dot{\beta}$  in Eq. (3.35) we imply derivatives for both  $\text{Re}(\beta)$  and  $\text{Im}(\beta)$ .

Combining the evolution equations both in the absence of a drive and from the drive itself, we finally obtain

$$\dot{W} = 8KW \text{Re}(\varepsilon/\beta), \quad (3.37)$$

$$\begin{aligned} \dot{K} = & \left( \frac{1-W^2}{4W^2} - 4K^2 \right) \text{Re}(\varepsilon/\beta) \\ & + \frac{1}{2} |\beta|^2 \left( d\omega_r^{(k)}/dn \right) \Big|_{n=|\beta|^2}, \end{aligned} \quad (3.38)$$

$$\dot{\beta} = -i\omega_r^{(k)}(n) \Big|_{n=|\beta|^2} \beta - i\varepsilon. \quad (3.39)$$

These equations together with the conversion formulas (3.30) and (3.32) is our *main result* for the evolution of the dressed squeezed state. They allow very efficient simulation, since they avoid the large dimensionality of the pure Fock-space evolution specified by Eq. (3.6). Equations (3.37)–(3.39) are a hybrid between the Fock-space and the phase-space representations, capable of describing evolution of the dressed squeezed state as it rings up due to a coherent drive  $\varepsilon$ . To our knowledge, this is a novel representation, which was not previously used in optics.

Note that the derivation of these equations assumes large  $|\beta|^2$ . However, they can be numerically applied even for evolution starting with vacuum,  $\beta(0) = 0$ . [There

is no divergence due to the factor of  $\beta$  in the denominator, because at small times  $\beta = -i\epsilon t$ , and therefore  $\text{Re}(\epsilon/\beta) = \text{Re}(i/t) = 0$ .] We used these relatively simple equations to compare with the numerical results for evolution due to Hamiltonian (3.6) in a system with typically  $7 \times 300$  levels, and found very good agreement. The reason why Eqs. (3.37)–(3.39) still work well when starting with the vacuum is that the effect of nonlinearity at short times is small ( $K \approx 0$ ,  $W \approx 1$ ), while by the time when the squeezing due to nonlinearity becomes important,  $|\beta|^2$  is already large. Note, however, that for  $|\beta|^2 \lesssim 100$  the sheared and squeezed states are significantly different, and then it is important to use the dressed squeezed state (3.31) [not the sheared state (3.22)] as the more accurate model for comparison with simulation results.

Figure 3.3(b) shows comparison between the Q-function for the numerically calculated state  $|\psi\rangle_0$  (solid lines) and for the dressed squeezed state (dashed lines) calculated using Eqs. (3.37)–(3.39). [At the end we have converted parameters  $K$  and  $W$  into the squeezing parameters  $r$  and  $\theta$  using Eqs. (3.30) and (3.32), and then calculated the Q-function using the standard formula [172] for a squeezed state.] If the parameter  $\beta$  is not calculated from Eq. (3.39) but is instead computed as  $\beta = {}_0\langle\psi|\bar{a}|\psi\rangle_0$ , then the visual agreement between the dashed and solid lines becomes insignificantly better. The visible difference between solid and dashed lines is because the numerical state  $|\psi\rangle_0$  is not exactly the dressed squeezed state; in particular, for Fig. 3.3(b)  $|q\beta|\sqrt{W} = |K/\beta|\sqrt{W} = 0.023$ , which is comparable to the value of 0.1, above which a significant crescent-shape appears. The dashed lines in Fig. 3.3(b) are drawn for the squeezing parameter  $r = 0.550$ . This corresponds to the minimum and maximum quadrature variances of 0.333 and 3.00 compared

with the coherent state (0.340 and 3.01 numerically for  $|\psi\rangle_0$ ) and the scaling factors of 0.816 and 1.41 for the short and long axes of the Q-function, compared with the coherent state (numerically 0.81 and 1.43 in the vicinity of the center).

#### 3.4.4 Accuracy of dressed squeezed state approximation

To quantify the accuracy of the dressed squeezed state approximation and evolution equations (3.37)–(3.39), we compare the numerically calculated state  $|\psi\rangle_0$  for the evolution shown in Fig. 3.2 (starting with  $|0, 0\rangle$ ) with the result from Eqs. (3.37)–(3.39) for the sheared Gaussian state, which is then converted into the dressed squeezed state  $|\beta, \xi\rangle_0$ . The infidelity  $1 - F = 1 - |{}_0\langle\beta, \xi|\psi\rangle_0|^2$  is shown in Fig. 3.5 as the dashed blue (lower) line. It can be compared with similar infidelity for the dressed coherent state shown as the dashed orange (upper) line, for which we also used Eq. (3.39). We see that the accuracy of the dressed squeezed state model is much better than for the dressed coherent state model when the infidelity of the latter exceeds  $10^{-3}$ . However, at short times both infidelities practically coincide and are significantly larger than the coherent-state infidelity  $1 - F_c$  shown in Fig. 3.2 (also copied as the solid orange line in Fig. 3.5). Since the difference between the orange dashed and orange solid lines is the method of  $\alpha(t)$  calculation, either via Eq. (3.39) or as  $\alpha = {}_0\langle\psi|\bar{a}|\psi\rangle_0$ , this indicates an inaccurate result of Eq. (3.39) for the state center in the phase space. Let us similarly calculate the center of the dressed squeezed state as  $\beta = {}_0\langle\psi|\bar{a}|\psi\rangle_0 = \alpha$ , while the squeezing parameter  $\xi$  is still calculated via Eqs. (3.37)–(3.39). This produces the blue (lower) solid line in Fig. 3.5, which is crudely two orders of magnitude lower than  $1 - F_c$ , thus confirming that the dressed squeezed state

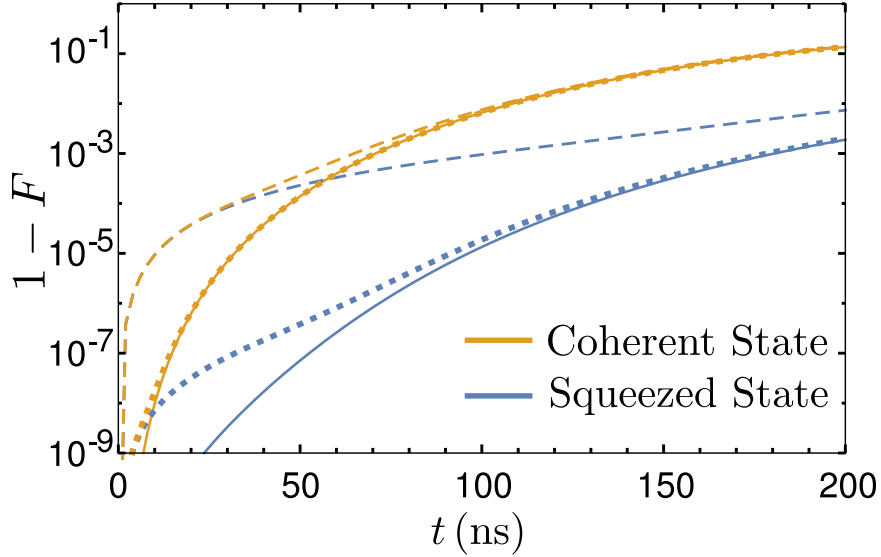


Figure 3.5: Comparison between the dressed squeezed state and dressed coherent state models within the “correct” eigenladder. Parameters are the same as in Figs. 3.2 and 3.3, evolution starts with  $|0, 0\rangle$ . Blue (lower) lines show time dependence of the infidelity  $1 - F = 1 - |\langle \beta, \xi | \psi \rangle_0|^2$  for the dressed squeezed states, orange (upper) lines show infidelity  $1 - |\langle \alpha | \psi \rangle_0|^2$  for the dressed coherent states. For solid lines the state centers  $\beta(t)$  and  $\alpha(t)$  are calculated as average values of the operator  $\bar{a}$ . For the dashed lines,  $\beta(t)$  and  $\alpha(t)$  are obtained from Eq. (3.39). For the dotted lines, in Eqs. (3.37)–(3.39) we use correction (3.40) for the drive amplitude. The dressed squeezed state model is about two orders of magnitude more accurate than the dressed coherent state model.

approximation is much better than the dressed coherent state approximation.

The reason for the inaccuracy of  $\beta(t)$  [or  $\alpha(t)$ ] calculation is rather simple. For the dashed lines in Fig. 3.5 we used the bare-basis value for the drive amplitude  $\varepsilon$ , while within an eigenladder it is actually slightly different. Using properly normalized eigenstates for  $n \ll n_c$ , it is possible to rewrite the lowering operator in the eigenbasis as:  $a \approx [1 + \frac{1}{2}(g/\Delta)^2 \sigma_z] \bar{a} - (g/\Delta) \bar{\sigma}_-$  (see, e.g., Eq. (53) in [153], and [127]), where  $\bar{\sigma}_-$  is the qubit-lowering operator in the eigenbasis. This leads to correction of the effective drive amplitude,

$$\tilde{\varepsilon} \approx \left[ 1 - \frac{1}{2} (g/\Delta)^2 \right] \varepsilon, \quad (3.40)$$

within the ground-state eigenladder at  $n \lesssim n_c$ . (Within the excited-state eigenladder the correction will then be  $\tilde{\varepsilon} \approx \{1 + \frac{1}{2}(g/\Delta)^2 - \frac{1}{2}[\sqrt{2}g/(\Delta + \eta)]^2\} \varepsilon$ .) Using the effective drive amplitude (3.40) in Eqs. (3.37)–(3.39) instead of  $\varepsilon$  produces dotted lines (instead of dashed lines) in Fig. 3.5. We see that the dotted lines are quite close to the solid lines; therefore, the simple correction (3.40) is sufficient for an accurate theory. Even better accuracy can be achieved if we use numerical matrix elements for the effective drive amplitude within the ground-state eigenladder,

$$\tilde{\varepsilon} = \frac{\overline{\langle n-1, 0 | a | n, 0 \rangle}}{\sqrt{\bar{n}}} \varepsilon, \quad (3.41)$$

which now depends on  $n \approx \bar{n}$ . For Fig. 3.5 this produces a line (not shown), which closely follows the blue solid line for the squeezed-state approximation and a line practically indistinguishable from the orange solid line for the coherent-state approximation.

We emphasize that in Fig. 3.5 the infidelity of the dressed squeezed state model is  $\lesssim 10^{-3}$ , while for the dressed coherent state model it is only  $\lesssim 10^{-1}$ . Note that we always convert the sheared state (3.22) with parameters  $K$  and  $W$  into the squeezed state (3.31) via Eqs. (3.30) and (3.32) before comparing with numerical  $|\psi\rangle_0$ . If this is not done, the infidelity of the sheared Gaussian state in Fig. 3.5 would be above  $10^{-3}$  at  $t < 100$  ns ( $\bar{n} < 40$ ), reaching  $3 \times 10^{-2}$  for  $\bar{n} < 0.5$  and becoming practically equal to the blue lines only at  $t > 160$  ns ( $\bar{n} > 100$ ).

Thus, we have numerically confirmed that the dressed squeezed state approximation performs much better than the dressed coherent state approximation. Nevertheless, the inaccuracy of the dressed squeezed state model still grows in time, and may eventually become significant.

### 3.5 Summary

In this chapter we analyzed the ring-up of a readout resonator coupled to a transmon qubit. The bare bases of the transmon and resonator hybridize into a joint eigenbasis that is organized into natural eigenladders associated with each nominal transmon state. As was pointed out previously, ringing up the resonator from its ground state using a coherent pump approximately creates a coherent state in this eigenbasis (i.e., a dressed coherent state) that is confined to the eigenladder corresponding to the initial transmon state. We analyzed the deviations from this first approximation and developed a more accurate dynamical model for the ring-up process.

Through numerical simulation, we demonstrated that the ring-up evolution deviates from the dressed coherent state model in two important respects. First, the initial transmon population may leak into other (“incorrect”) eigenladders that correspond to different initial transmon states. Second, even within the initial (“correct”) eigenladder the state may differ from a coherent state. We analyzed both deviations and developed analytical models to quantify the effects.

The stray population that leaks outside the correct eigenladder arises from the mismatch between the coherent pump (in the bare basis) and the hybridized resonator (in the eigenbasis). We found that this mismatch creates interesting dynamics over a relatively short timescale after the pump is applied, and were able to describe the resulting damped oscillations between neighboring eigenladders quantitatively. The most important result is that for typical experimental parameters the occupation of incorrect eigenladders remains small ( $\lesssim 10^{-4}$ ); therefore, this effect should not significantly contribute to the qubit mea-

surement error in present-day experiments. Note, however, that our analysis focuses solely on the population leakage caused by the pump itself during the ring-up process; as such, it neglects other important effects that contribute to the total leakage to incorrect eigenladders in practice, such as qubit energy relaxation, the Purcell effect, interactions with defects, dressed dephasing, and non-RWA effects. (Note that [151] extends the analysis presented here to include non-RWA effects, thus explaining an important example of experimentally observed leakage at high photon numbers.)

The dynamics of the hybridized resonator state remaining within the correct eigenladder is non-trivial due to the effective resonator nonlinearity induced by the interaction with the transmon. This nonlinearity leads to a significant deviation from the dressed coherent state picture—in our numerical simulations the infidelity of the dressed coherent state reaches  $\sim 10^{-1}$ . The nonlinear evolution shears the phase-space profile of the resonator state, deforming initially circular coherent state profiles into elliptical and crescent-shaped profiles over time. We showed that for practical ranges of parameters, these sheared profiles approximate ideal *squeezed states in the eigenbasis* (i.e., dressed squeezed states)—in our simulations the infidelity of the squeezed state picture reaches  $\sim 10^{-3}$ , or roughly two orders of magnitude better than that of a dressed coherent state. (Note that the dressed squeezed state is practically unentangled, similar to the dressed coherent state.) Using a hybrid phase-Fock-space approach, we derived simple equations of motion [Eqs. (3.37)–(3.39)] for the self-developing squeezing, which naturally generalize the evolution of a coherent state. These equations of motion depend only on the photon number-dependence of the dressed resonator frequency, which may be added phenomenologically from precomputed numerical

simulations or measured experimentally.

We emphasize that the self-developing squeezing may significantly affect the qubit measurement error, either decreasing or increasing it, depending on the squeezing axis angle relative to the line passing through the state centers in the phase space for the qubit states  $|0\rangle$  and  $|1\rangle$ . (The resonator field for the qubit state  $|0\rangle$  is affected by squeezing much more than for the state  $|1\rangle$  because of much more efficient level repulsion within the ground-state ladder of the Jaynes-Cummings Hamiltonian for the multi-level transmon.) Further analysis of this subject is definitely important.

The dressed squeezed state model provides an efficient and accurate description of the resonator physics during a sufficiently rapid ring-up process, when the resonator decay may be neglected (as was assumed in this chapter). This regime is also physically relevant for at least two known protocols: the catch-disperse-release measurement of a qubit [152] and the readout protocol [155] based on Josephson photomultipliers. However, in the standard method of transmon measurement, the resonator decay cannot be neglected (except during the ring-up), that will require an extension of our dressed squeezed state model. This generalization will be considered in Chapter 5.

## Chapter 4

# Measurement-Induced State Transitions in a Superconducting Qubit

Many superconducting qubit systems use the dispersive interaction between the qubit and a coupled harmonic resonator to perform quantum state measurement. Previous works have found that such measurements can induce state transitions in the qubit if the number of photons in the resonator is too high. These transitions can push the qubit out of the two-level subspace, and they show resonant behavior as a function of photon number. In this chapter, we develop a theory for these observations based on level crossings within the Jaynes-Cummings ladder, with transitions mediated by terms in the Hamiltonian that are typically ignored by the rotating wave approximation. We find that the most important of these terms comes from an unexpected broken symmetry in the qubit potential. The

theory is confirmed by measuring the photon occupation of the resonator when transitions occur while varying the detuning between the qubit and resonator.

## 4.1 Introduction

The Jaynes-Cummings (JC) Hamiltonian [167, 174] describes the interaction between a quantum two-level system and a harmonic oscillator, and is used to model a huge variety of physical systems. For example, in superconducting qubits, it describes the interaction between the qubit and a resonator used to measure the qubit's state. As predicted by the dispersive limit of the JC model, each qubit state induces a different frequency shift in the resonator, and the qubit state is inferred by measuring the resonator's response to a probe pulse [44, 78, 104]. Dispersive measurement itself played a key role in recent experiments exploring the nature of quantum measurement [106, 132, 133], and the high speed and accuracy of dispersive measurement has been critical in establishing superconducting qubits as a compelling technology for quantum computation [49, 68]. Furthermore, repetitive error protection and characterization protocols [50, 62, 98, 107, 113, 175] require that the qubit remain in a known state within the qubit subspace after the measurement is complete, a property guaranteed by the dispersive JC Hamiltonian.

However, several experiments with superconducting qubits have found that as the number of photons occupying the resonator  $\bar{n}$  is increased past a certain point, the qubit suffers anomalous state transitions [93, 176–178]. It was long believed that these transitions could be explained by the breakdown of the dispersive approximation of the JC model as  $\bar{n}$  exceeds a critical photon number  $n_c$ , but recent theory showed that the transitions are

not predicted by the JC interaction even with very large  $\bar{n}$  [79]. Perhaps more puzzling, the transition probability is observed to be non-monotonic with increasing photon number. As these transitions limit the speed and lower the fidelity of qubit measurement [93, 177], understanding and eliminating them is an important step in implementing high fidelity quantum algorithms, simulation, and error corrected computation.

In this chapter, we investigate the cause of anomalous qubit transitions in a superconducting qubit-resonator system. The transitions have been experimentally characterized by Google/UCSB team, by measuring the state of the qubit after driving the resonator with variable power, and it is observed that the qubit jumps outside the two-level subspace. Moreover, these transitions may show a resonant behavior as a function of drive power. By re-examining an important assumption of the JC Hamiltonian, namely the rotating wave approximation (RWA), we develop a theory based on level crossings with other states of the qubit-resonator system, and find that the theory matches experimental observations with no free parameters.

## 4.2 Experimental procedure and observations

The experiment [151, 179] was performed by Google/USCB team using a frequency-tunable superconducting transmon qubit [44, 46], with maximum  $|0\rangle \rightarrow |1\rangle$  transition frequency of  $\omega_{10}/2\pi = 5.4$  GHz, and anharmonicity of  $\eta/2\pi \equiv (\omega_{21} - \omega_{10})/2\pi = -221$  MHz at this frequency. The qubit is capacitively coupled to a readout resonator with coupling strength  $g/2\pi \approx 87$  MHz <sup>1</sup>. The readout resonator has a frequency of  $\omega_r/2\pi \approx 6.78$  GHz

---

<sup>1</sup>Coupling strength depends on qubit frequency, but varies by less than 5% in this work.

and is coupled with an energy decay rate of  $\kappa \approx 1/(37 \text{ ns})$  through a bandpass Purcell filter [92, 93] to an output line and amplifiers.

The transmon state is measured using standard cQED dispersive measurement [78], where each transmon level  $|i\rangle$  induces a different frequency shift on the resonator, yielding a set of distinct resonator frequencies  $\omega_{r,|i\rangle}$ . The resonator is then pumped to be populated with photons that leak out from the resonator. The amplitude and phase of the outgoing photons, which now depend on the transmon state, are extracted as a point in the IQ plane to distinguish qubit states.

To investigate the effect of resonator photons on the transmon state, the pulse sequence illustrated in Fig. 4.1 (a) is used. The transmon is initialized to  $|0\rangle$ , then the resonator is driven with a  $2 \mu\text{s}$  long, variable power pulse. This “stimulation pulse” injects a number of photons into the resonator that, when large enough, induces transitions in the transmon state. After a  $500 \text{ ns}$  (13 decay time constants) wait for the resonator to ring down <sup>2</sup>, the resonator is driven again with a fixed low power pulse to measure the transmon without inducing further transitions, and the IQ response of the resonator is recorded. After calibration, each IQ point is identified as one of the transmon states, or if the point is more than three standard deviations from any of the calibrated distributions, it is labeled as an “outlier”.

Experimental results of Google/UCSB team are striking in two ways. First, as the stimulation pulse power is raised, the transmon jumps from  $|0\rangle$  not only to  $|1\rangle$  but also to  $|2\rangle$ ,  $|3\rangle$  and even higher states, as shown in Fig. 4.1 (b). Although only the states up

---

<sup>2</sup>The transmon  $T_1$  is between  $20 \mu\text{s}$  and  $40 \mu\text{s}$  for the  $\omega_{10}$  values used, so the resonator ring-down incurs little qubit decay.

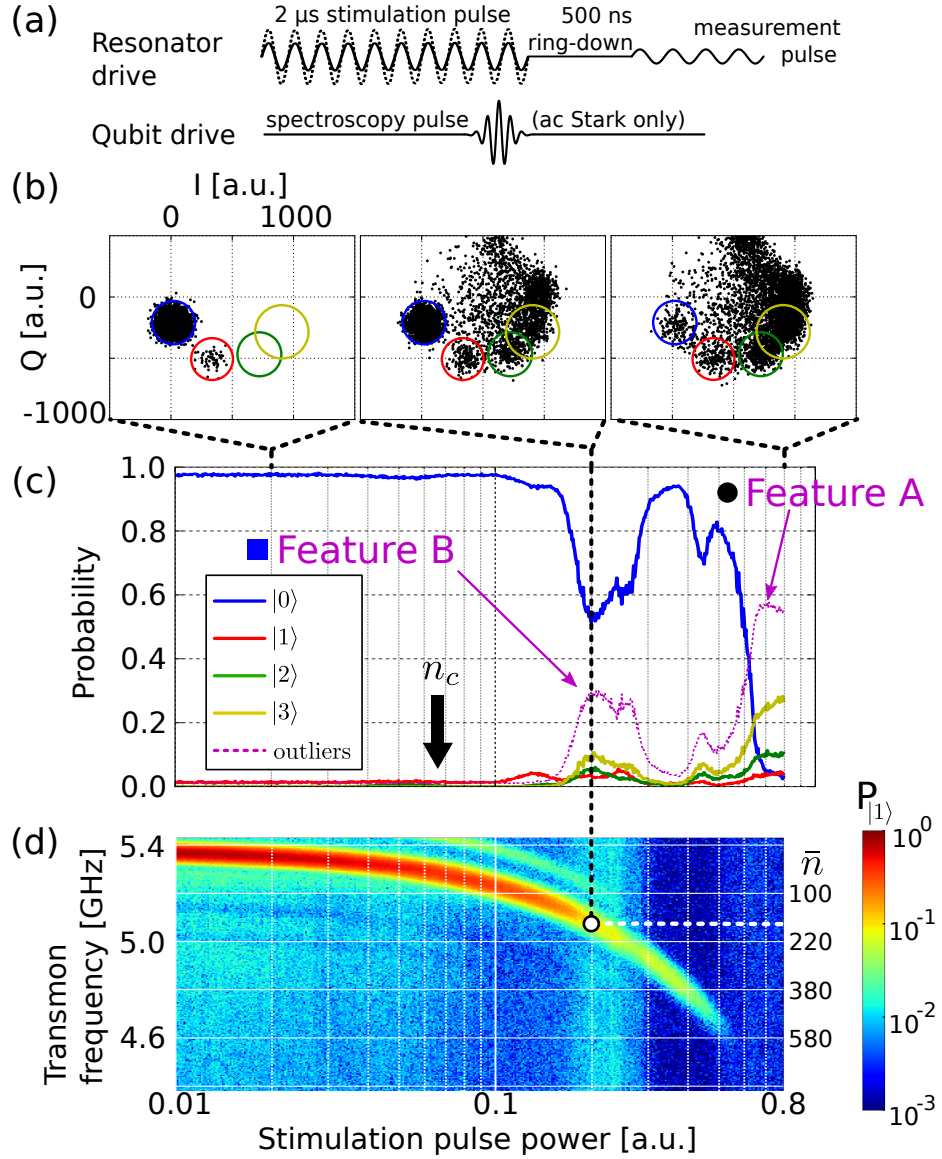


Figure 4.1: (a) Control sequence for probing the effect of resonator photons on the transmon. The spectroscopy pulse is used only in the ac Stark measurement. (b) IQ data for drive powers 0.02, 0.2, and 0.8 (arbitrary units), with  $\omega_{10} = 5.38$  GHz. The circles represent  $3\sigma$  for the four resolvable transmon states after calibration. At high power, the transmon is clearly driven to states higher than  $|3\rangle$ . (c) Transmon state probabilities versus stimulation power. In addition to the four calibrated transmon states, dashed purple line shows the probability that the measurement was  $> 3\sigma$  from any of the resolved states, labeled “outliers”. Note the two large resonance-like peaks labeled *A* and *B*. (d) Stark shifted transmon frequency  $\omega_{10}$  versus stimulation pulse power. We convert the shifted  $\omega_{10}$  to  $\bar{n}$  (right vertical axis) using a numerical theory discussed in Sec. 4.3.1. Figure adapted from Ref. [151].

to  $|3\rangle$  can be resolved, the characteristic arc of the IQ points with increasing state index appears to continue to what we estimate to be  $|5\rangle$  or higher. Second, the probability of transitions is highly non-monotonic with power, as was previously seen in Refs. [177, 178]. In particular, the shapes of the features in probability versus power resemble resonance peaks, with large peaks in the outlier probability at drive powers 0.7 (feature *A*) and 0.2 (feature *B*), a small peak in  $|1\rangle$  near 0.15, another small peak in  $|2\rangle$  near 0.05, and various other peaks at other powers. The peaked structure rules out any process that would have monotonically increasing transitions with increasing drive power, such as chip heating or dressed dephasing [126, 180], as the dominant mechanism.

In order to connect the experimental results to theoretical models, the stimulation pulse power is converted to photon number  $\bar{n}$ . The value of  $\bar{n}$  cannot be measured directly, but resonator photons cause the qubit frequency to shift downward<sup>3</sup> in what is called the ac Stark effect [181]. The drive power is mapped to  $\bar{n}$  by measuring the ac Stark shifted qubit frequency for each resonator drive power and converting that frequency to  $\bar{n}$  using a numerical model based on separately measured parameters  $g$  and  $\Delta$  (see Sec. 4.3.1). To measure the ac Stark shift, the previous experiment is repeated with the addition of a spectroscopic microwave pulse on the transmon after the driven resonator has reached the steady state (see Fig. 4.1 (a)). The results of the ac Stark shift measurement with the computed photon numbers is shown in Fig. 4.1 (d) for the same drive powers as in Fig. 4.1 (c). Note that feature *B* (black dashed line) occurs at  $170 \lesssim \bar{n} \lesssim 250$ , which is, interestingly, considerably larger than the critical photon number  $n_c \equiv (\Delta/g)^2/4 \approx 60$  introduced in Ref. [78].

---

<sup>3</sup>When  $\omega_{10} > \omega_r$ , the ac Stark shift can increase the qubit frequency. See Ref. [179]

The peaks in Fig. 4.1 (c) are thus seen to indicate particular values of  $\bar{n}$  at which the qubit-resonator system is especially susceptible to transitions. The association of  $\bar{n}$  with qubit frequency shift further suggests that the peaks are due to some form of frequency resonance. With the observation of resonant transitions to higher transmon levels, we now consider the transmon-resonator system and revisit the rotating wave approximation to explain these observations.

### 4.3 Theory of nonRWA transitions

#### 4.3.1 Energy resonances mediated by non-RWA terms

The Hamiltonian of the coupled qubit-resonator system can be written as

$$H = H_b + H_I \tag{4.1}$$

where  $H_b$  is the “bare” Hamiltonian of the qubit and resonator, while  $H_I$  describes their capacitive coupling. With the ket convention  $|qubit, resonator\rangle$ , the bare Hamiltonian has the form

$$H_b = \sum_{k,n} (E_k + n\hbar\omega_r) |k, n\rangle\langle k, n| \tag{4.2}$$

where  $\omega_r$  is the (bare) resonator frequency, and  $E_k$  is the transmon energy of level  $k$ , calculated numerically using Mathieu characteristic functions [44]. The transmon transition frequencies are  $\omega_{kl} \equiv (E_k - E_l)/\hbar$  and its anharmonicity is  $\eta \equiv \omega_{21} - \omega_{10}$ <sup>4</sup>. This bare Hamiltonian produces the Jaynes-Cummings (JC) ladder of energy levels, shown in Fig. 4.2.

---

<sup>4</sup>Note that in this chapter,  $\eta$  is defined with the opposite sign, compared with other chapters.

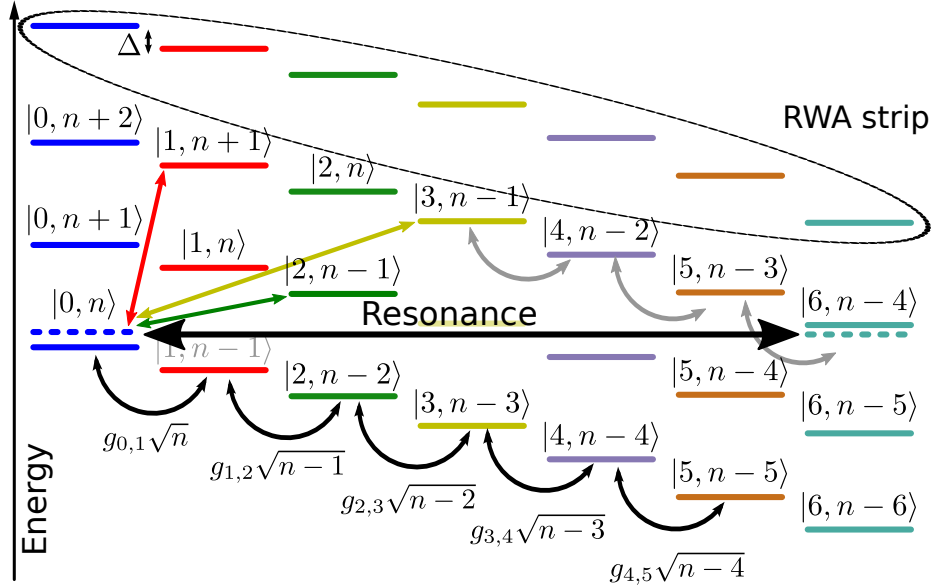


Figure 4.2: JC ladder for large values of  $n$ . Bare states are shown as solid lines and two of the eigenstates are shown as dashed lines. Dark curved arrows indicate coupling within an RWA strip with corresponding RWA coupling strengths shown below. The ladder has an energy resonance between  $|0, n\rangle$  and  $|6, n-4\rangle$  (long black arrow). Non-RWA couplings (short straight arrows) allow for interstrip transitions. The couplings to  $|1, n+1\rangle$  (red) and  $|3, n-1\rangle$  (yellow), along with those within the RWA strip, mediate the transition between the resonant levels. The coupling to  $|2, n-1\rangle$  (green), which mediates additional resonant transitions, requires a Hamiltonian term coupling transmon states of equal parity; this is forbidden if the transmon potential is symmetric. Note the energy spacing between states  $|k, n\rangle$  and  $|k+1, n-1\rangle$  is  $\Delta$  as indicated in the top left.

The interaction Hamiltonian  $H_I$  is due to charge-charge coupling between the resonator and transmon.

$$H_I = \sum_{k,k',n} \hbar g_{k,k'} \sqrt{n} |k', n-1\rangle \langle k, n| + \text{H.c.}, \quad (4.3)$$

where  $g_{k,k'} \equiv g \langle k|Q|k'\rangle / \langle 0|Q|1\rangle$  are the normalized matrix elements of the transmon charge operator  $Q$ . These matrix elements are calculated numerically using Mathieu functions.

For example, in the case  $k' = k+1$  and for not very large values of  $k$ , the matrix elements

are approximately (see Appendix A)

$$g_{k,k+1} \approx g\sqrt{k+1} \left( 1 + \frac{\eta}{2\omega_{10}} k \right). \quad (4.4)$$

This interaction imparts an  $n$ -dependent shift on the bare levels producing eigenstates, two of which are shown as dashed lines in Fig. 4.2. As indicated by the long horizontal arrow, at certain  $n$  the ladder contains resonances between states where the qubit goes from  $|0\rangle$  to higher levels such as  $|6\rangle$ . This critical observation could explain both the resonance structure and the transitions to higher transmon levels observed in the data. However, it remains to see how  $H_I$  couples the resonant levels.

The interaction Hamiltonian can be divided into two parts,

$$H_I = H_{\text{RWA}} + H_{\text{non-RWA}}, \quad (4.5)$$

where  $H_{\text{RWA}}$  contains only terms conserving total excitation number, while  $H_{\text{non-RWA}}$  contains the rest of the terms. Note that the full interaction  $H_I$  is typically simplified by the RWA, which has the form

$$H_{\text{RWA}} = \sum_{k,n} \hbar g_{k,k+1} \sqrt{n} |k+1, n-1\rangle \langle k, n| + \text{H.c.}, \quad (4.6)$$

These RWA terms (curved arrows in Fig. 4.2) divide the JC ladder into excitation preserving subspaces which we call ‘‘RWA strips’’. Under  $H_{\text{RWA}}$ , the system moves only *within* an RWA strip; taking the system out of the dispersive limit with  $n \gg n_c$  *only* results in a reduction of the resonator dispersive shift [79]. Therefore,  $H_{\text{RWA}}$  does not allow transitions between resonant levels.

By diagonalizing  $H_b + H_{\text{RWA}}$ , we find the eigenstates  $\overline{|k, n\rangle}$  and eigenenergies  $E_{\overline{|k, n\rangle}}$  (overline indicates eigenstate), which we use to numerically compute quantities of interest.

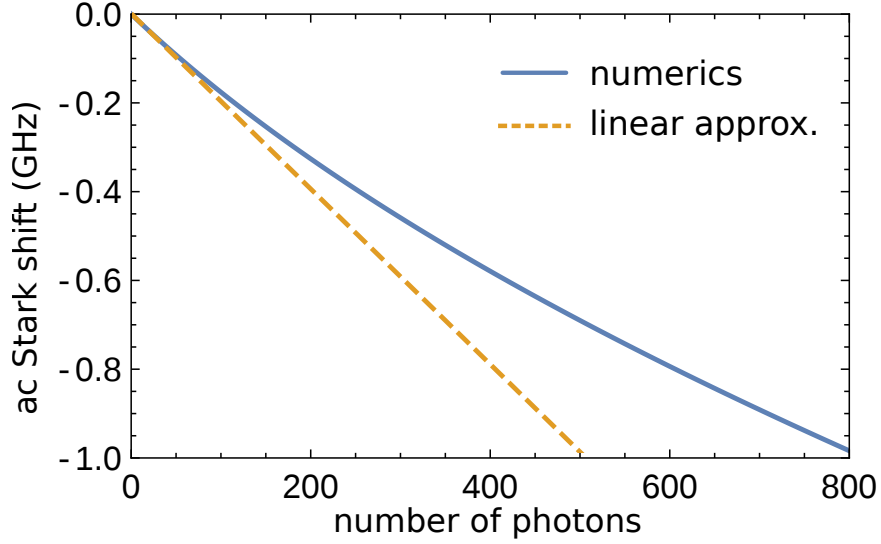


Figure 4.3: Ac Stark shift of the transmon frequency as a function of the number of resonator photons  $n$ , for parameters of Fig. 2 in the main text ( $n_c \approx 60$ ), using  $H_{\text{RWA}}$ . The solid line shows the value computed numerically, and the dashed line shows the conventional linear approximation  $\delta\omega_{10} = -2|\chi|n$ . As  $n$  becomes large, the relation between ac Stark shift and photon number becomes somewhat nonlinear.

We note that  $H_{\text{non-RWA}}$  induces slight changes in the calculated eigenenergies  $E_{|k,n\rangle}$ , but the effect is small enough that we neglect it (because non-RWA terms are off resonant). For example, we numerically compute the photon number dependent ac Stark shift  $\delta\omega_{10} \equiv (E_{|1,n\rangle} - E_{|0,n\rangle})/\hbar - \omega_{10}$ , as illustrated in Fig. 4.3. This gives us a map between resonator photon number and transmon ac Stark shift, which provides the calibration between drive power and photon number discussed in Sec. 4.2, and was the critical link between theory and experiment. Notice that Eq. (4.6) goes beyond the usual dispersive approximation [78]. In particular, the numerically computed curve deviates noticeably from the usual linear relation  $\delta\omega_{10} = -2|\chi|n$ .

The critical part of the interaction Hamiltonian is  $H_{\text{non-RWA}}$ , containing terms in

$H_I$  that do not conserve excitation number, called here “non-RWA” terms. These terms can be as large as the RWA terms, but are usually neglected on the grounds that they are more off resonant than the RWA terms (in our system the RWA terms are  $\sim 1$  GHz off resonance, while the non-RWA terms are  $\sim 13$  GHz off resonance). However, these terms connect RWA strips and therefore enable resonant transitions in the JC ladder, leading to the unwanted state transitions. In general, there are many types of non-RWA terms, which differ in coupling strength and in how close they are to resonantly connecting two JC ladder levels. We only consider terms involving  $g_{k,k+1}$  and  $g_{k,k+3}$ , as they are the largest and least off-resonant,

$$\begin{aligned}
H_{\text{non-RWA}}^{(1)} &= \sum_{k,n} \hbar g_{k,k+1} \sqrt{n+1} |k+1, n+1\rangle \langle k, n| + \text{H.c.} \\
&+ \sum_{k,n} \hbar g_{k,k+3} \sqrt{n} |k+3, n-1\rangle \langle k, n| + \text{H.c.} .
\end{aligned} \tag{4.7}$$

The couplings  $g_{k,k+3}$  are calculated numerically using Mathieu functions; they are much smaller than  $g_{k,k+1}$ , as seen from the approximate formula (see Appendix A)

$$g_{k,k+3} \approx g \sqrt{(k+1)(k+2)(k+3)} \frac{-\eta}{4\omega_{10}} . \tag{4.8}$$

In spite of being relatively small, these couplings are numerically more important in our problem than couplings  $g_{k,k+1}$ .

These non-RWA terms couple next-nearest neighboring RWA strips (i.e., those differing by 2 in total excitation number) together, as shown in Fig. 4.2. Combined with the intrastrip coupling provided by  $H_{\text{RWA}}$ , the non-RWA coupling allows multistep (i.e., higher order) processes to connect the resonant levels. For example,  $H_{\text{non-RWA}}^{(1)}$  carries the system from  $|0, n\rangle$  to  $|1, n+1\rangle$  in another RWA strip, and then  $H_{\text{RWA}}$  carries the system within

the strip to  $|6, n - 4\rangle$ . Note that although the full process conserves energy, the individual steps do not.

To find the condition under which the resonances occur, we use our numerical tool to compute the frequencies  $\bar{\omega}_k(n) \equiv E_{|k, n-k\rangle}/\hbar - n\omega_r$  of the levels within each RWA strip, as functions of  $n$ . As  $n$  increases, energy levels within each strip repel each other more strongly and fan out, as illustrated by the solid lines in the “fan diagram” in Fig. 4.4. By superimposing fan diagrams of two next-nearest neighboring RWA strips, as shown by the dashed lines, we see that they have multiple intersections, meaning that the JC ladder contains multiple resonances. For example, the left red dot in Fig. 4.4 shows that the transmon-resonator state  $|\overline{0, n}\rangle$  can be brought on resonance with  $|\overline{6, n - 4}\rangle$ . The presence of crossings with higher transmon states agrees with the experimental observation of transitions to states higher than  $|3\rangle$ .

Next, we compute the  $n$  at which various intersections occur as a function of the qubit-resonator detuning  $\Delta$ , yielding the lines in Fig. 4.5. As  $|\Delta|$  increases, the spacing between levels within an RWA strip also increases, see Fig. 4.2. However, the spacing between strips is fixed at  $\omega_r$ , so with increased  $|\Delta|$  fewer photons are required to bring  $|\overline{0, n}\rangle$  on resonance with states in higher strips and so the transitions occur at lower  $\bar{n}$ . Note that while we use  $n$  in the theory, the experiment drives the resonator into a coherent state with mean photon number  $\bar{n}$  and fluctuations  $\sqrt{\bar{n}} < 0.1\bar{n}$ . Also, although the  $n$  at which the energy resonance occurs is not related to  $n_c$ , the effective couplings between resonant levels are large enough to yield the experimental features only when  $n \gtrsim n_c$  (see Sec. 4.3.2).

To confirm the theoretical prediction, the experiment shown in Fig. 4.1 is repeated

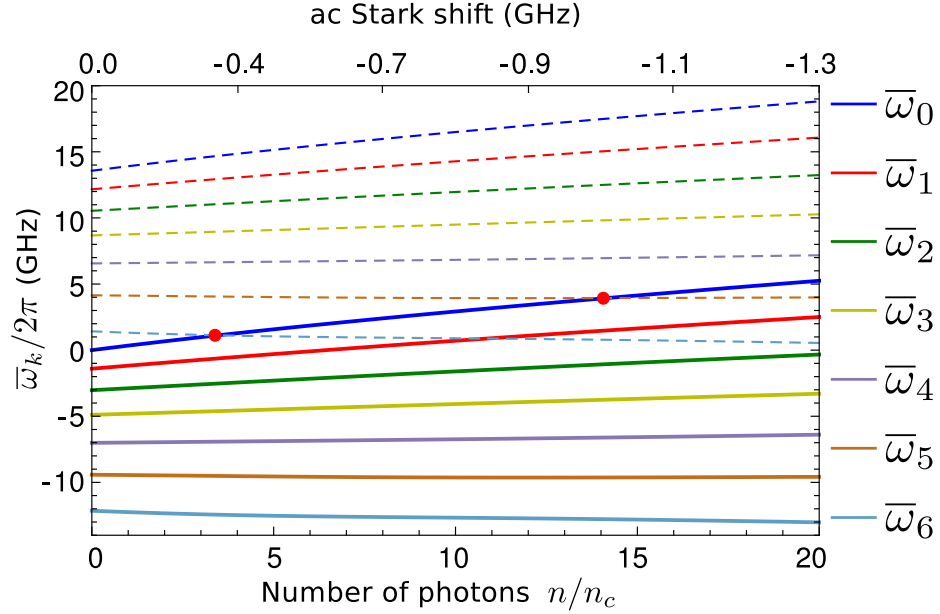


Figure 4.4: Fan diagram of the energy levels within an RWA strip. Solid: Frequencies  $\bar{\omega}_k(n) \equiv E_{|k,n-k\rangle}/\hbar - n\omega_r$  versus photon number  $n$  for  $|\Delta| = 1.4$  GHz. As  $n$  increases, the levels repel more strongly and fan out. Dashed: Same frequencies shifted by  $2\omega_r$ , which represent the next-nearest neighboring RWA strip. The red dots show energy resonances with the qubit state  $|0\rangle$  occurring at specific values of  $n$ . The left dot corresponds to the resonance shown in Fig 4.2. Top axis shows the numerically calculated ac Stark shift.

for several values of  $\omega_{10}$  by biasing the transmon's SQUID with magnetic flux. At each  $\omega_{10}$ , we find the values of  $\bar{n}$  of features *A* and *B*, as shown in Fig. 4.1 (d), and plot these points in Fig. 4.5. The experimental points for feature *A* (black circles) and feature *B* (blue squares) are well fit by numerically computed curves for the transitions from  $|\overline{0,n}\rangle$  to  $|\overline{6,n-4}\rangle$  and  $|\overline{3,n-2}\rangle$ , respectively. Note that the theory lines are calculated using only the measured  $\omega_r$ ,  $\omega_{10}$ , and  $g$ , with no free parameters fitted to the data.

However, the transition from  $|\overline{0,n}\rangle$  to  $|\overline{3,n-2}\rangle$  is actually unexpected. If the transmon potential is symmetric (in the phase basis), as is usually assumed [44], then  $g_{i,j}$  is only nonzero when  $j - i$  is odd. Therefore,  $H_I$  should only couple RWA strips where

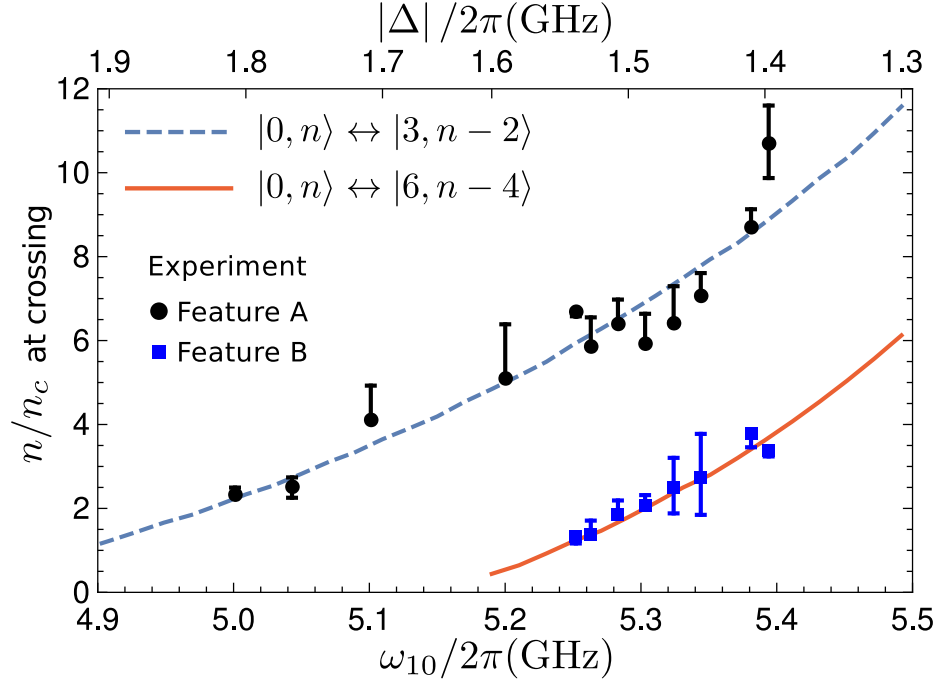


Figure 4.5: Photon number at level crossing versus  $\omega_{10}$ , compared between experiment and theory. Black circles and blue squares show experimental features A and B from Fig. 4.1 respectively, and the error bars represent the apparent widths of the features. Solid red line is the theory prediction for level crossing between eigenlevels of  $|0, n\rangle$  and  $|6, n - 4\rangle$ . Dashed blue line is the theory prediction for an asymmetric transmon that breaks the selection rule by at least 1%, yielding level crossings between eigenlevels of  $|0, n\rangle$  and  $|3, n - 2\rangle$ . Figure adapted from Ref. [151].

the difference in total excitation number is even, so the transition to  $\overline{|3, n - 2\rangle}$  should be forbidden. Nevertheless, the theory line for the  $\overline{|3, n - 2\rangle}$  transition fits the data well, indicating a possible asymmetry in the transmon potential. This asymmetry is experimentally confirmed by observing  $|0\rangle \rightarrow |2\rangle$  Rabi oscillations when driving the transmon at  $\omega_{01} + \omega_{12}$  (see Sec. 4.3.2). Accounting for this broken symmetry adds terms to  $H_{\text{non-RWA}}$ ,

$$H_{\text{non-RWA}}^{(2)} = \sum_{k,n} \hbar g_{k,k+2} \sqrt{n} |k + 2, n - 1\rangle \langle k, n| + \text{H.c.} . \quad (4.9)$$

The non-RWA terms of Eq. (4.9) connect RWA strips differing in total excitation number by 1, which we call “nearest neighbors” (see Fig. 4.2), leading to additional resonance processes,

such as  $\overline{|0, n\rangle} \rightarrow \overline{|3, n-2\rangle}$ . Through comparison with Rabi oscillations on the  $|0\rangle \rightarrow |1\rangle$  transition, we experimentally estimate  $|\langle 0|Q|2\rangle/\langle 0|Q|1\rangle| \approx 10^{-2}$ . This matrix element is large enough to explain the transitions to  $\overline{|3, n-2\rangle}$ , and so the level crossing theory appears to correctly predict both of the largest resonance features observed in the data.

We note that any spurious TLS coupled to transmon-resonator system can also participate in level crossings, and can lead to similar features (possibly the small peaks in Fig. 4.1 (c)), even at lower photon numbers (see Sec. 4.3.3).

### 4.3.2 Effective coupling at resonance

When a resonance occurs between the initial state  $\overline{|0, n\rangle}$  and, e.g.,  $\overline{|6, n-4\rangle}$ , the system can make a resonant transition. In the perturbative language, in making this transition the system goes through several intermediate off-resonant states (see Fig. 4.2); many different paths are available (i.e. different virtual processes). As an example, one path is  $|0, n\rangle \rightarrow |1, n-1\rangle \rightarrow |4, n-2\rangle \rightarrow |5, n-3\rangle \rightarrow |6, n-4\rangle$ , which involves the matrix element  $g_{1,4}$ . The condition of resonance is necessary but not sufficient to give these processes a measurably large probability; the process must also have large enough effective coupling between initial and final states. We define the effective coherent coupling  $g_{\text{eff}}^{\text{coh}}$  as

$$g_{\text{eff}}^{\text{coh}} = \overline{\langle k_f, n_f | H_{\text{non-RWA}} | k_i, n_i \rangle}, \quad (4.10)$$

where  $\overline{|k_i, n_i\rangle}$  and  $\overline{|k_f, n_f\rangle}$  are the initial and final eigenstates, respectively. To find  $g_{\text{eff}}^{\text{coh}}$ , we expand the (RWA) eigenstates in the bare state basis,

$$\overline{|k, n\rangle} = \sum_{l=0}^{k_{\text{max}}} c_l^{(k,n)} |l, n+k-l\rangle, \quad (4.11)$$

where  $k_{\max} \simeq 9$  is the highest transmon level taken into account. This expansion is then substituted into Eq. (4.10). In particular, for the transition  $\overline{|0, n\rangle} \rightarrow \overline{|k, n - k + 2\rangle}$  (to the next-nearest neighboring RWA strip) the effective coupling is

$$g_{\text{eff}}^{\text{coh}} = \sum_l c_l^{(0,n)} \hbar g_{l,l+1} \sqrt{n-l+1} \left[ c_{l+1}^{(k,n-k+2)} \right]^* + \sum_l c_l^{(0,n)} \hbar g_{l,l+3} \sqrt{n-l} \left[ c_{l+3}^{(k,n-k+2)} \right]^* . \quad (4.12)$$

Each term in Eq. (4.12) corresponds to a particular path in the picture of virtual processes. The paths in the first line are  $|0, n\rangle \rightarrow |l, n-l\rangle \rightarrow |l+1, n-l+1\rangle \rightarrow |k, n-k+2\rangle$ , where the first and last arrows describe subpaths within the RWA strips. Similarly, the terms in the second line correspond to paths  $|0, n\rangle \rightarrow |l, n-l\rangle \rightarrow |l+3, n-l-1\rangle \rightarrow |k, n-k+2\rangle$ .

The solid red line in Fig. 4.6 (a) shows  $g_{\text{eff}}^{\text{coh}}$  for the  $\overline{|0, n\rangle} \rightarrow \overline{|6, n-4\rangle}$  transition (so that  $n$  corresponds to the resonance condition  $E_{\overline{|0, n\rangle}} \approx E_{\overline{|6, n-4\rangle}}$ ), calculated using Eq. (4.10) or, equivalently, Eq. (4.12). Note that the terms in Eq. (4.12) are large at  $n > n_c$  because  $g_{l,l+1} \sqrt{n} \approx |\Delta| \sqrt{l+1} \sqrt{n/4n_c}$  (typically a few GHz) and the amplitudes  $c_l$  are significant for several states within the RWA strip. Nevertheless, the result for  $g_{\text{eff}}^{\text{coh}}$  shown by the solid red line in Fig. 4.6 (a) is smaller than even one such term. The reason is an almost perfect cancellation of the terms in Eq. (4.12), which happens because while the coefficients  $c_l^{(k,n-k+2)}$  alternate in sign with changing  $l$  for  $l < k$ , the coefficients  $c_l^{(0,n)}$  are all positive<sup>5</sup>. Therefore, the terms in Eq. (4.12) have alternating signs and efficiently cancel each other.

This cancellation is probably not so efficient in the real physical system. When the transmon is in an upper state, it is more sensitive to noise sources (such as charge noise) and therefore experiences increased dephasing. This and the relatively low coherence of the

---

<sup>5</sup>This follows from sequential perturbation theory

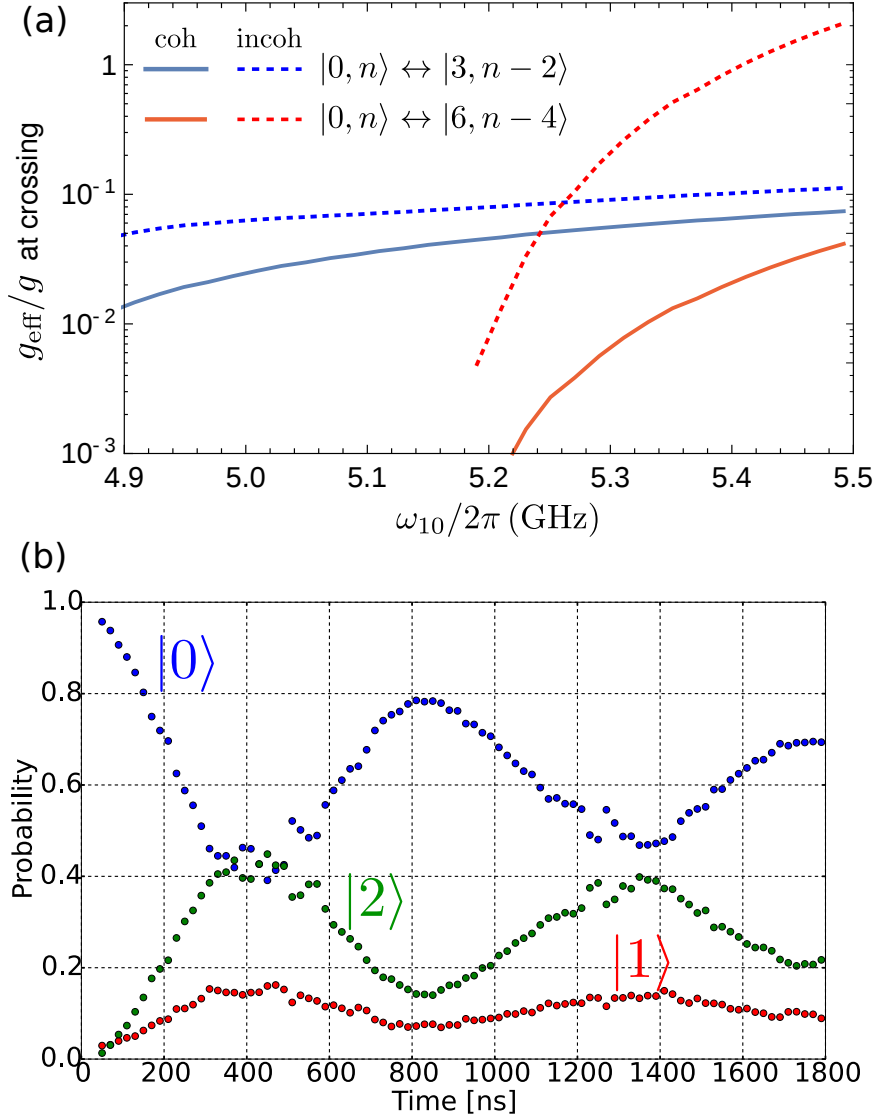


Figure 4.6: (a) Effective coupling between crossing levels for different qubit frequencies. Solid and dashed lines show coherent and incoherent effective couplings respectively. The blue line assumes  $g_{0,2}/g = 10^{-2}$ . (b) Experimental observation of Rabi oscillation between transmon levels  $|0\rangle$  and  $|2\rangle$ . Figure adapted from Ref. [151].

resonator ( $1/\kappa_r \approx 37$  ns) may suppress coherence between the different paths contributing to Eq. (4.12). While it is difficult to accurately calculate the effective coupling  $g_{\text{eff}}$  while accounting for decoherence, we can estimate the upper bound of the resulting  $g_{\text{eff}}$  as the fully incoherent sum of the terms in Eq. (4.12),

$$g_{\text{eff}}^{\text{incoh}} = \left( \sum_l \left| c_l^{(0,n)} \hbar g_{l,l+1} \sqrt{n-l+1} \left[ c_{l+1}^{(k,n-k+2)} \right]^* \right|^2 + \sum_l \left| c_l^{(0,n)} \hbar g_{l,l+3} \sqrt{n-l} \left[ c_{l+3}^{(k,n-k+2)} \right]^* \right|^2 \right)^{1/2}. \quad (4.13)$$

The red dashed line in Fig. 4.6 (a) shows  $g_{\text{eff}}^{\text{incoh}}$  for the  $|\overline{0}, n\rangle \rightarrow |\overline{6}, n-4\rangle$  transition. We expect that the effective couplings in real system are between the results for fully coherent and fully incoherent cases (solid and dashed lines). The experimental feature B (which corresponds to the transition  $|\overline{0}, n\rangle \rightarrow |\overline{6}, n-4\rangle$ ) can be well explained by effective coupling on the order of 1 MHz, which is in agreement with these theoretical values (note that  $g/2\pi \approx 87$  MHz).

The experimental feature A can be explained only if the state can transition between neighboring RWA strips (differing in total excitation number by 1). However, if the transmon potential were exactly left/right symmetric, as is usually assumed, then  $g_{k,k+2} = 0$ , and this transition is forbidden. Therefore, to explain the feature A, we must assume that the transmon's symmetry is broken, leading to the additional non-RWA terms given in Eq. (4.9). We calculated the effective coupling at the  $|\overline{0}, n\rangle \rightarrow |\overline{3}, n-2\rangle$  resonance, hypothesizing that  $g_{k,k+2} = 0.01 g \sqrt{(k+1)(k+2)}$  (i.e., 1% violation of the selection rule). The coupling for a coherent process is calculated via Eq. (4.10), which for the transitions  $|\overline{0}, n\rangle \rightarrow |\overline{k}, n-k+1\rangle$  between the nearest-neighbor RWA strips produces

$$g_{\text{eff}}^{\text{coh}} = \sum_l c_l^{(0,n)} \hbar g_{l,l+2} \sqrt{n-l} \left[ c_{l+2}^{(k,n-k+1)} \right]^*. \quad (4.14)$$

The numerical result, indicated by the solid blue line in Fig. 4.6 (a), shows that this 1% violation of the selection rule yields an effective coupling of a few MHz, which is large enough to explain the experimental feature A. The coupling becomes a few times larger if we assume the fully incoherent sum of the contributions from the paths in Eq. (4.14) (constructed similarly as Eq. (4.13))– see the dashed blue line in Fig. 4.6 (a). However, since the qubit state  $|3\rangle$  is not supposed to experience a significant level of decoherence, we believe that the solid blue line is more relevant to the experimental situation than the dashed blue line. It is interesting to note that the difference between the dashed and solid blue lines is much smaller than between the dashed and solid red lines, indicating that the cancellation of terms in Eq. (4.14) is not as efficient as in Eq. (4.12). This is because for the transition  $|\overline{0, n}\rangle \rightarrow |\overline{3, n-2}\rangle$  there are only two main terms in Eq. (4.14): those involving  $g_{0,2}$  and  $g_{1,3}$ .

The selection rule violation for  $g_{0,2}$  was experimentally looked for and observed [151, 179] by directly driving Rabi oscillations between transmon levels  $|0\rangle$  and  $|2\rangle$ , as shown in Fig. 4.6 (b). By comparing the  $|0\rangle \rightarrow |2\rangle$  Rabi oscillation period against the  $|0\rangle \leftrightarrow |1\rangle$  Rabi oscillation period, and correcting for the differing microwave amplitude needed to drive those two transitions, it was found experimentally that  $g_{0,2}/g \simeq 10^{-2}$ , surprisingly in good agreement with the guessed value. We emphasize that the experimental value of  $10^{-2}$  should be considered only as an order of magnitude estimate.

We can offer only speculations about the possible physical mechanism behind the broken symmetry in the transmon. For example, it could result from SQUID asymmetry under external flux [182] or from a gradient of the magnetic field which couples to oscillating

current in the circuit. However, these mechanisms are not investigated here and will be the subject of further studies.

### 4.3.3 TLS-assisted transitions

It is well known that microscopic defects in the materials comprising the transmon circuit can act as two level systems (TLS) and lead to qubit relaxation [183]. This relaxation can depend on the number of photons  $n$  in the resonator because of the ac Stark shift. Since ac Stark shift is approximately  $\delta\omega_{10} = -2|\chi|n \simeq -(|\eta|/2)(n/n_c)$ , the change of the qubit frequency is quite significant ( $\sim \eta \approx -200$  MHz) when  $n$  is comparable to  $n_c$ . Therefore, even if the bare qubit frequency is chosen away from the TLS frequencies, it is possible that the qubit frequency will cross a TLS during measurement with a moderate value of  $n/n_c$ . In fact, this effect has been experimentally observed [151, 179] by comparing the transmon relaxation rate as a function of  $\omega_{10}$  with  $n = 0$  against that same relaxation rate during dispersive measurement. It was found that the ac Stark shift induced by the resonator photons during dispersive measurement pushes the transmon into resonance with TLS's and therefore increases the relaxation rate. Of course, increased relaxation degrades the fidelity of the quantum state measurement, so these crossings should be avoided.

Interestingly, coupling between the transmon and TLS's may also lead to transitions of the transmon to *higher* levels, similar to the effect of the non-RWA couplings associated with resonator. The level crossings associated with TLS's produce features similar to those produced by the non-RWA processes, such as dependence on  $\Delta$ .

For example, the transmon can be excited from  $|0\rangle$  to  $|2\rangle$  via the following virtual

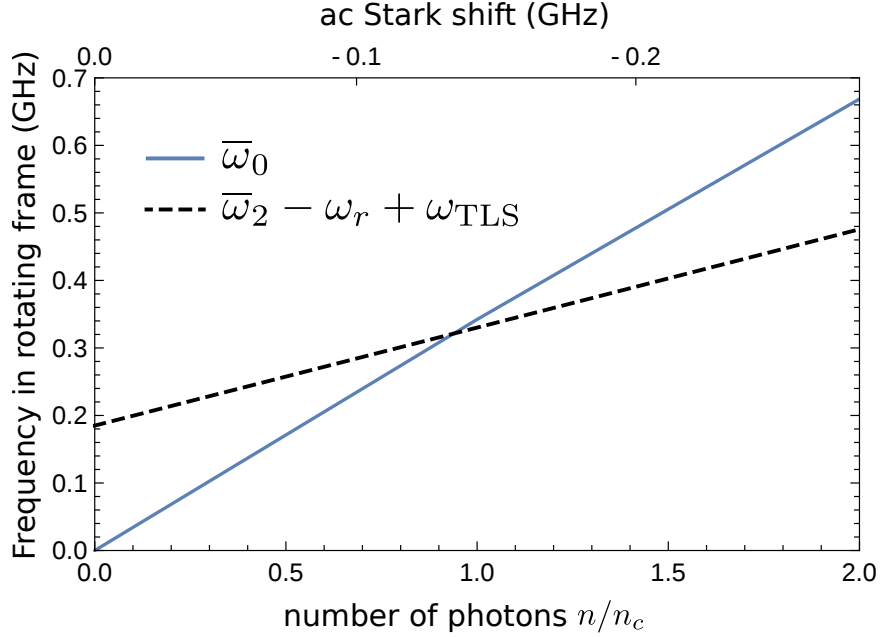


Figure 4.7: Example of a resonance between transmon and a TLS. For a TLS with frequency 10 GHz, the level crossing occurs between  $|0, n\rangle|0\rangle_{\text{TLS}}$  and  $|2, n-3\rangle|1\rangle_{\text{TLS}}$ .

process:  $|0, n\rangle|0\rangle_{\text{TLS}} \rightarrow |1, n-1\rangle|0\rangle_{\text{TLS}} \rightarrow |2, n-2\rangle|0\rangle_{\text{TLS}} \rightarrow |3, n-3\rangle|0\rangle_{\text{TLS}} \rightarrow |2, n-3\rangle|1\rangle_{\text{TLS}}$ . This process requires  $\omega_{\text{TLS}} \approx \omega_r + 2|\Delta| + |\eta|$  (the exact value is a little larger because of the level repulsion – see Fig. 4.7). The effective coupling for these resonances can be large enough to yield noticeable population transfer at lower photon numbers than for the non-RWA resonances. The example shown in Fig. 4.7 has a TLS with a frequency of 10 GHz and the resonance for the process described above occurs at  $n/n_c \approx 1$ . This value is sufficient for a noticeable amplitude of the bare state  $|3, n-3\rangle$  ( $c_3^{(0,n)} \approx 0.03$ ) and therefore a noticeable effective coupling for the process.

A TLS-assisted qubit transition from  $|0\rangle$  to  $|1\rangle$  requires only population of the bare state  $|2, n-2\rangle$ , and therefore the effective coupling becomes significant at values of  $n/n_c$  smaller than for the transition  $|0\rangle \rightarrow |2\rangle$ . For example, for the parameters, corresponding

to the peak in the  $|1\rangle$  probability (red line) in Fig. 4.1 (c) ( $n/n_c \approx 1.7$ ), the amplitude of the  $|2\rangle$  component is quite significant,  $c_2^{(0,n)} \approx 0.2$ . Therefore, even a weak coupling between the transmon and a TLS with frequency  $\omega_{\text{TLS}}/2\pi \approx 8.4$  GHz can explain this experimental peak. Note that when the TLS is sufficiently incoherent (e.g., because of fast energy relaxation), then the resonance condition could transform into a threshold-like condition, i.e., it should be enough energy to excite the TLS, also exciting the qubit, by transferring two photons from the resonator into the qubit-TLS system.

With increasing  $n/n_c$  and therefore increasing population of bare states  $|k, n - k\rangle$ , the number of possible TLS-assisted processes becomes larger (involving more final states), which increases the possibility of a transition away from the initial qubit state. We guess that the TLS-assisted processes may be responsible for the usual deterioration of qubit measurement fidelity in many experiments when increasing  $n$  becomes comparable to  $n_c$  (causing either excitation or relaxation of the transmon state).

#### 4.4 Other energy resonances in the JC ladder

Besides the non-RWA level crossings discussed in previous sections of this chapter, there are other types of energy resonances in the JC ladder that can lead to similar spurious qubit state deterioration during the measurement. Let us consider the measurement of a transmon in presence of an excited neighboring qubit, where the measured transmon can be Stark shifted into resonance with its neighbor and absorb its excitation, i.e., the qubit's  $|0\rangle \leftrightarrow |1\rangle$  frequency will match that of its neighbor. Besides this simple process, the readout resonator photons can also participate in such resonances by providing extra

excitations through the JC ladder. For example, in addition to becoming on resonance with  $\overline{|0, n\rangle} \leftrightarrow \overline{|1, n\rangle}$  transition, the excited neighboring qubit can become on resonance with  $\overline{|0, n\rangle} \leftrightarrow \overline{|l, n + 1 - l\rangle}$  transition and lose its excitation to the measured qubit. Such events degrade the measurement of qubit by exciting it from  $|0\rangle$  to  $|l\rangle$ , and also erroneously change the state of the neighbors. As a side note, let us remind the reader that Chapter 2 and Ref. [184] studied the dispersive measurement of a qubit in presence of a detuned neighbor, and showed that the excitation can also jump (typically rarely) between the joint eigenstates of the two qubits.

The coupling between the states involved in the resonant transitions discussed above is provided by a combination of RWA couplings within the JC ladder of the measured qubit and its resonator, the directly coupled neighboring qubit (which can add or remove excitation from the JC ladder), and non-RWA terms that couple nearest neighboring RWA strips. Through paths provided by these couplings, the measured qubit can receive energy from its excited neighbor and move between RWA strips (e.g., from  $\overline{|0, n\rangle}$  to  $\overline{|2, n - 1\rangle}$ ).

Similar to non-RWA transitions, these resonance conditions depend on the number of photons in the readout resonator, and can be found by calculating the eigenenergies of the JC ladder. Reference [179] experimentally studies these transitions in detail by directly driving a qubit during the measurement, and compares the results with the theory to find a good agreement.

## 4.5 Summary

In summary, we find that strong dispersive measurement of a transmon induces transitions to states above  $|3\rangle$ . These transitions occur at specific values of the photon occupation in the measurement resonator, and are caused by energy resonances within the qubit-resonator system. Coupling between the resonant levels is mediated by Hamiltonian terms usually dropped in the rotating wave approximation, and the most important such term involves an unexpected broken symmetry in the transmon potential. An interesting consequence of these results is that a system with smaller  $|\Delta|$ <sup>6</sup> should allow larger photon numbers before resonant transitions occur. This observation could be critical to improving measurement accuracy in dispersively measured systems, and may explain the large photon numbers used in Ref. [150]. Other energy resonances and transitions within JC ladder of the qubit-resonator can be understood and studied with the tools and theory developed in this chapter. This work suggests several further avenues of research: characterizing level crossings with the qubit initialized in  $|1\rangle$ , determining the mechanism for the transmon's broken symmetry, clarifying the role of TLSs in non-RWA transitions, and understanding the  $n$ -dependent rates of the non-RWA transitions.

## 4.6 Contributions

Daniel Sank and Zijun (Jimmy) Chen contributed significantly to the data, text, and figures of this chapter. The experiments were performed by Daniel Sank, Zijun (Jimmy) Chen, and Google/UCSB team (see Refs. [151, 179]). The theory was developed by Mostafa

---

<sup>6</sup>When  $\omega_{10} < \omega_r$ .

Khezri and Alexander N. Korotkov.

## Chapter 5

# Hybrid phase-space–Fock-space approach to evolution of a driven nonlinear resonator

In this chapter, we analyze the quantum evolution of a weakly nonlinear resonator due to a classical near-resonant drive and damping. The resonator nonlinearity leads to squeezing and heating of the resonator state. Using a hybrid phase-space–Fock-space representation for the resonator state within the Gaussian approximation, we derive evolution equations for the four parameters characterizing the Gaussian state. Numerical solution of these four ordinary differential equations is much simpler and faster than simulation of the full density matrix evolution, while providing good accuracy for the system analysis during transients and in the steady state. We show that steady-state limit of 3 dB can be exceeded during transients.

## 5.1 Introduction

Nonlinear quantum oscillators have been a subject of various studies for a long time [168, 185–188]. The renewed interest in this system is caused by the wide use of microwave resonators in superconducting quantum computing circuits [104, 189], as well as reaching a quantum regime for nanomechanical resonators [190–193]. In particular, during dispersive measurement of superconducting qubits [49, 78, 93, 104, 194], nonlinearity of the measurement resonator is induced by its coupling with the qubit; this nonlinearity causes significant deviations from the standard dispersive regime in the case of a moderately or strongly driven resonator [79, 148, 176]. The nonlinearity of Josephson-junction-based resonators is used in experiments for near-quantum-limited microwave signal amplification [82, 84, 85, 195].

Driven nonlinear resonators can produce squeezed states [168–171, 187, 196] (note that quantum squeezing is closely related to classical fluctuations, e.g., [197–199]). Even though squeezed states are usually discussed for parametrically driven linear resonators [89, 200] (in optics a nonlinear material can be used to produce a parametric drive at a doubled frequency), there is a similarity between these two systems [195, 201, 202]. In particular, it can be shown that a nonlinear resonator near the bifurcation point at large photon numbers is equivalent to a degenerate parametric amplifier driven with a detuned pump [202]. Squeezed states can be used to improve measurement accuracy [203, 204] in a range of applications, such as gravitational wave detectors [205], superconducting qubit readout [152, 160, 161, 206–208], and nano/micromechanical position measurement [193, 209, 210]. There is currently a significant experimental interest in producing squeezed microwave states

with Josephson parametric amplifiers [83, 84, 164–166, 211]; the self-developing squeezing due to the nonlinearity of a microwave resonator (with revival and formation of “cat” states) has also been demonstrated experimentally [159].

It is well known that the steady state of a parametrically driven resonator cannot be squeezed beyond 3 dB [89, 212, 213]; in other words, any (instantaneous) quadrature variance is not less than 1/2 of the ground-state value (the 3 dB squeezing is reached in the ideal case at the threshold of parametric instability; note that for the narrow-band definition, squeezing in the same case is 6 dB [214]). This limit applies only to the resonator state (intracavity field), while squeezing of the reflected field outside of the cavity is unlimited [213, 215]. Various theoretical ideas [209, 216–220] (based on reservoir engineering, weak measurements, injection of squeezed light, etc.) have been proposed to overcome the 3 dB limit for a nanomechanical resonator; recently this limit has been exceeded experimentally [221].

Because of the similarity between nonlinear and parametrically driven resonators in their use as amplifiers [195, 202], it can be expected that squeezing of driven nonlinear resonators is also limited by 3 dB. However, we are not aware of papers, which discuss this limit explicitly (related works are, e.g., Refs. [186, 196, 222–225]; note explicit results for steady-state quantum fluctuations in Refs. [186] and [196]). As a side result of this work, we will show that the steady-state squeezing of a coherently driven nonlinear resonator is indeed limited by 3 dB. We will also show that during transients the squeezing can exceed this limit.

Previous studies of quantum dynamics of coherently driven nonlinear oscillators

have used a variety of theoretical methods, including stochastic differential equations, Fokker-Planck equation, generalized  $P$ -representation, linearization of evolution equation, formalism of quasienergies, etc. Usually the transients are neglected and only the steady state is analyzed. Moreover, most of the research has been focused on the regimes close to bifurcation or within the bistability range, in particular, with the goals to analyze switching between the quasistable states and to analyze amplification properties near the bifurcation point. In this chapter we are mainly interested in the opposite regime: far from the bifurcation and/or bistability, so that the effects of nonlinearity are not yet very strong. This regime is relevant to the measurement of superconducting qubits, in which the weak nonlinearity of the microwave resonator is induced by its interaction with the qubit. Nevertheless, this weak nonlinearity may lead to a significant self-developing squeezing of the microwave field [152], which affects qubit measurement fidelity. Another difference of our analysis from most of the previous studies is that we are mainly interested in transients, not the steady state. This is also motivated by the importance of transients in fast measurement of superconducting qubits. Even though our motivation mainly comes from the use of weakly nonlinear microwave resonators for qubit measurement, our results are equally applicable to the quantum dynamics of driven nanomechanical resonators, which always show some nonlinearity [226].

In this chapter, we analyze the evolution of a coherently driven weakly nonlinear resonator using a hybrid phase-space–Fock-space approach [79]. This approach is based on the observation that quantum state evolution due to nonlinearity can be easily described in Fock space, while the effect of the drive and dissipation for a linear resonator is well

described in phase space. We show that for large photon numbers, a Gaussian state [88] in phase space has also an approximately Gaussian form in Fock space, thus obtaining a rather simple conversion between the Fock-space and phase-space representations within the Gaussian-state approximation. The conversion equations are then used to derive reasonably simple first-order ordinary differential equations, describing state evolution due to drive, dissipation, and weak nonlinearity.

These evolution equations are for one complex and three real parameters, which characterize the Gaussian state of the resonator. The complex parameter describes the center of the Gaussian state in the phase plane; its evolution is given by an essentially classical equation, which takes into account nonlinearity. The three real parameters are Fock-space parameters, which after conversion into the phase space correspond to the minimum and maximum quadrature variances (therefore to squeezing and “unsqueezing”) and to the phase of the minimum-variance quadrature. The product of the minimum and maximum variances (ratio of unsqueezing and squeezing) corresponds to an effective temperature, which can be significantly higher [196] than the bath temperature. We note that our approach is physically similar to linearization of fluctuations around the classical trajectory within the Gaussian approximation [199], even though it is based on a different framework.

After deriving the hybrid phase-Fock-space evolution equations, we numerically compare their results with the master (Lindblad) equation simulations. We find quite good accuracy, with an inaccuracy scaling inversely proportional to the number of photons in the system. Even though our approximation formally requires large number of photons, it still works well when the resonator evolution starts from the ground state. In our simulations

with a few hundred photons in the system, the typical infidelity compared with the master equation simulations is about  $10^{-3}-10^{-4}$ , while being faster by a factor of over  $10^5$  (fractions of a second instead of hours). Compared with the coherent-state approximation, our method for the simulated cases is more accurate by about a factor of  $10^2$ , which indicates the importance of taking into account self-developing squeezing and heating.

Thus, our main result in this chapter is the derivation of relatively simple and computationally efficient equations, which describe the quantum evolution of a driven and damped weakly nonlinear resonator in the case of large photon numbers. As an example of using these equations, we derive the 3 dB squeezing limit discussed above for the steady state and numerically show that this limit can be exceeded during transients. Note that we analyze only the state of the resonator (intracavity field), while the analysis of the reflected field is presented in Chapter 6.

The range of validity for our approach seems to be essentially the same as for validity of the Gaussian approximation. Note that for small number of photons in the resonator, the resonator is practically linear, while for large number of photons, the resonator is practically semi-classical, and in both cases the Gaussian approximation is applicable. This is why our approach works well in a rather wide range, except the vicinity of the bifurcation point, where unsqueezing becomes too large; also, within the bistability region our approach cannot describe gradual mixing of quasistable states, which corresponds to classical switching between them. We analyze the accuracy of our approach numerically, by comparing its results with results of simulations based on the master equation.

The chapter is organized as follows. In Sec. 5.2 we describe the system and pose

the problem. In Sec. 5.3 we review the Gaussian states and corresponding phase-space evolution equations for a driven and damped linear resonator. Then in Sec. 5.4.1 we introduce Fock-space Gaussian states and discuss their equivalence to the usual (phase-space) Gaussian states in the case of large photon numbers, with explicit conversion relations between parameters of the phase-space and Fock-space representations. Using these conversion relations, in Sec. 5.4.2 we combine the Fock-space evolution due to nonlinearity with the phase-space evolution due to drive and damping, thus deriving the hybrid phase-Fock-space evolution equations, which are the main result of this chapter. Section 5.5 is devoted to analysis of the numerical accuracy of our approach. We start with calculating the fidelity of the conversion between the Gaussian and Fock-space Gaussian states in Sec. 5.5.1, and then in Sec. 5.5.2 we compare results of the hybrid evolution equations with the master equation simulations. In Sec. 5.6 the hybrid evolution equations are used to show that steady-state squeezing of the resonator state is limited by 3 dB, and it is also shown numerically that squeezing during transients can exceed the 3 dB limit. We conclude in Sec. 5.7. In Appendix F we discuss derivation of the Gaussian state evolution equations for a linear resonator under coherent drive and damping. In Appendix G we show that at large photon numbers, a Fock-space Gaussian state can be approximated by a phase-space Gaussian state, and derive the corresponding conversion relations. Appendix H discusses analytical results for squeezing in the steady state.

## 5.2 System and problem

We analyze the quantum state evolution of a weakly nonlinear resonator, which is coherently (classically) driven at frequency  $\omega_d$  and damped due to energy relaxation with rate  $\kappa$  at bath temperature  $T_b$ . The goal is to find a reasonably simple approximate description of this evolution, suitable for large number of photons in the resonator (we will use the terminology of photons, though for a mechanical resonator the terminology of phonons would be more appropriate).

Without damping, the laboratory-frame Hamiltonian of the considered system is ( $\hbar = 1$ )

$$H_{\text{lf}} = H_{\text{r}}^{\text{lf}} + H_{\text{d}}^{\text{lf}}, \quad (5.1)$$

$$H_{\text{r}}^{\text{lf}} = \sum_n E(n) |n\rangle\langle n|, \quad E(n) = \sum_{k=0}^{n-1} \omega_{\text{r}}(k), \quad (5.2)$$

$$H_{\text{d}}^{\text{lf}} = 2\text{Re}[\varepsilon(t) e^{-i\omega_d t}] (a^\dagger + a), \quad (5.3)$$

where  $|n\rangle$  is  $n$ th eigenstate of the resonator, with corresponding eigenenergy  $E(n)$  expressed via the resonator frequency  $\omega_{\text{r}}(n) = E(n+1) - E(n)$ , which slightly changes with the level number [we use  $E(0) = 0$ ],  $\varepsilon(t)$  is the complex amplitude of the drive at frequency  $\omega_d$ , and  $a = \hat{x} + i\hat{p}$  is the annihilation operator, while  $a^\dagger = \hat{x} - i\hat{p}$  is the creation operator. Here  $\hat{x}$  and  $\hat{p}$  are normalized position and momentum operators,  $\hat{x} = \hat{X} \sqrt{m\omega_{\text{r}0}/2}$  and  $\hat{p} = \hat{P}/\sqrt{2m\omega_{\text{r}0}}$ , where  $\hat{X}$  and  $\hat{P}$  are actual position and momentum operators,  $m$  is effective mass, and in the normalization we use  $\omega_{\text{r}0} \equiv \omega_{\text{r}}(0)$ ; however, this particular value is not important, since we assume a weak nonlinearity,  $|\omega_{\text{r}}(n) - \omega_{\text{r}}(0)| \ll \omega_{\text{r}}(0)$ . The assumption of weak nonlinearity also allows us to use the standard matrix elements for the annihilation operators,  $\langle k|a|n\rangle =$

$\sqrt{n} \delta_{n-1,k}$ . Note that for a linear resonator,  $\omega_r(n) = \omega_{r0}$ , the Hamiltonian (5.2) reduces to the standard form  $H_r^{\text{lf}} = \omega_{r0} a^\dagger a$ . Within the rotating wave approximation (RWA), the drive Hamiltonian (5.3) becomes  $H_d^{\text{lf}} = \varepsilon(t) e^{-i\omega_d t} a^\dagger + \varepsilon^*(t) e^{i\omega_d t} a$ . The RWA is natural for a weakly nonlinear resonator and near-resonant drive,  $|\omega_d - \omega_r(n)| \ll \omega_d$ . In some cases RWA misses experimentally important effects [151]; however, it should be sufficient for the simple system we consider here.

In the rotating frame based on the drive frequency  $\omega_d$ , the RWA Hamiltonian becomes  $H_{\text{rf}} = H_r^{\text{rf}} + H_d^{\text{rf}}$  with

$$H_r^{\text{rf}} = \sum_n E_{\text{rf}}(n) |n\rangle\langle n|, \quad E_{\text{rf}}(n) = \sum_{k=0}^{n-1} [\omega_r(k) - \omega_d], \quad (5.4)$$

$$H_d^{\text{rf}} = \varepsilon(t) a^\dagger + \varepsilon^*(t) a. \quad (5.5)$$

In this chapter we will mostly use the rotating frame.

The evolution of the system density matrix  $\rho$  due to Hamiltonian  $H$  (in either laboratory or rotating frame) and energy relaxation with rate  $\kappa$  is described by the standard master equation in the Lindblad form [89, 227, 228],

$$\begin{aligned} \dot{\rho} = & i[\rho, H] + \kappa(n_b + 1)(a\rho a^\dagger - a^\dagger a\rho/2 - \rho a^\dagger a/2) \\ & + \kappa n_b(a^\dagger \rho a - a a^\dagger \rho/2 - \rho a a^\dagger/2), \end{aligned} \quad (5.6)$$

where

$$n_b = \frac{1}{e^{\omega_{r0}/T_b} - 1} = \frac{\coth(\omega_{r0}/2T_b) - 1}{2} \quad (5.7)$$

is the average number of thermal photons for the bath temperature  $T_b$ . Note that the evolution equation (5.6) is generally not correct for a nonlinear resonator (e.g., Appendix B4 of [229]); however, we use it, assuming a weak nonlinearity. The problem with applicability

of the Lindblad equation (5.6) stems from the fact that it requires indistinguishability of the emitted and/or absorbed photons [229]. However, for a weakly nonlinear resonator, the photons emitted from (absorbed by) different levels have slightly different frequencies and can be distinguished spectroscopically if the frequency difference exceeds the level width. To estimate the effect, let us assume that unsqueezing is not too large, so the typical number of photons is  $\bar{n} \pm \sqrt{\bar{n}}$ , where  $\bar{n}$  is the average photon number. Then the frequency difference is about  $\sqrt{\bar{n}}(d\omega_r/dn)$ , while the level width is approximately  $\kappa\bar{n}$ . Therefore, indistinguishability requires  $\bar{n} \gg \kappa^{-2}(d\omega_r/dn)^2$ . For our typical parameters used in Sec. 5.5, the nonlinearity is quite small, so that  $\kappa^{-2}(d\omega_r/dn)^2 \sim 10^{-5}$ ; therefore, the indistinguishability condition is well satisfied and the Lindblad equation (5.6) is accurate.

Solving Eq. (5.6) numerically in the Fock space, we can find the resonator state evolution. However, for over  $\sim 100$  average photons in the resonator the numerical solution becomes slow, and for over  $\sim 500$  photons it becomes computationally intractable on a personal computer because of too large Hilbert space. Note that over 500 photons in the resonator can be used for a dispersive measurement of a superconducting qubit [150, 151].

In this chapter, we develop an approach which permits a simple analysis of evolution at this large number of photons. To a significant extent, the approach is based on the observation that evolution of a *linear* resonator can be described by Gaussian states in many situations [230]. Using the fact that a weak nonlinearity keeps the evolving state Gaussian (in the leading order), we will find the corresponding evolution equations. This greatly simplifies analysis, since a Gaussian state is characterized by only 5 real parameters, instead of  $N^2$  parameters for a density matrix involving up to  $N$  Fock states.

We will first review Gaussian states and evolution of a driven linear resonator, and then will show how a Gaussian state can be approximately converted into a Fock-space state, for which it is easy to introduce evolution due to nonlinearity.

## 5.3 Evolution of a linear resonator

Without nonlinearity, a Gaussian initial state remains Gaussian during evolution, while initially non-Gaussian state gradually becomes Gaussian [230, 231]. In this section we briefly review properties of the Gaussian states and discuss evolution of a linear resonator state due to applied drive and damping.

### 5.3.1 Brief review of Gaussian states

Gaussian states [88, 232–234] are defined as states for which the Wigner function [88, 173] has a Gaussian form (generally with an arbitrary number of dimensions). For a one-dimensional (single-mode) system with position operator  $\hat{X}$  and conjugate momentum operator  $\hat{P}$ , the Wigner function of a Gaussian state is

$$\mathcal{W}(X, P) = \frac{\exp\left(-\frac{1}{2}\vec{V}^T \mathbf{D}^{-1} \vec{V}\right)}{2\pi\sqrt{\text{Det}(\mathbf{D})}} \quad (5.8)$$

where  $\vec{V} = (X - X_c, P - P_c)^T$ ,  $X_c = \langle \hat{X} \rangle$ ,  $P_c = \langle \hat{P} \rangle$ , and elements of the covariance matrix  $\mathbf{D}$  are  $D_{11} = D_X = \langle \hat{X}^2 \rangle - \langle \hat{X} \rangle^2$ ,  $D_{22} = D_P = \langle \hat{P}^2 \rangle - \langle \hat{P} \rangle^2$ , and  $D_{12} = D_{21} = D_{XP} = \langle \hat{X}\hat{P} + \hat{P}\hat{X} \rangle / 2 - \langle \hat{X} \rangle \langle \hat{P} \rangle$ . The Husimi  $Q$ -function, Glauber-Sudarshan  $P$ -function and density matrix (in  $X$  or  $P$  space) of a Gaussian state have a Gaussian form as well [88, 235].

For a linear resonator with Hamiltonian  $H_r^{\text{lf}} = \omega_r a^\dagger a$  (constant frequency  $\omega_r$ ),

we can introduce the dimensionless (normalized) operators of position and momentum in the standard way as  $\hat{x} = \hat{X}/(2\sigma_{x,\text{gr}})$  and  $\hat{p} = \hat{P}/(2\sigma_{p,\text{gr}})$ , where  $\sigma_{x,\text{gr}}$  and  $\sigma_{p,\text{gr}}$  are the standard deviations of the ground state in the position and momentum representations, so that  $\hat{x} = (a + a^\dagger)/2$  and  $\hat{p} = (a - a^\dagger)/2i$ . For the normalized operators, the Wigner function  $W(x, p)$  has exactly the same form as Eq. (5.8), except now  $\vec{V} = (x - x_c, p - p_c)^T$ ,  $x_c = \langle \hat{x} \rangle$ ,  $p_c = \langle \hat{p} \rangle$ , and elements of the covariance matrix are now  $D_{11} = D_x = \langle \hat{x}^2 \rangle - \langle \hat{x} \rangle^2$ ,  $D_{22} = D_p = \langle \hat{p}^2 \rangle - \langle \hat{p} \rangle^2$ , and  $D_{12} = D_{21} = D_{xp} = \langle \hat{x}\hat{p} + \hat{p}\hat{x} \rangle/2 - \langle \hat{x} \rangle \langle \hat{p} \rangle$ . Explicit form of the Wigner function for a Gaussian state is

$$W(x, p) = \left(2\pi\sqrt{D_x D_p - D_{xp}^2}\right)^{-1} \times \exp\left[-\frac{D_p(\Delta x)^2 + D_x(\Delta p)^2 - 2D_{xp}\Delta x\Delta p}{2(D_x D_p - D_{xp}^2)}\right], \quad (5.9)$$

where  $\Delta x = x - x_c$  and  $\Delta p = p - p_c$ . The Wigner functions (5.8) and (5.9) are normalized as  $\int \mathcal{W}(X, P) dX dP = \int W(x, p) dx dp = 1$ .

With the quadrature operator along direction  $\varphi$  defined as

$$\hat{x}_\varphi \equiv \frac{ae^{-i\varphi} + a^\dagger e^{i\varphi}}{2} = \hat{x} \cos \varphi + \hat{p} \sin \varphi, \quad (5.10)$$

the variance  $\sigma_{x_\varphi}^2 \equiv \langle \hat{x}_\varphi^2 \rangle - \langle \hat{x}_\varphi \rangle^2$  of this quadrature for the Gaussian state is

$$\sigma_{x_\varphi}^2 = D_x \cos^2 \varphi + D_p \sin^2 \varphi + 2D_{xp} \cos \varphi \sin \varphi. \quad (5.11)$$

Let us introduce real variables  $D_0 > 0$  and  $b \geq 0$  as

$$D_0 \equiv \frac{D_x + D_p}{2}, \quad b^2 \equiv \frac{(D_x - D_p)^2}{4} + D_{xp}^2, \quad (5.12)$$

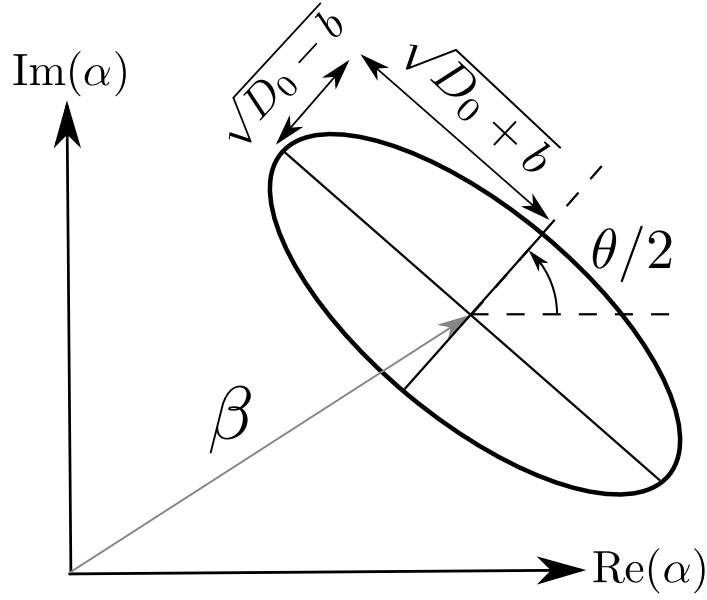


Figure 5.1: Phase-space illustration of a Gaussian state. The ellipse corresponds to one standard deviation for the quadrature operators along any direction. It is also the contour line for the Wigner function being a factor  $\sqrt{e}$  less than its maximum value. The ellipse center has coordinates  $(x_c, p_c)$ , which on the complex plane correspond to  $\langle a \rangle = x_c + ip_c$ . The minimum and maximum quadrature variances are  $D_0 - b$  and  $D_0 + b$ , respectively. The minimum-variance-direction angle is  $\Theta/2$ . In the rotating frame we use notation  $\theta$  instead of  $\Theta$ .

then the quadrature variance (5.11) can be rewritten as

$$\sigma_{x_\varphi}^2 = D_0 - b \cos(2\varphi - \Theta), \quad (5.13)$$

$$\Theta = \arctan\left(\frac{2D_{xp}}{D_x - D_p}\right) + \frac{\pi}{2}[1 + \text{sign}(D_x - D_p)]. \quad (5.14)$$

Equation (5.13) shows that  $D_0 - b$  and  $D_0 + b$  are the minimum and maximum quadrature variances respectively, and the direction of the minimum quadrature makes the angle  $\Theta/2$  with the  $x$ -axis (see Fig. 5.1). Note that

$$(D_0 + b)(D_0 - b) = D_x D_p - D_{xp}^2. \quad (5.15)$$

The Wigner function in the rotated “diagonal basis” with  $x^d$  being the coordinate

along the *minimum* quadrature is

$$W(x^d, p^d) = \left(2\pi\sqrt{(D_0 - b)(D_0 + b)}\right)^{-1} \times \exp\left[-\frac{(x^d - x_c^d)^2}{2(D_0 - b)} - \frac{(p^d - p_c^d)^2}{2(D_0 + b)}\right], \quad (5.16)$$

where  $x^d + ip^d = (x + ip)e^{-i\Theta/2}$  and similarly  $x_c^d + ip_c^d = (x_c + ip_c)e^{-i\Theta/2}$ . This formula shows that the contour lines for the Wigner function in the phase space of  $x$  and  $p$  are ellipses (Fig. 5.1).

The Husimi  $Q$ -function [89] for the Gaussian state can be obtained using the standard relation  $Q(x, p) = \frac{2}{\pi} \int W(x', p') e^{-2[(x-x')^2 + (p-p')^2]} dx' dp'$ . In particular, in the diagonal basis we find

$$Q(x^d, p^d) = \left(2\pi\sqrt{(D_0 - b + 1/4)(D_0 + b + 1/4)}\right)^{-1} \times \exp\left[-\frac{(x^d - x_c^d)^2}{2(D_0 - b + 1/4)} - \frac{(p^d - p_c^d)^2}{2(D_0 + b + 1/4)}\right]. \quad (5.17)$$

We see that the  $Q$ -function (5.17) has the same Gaussian form as the Wigner function (5.16), but variances for the both axes are increased by  $1/4$ .

It is useful to write the Gaussian state parameters in terms of average values of

the operators  $a$ ,  $a^2$ , and  $a^\dagger a$ ,

$$D_0 = \frac{1}{2} \left[ \langle a^\dagger a \rangle + \frac{1}{2} - (\text{Re}\langle a \rangle)^2 - (\text{Im}\langle a \rangle)^2 \right], \quad (5.18)$$

$$b = \frac{1}{2} \left[ [\text{Re}\langle a^2 \rangle - (\text{Re}\langle a \rangle)^2 + (\text{Im}\langle a \rangle)^2]^2 + (\text{Im}\langle a^2 \rangle - 2\text{Re}\langle a \rangle \text{Im}\langle a \rangle)^2 \right]^{1/2} \quad (5.19)$$

$$\Theta = \arctan \left( \frac{\text{Im}\langle a^2 \rangle - 2\text{Re}\langle a \rangle \text{Im}\langle a \rangle}{\text{Re}\langle a^2 \rangle - (\text{Re}\langle a \rangle)^2 + (\text{Im}\langle a \rangle)^2} \right) + \frac{\pi}{2} \{1 + \text{sign}[\text{Re}\langle a^2 \rangle - (\text{Re}\langle a \rangle)^2 + (\text{Im}\langle a \rangle)^2]\}, \quad (5.20)$$

$$x_c + ip_c = \langle a \rangle. \quad (5.21)$$

Besides introducing the Gaussian states via the Wigner function, it is also possible to introduce them as displaced squeezed thermal states (DSTS) [235–237], so that the density matrix is

$$\rho_{\text{DSTS}} = D(\alpha) S(\xi) \nu_{n_{\text{th}}} S(\xi)^\dagger D(\alpha)^\dagger, \quad (5.22)$$

where  $\alpha = \langle a \rangle = x_c + ip_c$  is the phase-plane state center,  $D(\alpha) = \exp(\alpha a^\dagger - \alpha^* a)$  is the displacement operator,  $S(\xi) = \exp[\frac{1}{2}\xi^* a^2 - \frac{1}{2}\xi(a^\dagger)^2]$  is the squeezing operator with squeezing parameter  $\xi = r e^{i\Theta}$  (the angle  $\Theta/2$  determines the short axis direction and therefore  $\Theta$  is the same as discussed above), and  $\nu_{n_{\text{th}}}$  is the thermal state, defined as

$$\nu_{n_{\text{th}}} = \frac{1}{1 + n_{\text{th}}} \sum_{k=0}^{\infty} \left( \frac{n_{\text{th}}}{1 + n_{\text{th}}} \right)^k |k\rangle\langle k|, \quad (5.23)$$

where  $|k\rangle$  is  $k$ th Fock state and  $n_{\text{th}} = \text{Tr}(a^\dagger a \nu_{n_{\text{th}}})$  is the average number of thermal photons. Note that Eq. (5.23) describes an equilibrium state of a linear resonator at finite temperature without drive, and in that case  $n_{\text{th}}$  is equal to the thermal photon number for the bath,  $n_{\text{b}}$ , given by Eq. (5.7). However, in the non-equilibrium case considered in this chapter,  $n_{\text{th}}$  is

not equal to  $n_b$ . It is still possible to define an *effective* temperature  $T_{\text{eff}}$  for a Gaussian state (5.22) via the same relation,

$$\coth(\omega_r/2T_{\text{eff}}) = 1 + 2n_{\text{th}}. \quad (5.24)$$

Note that the average photon number  $\bar{n}$  for a Gaussian state has a contribution proportional (but not equal) to  $n_{\text{th}}$ ,

$$\bar{n} = \text{Tr}(a^\dagger a \rho_{\text{DSTS}}) = |\alpha|^2 + (1 + 2n_{\text{th}}) \sinh^2 r + n_{\text{th}}, \quad (5.25)$$

while from Eq. (5.18) we find a simple expression

$$\bar{n} = |\alpha|^2 + 2D_0 - 1/2. \quad (5.26)$$

To relate parameters  $r$  and  $n_{\text{th}}$  of the DSTS state to the parameters of the Gaussian state (5.9), we can calculate averages  $\langle a \rangle$ ,  $\langle a^2 \rangle$ , and  $\langle a^\dagger a \rangle$  for the state (5.22), and use these results to find the variances

$$D_x = (1/4 + n_{\text{th}}/2)(\cosh 2r - \sinh 2r \cos \Theta), \quad (5.27)$$

$$D_p = (1/4 + n_{\text{th}}/2)(\cosh 2r + \sinh 2r \cos \Theta), \quad (5.28)$$

$$D_{xp} = -(1/4 + n_{\text{th}}/2) \sinh 2r \sin \Theta. \quad (5.29)$$

Comparing Eqs. (5.27)–(5.29) with Eqs. (5.12)–(5.14), we find the equivalence for

$$n_{\text{th}} = 2\sqrt{(D_0 + b)(D_0 - b)} - \frac{1}{2}, \quad \tanh 2r = \frac{b}{D_0}, \quad (5.30)$$

and the same angle  $\Theta$ .

As follows from the discussion above, a Gaussian state is determined by five real parameters. Two parameters,  $x_c$  and  $p_c$ , define the state center on the phase plane; it is

convenient to use their complex combination  $\alpha = x_c + ip_c$ . Three real parameters define the “shape” (see Fig. 5.1), which can be characterized either by  $D_x$ ,  $D_p$ , and  $D_{xp}$  or by  $D_0$ ,  $b$ , and  $\Theta$  or by  $r$ ,  $\Theta$ , and  $n_{\text{th}}$ . A Gaussian state is in general a mixed state. A pure Gaussian state is a minimum-uncertainty squeezed state, characterized by 4 real parameters; for such a state  $D_x D_p - D_{xp}^2 = (D_0 - b)(D_0 + b) = 1/16$  and  $n_{\text{th}} = 0$ . A coherent state is characterized by only 2 real parameters, which define the center; then  $D_x = D_p = D_0 = 1/4$ ,  $D_{xp} = b = n_{\text{th}} = 0$ , and  $\Theta$  is not important.

Note that our discussion in this section used the laboratory frame. In this frame, the evolution due to Hamiltonian  $H_{\text{r}}^{\text{lf}} = \omega_{\text{r}} a^\dagger a$  (in the absence of drive and damping) rotates the state center in Fig. 5.1 *clockwise* with angular velocity  $\omega_{\text{r}}$ . Moreover, the whole phase-space picture in Fig. 5.1 rotates clockwise with  $\omega_{\text{r}}$ . This means that parameters  $D_0$  and  $b$  do not change with time, while the angle  $\Theta/2$  evolves as  $d(\Theta/2)/dt = -\omega_{\text{r}}$ , and therefore  $\dot{\Theta} = -2\omega_{\text{r}}$ . Since  $D_0$  and  $b$  do not change, the parameters  $r$  and  $n_{\text{th}}$  are also constant – see Eq. (5.30). In the rotating frame based on the frequency  $\omega_{\text{d}}$ , the picture in Fig. 5.1 additionally rotates counterclockwise with angular velocity  $\omega_{\text{d}}$ , so that the net evolution is clockwise rotation with angular velocity  $\omega_{\text{r}} - \omega_{\text{d}}$ . Thus, in the rotating frame, the parameters  $D_0$ ,  $b$ ,  $r$ , and  $n_{\text{th}}$  are the same as in the laboratory frame, while the rotating-frame angle parameter  $\theta$  is related to  $\Theta$  as

$$\theta = \Theta + 2\omega_{\text{d}}t, \quad (5.31)$$

and it evolves as  $\dot{\theta} = -2(\omega_{\text{r}} - \omega_{\text{d}})$ . Descriptions of the Gaussian states in the rotating and laboratory frames are practically the same, except  $\Theta$  is replaced with  $\theta$  and  $\omega_{\text{r}}$  is replaced with  $\omega_{\text{r}} - \omega_{\text{d}}$ , as expected for the rotating-frame Hamiltonian  $H_{\text{r}}^{\text{rf}} = (\omega_{\text{r}} - \omega_{\text{d}}) a^\dagger a$ . Note,

however, that the conversion between the actual position and momentum operators ( $\hat{X}$ ,  $\hat{P}$ ) and the corresponding normalized operators ( $\hat{x}$ ,  $\hat{p}$ ) should still be based on the actual frequency  $\omega_r$  and not on  $\omega_r - \omega_d$ . The relation between the laboratory frame and the rotating frame is discussed in more detail in the Appendix F. Evolution in the presence of drive and damping is discussed next.

### 5.3.2 Evolution equations

For a linear harmonic oscillator with  $H_r^{\text{lf}} = \omega_r a^\dagger a$ , the evolution (5.6) due to drive (5.3) and damping  $\kappa$  at bath temperature  $T_b$ , preserves state Gaussianity and leads to the following evolution equations in the *laboratory frame* [209, 230, 238, 239],

$$\dot{x}_c = \omega_r p_c, \quad (5.32)$$

$$\dot{p}_c = -\omega_r x_c - \kappa p_c - 2\text{Re}(\varepsilon e^{-i\omega_d t}), \quad (5.33)$$

$$\dot{D}_x = 2\omega_r D_{xp}, \quad (5.34)$$

$$\dot{D}_p = -2\omega_r D_{xp} - 2\kappa D_p + (\kappa/2) \coth(\omega_r/2T_b), \quad (5.35)$$

$$\dot{D}_{xp} = -\omega_r(D_x - D_p) - \kappa D_{xp}. \quad (5.36)$$

Note that the evolution of the state center ( $x_c$  and  $p_c$ ) is decoupled from the evolution of the variances, and the drive  $\varepsilon$  contributes only to  $\dot{p}_c$  (as a classical force). The state center oscillates with the resonator frequency  $\omega_r$  (intrinsically, neglecting effects of  $\kappa$  and  $\varepsilon$ ), while the variances oscillate with doubled frequency,  $2\omega_r$ . Also note that Eqs. (5.32)–(5.36) do not rely on the RWA assumption.

Using the RWA (which symmetrizes coordinates  $x$  and  $p$ ) and going into the *rotating frame* based on the drive frequency  $\omega_d$ , so that the Gaussian state center is characterized

by a slowly changing complex number  $\beta$  in the standard phase space,

$$\beta = (x_c + ip_c) e^{i\omega_d t}, \quad (5.37)$$

from Eqs. (5.32)–(5.36) we can derive (see Appendix F) the following evolution equations [227, 240] (see also [235, 241]) for the parameters  $\beta$ ,  $D_0$ ,  $b$ , and  $\theta$ ,

$$\dot{\beta} = -i(\omega_r - \omega_d)\beta - (\kappa/2)\beta - i\varepsilon, \quad (5.38)$$

$$\dot{D}_0 = -\kappa D_0 + (\kappa/4) \coth(\omega_r/2T_b), \quad (5.39)$$

$$\dot{b} = -\kappa b, \quad (5.40)$$

$$\dot{\theta} = -2(\omega_r - \omega_d). \quad (5.41)$$

Note that the drive does not affect evolution of the diagonal-basis variances  $D_0 \pm b$ ; however, the short-axis direction  $\theta/2$  rotates clockwise with the detuning frequency  $\omega_r - \omega_d$ , similar to the rotation of the state center.

Equations (5.38)–(5.41) are the starting point of our analysis. They describe evolution of a linear resonator using the phase-space language. However, to include nonlinearity, we will need to approximately convert them into the Fock-space representation. From now on, we will use only the rotating frame.

## 5.4 Evolution of a weakly nonlinear resonator

### 5.4.1 Fock-space Gaussian state

Generalizing the idea of Ref. [79], let us introduce a state, for which the density matrix in the basis of eigenstates  $|n\rangle$  (Fock space) has the following form,

$$\begin{aligned} \rho_{mn} = & \frac{1}{\sqrt{2\pi W_1 |\beta|^2}} \exp \left[ -\frac{(\frac{n+m}{2} - |\beta|^2)^2}{2W_1 |\beta|^2} - \frac{(n-m)^2}{8W_2 |\beta|^2} \right] \\ & \times \exp \left[ i\phi_\beta (n-m) - i\frac{2K}{|\beta|^2} \left( \frac{n+m}{2} - |\beta|^2 \right) (n-m) \right]. \end{aligned} \quad (5.42)$$

We call it a Fock-space Gaussian state (because of quadratic dependence on  $n$  and  $m$  inside exponents) or, following the terminology of Ref. [79], a sheared Gaussian state (because of a shearing effect produced by the  $K$ -term in the phase space). The state (5.42) is characterized by five real parameters:  $|\beta|$ ,  $\phi_\beta$ ,  $W_1$ ,  $W_2$ , and  $K$ . Note that a physical  $\rho_{mn}$  requires

$$0 < W_2 \leq W_1. \quad (5.43)$$

As shown in the Appendix G, in the case  $|\beta| \gg 1$  (while  $W_1$ ,  $W_2$ , and  $K$  are on the order of unity) this state is *approximately equal* to the standard Gaussian state discussed in Sec. 5.3, so that

$$\beta = e^{i\phi_\beta} |\beta| \quad (5.44)$$

is (approximately) the state center, while the (approximate) conversion relations for the

parameters  $D_0$ ,  $b$ , and  $\theta$  are

$$D_0 = \frac{1}{8} \left[ \frac{1}{W_2} + W_1(1 + 16K^2) \right], \quad (5.45)$$

$$b = \sqrt{D_0^2 - W_1/(16W_2)}, \quad (5.46)$$

$$\begin{aligned} \theta = 2\phi_\beta + \arctan\left(\frac{KW_1}{D_0 - W_1/4}\right) \\ + (\pi/2) [1 - \text{sign}(D_0 - W_1/4)]. \end{aligned} \quad (5.47)$$

The conversion becomes exact for  $|\beta| \rightarrow \infty$ .

While in the leading order  $\langle a \rangle = e^{i\phi_\beta} |\beta|$  for the Fock-space Gaussian state (5.42), more accurate calculations show the next-order correction proportional to  $|\beta|^{-1}$ ,

$$\langle a \rangle = e^{i\phi_\beta} \left[ |\beta| - \frac{W_1 + 1/W_2 - 2}{8|\beta|} - \frac{2K^2W_1}{|\beta|} - i \frac{KW_1}{|\beta|} \right]. \quad (5.48)$$

The overlap fidelity between the Gaussian and Fock-space Gaussian states becomes somewhat better if this correction is taken into account, so that a slightly shifted center corresponds to the same  $\langle a \rangle$  for the Gaussian and Fock-space Gaussian states (see numerical results in Sec. 5.5.1). However, for simplicity we will not use the center correction (5.48) unless specifically mentioned.

Note that the trace of the state (5.42) is not exactly 1; however, the difference is negligible (exponentially small) for  $|\beta| \gg 1$ . The Fock-space Gaussian state (5.42) is in general mixed; it becomes pure if  $W_2 = W_1$ , and in this case it reduces to the sheared Gaussian state introduced in Ref. [79]. [Note a misprint in Eq. (33) of Ref. [79], where the last exponent should actually be  $-iK(n - |\beta|^2)^2/|\beta|^2$ .] Comparing Eqs. (5.45) and (5.46) with Eq. (5.30), we find a useful relation for the thermal photon number,

$$n_{\text{th}} = (\sqrt{W_1/W_2} - 1)/2, \quad (5.49)$$

which is equivalent to the relation

$$W_1/W_2 = \coth^2(\omega_r/2T_{\text{eff}}) = 16(D_0 + b)(D_0 - b). \quad (5.50)$$

Note that the ratio of the variances,  $(D_0 + b)/(D_0 - b)$ , and the angle  $\theta/2 - \phi_\beta$  are both functions of only two parameters:  $K$  and  $W_1W_2$ .

The quadrature variance  $\sigma_{x_\varphi}^2$  along a direction  $\varphi$  for the state (5.42) can be calculated as  $\sigma_{x_\varphi}^2 = D_0 - b \cos(2\varphi - \theta)$  from Eqs. (5.45)–(5.47). In particular, for the direction along  $\beta$  ( $\varphi = \phi_\beta$ ) we find the variance  $\sigma_{x_\varphi}^2 = W_1/4$ , while for the orthogonal direction ( $\varphi = \phi_\beta + \pi/2$ ) we find the variance  $\sigma_{x_\varphi}^2 = 1/(4W_2) + 4K^2W_1$ .

As follows from Eq. (5.47), in the case  $K = 0$ , the short axis (minimum variance) is either along the direction of  $\beta$  ( $\theta/2 = \phi_\beta$ ) or orthogonal to it ( $\theta/2 = \phi_\beta + \pi/2$ ). Since in this case the quadrature variance along  $\beta$  is  $W_1/4$ , while along the orthogonal direction [ $\varphi = \phi_\beta + \pi/2$ ] the variance is  $1/4W_2$ , the short axis is along  $\beta$  if  $W_1W_2 < 1$ , and it is orthogonal to the direction of  $\beta$  if  $W_1W_2 > 1$ .

While Eqs. (5.45)–(5.47) show the conversion (for  $|\beta| \rightarrow \infty$ ) from the Fock-space parameters  $W_1$ ,  $W_2$ , and  $K$  to the phase-space parameters  $D_0$ ,  $b$ , and  $\theta$ , the inverse conversion is given by equations

$$W_1 = 4[D_0 - b \cos(\theta - 2\phi_\beta)], \quad (5.51)$$

$$W_2 = \frac{D_0 - b \cos(\theta - 2\phi_\beta)}{4(D_0^2 - b^2)}, \quad (5.52)$$

$$K = \frac{b \sin(\theta - 2\phi_\beta)}{4[D_0 - b \cos(\theta - 2\phi_\beta)]}. \quad (5.53)$$

The main idea of introducing the Fock-space Gaussian state (5.42) is that it has a simple evolution due to resonator nonlinearity. Let us consider the evolution *only* due to

Hamiltonian (5.4), i.e., with  $\varepsilon = \kappa = 0$ . Then  $\rho_{nm}(t) = \rho_{nm}(0) \exp\{-i[E_{\text{rf}}(n) - E_{\text{rf}}(m)]t\}$ . Comparing this phase evolution with the second line of Eq. (5.42) and expanding the resonator frequency  $\omega_{\text{r}}(n)$  in Eq. (5.4) up to first order around  $n \approx |\beta|^2$  (assuming that nonlinearity is practically constant within the range  $|n - |\beta|^2| \lesssim \sqrt{W_1} |\beta|$ ), we find evolution equations

$$\dot{\phi}_{\beta} = -[\omega_{\text{r}}(|\beta|^2) - \omega_{\text{d}}], \quad (5.54)$$

$$\dot{K} = \frac{1}{2} |\beta|^2 \left. \frac{d\omega_{\text{r}}(n)}{dn} \right|_{|\beta|^2}, \quad (5.55)$$

where we neglected discreteness of  $\omega_{\text{r}}(n)$ . We see that  $\beta$  rotates due to detuning of the resonator frequency  $\omega_{\text{r}}(|\beta|^2)$  at the state center from the rotating-frame frequency  $\omega_{\text{d}}$  (as should be expected), while nonlinearity changes  $K$ , leading to accumulation of the quadratic phase factor in Eq. (5.42).

We emphasize that a weak nonlinearity approximately preserves the Fock-space Gaussian form (5.42), and therefore approximately preserves the Gaussian-state form in the phase space, assuming a large photon number  $|\beta|^2$ . Since the evolution due to the drive and damping also preserves the Gaussian-state form, as discussed in Sec. 5.3 (for weak nonlinearity we can use approximately the same matrix elements of operator  $a$  in the Fock space as for a linear oscillator), the state remains approximately Gaussian in both phase and Fock spaces during the combined evolution.

#### 5.4.2 Hybrid phase-Fock-space evolution equations

We have separately described the evolution due to nonlinearity, Eqs. (5.54)–(5.55), and due to drive and damping, Eqs. (5.38)–(5.41). The combined evolution is simply the

sum of the corresponding terms. However, Eqs. (5.38)–(5.41) assume the phase-space representation of Fig. 5.1, while Eq. (5.55) is based on the Fock-state representation (5.42). Thus, we need to convert the equations into a common representation using the conversion formulas (5.44)–(5.47).

We will characterize the evolving state by four parameters:  $\beta(t)$ ,  $W_1(t)$ ,  $W_2(t)$ , and  $K(t)$ . We call it a hybrid representation, since  $\beta$  is a phase-space parameter, while  $W_1$ ,  $W_2$ , and  $K$  originate from the Fock-space description.

As discussed in Sec. 5.4.1, evolution due to nonlinearity produces Eq. (5.55) for  $\dot{K}$ , the center  $\beta$  evolves as

$$\dot{\beta} = -i[\omega_r(|\beta|^2) - \omega_d] \beta, \quad (5.56)$$

while  $W_1$  and  $W_2$  do not evolve,  $\dot{W}_1 = \dot{W}_2 = 0$ . Note that Eq. (5.56) essentially implies that the average number of photons in the resonator is  $\bar{n} \approx |\beta|^2$ , neglecting corrections in Eq. (5.25).

To find evolution of parameters  $W_1$ ,  $W_2$ , and  $K$  due to drive and damping, we write Eqs. (5.39)–(5.41) expressing the time derivatives  $\dot{D}_0$ ,  $\dot{b}$ , and  $\dot{\theta}$  via the partial derivatives over the parameters of the conversion equations (5.45)–(5.47),

$$\begin{aligned} \frac{\partial D_0}{\partial W_1} \dot{W}_1 + \frac{\partial D_0}{\partial W_2} \dot{W}_2 + \frac{\partial D_0}{\partial K} \dot{K} = -\kappa D_0 \\ + (\kappa/4) \coth(\omega_{r0}/2T_b), \end{aligned} \quad (5.57)$$

$$\frac{\partial b}{\partial W_1} \dot{W}_1 + \frac{\partial b}{\partial W_2} \dot{W}_2 + \frac{\partial b}{\partial K} \dot{K} = -\kappa b, \quad (5.58)$$

$$\frac{\partial \theta}{\partial W_1} \dot{W}_1 + \frac{\partial \theta}{\partial W_2} \dot{W}_2 + \frac{\partial \theta}{\partial K} \dot{K} + 2 \frac{d[\arg(\beta)]}{dt} = 0, \quad (5.59)$$

where in the last term of Eq. (5.59) we need to use  $\dot{\beta} = -\beta\kappa/2 - i\varepsilon$ , not including the

evolution (5.56) due to detuning. This is because the evolution (5.56) compensates the right-hand-side term of Eq. (5.41), which we therefore do not write in Eq. (5.59). Another justification of writing Eq. (5.59) in this way is that we consider evolution only due to drive and damping [not due to detuning, which is already considered in Eq. (5.56)]; then the angle  $\theta$  does not change in time, and we should exclude the detuning term from  $\dot{\beta}$ .

Equations (5.57)–(5.59) with the partial derivatives obtained from Eqs. (5.45)–(5.47), give us a system of three linear equations for  $\dot{W}_1$ ,  $\dot{W}_2$ , and  $\dot{K}$ . Solving this system, we find

$$\dot{W}_1 = 8KW_1 \operatorname{Re}(\varepsilon/\beta) + \kappa [\coth(\omega_{r0}/2T_b) - W_1], \quad (5.60)$$

$$\begin{aligned} \dot{W}_2 = 8KW_2 \operatorname{Re}(\varepsilon/\beta) \\ + \kappa W_2 [1 - W_2(1 + 16K^2) \coth(\omega_{r0}/2T_b)], \end{aligned} \quad (5.61)$$

$$\begin{aligned} \dot{K} = \frac{1}{4} [(W_1 W_2)^{-1} - (1 + 16K^2)] \operatorname{Re}(\varepsilon/\beta) \\ - \kappa (K/W_1) \coth(\omega_{r0}/2T_b). \end{aligned} \quad (5.62)$$

Note that in the term  $\coth(\omega_{r0}/2T_b)$  we neglect changing resonator frequency because of the weak nonlinearity assumption. In the special case when  $\kappa = 0$ , Eqs. (5.60)–(5.62) reduce to Eq. (47) of Ref. [79].

Finally, combining the terms from Eqs. (5.55)–(5.56) (for evolution due to nonlinearity) and from Eqs. (5.60)–(5.62) (for evolution due to drive and damping), we obtain the

hybrid phase-Fock-space evolution equations

$$\dot{\beta} = -i[\omega_r(\bar{n}) - \omega_d] \beta - \frac{\kappa}{2} \beta - i\varepsilon, \quad \bar{n} \approx |\beta|^2, \quad (5.63)$$

$$\dot{W}_1 = 8KW_1 \operatorname{Re}(\varepsilon/\beta) + \kappa [\coth(\omega_{r0}/2T_b) - W_1], \quad (5.64)$$

$$\begin{aligned} \dot{W}_2 = 8KW_2 \operatorname{Re}(\varepsilon/\beta) \\ + \kappa W_2 [1 - W_2(1 + 16K^2) \coth(\omega_{r0}/2T_b)], \end{aligned} \quad (5.65)$$

$$\begin{aligned} \dot{K} = \left( \frac{1}{4W_1W_2} - \frac{1 + 16K^2}{4} \right) \operatorname{Re}(\varepsilon/\beta) \\ - \frac{\kappa K}{W_1} \coth(\omega_{r0}/2T_b) + \frac{1}{2} |\beta|^2 \left. \frac{d\omega_r(n)}{dn} \right|_{n=|\beta|^2}. \end{aligned} \quad (5.66)$$

Evolution equations (5.63)–(5.66) complemented with the conversion formulas (5.45)–(5.47) are the *main result* of this chapter. To our knowledge, this approach to the quantum evolution of a weakly nonlinear resonator has never been used previously.

Equations (5.63)–(5.66) describe evolution of five real parameters of a Gaussian state. Equation (5.63) describing evolution of the state center (2 real parameters) is decoupled from the other three equations. The equations are approximate and assume  $|\beta| \gg 1$  (more detailed discussion later); in general an evolving nonlinear resonator cannot be described by a Gaussian state exactly. In spite of the requirement  $|\beta| \gg 1$ , Eqs. (5.63)–(5.66) can be used to numerically analyze evolution starting even from  $\beta = 0$  with a good accuracy (the numerical results are discussed later). There is no divergence of  $\operatorname{Re}(\varepsilon/\beta)$  in Eqs. (5.64)–(5.66) at  $\beta = 0$  because if  $\beta(t_0) = 0$ , then close to this time moment  $\beta = -i\varepsilon(t - t_0)$  and therefore  $\operatorname{Re}(\varepsilon/\beta) = \operatorname{Re}[i/(t - t_0)] = 0$ . A numerical divergence can be easily avoided by shifting the denominator of  $\operatorname{Re}(\varepsilon/\beta)$  by a negligible amount.

Equation (5.63) has a simple physical meaning; it takes into account that the

resonator frequency  $\omega_r(n)$  changes with the photon number  $n$ , and approximates  $n$  with the average photon number  $\bar{n} \approx |\beta|^2$ . One may think that a simple generalization of Eq. (5.63) is to use a more accurate value for  $\bar{n}$  from Eq. (5.25) in  $\omega_r(\bar{n})$  [it would also require conversion equations (5.30) and (5.45)–(5.47)]. However, numerical simulations show that this correction does not always give a better agreement with full master equation simulations using Eq. (5.6). Because of that, we do not use this correction in the numerical analysis in Secs. 5.5 and 5.6.

Note that Eqs. (5.63)–(5.66) permit three natural rescalings. First, by rescaling the time axis, it is possible to use  $\kappa = 1$ . Second, since discreteness of  $n$  is not important in our approach, we can rescale the  $n$  axis and normalize nonlinearity, for example setting  $d\omega_r(n)/dn|_{n=0} = \pm 1$ . Third, non-zero bath temperature  $T_b$  is equivalent to rescaling  $W_1 \rightarrow W_1 \coth(\omega_{r0}/2T_b)$  and  $W_2 \rightarrow W_2/\coth(\omega_{r0}/2T_b)$ , while using  $T_b = 0$  in Eqs. (5.63)–(5.66); this leads to  $D_0 \rightarrow D_0 \coth(\omega_{r0}/2T_b)$  and  $b \rightarrow b \coth(\omega_{r0}/2T_b)$ , with unchanged  $\beta$  and  $\theta$ .

Equations (5.64)–(5.66) describe evolution of the Fock-space parameters  $W_1$ ,  $W_2$ , and  $K$ . It is also possible to write evolution equations for the phase-space parameters  $D_0$ ,  $b$ , and  $\theta$ . Note that without the last term in Eq. (5.66), Eqs. (5.64)–(5.66) exactly correspond to Eqs. (5.39)–(5.41). Therefore, we only need to convert the last term in (5.66) into the phase space, that can be done by using partial derivatives from the conversion relations (5.51)–(5.53). In this way we obtain the following evolution equations,

$$\dot{D}_0 = -\kappa D_0 + (\kappa/4) \coth(\omega_{r0}/2T_b) + 2\eta_\beta |\beta|^2 b \sin(\Delta\theta), \quad (5.67)$$

$$\dot{b} = -\kappa b + 2\eta_\beta |\beta|^2 D_0 \sin(\Delta\theta), \quad (5.68)$$

$$\frac{d(\Delta\theta)}{dt} = 2 \operatorname{Re}(\varepsilon/\beta) - 2\eta_\beta |\beta|^2 \frac{b - D_0 \cos(\Delta\theta)}{b}, \quad (5.69)$$

where  $\Delta\theta \equiv \theta - 2 \arg(\beta)$ ,  $\eta_\beta \equiv d\omega_r(n)/dn|_{n=|\beta|^2}$ , and evolution of  $\beta$  is still given by Eq. (5.63). Note that divergence in Eq. (5.69) at  $\beta = 0$  can be avoided numerically in the same way as discussed above: by a negligible shift of  $\beta$ . The divergence in Eq. (5.69) at  $b = 0$  can also be avoided numerically by a negligible increase of  $b$  (physically, this divergence is because  $\Delta\theta$  is undefined at  $b = 0$ ). Equations (5.67)–(5.69) are equivalent to Eqs. (5.64)–(5.66). We have checked this equivalence numerically. However, in the simulations discussed below we used Eqs. (5.64)–(5.66) rather than Eqs. (5.67)–(5.69). One of the reasons for our preference is that evolution of  $W_1$ ,  $W_2$ , and  $K$  is always smooth, while  $\Delta\theta$  evolves very fast when  $b$  approaches zero, thus potentially creating a problem with numerical solution of differential equations (even though our simulations never suffered from this potential problem).

Note that from Eqs. (5.67) and (5.68) we can obtain

$$\begin{aligned} \frac{d}{dt}(D_0 \pm b) &= -[\kappa \mp 2\eta_\beta |\beta|^2 \sin(\Delta\theta)] (D_0 \pm b) \\ &\quad + (\kappa/4) \coth(\omega_{r0}/2T_b), \end{aligned} \tag{5.70}$$

which shows that for the maximum-variance and minimum-variance quadratures, the effective damping rate is different,  $\kappa_{\text{eff}} = \kappa \mp 2\eta_\beta |\beta|^2 \sin(\Delta\theta)$ , and changes with time. Similarly, the effective bath temperature is also different,  $\coth(\omega_{r0}/2T_b) \rightarrow (\kappa/\kappa_{\text{eff}}) \coth(\omega_{r0}/2T_b)$ . Discussion in terms of different effective damping rates for the two quadratures makes an obvious connection to the case of a parametric drive with doubled frequency.

We have checked that Eqs. (5.67)–(5.69) are consistent with the results of Ref. [199] for Gaussian variances of classical fluctuations around the trajectory (5.63), caused by classical (complex) white noise  $\sqrt{\kappa}\zeta(t)$  applied to the resonator, with the correlation

function  $\langle \zeta^*(t) \zeta(t') \rangle = (1/2) \coth(\omega_r/2T_b) \delta(t - t')$ ,  $\langle \zeta(t) \zeta(t') \rangle = 0$  (as in, e.g., [139]). Note, however, that in order to get correct equations, we had to exchange  $B$  with  $B^\dagger$  in Eq. (3.2.4) of Ref. [199]. The correspondence between Eqs. (5.67)–(5.69) and results of Ref. [199] confirms that the quantum squeezing is similar to squeezing of classical fluctuations, and it also shows that our approach is physically similar to linearization of fluctuations around the classical trajectory within the Gaussian approximation.

In Appendix H we derive analytical results for  $D_0$ ,  $b$ , and  $\Delta\theta$  in the steady state and discuss their equivalence to the results of Refs. [186] and [196] for a Duffing oscillator (Kerr nonlinearity).

## 5.5 Numerical accuracy

In this section we discuss numerical accuracy of our approach. We start with analyzing fidelity of the conversion between the Gaussian and Fock-space Gaussian states, and then discuss numerical accuracy of the hybrid phase-Fock-space evolution equations by comparing results with full simulation.

### 5.5.1 Fidelity of the conversion

As was discussed in Sec. 5.4.1, the Gaussian state (5.9) is approximately equal to the Fock-space Gaussian state (5.42) with the conversion relations (5.44)–(5.47), in the case of large photon numbers,  $|\beta|^2 \gg 1$ . Let us check the accuracy of this conversion numerically. For that we calculate the overlap fidelity  $F$  between the states (5.9) and (5.42) using the

standard definition [58]

$$F = \frac{\left(\text{Tr}\sqrt{\sqrt{\rho_1}\rho_2\sqrt{\rho_1}}\right)^2}{\text{Tr}(\rho_1)\text{Tr}(\rho_2)}, \quad (5.71)$$

where  $\rho_1$  and  $\rho_2$  are the density matrices of the compared states. Note that for normalized states the denominator in Eq. (5.71) is not needed, but we use the more general version (5.71) because the Fock-space Gaussian state (5.42) is not exactly normalized. When at least one of the states is pure, Eq. (5.71) reduces to the usual state overlap, e.g.,  $F = \langle\psi_1|\rho_2|\psi_1\rangle = \text{Tr}(\rho_1\rho_2)$  if  $\rho_1 = |\psi_1\rangle\langle\psi_1|$  and both states are normalized.

To find the conversion fidelity for a Gaussian state with parameters  $\beta$ ,  $D_0$ ,  $b$ , and  $\theta$ , we use conversion relations (5.45)–(5.47) to find corresponding parameters  $W_1$ ,  $W_2$ , and  $K$  [ $\beta$  is the same unless we use the correction (5.48)], which gives us the Fock-space Gaussian state (5.42). Then we calculate exact Fock-space representation of the Gaussian state of (5.9) using Eq. (5.22) with parameters  $|\xi|$  and  $n_{\text{th}}$  obtained from the relations (5.30) (using  $\alpha = \beta$  and  $\Theta = \theta$ ). Finally, we use Eq. (5.71) in the Fock space to find the fidelity  $F$  between the Gaussian and Fock-space Gaussian states. Note that  $F$  does not depend on the phase  $\arg(\beta)$  for a fixed value of  $\theta/2 - \arg(\beta)$ , so it is sufficient to consider  $\arg(\beta) = 0$ , i.e.,  $\beta = |\beta|$ ; this is what we assume below in the numerical analysis of the conversion fidelity; in this case  $\theta/2 - \arg(\beta) \rightarrow \theta/2$ .

Figure 5.2 shows infidelity  $1 - F$  as a function of  $|\beta|$  on a log-log scale for several values of other parameters:  $4(D_0 + b) = 1, 2$ , and  $4$  (this parameter is the long-axis variance compared with the coherent state; we call it “unsqueezing factor”),  $\theta/2 = 0, \pi/2$ , and  $\pi/4$  (this is the direction of the short axis in Fig. 5.1),  $n_{\text{th}} = 0$  and  $1/2$ . The lines in Fig. 5.2 are labeled with a pair of numbers:  $4(D_0 + b)$  and  $\theta/2$ ; solid and dashed lines

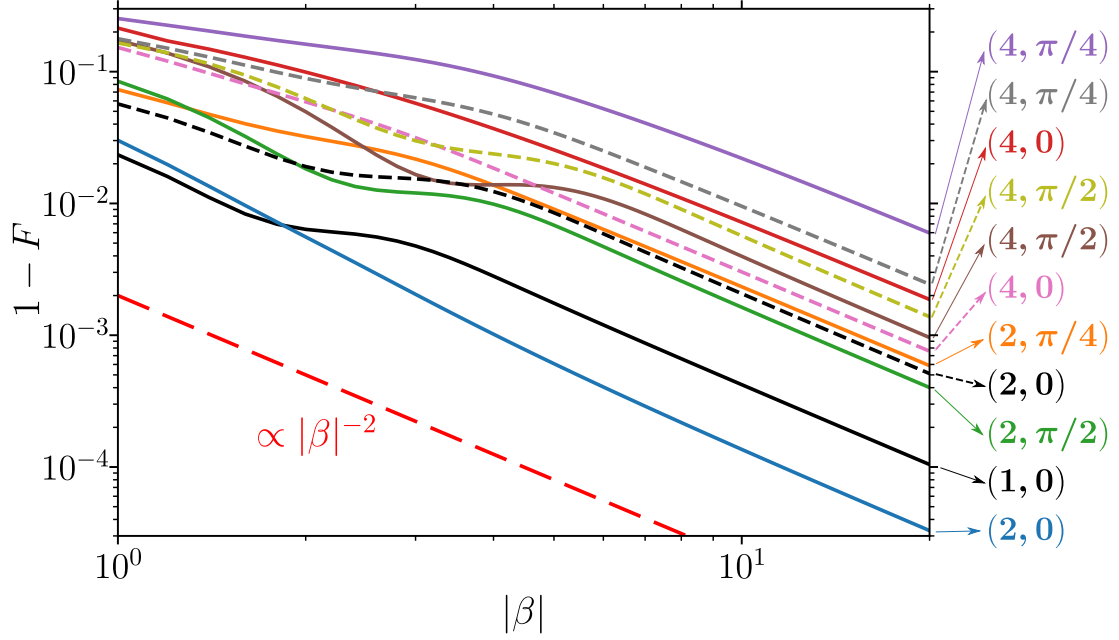


Figure 5.2: Infidelity  $1 - F$  between the Gaussian and Fock-space Gaussian states as a function of (real)  $\beta$  for several values of the parameters  $4(D_0 + b)$  and  $\theta/2$  (labeled respectively at the right side), for  $n_{\text{th}} = 0$  (solid lines) and  $n_{\text{th}} = 1/2$  (dashed lines). At large  $|\beta|$  all lines show the scaling  $|\beta|^{-2}$ , illustrated by the long-dashed line.

correspond to  $n_{\text{th}} = 0$  and  $1/2$  respectively. Note that there is no dependence on  $\theta$  when  $4(D_0 + b) = 1 + 2n_{\text{th}}$  [see Eq. (5.30)], then we show only the line  $\theta = 0$ ; also note that for  $n_{\text{th}} = 1/2$  it is always  $4(D_0 + b) \geq 2$ .

Most importantly, we see that all lines in Fig. 5.2 show the scaling  $1 - F \propto |\beta|^{-2}$  at large  $|\beta|$  (this scaling is illustrated by the long-dashed line). The deviation from this dependence at small  $|\beta|$  is mainly caused by two reasons. First, the “shoulder” feature may develop when  $|\beta| < 3\sqrt{4(D_0 - b \cos \theta)} \leq 3\sqrt{4(D_0 + b)}$  because then  $|\beta| < 3\sqrt{W_1}$  in Eq. (5.42) and thus the Gaussian approximation near  $n = 0$  becomes inaccurate (less than 3 standard deviations). Second, deviation from the scaling  $|\beta|^{-2}$  starts to develop when  $1 - F \gtrsim 0.05$  because  $F$  cannot exceed 1; actually, a natural metric for distance between

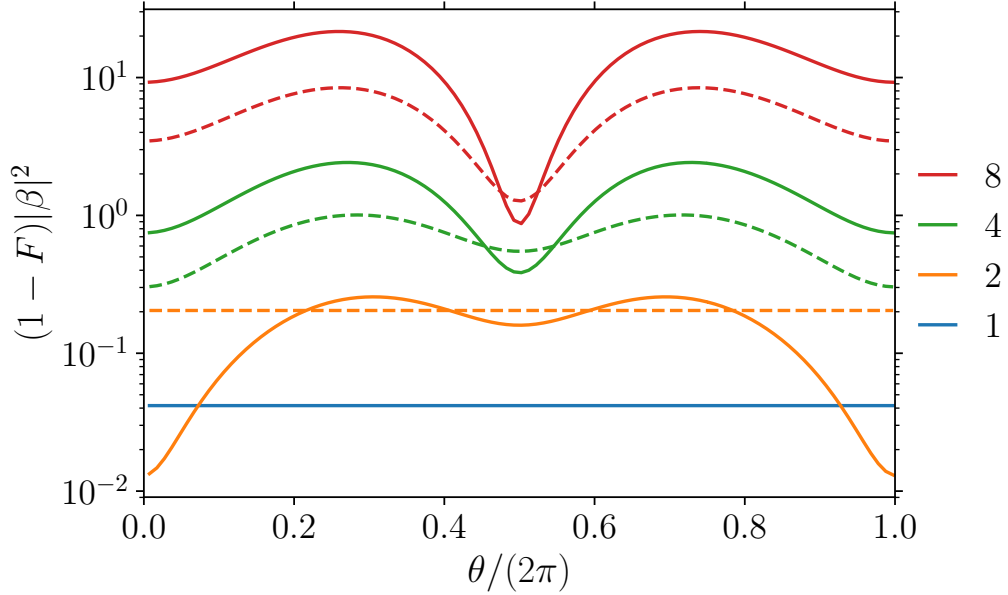


Figure 5.3: Scaled infidelity  $(1 - F)|\beta|^2$  as a function of the short-axis angle  $\theta/2$ . Solid lines are for  $n_{\text{th}} = 0$  (pure states) and  $4(D_0 + b) = 8, 4, 2,$  and  $1$  (top to bottom); dashed lines are for  $n_{\text{th}} = 1/2$  and  $4(D_0 + b) = 8, 4,$  and  $2$  (top to bottom). We used  $\beta = 40$ , which is sufficiently large so that the presented results do not depend on  $|\beta|$ .

the states is  $\arccos(\sqrt{F})$  [58], which is approximately  $\sqrt{1 - F}$  when  $1 - F \ll 1$ ; for this metric the above condition is  $\sqrt{1 - F} \gtrsim 0.22$ . From Fig. 5.2 we conclude that the scaling  $1 - F \propto |\beta|^{-2}$  is almost perfect if  $|\beta| > 3\sqrt{4(D_0 + b)}$  and  $1 - F < 0.05$ .

Figure 5.3 shows the scaled infidelity  $(1 - F)|\beta|^2$  for sufficiently large  $|\beta|$  (here we used  $\beta = 40$ ), as a function of the short-axis angle  $\theta/2$ . We used parameters  $4(D_0 + b) = 1, 2, 4,$  and  $8$ , while  $n_{\text{th}} = 0$  (solid lines) and  $1/2$  (dashed lines). As expected, we see no dependence on  $\theta/2$  when  $4(D_0 + b) = 1 + 2n_{\text{th}}$ , since in this case the long-axis and short-axis variances coincide,  $D_0 + b = D_0 - b$ . When  $4(D_0 + b) > 1 + 2n_{\text{th}}$ , the local minima of the infidelity are reached at  $\theta/2 = 0$  and  $\theta/2 = \pi/2$ ; both these cases correspond to  $K = 0$  in Eq. (5.42) [note that  $K = 0$  minimizes the state center shift in Eq. (5.48), which affects

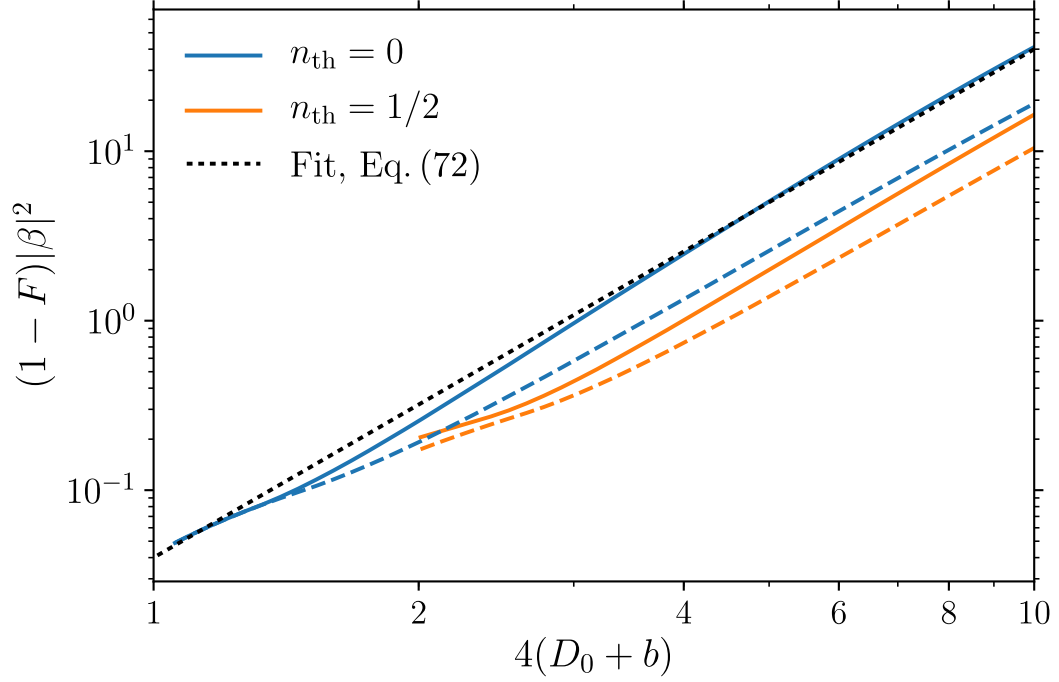


Figure 5.4: Solid lines: scaled infidelity  $(1 - F)|\beta|^2$  maximized over the angle  $\theta/2$  (for  $\beta = 40$ ), as a function of the quadrupled long-axis variance  $4(D_0 + b)$ . The upper (blue) solid line is for  $n_{\text{th}} = 0$ , the lower (orange) solid line is for  $n_{\text{th}} = 1/2$ . For the corresponding dashed lines we used the correction to the state center via Eq. (5.48). The black dotted line is a crude fit given by Eq. (5.72).

infidelity, as discussed below]. For relatively small values of  $4(D_0 + b)$ , the minimum is reached at  $\theta/2 = 0$  (“photon number squeezing”), while at larger  $4(D_0 + b)$ , the minimum infidelity is at  $\theta/2 = \pi/2$  (“phase squeezing”). The maximum infidelity is reached when  $\theta/2$  is (crudely) near  $\pm\pi/4$ . Note that the infidelity dependence on  $\theta/2$  has a period of  $\pi$ , and the dependence is symmetric about the points  $\theta/2 = 0$  and  $\theta/2 = \pi/2$ .

The upper (blue) solid line in Fig. 5.4 shows the scaled infidelity  $(1 - F)|\beta|^2$  maximized over the angle  $\theta/2$  (the worst case), as a function of the unsqueezing factor  $4(D_0 + b)$  (long-axis variance in units of the coherent state variance) for the case  $n_{\text{th}} = 0$

(zero effective temperature). We see that this line can be approximately fitted by the formula

$$1 - F \approx 0.04 \frac{[4(D_0 + b)]^3}{|\beta|^2}, \quad (5.72)$$

which is drawn as the dotted black line.

The infidelity scaling  $1 - F \propto (D_0 + b)^3$  can be crudely understood as a consequence of the Fock-space Gaussian state center shift described by Eq. (5.48). Considering for simplicity the case  $K = 0$  and  $W_1 = W_2 \ll 1$  (i.e.,  $n_{\text{th}} = 0$ ,  $\theta/2 = 0$  – see Figs. 5.2 and 5.3), we find that the state center is shifted by  $\Delta|\beta| \approx -(8W_2|\beta|)^{-1} \approx -(D_0 + b)/(2|\beta|)$  along the short axis. The relative shift compared with the “width” of the state along the short axis is then  $\Delta|\beta|/\sqrt{D_0 - b} \approx -[4(D_0 + b)]^{3/2}/(4|\beta|)$ . Since the infidelity scales quadratically with this relative shift,  $1 - F \propto (\Delta|\beta|/\sqrt{D_0 - b})^2$ , we obtain the scaling  $1 - F \propto [4(D_0 + b)]^3/|\beta|^2$ .

The same numerical scaling of the infidelity in Eq. (5.72) indicates that the state center shift may play a significant role in fidelity reduction. To check this hypothesis, we used the correction from Eq. (5.48) to produce Gaussian and Fock-space Gaussian states with the same  $\langle a \rangle$  by making a small compensating shift of  $\beta$ . The corresponding result for the infidelity  $1 - F$  is shown by the upper (blue) dashed line in Fig. 5.4. As we see, the correction has really decreased the infidelity; however, the improvement is only by a factor of about 2, so the scaling is approximately the same as in Eq. (5.72), with the factor 0.04 replaced by 0.02. We have also checked that numerical optimization of the infidelity over the center shift of the Fock-space Gaussian state [instead of using Eq. (5.48)] produces practically the same result. The infidelity decrease by a factor of about 2 can be crudely understood in the following way. The Fock-space Gaussian state has a slightly crescent

(non-elliptical) shape of the Wigner function in the phase plane. Slightly shifting its center, it is possible to improve the state fidelity compared with the Gaussian state (which has a perfect elliptical shape); however, this improvement cannot be very significant.

Now let us discuss the lower (orange) lines in Fig. 5.4, for which  $n_{\text{th}} = 1/2$  (i.e., effective temperature is  $T_{\text{eff}} = 0.91 \omega_r$ ); as above, the dashed line takes into account the center correction (5.48), while the solid line is without the correction. We see that non-zero  $n_{\text{th}}$  improves the fidelity compared with the case  $n_{\text{th}} = 0$  for the same long-axis variance  $D_0 + b$  (the short-axis variance in this case is increased by a factor of 4). The improvement can be qualitatively understood using the above derivation based on the state center shift: since the short-axis “width” is now larger, the relative inaccuracy is smaller, thus decreasing the infidelity. Note, however, that such derivation would predict infidelity reduction by a factor of 4, while numerically the distance between the upper and lower solid lines in Fig. 5.4 is less than a factor of 2.5. Comparing the solid and dashed orange lines, we see that the state center correction decreases the infidelity; however, the improvement is only by crudely a factor of 1.5, even less than in the zero-temperature case.

We can make the following conclusions from the numerical results discussed in this section. First, the infidelity of the conversion between the Gaussian and Fock-space Gaussian states is not larger than in Eq. (5.72), so the conversion becomes almost perfect for sufficiently large  $|\beta|$ . Second, correction (5.48) to the state center improves the fidelity; however, the improvement is not very significant (we will not use this correction in analyzing the evolution). Let us also note that the change of effective temperature from zero to  $0.9 \omega_r$  ( $n_{\text{th}} = 1/2$ ) did not produce a very significant change in the infidelity.

### 5.5.2 Accuracy of the hybrid phase-Fock-space evolution equations

The main result of this chapter is the hybrid phase-Fock-space evolution equations (5.63)–(5.66), which permit a very efficient approximate simulation of the state dynamics for a slightly nonlinear resonator in the large-photon-number regime. In contrast, full simulation using the master equation (5.6) is highly resource-consuming in this regime because of large Hilbert space. In this section we numerically analyze the accuracy of our hybrid equations by comparing the results with the full master equation simulation.

For the numerical analysis let us consider a constant drive,  $\varepsilon(t) = \varepsilon$ , and a constant (Kerr) nonlinearity,

$$\omega_r(n) = \omega_{r0} + n\eta, \quad (5.73)$$

which corresponds to the rotating-frame resonator energy levels  $E_{\text{rf}}(n) = (\omega_{r0} - \omega_d)n + n(n-1)\eta/2$ . We also assume that initial state is vacuum,  $\rho(0) = |0\rangle\langle 0|$ . Note that the hybrid evolution equations still work well when initial state is vacuum, because for sufficiently weak nonlinearity, the photon number becomes large before the effects due to nonlinearity (e.g., squeezing) become important. Also note that in RWA the considered resonator Hamiltonian is equivalent to  $H_r^{\text{lf}} = P^2/(2m) + (m/2)\tilde{\omega}_{r0}^2 X^2 + (\eta/3)m^2\tilde{\omega}_{r0}^2 X^4$ , where  $\tilde{\omega}_{r0} = \omega_{r0} - \eta$ . The difference between the first-excitation frequency  $\omega_{r0}$  and the “plasma frequency”  $\tilde{\omega}_{r0}$  for a Duffing oscillator is negligible because we focus on the regime of large  $n$ .

In the considered case, the RWA dynamics described by the master equation (5.6) depends on five parameters: nonlinearity  $\eta$ , drive amplitude  $\varepsilon$ , initial detuning  $\omega_{r0} - \omega_d$ , damping rate  $\kappa$ , and bath temperature  $T_b$  characterized by the bath photon number  $n_b$  via Eq. (5.7). Rescaling the time axis (using  $\kappa^{-1}$  as the time unit), it is easy to see that the

dynamics depends on four dimensionless parameters:  $\eta/\kappa$ ,  $\varepsilon/\kappa$ ,  $(\omega_{r0} - \omega_d)/\kappa$ , and  $n_b$ .

For simulation using the hybrid evolution equations (5.63)–(5.66), it is possible to further reduce the number of free parameters from four to only two (this is not possible for full master equation simulation). Since discreteness of  $n$  is not used in Eqs. (5.63)–(5.66), it is possible to rescale  $n$ -axis using  $\kappa/|\eta|$  as the unit of  $n$ ; this eliminates nonlinearity as a free parameter,  $d(\omega_r/\kappa)/d[n/(\kappa/|\eta|)] = \pm 1$  (the sign here is the sign of  $\eta$ ). This rescaling renormalizes the drive amplitude as  $(\varepsilon/\kappa)/\sqrt{\kappa/|\eta|}$ , while not affecting dimensionless detuning. Furthermore, it is possible to rescale  $W_1$  and  $W_2$  using  $1/\coth(\omega_{r0}/2T_b)$  and  $\coth(\omega_{r0}/2T_b)$  respectively; this eliminates bath temperature as a free parameter, such that it can always be assumed zero. Then the rescaled dynamics is determined by only two free parameters:  $\varepsilon\sqrt{|\eta|}/\kappa^{3/2}$  and  $(\omega_{r0} - \omega_d)/\kappa$ , and we can use Eqs. (5.63)–(5.66) with the following parameters:  $\kappa \rightarrow 1$ ,  $d\omega_r/dn \rightarrow \pm 1$  (depending on the sign of  $\eta$ ),  $\varepsilon \rightarrow \varepsilon\sqrt{|\eta|}/\kappa^{3/2}$ ,  $\omega_{r0} - \omega_d \rightarrow (\omega_{r0} - \omega_d)/\kappa$ , and  $T_b \rightarrow 0$ ; this automatically rescales  $\beta$  as  $\beta \rightarrow \beta/\sqrt{\kappa/|\eta|}$ , time as  $t \rightarrow \kappa t$ , variables  $W_1$  and  $W_2$  as  $W_1 \rightarrow W_1 \coth(\omega_{r0}/2T_b)$  and  $W_2 \rightarrow W_2/\coth(\omega_{r0}/2T_b)$ , while  $K$  does not change.

To check accuracy of the hybrid phase-Fock-space evolution equations, let us calculate the time-dependent fidelity  $F(t)$  [Eq. (5.71)] between the exact solution  $\rho_m(t)$  of the master equation (5.6) and the state  $\rho_h(t)$  obtained from our approximate hybrid equations (5.63)–(5.66). Note that in the hybrid method we evolve variables  $\beta$ ,  $W_1$ ,  $W_2$ , and  $K$ , but the resulting state is always converted into a Gaussian state using Eqs. (5.45)–(5.47), so the fidelity  $F(t)$  is calculated between this Gaussian state and Fock-space solution of the master equation [for that the Gaussian state is represented in the Fock space using Eq. (5.22)]. In

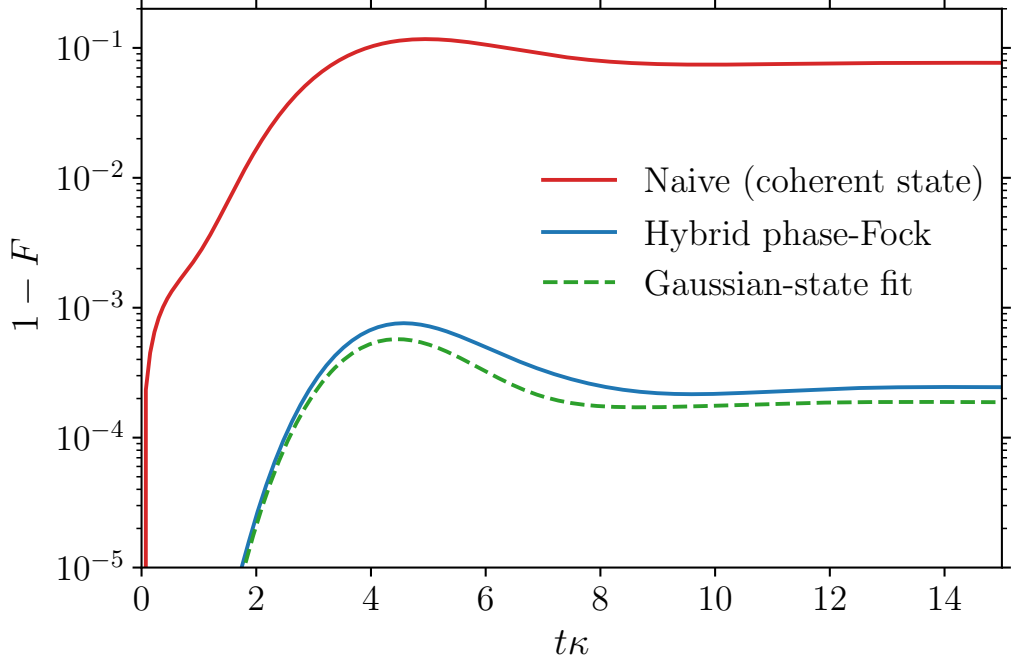


Figure 5.5: Blue (lower) solid line: time dependence of infidelity  $1 - F(t)$  between the exact solution  $\rho_m(t)$  obtained from the master equation (5.6) and state  $\rho_h(t)$  obtained from the hybrid evolution equations (5.63)–(5.66). Parameters are close to typical circuit QED parameters (see text), time  $t$  is normalized by the resonator decay time  $\kappa^{-1}$ . Dashed green line: infidelity between  $\rho_m(t)$  and its Gaussian-state fit. Red (upper) solid line: infidelity of the conventional approach based on coherent states.

simulations we will use parameters somewhat close to typical parameters in circuit QED experiments for measurement of superconducting transmon qubits; a weak nonlinearity of the resonator in this case is induced by the qubit nonlinearity; the resonator nonlinearity is much more significant when the transmon is in the ground state [79].

The lower (blue) solid line in Fig. 5.5 shows the time-dependent infidelity  $1 - F$  of the calculation based on the hybrid phase-Fock-space evolution equations (5.63)–(5.66). Here we used parameters  $\kappa/2\pi = 5$  MHz,  $\omega_{r0} - \omega_d = 0$ ,  $\eta/2\pi = -0.02$  MHz,  $\varepsilon/2\pi = 32$  MHz (this corresponds to 100 photons in the steady state), and  $n_b = 3.2 \times 10^{-3}$  (this corresponds

to  $T_b = 50$  mK for  $\omega_{r0}/2\pi = 6$  GHz; we start with the vacuum state instead of the thermal state, but the difference is negligible). We see a very good accuracy provided by our approach, with infidelity below  $10^{-3}$ . For comparison, the upper (red) solid line shows the infidelity for the conventional naive approach, in which we assume a coherent state of the resonator, with the same center  $\beta(t)$  given by Eq. (5.63). We see that the conventional approach fails to describe the evolution with a good accuracy, thus emphasizing importance of considering Gaussian states in our approach.

For the dashed green line in Fig. 5.5, at each time  $t$  we fitted  $\rho_m(t)$  by a Gaussian state having the same values of  $\langle a \rangle$ ,  $\langle a^2 \rangle$ , and  $\langle a^\dagger a \rangle$ , and then calculated fidelity between this Gaussian state and  $\rho_m(t)$ . Therefore, the dashed line essentially shows the non-Gaussianity of the actual state  $\rho_m(t)$  (we have checked that numerical optimization over the state center  $\beta$  does not provide a noticeable further improvement of the infidelity). Comparing the dashed green line with the blue solid line, we see that our hybrid evolution equations (5.63)–(5.66) describe the resonator state almost as good as this Gaussian-state fit. We have found numerically that almost all difference between the solid blue and dashed green lines in Fig. 5.5 comes from a small inaccuracy in calculation of the state center using Eq. (5.63) [see Fig. 5.6(b)]. We tried to improve this accuracy by using  $\bar{n}$  from Eq. (5.25) for the center evolution (5.63) and also by using the center correction (5.48). While this decreased infidelity for some parameters, it increased it for some other parameters, so we decided to use the simplest equation (5.63) for the state center evolution. As follows from Fig. 5.5, this already gives a very good accuracy.

To clarify the origin of the “bump” on the lower lines in Fig. 5.5, in Fig. 5.6(a) we

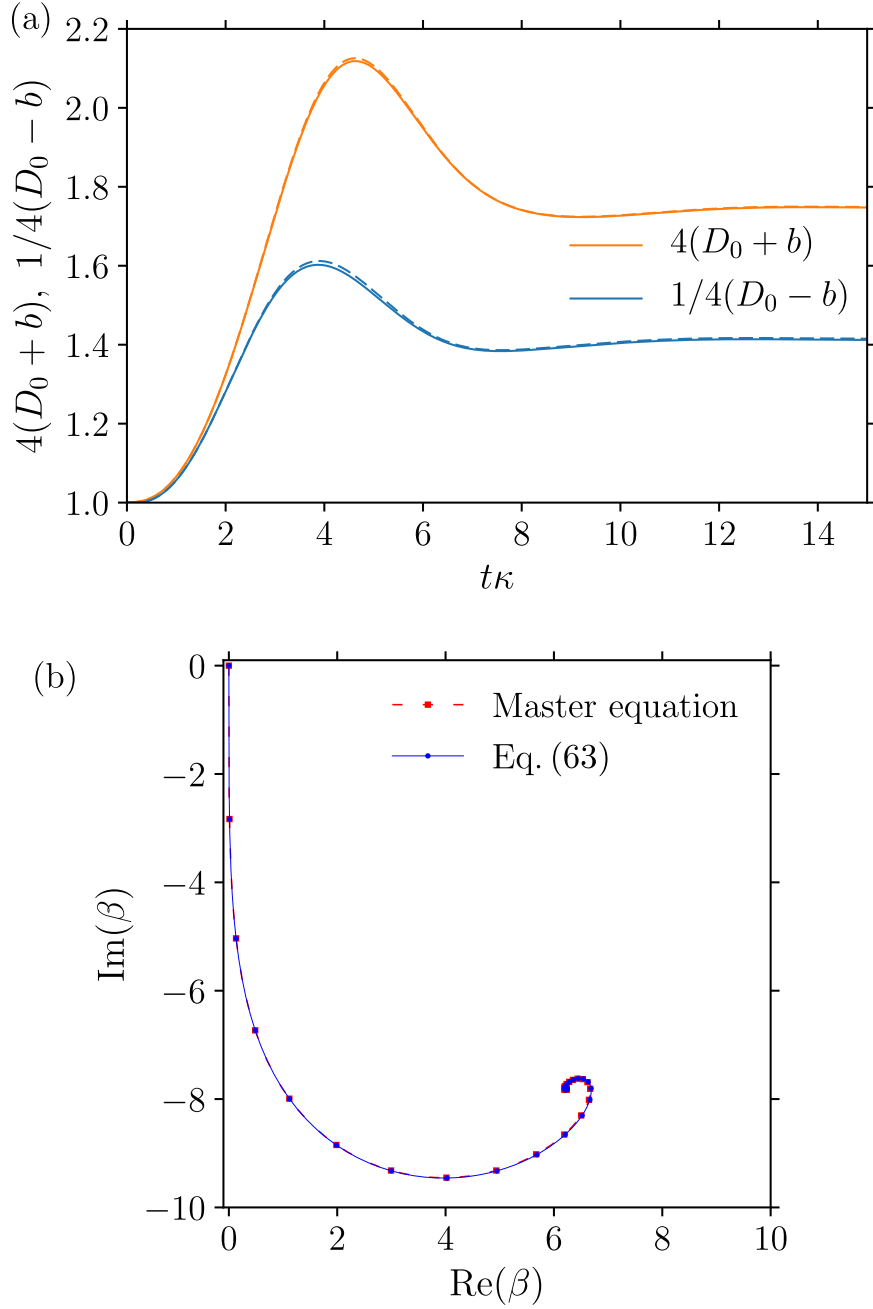


Figure 5.6: Panel (a): “Squeezing factor”  $[4(D_0 - b)]^{-1}$  (lower lines) and “unsqueezing factor”  $4(D_0 + b)$  (upper lines) as functions of time, for parameters of Fig. 5.5. Solid lines are obtained from the hybrid evolution equations (5.63)–(5.66), dashed lines are obtained from the Gaussian-state fit to the master-equation result  $\rho_m(t)$ . Panel (b): Corresponding evolution of the state center  $\beta(t)$  on the phase plane, with points spaced in time by  $0.5/\kappa$ . Solid blue line with dots is calculated using Eq. (5.63), almost coinciding red dashed line with squares show  $\langle a \rangle$  for  $\rho_m(t)$ .

show the corresponding evolution of “squeezing parameter”  $1/[4(D_0 - b)]$  (lower lines) and “unsqueezing parameter”  $4(D_0 + b)$  (upper lines). We see that the maximum infidelity in Fig. 5.5 occurs at approximately the same time as the maximum unsqueezing in Fig. 5.6(a), thus hinting that the infidelity during evolution originates from a mechanism similar to the infidelity between the Gaussian and Fock-space Gaussian states estimated by Eq. (5.72). The quantitative comparison shows that the maximum of the lower solid line in Fig. 5.5 is about a factor of 4 smaller than the estimate given by Eq. (5.72), while the steady-state infidelity is smaller than this estimate by a factor of 9.

The solid lines in Fig. 5.6(a) are calculated using the hybrid evolution equations (5.63)–(5.66), while dashed lines are obtained from the Gaussian-state fit of the master-equation result  $\rho_m(t)$ . We see that the dashed and solid lines are very close to each other, indicating that our hybrid approach is quite accurate in calculating the quadrature variances.

Note that for a minimum-uncertainty (pure) state, the lower and upper lines (squeezing and unsqueezing) in Fig. 5.6(a) should coincide; the ratio between these parameters is  $\coth^2(\omega_{r0}/2T_{\text{eff}})$  – see Eq. (5.50). From Fig. 5.6(a) we see that the resonator state is considerably mixed, with the effective temperature  $T_{\text{eff}}$  significantly exceeding [196] the bath temperature  $T_b$ ; for example, in the steady state  $T_{\text{eff}} = 98 \text{ mK}$ , in contrast to  $T_b = 50 \text{ mK}$ . A large corresponding ratio of thermal photon numbers,  $n_{\text{th}}/n_b = 17.3$ , indicates that the effective temperature  $T_{\text{eff}}$  in this case is practically independent of the bath temperature. Indeed, the same simulations with  $T_b = 0$  showed a very close effective temperature,  $T_{\text{eff}} = 96 \text{ mK}$ .

In Fig. 5.6(b) we show evolution of the state center  $\beta(t)$  on the phase plane for the same parameters as in Figs. 5.5 and 5.6(a). The dots (and squares) are separated by time intervals  $0.5/\kappa$  (which is 15.9 ns); the solid blue line with dots is for calculation using Eq. (5.63), while the dashed red line with squares shows  $\langle a \rangle$  for the master-equation simulation result  $\rho_m(t)$ . We see that Eq. (5.63) is quite accurate for calculating the state center. However, there is a tiny (almost unnoticeable) difference between positions of the dots and squares in Fig. 5.6(b); as mentioned above, this tiny shift is mainly responsible for the difference between the lower solid and dashed lines in Fig. 5.5. As another observation, the maximum photon number  $|\beta|^2$  is achieved at almost the same time as the maximum of  $4(D_0 + b)$ ; however, we think that the infidelity bump in Fig. 5.5 is caused by the maximum of  $4(D_0 + b)$  and not by the almost simultaneous maximum of  $|\beta|^2$ .

The main advantage of our method is a simple calculation of the resonator state deviation from a coherent state. For illustration, Fig. 5.7 shows the contour plot of the Wigner function  $W(\alpha)$  of the resonator state at time moment  $t = 15/\kappa$  (practically the steady state) for the same parameters as in Figs. 5.5 and 5.6. The solid black lines are calculated for our approximate hybrid-evolution state  $\rho_h$ , while the dashed red lines correspond to the exact state  $\rho_m$  (at this snapshot  $1 - F = 2.5 \times 10^{-4}$ ). We see that our approach gives a quite good approximation for the Wigner function; the difference is mainly because  $W(\alpha)$  contour plot for the actual state  $\rho_m$  has a slightly crescent shape, while in our Gaussian-state approximation the contours are strictly elliptical. We used Eq. (5.16) to calculate  $W(\alpha)$  for the Gaussian state  $\rho_h$ , while for  $\rho_m$  we used the formula [242, 243]

$$W(\alpha) = \frac{2}{\pi} \text{Tr} \left[ D(-\alpha) \rho D(\alpha) e^{i\pi a^\dagger a} \right], \quad (5.74)$$

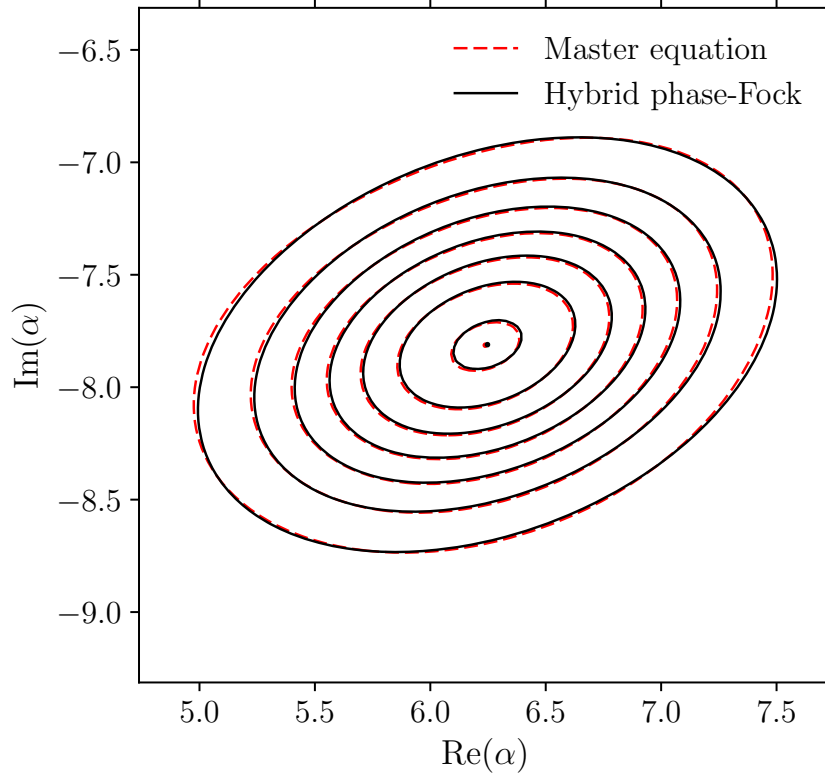


Figure 5.7: Contour plot for the Wigner function  $W(\alpha)$  of the resonator state. The black solid lines are calculated using the hybrid evolution equations (5.63)–(5.66), the red dashed lines are calculated using the master equation (5.6). The parameters are the same as in Figs. 5.5 and 5.6, the snapshot is taken at time  $t = 15/\kappa$ . The contours are drawn at the levels of  $1/4\pi, 2/4\pi, \dots, 7/4\pi$ . The centers are indicated by black and red dots.

in which the displacement operator  $D(\alpha)$  was applied numerically in the Fock space.

Now let us check numerically the expectation that our approach should become more accurate with more photons in the resonator. The solid lines in Fig. 5.8 show the time-dependent infidelity  $1 - F(t)$  for the calculations using Eqs. (5.63)–(5.66) (compared with the master equation results) for different number of photons. All solid lines correspond to the same normalized drive amplitude and detuning as in Figs. 5.5–5.7:  $\varepsilon\sqrt{|\eta|}/\kappa^{3/2} = 0.40$  and  $(\omega_{r0} - \omega_d)/\kappa = 0$ ; however, nonlinearity  $\eta$  varies: from top to bottom  $\eta/2\pi = -0.04$ ,

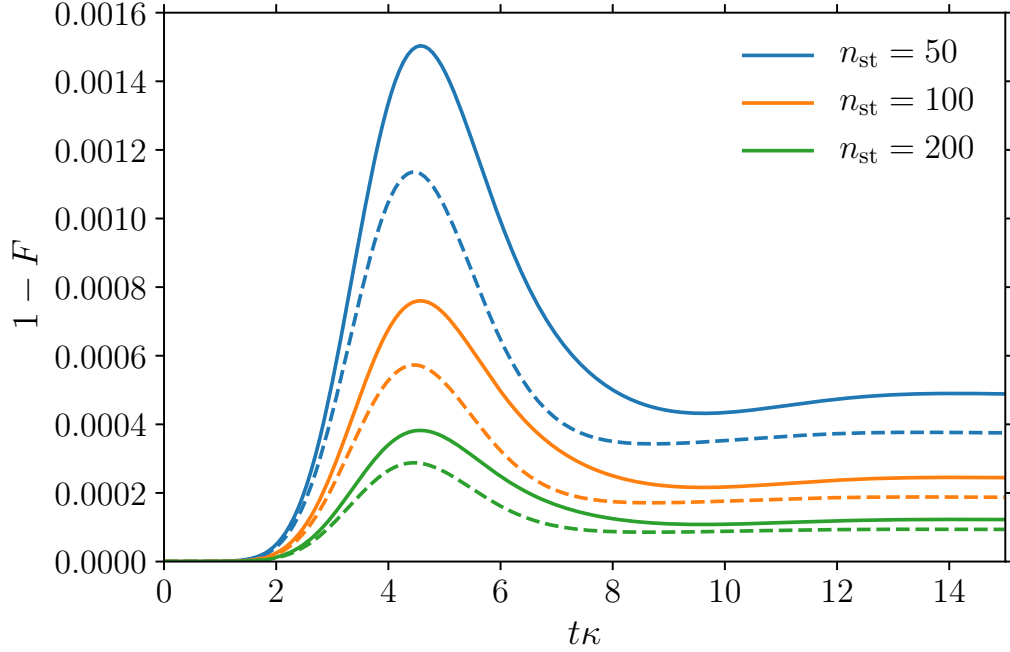


Figure 5.8: Solid lines: time dependence of infidelity  $1 - F(t)$  between the simulations based on the master equation and on our hybrid evolution equations, for the stationary-state photon numbers  $n_{\text{st}} \approx 50, 100,$  and  $200$  from top to bottom. The corresponding (color-matched, the same order) dashed lines show infidelity of the Gaussian-state fit to the master-equation simulations. The dimensionless parameters,  $\varepsilon\sqrt{|\eta|}/\kappa^{3/2} = 0.40$  and  $(\omega_{\text{r}0} - \omega_{\text{d}})/\kappa = 0$ , are the same as in Figs. 5.5–5.7, while  $\varepsilon$  and  $\eta$  change from line to line (see text).

–0.02, and –0.01 MHz; correspondingly, the drive amplitude  $\varepsilon$  also varies (with decay rate  $\kappa/2\pi = 5$  MHz kept constant):  $\varepsilon/2\pi = 32/\sqrt{2}, 32,$  and  $32\sqrt{2}$  MHz. This corresponds to the steady-state average photon number  $n_{\text{st}} \approx |\beta_{\text{st}}|^2$  approximately equal to 50, 100, and 200 from top to bottom (note that the scaled evolution is the same as in Fig. 5.6). As expected, the solid lines in Fig. 5.8 show that the infidelity becomes smaller with more photons in the resonator. The scaling is crudely  $1 - F \propto |\beta_{\text{st}}|^{-2}$ , as expected from Fig. 5.2 and Eq. (5.72).

In addition to better accuracy, for larger  $|\beta_{\text{st}}|$  our approach becomes much more preferable computationally in comparison with the master-equation calculations. As an

example, for our codes (which are rather simple, Mathematica-based) the calculation of the hybrid evolution  $\rho_h(t)$  for the solid lines in Fig. 5.8 took about 0.02 seconds, while obtaining the numerical master-equation solution  $\rho_m(t)$  took 0.2, 1, and 4 hours on a high-end desktop computer (longer time for larger  $|\beta_{\text{st}}|$ ). The master-equation simulation duration scales crudely quadratically with the size of the Fock space, while for our hybrid equations there is no scaling with the system size. For the lower solid line in Fig. 5.8, our method was faster by a factor exceeding  $10^5$ .

Dashed lines in Fig. 5.8 show infidelity of the Gaussian-state fit of  $\rho_m(t)$  for the same parameters. Comparing the solid and dashed lines, we see that most of the infidelity in our approach comes from *non-Gaussianity* of the actual state, thus making unimportant any possible improvements in the state center calculation by improving Eq. (5.63). We also see that the fraction of the infidelity coming from non-Gaussianity does not change significantly with changing number of photons.

Note that with zero initial detuning,  $\omega_d = \omega_{r0}$ , assumed in Figs. 5.5–5.8, we automatically avoid the bistability region [244, 245] for the steady state of a classical resonator with Kerr nonlinearity (5.73). Our method is generally not intended to work inside or close to this bistability region. In particular, quantum treatment formally removes the bistability [186] because of transitions due to quantum fluctuations (tunneling or quantum activation [201]), even though the rate of these transitions can be exponentially small. In contrast, our approach uses the classical equation (5.63) for the state center evolution, showing full bistability. The critical point [244, 245] (start of the bistability) occurs at  $|\tilde{\epsilon}| = 3^{-3/4} \approx 0.44$

and  $\Delta\tilde{\omega}_d = \sqrt{3}/2$  for the dimensionless parameters

$$\tilde{\varepsilon} \equiv \frac{\varepsilon\sqrt{|\eta|}}{\kappa^{3/2}}, \quad \Delta\tilde{\omega}_d \equiv -\text{sign}(\eta) \frac{\omega_{r0} - \omega_d}{\kappa}. \quad (5.75)$$

For larger  $|\tilde{\varepsilon}|$ , the bistability range for  $\Delta\tilde{\omega}_d$  becomes non-zero and grows. For a given  $\Delta\tilde{\omega}_d$  above  $\sqrt{3}/2$ , the bistability region for the dimensionless drive amplitude is  $|\tilde{\varepsilon}_-| \leq |\tilde{\varepsilon}| \leq |\tilde{\varepsilon}_+|$ , where  $|\tilde{\varepsilon}_\mp|^2 = \tilde{n}_\pm[\tilde{n}_\pm - \Delta\tilde{\omega}_d]^2 + \tilde{n}_\pm/4$  and  $\tilde{n}_\pm = [2\Delta\tilde{\omega}_d \pm \sqrt{\Delta\tilde{\omega}_d^2 - 3/4}]/3$  [186] (here  $\tilde{n}$  is related to the photon number  $n_{\text{st}} = |\beta_{\text{st}}|^2$  as  $\tilde{n} = n_{\text{st}}|\eta|/\kappa$ ). As mentioned above, we should avoid this bistability region when using our approach (5.63)–(5.66). We have checked numerically that in the vicinity of the critical point as well as near the bistability region, the unsqueezing parameter  $4(D_0 + b)$  may become large, indicating that our approach could become accurate only at very large number of photons.

The numerical results presented in this section show that our approach based on the hybrid evolution equations (5.63)–(5.66) typically provides a good accuracy, which is orders of magnitude better than using the conventional approximation based on the coherent-state assumption. On the other hand, our approach is orders of magnitude faster than the full simulation based on the master equation.

## 5.6 3 dB squeezing limit and its violation in transients

Squeezing of a resonator state due to Kerr nonlinearity (5.73) has been discussed long ago [168–171] (see also [79]). A somewhat similar squeezing of the vacuum state can be produced by a parametric drive at the doubled frequency [89, 200], and in this case the steady-state squeezing of the resonator state is always less than 3 dB, i.e.,  $[4(D_0 - b)]^{-1} \leq 2$  [89, 212, 213]. There were several proposals to exceed this limit in a nanomechanical sys-

tem, in particular based on reservoir engineering [216, 217], weak measurements [209, 218], injection of squeezed light [219], and short optical pulses [220]. The 3 dB limit for a mechanical oscillator was recently exceeded experimentally [221] by using reservoir engineering and backaction-evading measurement. Note that squeezing of a micro-mechanical resonator by more than 3 dB below the *thermal* noise was realized earlier [246].

Because of a similarity [195, 202] between squeezing produced by a doubled-frequency parametric driving and by the usual non-parametric driving of a nonlinear resonator, it is natural to expect a similar 3 dB limit for squeezing in the system considered in this chapter. However, we are not aware of papers, which discussed such a limit explicitly. In this section we prove that the hybrid phase-Fock-space evolution equations (5.63)–(5.66) indeed show the 3 dB limit for the steady-state squeezing. We also show that squeezing may exceed this limit during the evolution.

First, let us consider squeezing in the steady state. Substituting  $\dot{W}_1 = \dot{W}_2 = 0$  into Eqs. (5.64) and (5.65), we find that in the steady state

$$1 + 16K^2 = \frac{2W_1/\coth(\omega_{r0}/2T_b) - 1}{W_1W_2}. \quad (5.76)$$

Therefore, from Eq. (5.45) we obtain  $D_0 = W_1/[4W_2 \coth(\omega_{r0}/2T_b)]$ . Now using Eq. (5.46) for the parameter  $b$ , we obtain the scaled minimum quadrature variance  $4(D_0 - b) = W_1/[W_2 \coth(\omega_{r0}/2T_b)] - \sqrt{[W_1/W_2 \coth(\omega_{r0}/2T_b)]^2 - W_1/W_2}$ . Representing this result as

$$4(D_0 - b) = \frac{\coth(\omega_{r0}/2T_b)}{1 + \sqrt{1 - \coth^2(\omega_{r0}/2T_b) W_2/W_1}}, \quad (5.77)$$

we obtain  $[4(D_0 - b)]^{-1} < 2$  since  $\coth(\omega_{r0}/2T_b) \geq 1$  and  $W_2/W_1$  is positive. Thus, squeezing is less than 3 dB in the steady state.

Note that the 3 dB squeezing limit can be approached only when the bath temperature  $T_b$  is zero [so that  $\coth(\omega_{r0}/2T_b) = 1$ ] and when  $W_1/W_2 \rightarrow \infty$ . Correspondingly, effective temperature  $T_{\text{eff}}$  becomes infinitely large because  $n_{\text{th}} \rightarrow \infty$ , as follows from Eqs. (5.49) and (5.50). We also see that in this case the maximum quadrature variance becomes infinitely large,  $4(D_0 + b) \rightarrow \infty$ , which indicates instability (similar to the case of reaching the 3 dB limit for parametric doubled-frequency drive [89, 212]). Using Eqs. (5.63)–(5.66), we have checked numerically that 3 dB squeezing can be approached near the critical point and also near the switching point on the upper branch in the bistability region. As discussed above, our formalism is not actually intended to work in this parameter range. The hybrid equations do not have any mathematical problems in this range; however, there can be a problem with accuracy compared to the exact (master equation) evolution. In particular, when  $4(D_0 + b)$  becomes large near the critical point, the accuracy of the formalism requires a very large number of photons [see estimate (5.72)]. In addition, within the bistability region our formalism neglects switching between the quasistable states caused by fluctuations, so it can be reasonably accurate only when the switching rate is very small (that also requires a large number of photons). In spite of these issues, we can still formally use our equations, keeping in mind the potential problems.

Even simpler derivation of the 3 dB limit can be obtained using Eq. (5.70). This derivation follows very closely the underlying physical idea of the derivation [89, 213] for the case of a parametric drive. From Eq. (5.70) we find that in the steady state the unsqueezing and inverse squeezing factors are

$$4(D_0 \pm b) = \frac{\coth(\omega_{r0}/2T_b)}{1 \mp 2\eta_\beta |\beta|^2 \sin(\Delta\theta)/\kappa}. \quad (5.78)$$

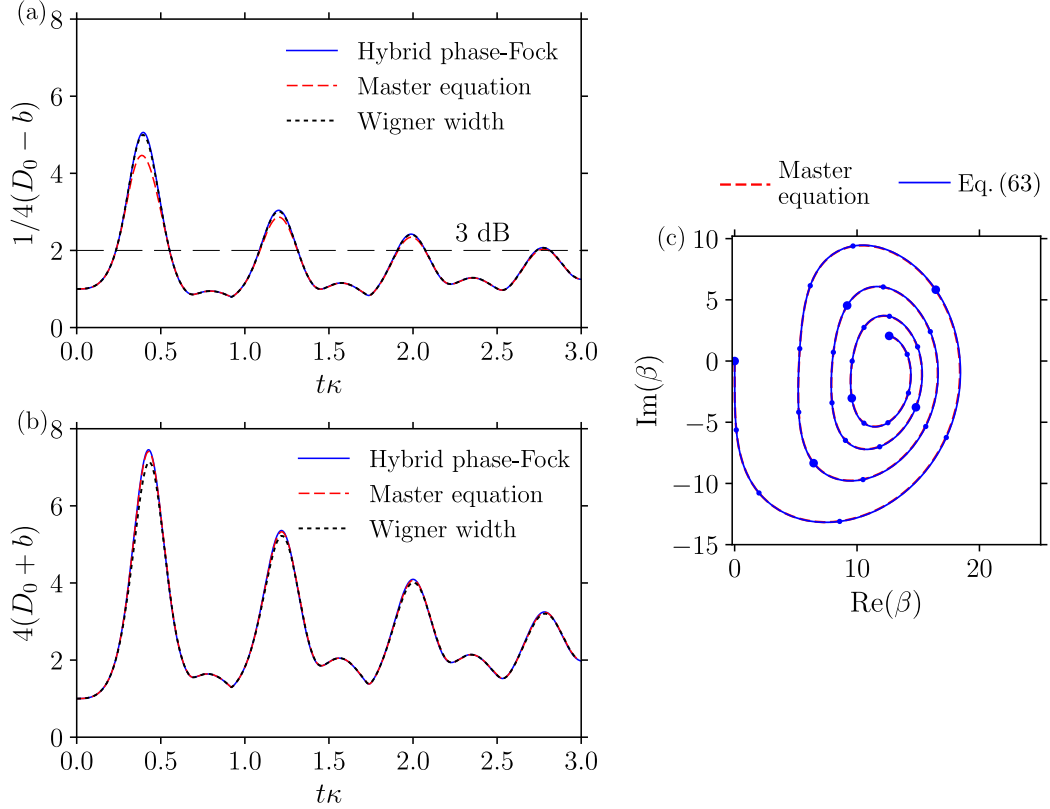


Figure 5.9: Panel (a): Squeezing factor  $[4(D_0 - b)]^{-1}$  as a function of time  $t$  for  $\omega_d/2\pi = \omega_{r0}/2\pi = 6$  GHz,  $\kappa/2\pi = 5$  MHz,  $\eta/2\pi = -0.15$  MHz,  $T_b = 0$ , and  $\varepsilon/2\pi = 290$  MHz (so that  $\varepsilon\sqrt{|\eta|}/\kappa^{3/2} = 10$ ). The solid blue line is calculated using the hybrid evolution equations, the dashed red line is obtained from the master equation simulation, and the dotted black line is the variance of the master-equation Wigner function along the short axis. Panel (b): Unsqueezing factor  $4(D_0 + b)$  for the same parameters (solid blue and dashed red lines). Dotted black line is the Wigner function variance along the long axis. Panel (c): the corresponding evolution of the state center  $\beta(t)$  on the phase plane. The dots are separated in time by  $0.1/\kappa$ , larger dots are separated by  $0.5/\kappa$ .

Since  $D_0 + b > 0$ , there is a limitation  $2\eta_\beta|\beta|^2 \sin(\Delta\theta) < \kappa$  (which is similar to the constraint of the parametric instability). Therefore, for  $4(D_0 - b)$  the denominator in Eq. (5.78) is less than 2 (and obviously positive), thus leading to the inequality  $4(D_0 - b) > (1/2) \coth(\omega_{r0}/2T_b) \geq 1/2$ .

Even though the steady-state squeezing is always below 3 dB, this limit can be

violated before reaching the steady state. For example, Ref. [246] experimentally achieves below 3 dB squeezing of *thermal* noise during the transient in a micro-mechanical oscillator. As an example in our system for squeezing below the *quantum* noise, the solid blue line in Fig. 5.9(a) shows the squeezing factor  $[4(D_0 - b)]^{-1}$  as a function of time for the dimensionless drive amplitude  $\tilde{\varepsilon} = \varepsilon\sqrt{|\eta|}/\kappa^{3/2} = 10$ , no initial detuning,  $\omega_d = \omega_{r0}$ , and zero temperature of the bath. We see that the 3 dB limit squeezing limit (horizontal line) is exceeded repeatedly, even though in the stationary state the squeezing is below 3 dB. The numerical result was obtained using Eqs. (5.63)–(5.66). To check it, we also performed the simulations using the master equation (5.6). The dashed red line in Fig. 5.9(a) shows the corresponding result for the same parameters and  $\eta/\kappa = -0.03$  (as discussed above, master equation requires more dimensionless parameters than the hybrid evolution equations); for example, this case can be realized with  $\omega_d/2\pi = \omega_{r0}/2\pi = 6$  GHz,  $\kappa/2\pi = 5$  MHz,  $\eta/2\pi = -0.15$  MHz,  $T_b = 0$ , and  $\varepsilon/2\pi \approx 290$  MHz (these parameters can in principle be realized with a circuit QED setup by increasing the effective resonator nonlinearity  $|\eta|$  using an increased qubit-resonator coupling). The maximum average number of photons in this case is approximately 350 (at  $\kappa t \approx 0.4$ ) – see Fig. 5.9(c). Comparing the solid blue and dashed red lines in Fig. 5.9(a), we see that the master equation gives a slightly smaller squeezing than the hybrid equations, but it still significantly exceeds the 3 dB value at the peaks. Note that the hybrid-equation calculation took about 0.02 seconds on a desktop computer, while the master-equation simulation took over 15 hours (the ratio of over  $10^6$ ).

A noticeable inaccuracy of the squeezing calculation in Fig. 5.9(a) using the hybrid equations is related to large values of the unsqueezing parameter  $4(D_0 + b)$  shown in Fig.

5.9(b). At the first peak ( $\kappa t \approx 0.4$ ) the infidelity estimate using Eq. (5.72) for  $|\beta|^2 \approx 350$  gives 0.05, so we would expect a noticeable inaccuracy. We checked that the inaccuracy decreases with decreasing nonlinearity  $|\eta|/\kappa$  while keeping  $\varepsilon\sqrt{|\eta|}/\kappa^{3/2}$  fixed; this increases the number of photons, which scales as  $\kappa/|\eta|$ . (Since further increase of the photon number is very difficult for the master-equation simulations, we actually checked that the inaccuracy in Fig. 5.9(a) increases with decreasing number of photons by increasing  $|\eta|/\kappa$ .) Note that the unsqueezing parameters calculated by the hybrid equations and by the master equation [solid blue and dashed red lines in Fig. 5.9(b)] practically coincide with each other.

Figure 5.9(c) shows the evolution of the state center  $\beta(t)$  on the phase plane, with dots separated in time by  $0.1/\kappa$  (larger dots are separated by  $0.5/\kappa$ ); the results from Eq. (5.63) and master equation practically coincide with each other. Comparing Fig. 5.9(c) with Figs. 5.9(a) and 5.9(b), we see that peaks in squeezing and unsqueezing approximately correspond to maxima of the photon number  $|\beta|^2$ . The minima of the photon number correspond to small bumps on the lines in Figs. 5.9(a) and 5.9(b).

We expect that the difference between the solid blue and dashed red lines for the squeezing factor in Fig. 5.9(a) can be mostly explained by a non-Gaussian shape of the actual states produced by the master equation. This non-Gaussianity can be seen as a slightly crescent shape of the Wigner function in the phase plane (see Fig. 5.7), with slightly curved “arms” along the long axis, instead of the perfect elliptical shape. However, the bending of the “arms” produces a smaller effect along the short axis. To check this hypothesis, we have calculated the Wigner function variance along the short axis by numerically fitting the master-equation Wigner function along the short axis (passing through the state center)

with a one-dimensional Gaussian model. The result is shown by the dotted black line in Fig. 5.9(a). It is almost indistinguishable from the blue solid line, thus confirming that squeezing calculated by our hybrid-evolution method is essentially the squeezing of the Wigner function along the short axis (which is slightly different from the usual “integrated” definition based on the quadrature variance, which is affected by bending of the “arms”). In contrast, the Wigner function variance along the long axis, shown by black dotted line in Fig. 5.9(b), noticeably differs from the quadrature variance shown by the solid blue (or dashed red) line. This is expected because the Wigner function along the long axis is significantly more affected by bending of the “arms”.

Figure 5.10 shows time-dependence of the squeezing factor  $[4(D_0 - b)]^{-1}$  for various parameters; these results are obtained using the hybrid equations (5.63)–(5.66). In Fig. 5.10(a) we assume zero initial detuning and zero bath temperature,  $\omega_d = \omega_{r0}$ ,  $T_b = 0$ , while varying the dimensionless drive amplitude,  $\tilde{\varepsilon} \equiv \varepsilon\sqrt{|\eta|}/\kappa^{3/2} = 5, 10, \text{ and } 15$ . In Fig. 5.10(b) we keep the amplitude fixed,  $\tilde{\varepsilon} = 10$ , and vary the detuning,  $\Delta\tilde{\omega}_d \equiv \text{sign}(\eta)(\omega_d - \omega_{r0})/\kappa = -3, 0, \text{ and } 3$  (the temperature is still zero). We see that a larger squeezing can be achieved with a larger amplitude of the drive and also with a detuning, which moves the operating point closer to the bistability region (for  $\tilde{\varepsilon} = 10$  the bistability region starts at  $\Delta\tilde{\omega}_d = 8.75$ ). Note that a larger squeezing also leads to a larger unsqueezing  $4(D_0 + b)$ ; for example, the maximum squeezing factor of 5.6 in Fig. 5.10(a) for  $\tilde{\varepsilon} = 15$  corresponds to  $4(D_0 + b) = 7.8$  (at this point  $|\beta|^2 = 13.9\kappa/\eta$ ). Similarly, the maximum squeezing factor of 7.6 in Fig. 5.10(b) for  $\Delta\tilde{\omega}_d = 3$  corresponds to  $4(D_0 + b) = 16.3$  (at this point  $|\beta|^2 = 14.1\kappa/\eta$ ). This means that to observe these large values of squeezing, we would need very many photons in

the resonator. From Eq. (5.72) and numerical results in Sec. 5.5.2, we expect that validity of our formalism requires

$$\bar{n} \approx |\beta|^2 \gg [4(D_0 + b)]^3. \quad (5.79)$$

Therefore, we estimate that for the upper (green) lines in Figs. 5.10(a) and 5.10(b) to be reasonably accurate, we need over 500 and 4,000 photons, respectively. Therefore, we cannot check results of Fig. 5.10 against the master equation. However, since the results of the hybrid equations and the master equation agree well with each other in the range where the master equation requires reasonable computational resources, we believe that our Eqs. (5.63)–(5.66) can still be reliably used for parameters when the master equation already cannot be used because of too large Hilbert space.

## 5.7 Summary

In this chapter we have introduced a new approximate method for numerical calculation of quantum evolution of a weakly nonlinear resonator due to drive and dissipation. This method is most accurate for large number of photons in the resonator (hundreds, thousands or more). This is exactly the regime where the conventional method based on the master equation becomes inapplicable because of too large Hilbert space. For a few hundred photons in the resonator (when the master equation can still be used), our method is faster by a factor of over  $10^5$ , while providing a very good accuracy.

The method is based on a hybrid description of a quantum state, which uses both phase-space and Fock-space parameters. The advantage is that evolution due to drive and dissipation can be naturally described in the phase space, while evolution due to

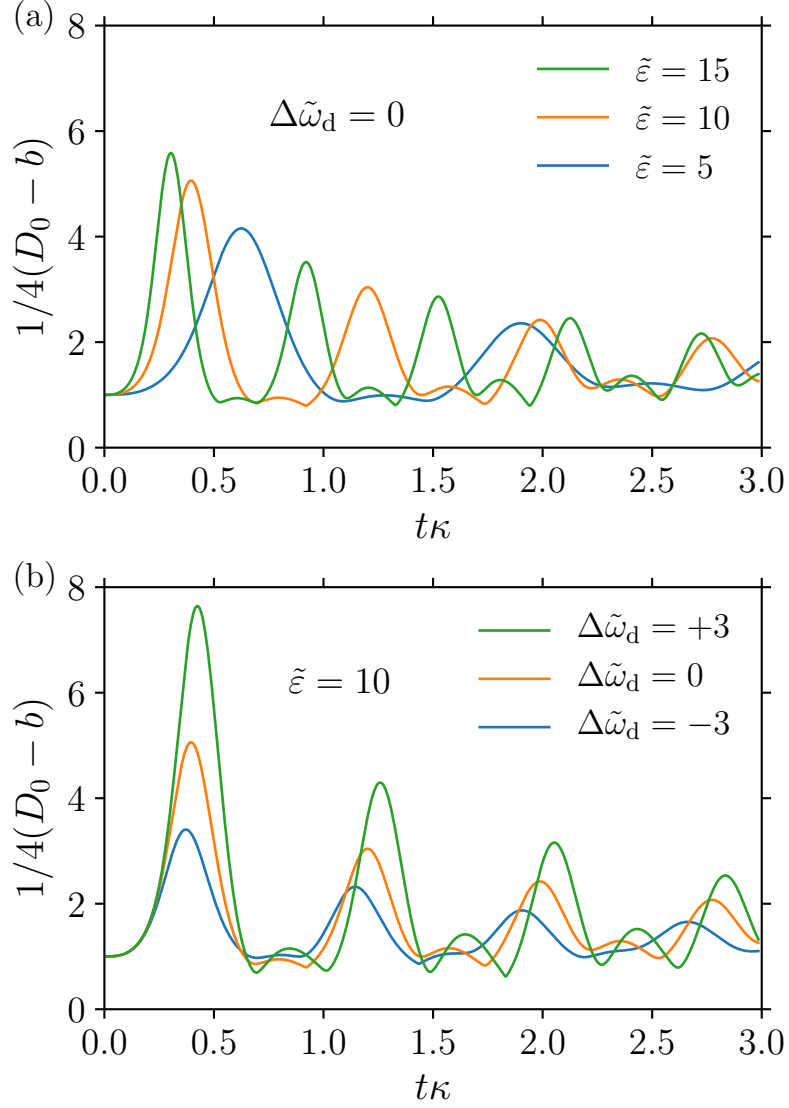


Figure 5.10: Time dependence of the squeezing factor  $[4(D_0 - b)]^{-1}$ , calculated using the hybrid evolution equations (5.63)–(5.66). The lines in panel (a) are for zero initial detuning,  $\omega_d = \omega_{r0}$ , zero bath temperature,  $T_b = 0$ , and dimensionless drive amplitudes  $\varepsilon\sqrt{|\eta|}/\kappa^{3/2} = 15, 10, \text{ and } 5$  (from top to bottom). The lines in panel (b) are for  $\varepsilon\sqrt{|\eta|}/\kappa^{3/2} = 10$ ,  $T_b = 0$ , and dimensionless initial detunings  $(\omega_d - \omega_{r0})/\kappa \text{ sign}(\eta) = 3, 0, \text{ and } -3$  (from top to bottom). All lines repeatedly exceed the 3 dB squeezing limit (factor of 2).

nonlinearity has a simple description in the Fock space. We combined both descriptions by proving that a phase-space Gaussian state with many photons has a simple approximate representation in the Fock space, Eq. (5.42), which is also Gaussian. Thus, our method essentially uses the Gaussian-state approximation for an evolving quantum state. It is not applicable for quantum dynamics involving cat-states, but is well-applicable for analyzing squeezing, unsqueezing, and effective heating of the resonator state due to weak nonlinearity.

The method describes the quantum evolution via solving four ordinary differential equations, Eqs. (5.63)–(5.66). One of them, Eq. (5.63), is decoupled from other equations and describes the evolution of the state center  $\beta(t)$  on the (complex) phase plane. This is the usual classical equation, which takes into account resonator nonlinearity. (This equation can be generalized by coupling it with other equations; however, in our numerical analysis we did not find a significant improvement of accuracy by doing this.) Other three equations, Eqs. (5.64)–(5.66), essentially describe evolution of the three quantum parameters of a Gaussian state (maximum and minimum quadrature variances  $D_0 \pm b$  and the short-axis angle  $\theta/2$  on the phase plane); however, this is done using the Fock-space parameters ( $W_1$ ,  $W_2$ , and  $K$ ). For conversion of the results into the phase-space description we use Eqs. (5.45)–(5.47). It is also possible to use Eqs. (5.67)–(5.69) to simulate evolution of the parameters  $D_0$ ,  $b$ , and  $\theta$  directly, though in this chapter we have not focused on this way of analysis. Physically, our approach is related to linearization of fluctuations around a classical trajectory [199]; however, formally it is based on a different framework.

Numerical accuracy of our method has been studied in Sec. 5.5. Somewhat surprisingly, it works well not only for a very large number of photons (as expected), but

may also provide a reasonable accuracy when there are only a few dozen photons in the resonator. It is important that the method accurately describes the evolution starting with vacuum (where it formally should not work); this is because during the evolution, effects of nonlinearity become important at larger number of photons where the method already works well.

The method becomes inaccurate when a quantum state cannot be reasonably represented as a Gaussian state. In our simulations this has been usually the case when the long-axis quadrature variance  $D_0 + b$  is large, while the number of photons  $|\beta|^2$  is not sufficiently large, so that the Wigner function of the state has a noticeable crescent shape in the phase plane. We have found numerically that Eq. (5.79) can be used for a crude estimate of the applicability range of the method; a weaker condition,  $|\beta|^2 > [4(D_0 + b)]^3$ , still provides a reasonably good accuracy. Because of a growing inaccuracy, the method is not intended to be used close to the critical point of the resonator bistability, where the long-axis quadrature variance  $D_0 + b$  becomes large. Similarly, the method is not intended to be used within the bistability region, since it neglects switchings between the quasistable states caused by fluctuations. Nevertheless, the equations of the method can be formally used in any regime, keeping in mind these reasons for potential inaccuracy of the results compared with full master-equation simulations. We have checked (Appendix H) that our analytical results for the steady state agree with the results of Refs. [186] and [196].

As an example, In Sec. 5.6 the equations of our method have been used to derive the 3 dB limit for the steady-state squeezing of a pumped and damped weakly nonlinear resonator. We have also shown numerically that squeezing during transients can significantly

exceed this 3 dB limit (Fig. 5.10). We emphasize that such an analysis is very difficult using the master equation because a large squeezing typically requires large number of photons in the resonator and therefore large Hilbert space. In contrast, our calculations take only a fraction of a second, independently of the photon number.

We hope that our method can be useful in various fields of research involving squeezing of weakly nonlinear resonators with large number of quantum excitations. In particular, it can be useful for circuit QED systems, in which a weak resonator nonlinearity is induced by interaction with a qubit. Note that our method describes squeezing of the resonator state, but it is not directly applicable to a transmitted/reflected microwave field outside of the resonator (such generalization is discussed in Chapter 6). Our method can also be useful in analysis of nanomechanical systems at low temperatures.

## Chapter 6

# Two-time correlators for propagating squeezed microwave in transients

In this chapter, we analyze two-time correlators as the most natural characteristic of a propagating quadrature-squeezed field in the transient regime. The considered system is a parametrically driven resonator with a time-dependent drive. Using a semiclassical approach derived from the input-output theory, we develop a technique for calculation of the two-time correlators, which are directly related to fluctuations of the measured integrated signal. While in the steady state the correlators are determined by three parameters (as for the phase-space ellipse describing a squeezed state), four parameters are necessary in the transient regime. The formalism can be generalized to weakly nonlinear resonators with additional coherent drive. We focus on squeezed microwave fields relevant to the

measurement of superconducting qubits; however, our formalism is also applicable to optical systems. The results can be readily verified experimentally.

## 6.1 Introduction

Squeezed microwave fields (SMFs) [211] have recently become the focus of extensive research efforts, related to superconducting quantum computing. This was enabled by a rapid progress in the development of practical superconducting parametric amplifiers [81, 82, 85, 247, 248], which have become versatile sources as well as detectors of SMFs. Applications of intracavity and propagating (itinerant) SMFs include qubit readout [161, 208], metrology [203, 249, 250], continuous-variable entanglement [83, 164], control of artificial-atom fluorescence [166], etc. Among other experimental achievements are demonstrations of the dynamic Casimir effect [251, 252], tomography of an itinerant SMF [84], and detection of SMF radiation pressure [253].

Besides generation in phase-sensitive parametric amplification, SMFs are also self-generated in the process of circuit QED measurement of superconducting qubits [79, 152] due to effective nonlinearity of the resonator induced by coupling with the qubit. Since squeezing affects the qubit measurement error, and for fast readout the steady-state regime is not reached, analysis of squeezing in transients is very important. The corresponding dynamics of the intracavity squeezing has been recently analyzed [80]; however, there is still no theory for transient squeezing of the propagating SMF, which determines the qubit measurement accuracy. Moreover, our extensive search for any papers discussing transient evolution for a resonator-produced propagating squeezed field resulted in only a few remotely

related references [254–257], which cannot serve as a starting point in developing a theory to answer this physically interesting and practically important question.

In this chapter, we analyze the *transient regime* of the propagating SMF, generated by a parametrically-driven linear resonator [188], as shown in Fig. 6.1(a). The case of a weakly nonlinear resonator with a coherent drive (as in the qubit measurement) is slightly more complicated but equivalent, as discussed in the supplemental material of Ref. [258]. As needed for practical applications, we focus on two-time correlators [259] for the quadrature (homodyne) measurement [89, 260], with quadrature angle  $\varphi$  changing in time. In particular, we find that in transients the dependence of the correlator on two angles  $\varphi_1$  and  $\varphi_2$  is characterized by four parameters, in contrast to only three parameters needed in a steady state, as for the ellipse in phase space, which is traditionally used to describe squeezing. Our results can be readily checked experimentally.

## 6.2 System and Hamiltonian

Let us consider a parametrically modulated resonator [Fig. 6.1(a)] described in the rotating-wave approximation by the Hamiltonian ( $\hbar = 1$ )

$$H = \Omega(t) a^\dagger a + \frac{i}{4} \left[ \varepsilon^*(t) a^2 - \varepsilon(t) a^{\dagger 2} \right], \quad (6.1)$$

where the resonator detuning  $\Omega(t) = \omega_r(t) - \omega_d$  and the parametric drive amplitude  $\varepsilon(t) = |\varepsilon(t)| e^{i\theta(t)}$  can depend on time (slowly in comparison with the rotating frame frequency  $\omega_d$ ). In the laboratory frame, this Hamiltonian corresponds to the resonator frequency modulation at the double-frequency,  $\omega_r - |\varepsilon| \sin(2\omega_d t - \theta)$ . The more general case of a

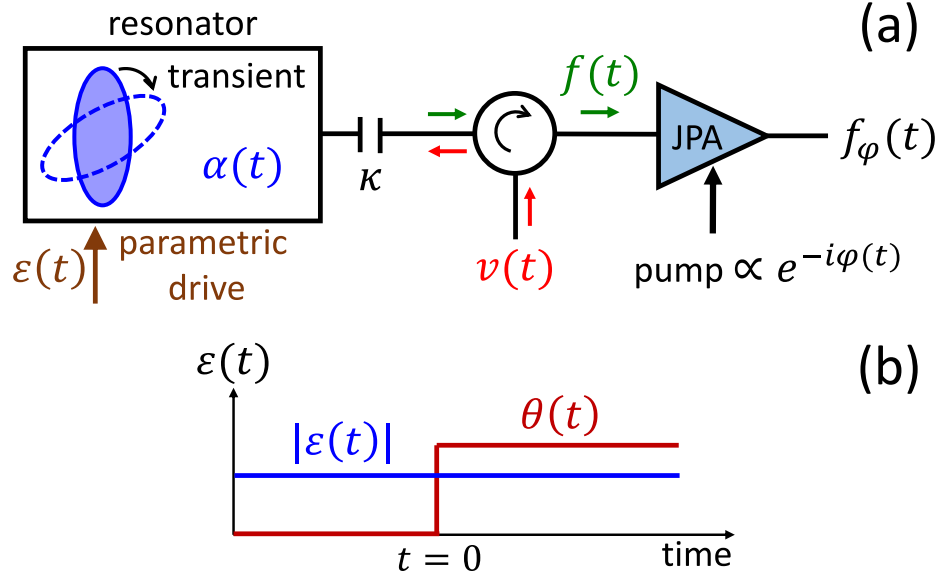


Figure 6.1: (a) Analyzed system. Propagating microwave field [described by operator  $F(t)$  or complex stochastic variable  $f(t)$ ] is squeezed due to parametric drive of the resonator with changing in time amplitude  $\varepsilon(t) = |\varepsilon(t)| e^{i\theta(t)}$ . The amplified quadrature phase  $\varphi(t)$  also changes in time, producing the noisy output signal  $f_\varphi(t)$ . The resonator damping rate is  $\kappa$ , and the incoming vacuum noise is described by  $v(t)$ . (b) An example of the parametric drive change, producing transient evolution of the resonator field [depicted in panel (a)] and of the propagating field.

nonlinear resonator and added coherent drive is discussed in the supplemental material of Ref. [258].

The propagating microwave field leaking from the resonator, described by operator  $F(t)$ , is amplified by a *phase-sensitive* amplifier, which amplifies the quadrature phase  $\varphi$ , so that the measured operator is  $F_\varphi(t) = [F(t) e^{-i\varphi} + F^\dagger(t) e^{i\varphi}]/2$ . In contrast to most previous works, we assume a time-dependent phase  $\varphi(t)$ . After the mixer [not shown in Fig. 6.1(a)], the  $\varphi$ -quadrature measurement produces a *classical* (normalized) fluctuating output signal  $f_\varphi(t)$ , which in a typical experiment is integrated with a weight function  $w(t)$  to produce the measurement result  $R = \int w(t) f_\varphi(t) dt$ . To analyze fluctuations of

$R$ , we need  $\langle R^2 \rangle = \iint w(t_1)w(t_2)\langle f_{\varphi_1}(t_1)f_{\varphi_2}(t_2) \rangle dt_1dt_2$ , where  $\varphi_k \equiv \varphi(t_k)$ . Therefore, in experiments it is important to know the correlator

$$K_{\varphi_1\varphi_2}(t_1, t_2) \equiv \langle f_{\varphi_1}(t_1) f_{\varphi_2}(t_2) \rangle, \quad (6.2)$$

which will be the main object analyzed in this chapter. Note that in our model,  $f_\varphi(t)$  is only noise (amplified and measured propagating squeezed vacuum), i.e.  $\langle f_\varphi(t) \rangle = 0$ ; it is simple to add a non-zero signal by adding a coherent drive [258] into Eq. (6.1), but this does not affect fluctuations because of linearity. For simplicity, we assume that the resonator energy decay rate  $\kappa$  is only due to coupling  $\kappa_{\text{out}}$  with the transmission line,  $\kappa = \kappa_{\text{out}}$  (generalization to the case  $\kappa > \kappa_{\text{out}}$  is trivial in the same-temperature case, see below).

In the simplest case of zero detuning ( $\Omega = 0$ ), zero temperature, and time-independent  $\varphi$  and  $\varepsilon$ , the propagating squeezed vacuum produces the steady-state correlator

$$\begin{aligned} K_{\varphi\varphi}(0, \tau) &= \frac{\delta(\tau)}{4} - \frac{\kappa|\varepsilon|}{4\kappa_+} e^{-\kappa_+|\tau|/2} \cos^2(\varphi - \theta/2) \\ &+ \frac{\kappa|\varepsilon|}{4\kappa_-} e^{-\kappa_-|\tau|/2} \sin^2(\varphi - \theta/2), \quad \kappa_\pm = \kappa \pm |\varepsilon|, \end{aligned} \quad (6.3)$$

as can be obtained via the conventional input-output formalism [88, 90], assuming  $|\varepsilon| < \kappa$ . Correspondingly, the integrated correlator for  $\varphi = \theta/2$  is  $\int_{-\infty}^{\infty} K_{\varphi\varphi}(0, \tau) d\tau = (1/4)(\kappa_-/\kappa_+)^2$ , so it is squeezed compared with the vacuum value of  $1/4$ , while for  $\varphi = (\theta + \pi)/2$  it is unsqueezed:  $\int_{-\infty}^{\infty} K_{\varphi\varphi}(0, \tau) d\tau = (1/4)(\kappa_+/\kappa_-)^2$ .

Note that dependence of the correlator  $K_{\varphi\varphi}(0, \tau)$  on  $\varphi$  is described by three real parameters. Also note that since in the steady state  $K_{\varphi\varphi}(0, \tau)$  depends only on the time difference  $\tau \equiv t_2 - t_1$ , it is natural to use the Fourier transform, so the squeezing is usually analyzed in terms of the squeezing spectrum [89, 200]  $S_\varphi(\omega) \equiv 4 \int_{-\infty}^{\infty} e^{-i\omega\tau} K_{\varphi\varphi}(0, \tau) d\tau$ .

However, during transients such a Fourier transform is not natural, so we will focus on the two-time correlator  $K_{\varphi_1\varphi_2}(t_1, t_2)$ .

### 6.3 Semiclassical model for measured fluctuations

Instead of using the conventional input-output formalism [88], we will use a simpler semiclassical stochastic model [261] to analyze the temporal correlations of the output signal  $f_\varphi(t)$ . As shown in [258], the correlators obtained using this model are *exact* for our linear system (6.1); the model is still a good approximation for a weakly nonlinear resonator.

In this semiclassical model, the fluctuation of the (quantum) propagating output field  $F(t)$  is treated as a complex-valued stochastic variable,

$$f(t) = -v(t) + \sqrt{\kappa} \alpha(t), \quad (6.4)$$

where the complex-valued stochastic variable  $\alpha(t)$  describes fluctuations of the intracavity field, while the incoming vacuum noise [Fig. 6.1(a)] is described by a complex-valued Gaussian noise  $v(t)$  with two-time correlators

$$\langle v(t) v^*(t') \rangle = (\bar{n}_b + 1/2) \delta(t - t'), \quad \langle v(t) v(t') \rangle = 0, \quad (6.5)$$

where  $\langle \dots \rangle$  denotes ensemble average and  $\bar{n}_b = [\exp(\omega_r/T) - 1]^{-1}$  is the average number of bath thermal photons. For brevity of formulas, we will assume the temperature  $T$  to be zero (so  $\bar{n}_b = 0$ ); however, for  $T \neq 0$  all correlators in this chapter can be simply multiplied by the factor  $1 + 2\bar{n}_b$ .

The intracavity field fluctuation  $\alpha(t)$  for a parametrically modulated resonator

(6.1) evolves as

$$\dot{\alpha}(t) = -\left(\frac{\kappa}{2} + i\Omega\right)\alpha(t) - \frac{\varepsilon(t)}{2}\alpha^*(t) + \sqrt{\kappa}v(t). \quad (6.6)$$

Note that in our normalization,  $|\alpha|^2$  corresponds to the number of photons in the resonator, while  $|f|^2$  corresponds to the propagating number of photons per second. The decay rate  $\kappa$  is frequency-independent, i.e., we use the Markovian approximation [259]. The term  $-\varepsilon\alpha^*/2$  describes effective increase of  $\kappa$  by  $|\varepsilon|$  for the quadrature phase  $\varphi = \theta/2$  and its decrease by  $|\varepsilon|$  for  $\varphi = (\theta + \pi)/2$ .

The output signal  $f_\varphi(t)$  from the quadrature measurement is given by the real-valued stochastic variable

$$f_\varphi(t) = \text{Re}[e^{-i\varphi(t)}f(t)], \quad (6.7)$$

so the correlator of interest (6.2) can be calculated as

$$K_{\varphi_1\varphi_2}(t_1, t_2) = \frac{1}{2} \text{Re} \left[ K_{ff}(t_1, t_2) e^{-i(\varphi_1+\varphi_2)} \right] + \frac{1}{2} \text{Re} \left[ K_{ff^*}(t_1, t_2) e^{-i(\varphi_1-\varphi_2)} \right], \quad (6.8)$$

$$K_{ff}(t_1, t_2) \equiv \langle f(t_1) f(t_2) \rangle, \quad (6.9)$$

$$K_{ff^*}(t_1, t_2) \equiv \langle f(t_1) f^*(t_2) \rangle. \quad (6.10)$$

We see that for given  $t_1$  and  $t_2$ , the dependence of  $K_{\varphi_1\varphi_2}(t_1, t_2)$  on  $\varphi_1$  and  $\varphi_2$  is described by *four real parameters* [e.g.,  $\text{Re}(K_{ff})$ ,  $\text{Im}(K_{ff})$ ,  $\text{Re}(K_{ff^*})$ , and  $\text{Im}(K_{ff^*})$ ]. As will be discussed later, in the steady state there are only three independent real parameters because  $K_{ff^*}$  in this case is real. Note that  $K_{ff}$  and  $K_{ff^*}$  obviously satisfy the symmetry relations [262],

$$K_{ff}(t, t') = K_{ff}(t', t), \quad K_{ff^*}(t, t') = [K_{ff^*}(t', t)]^*. \quad (6.11)$$

Now let us calculate the correlators  $K_{ff}(t_1, t_2)$  and  $K_{ff^*}(t_1, t_2)$  using the semi-classical model (6.4)–(6.6). Because of the symmetry, it is sufficient to assume  $t_2 > t_1$  (the  $\delta$ -function contribution to  $K_{ff^*}$  at  $t_1 = t_2$  is discussed below). Let us introduce the column vector containing both correlators,  $\mathbf{K}(t_1, t_2) = (K_{ff}(t_1, t_2), K_{ff^*}(t_1, t_2))^T$ . From Eq. (6.4) we obtain

$$\mathbf{K}(t_1, t_2) = \kappa \begin{bmatrix} \langle \alpha(t_2) \alpha(t_1) \rangle \\ \langle \alpha^*(t_2) \alpha(t_1) \rangle \end{bmatrix} - \sqrt{\kappa} \begin{bmatrix} \langle \alpha(t_2) v(t_1) \rangle \\ \langle \alpha^*(t_2) v(t_1) \rangle \end{bmatrix}, \quad (6.12)$$

since  $\langle v(t_2) \alpha(t_1) \rangle = \langle v^*(t_2) \alpha(t_1) \rangle = 0$  because of causality. Now using Eq. (6.6), we find the evolution of  $\mathbf{K}(t_1, t_2)$  as a function of  $t_2$ ,

$$\partial \mathbf{K}(t_1, t_2) / \partial t_2 = M(t_2) \mathbf{K}(t_1, t_2), \quad (6.13)$$

where the matrix  $M(t)$  describes the ensemble-averaged evolution of the vector  $(\alpha, \alpha^*)^T$  following from Eq. (6.6) without the noise term (contribution from the noise  $v$  averages to zero because of linearity),

$$M(t) = \begin{bmatrix} -\kappa/2 - i\Omega & -\varepsilon(t)/2 \\ -\varepsilon^*(t)/2 & -\kappa/2 + i\Omega \end{bmatrix}. \quad (6.14)$$

Note that  $M(t)$  is Hermitian only if  $\Omega = 0$ .

To find the initial condition for Eq. (6.13) at  $t_2 = t_1 + 0$ , we use Eq. (6.12) with  $\langle \alpha(t_1 + 0) v(t_1) \rangle = 0$  and  $\langle \alpha^*(t_1 + 0) v(t_1) \rangle = \sqrt{\kappa}/2$ , where the last equation follows from Eq. (6.6):  $\alpha^*(t_1 + dt) \approx \alpha^*(t_1) + \sqrt{\kappa} v^*(t_1) dt$ , while  $\langle |v(t_1)|^2 \rangle = 1/(2 dt)$  from Eq. (6.5). Therefore,

$$\mathbf{K}(t_1, t_1 + 0) = \kappa \begin{bmatrix} \langle \alpha^2(t_1) \rangle \\ \langle |\alpha^2(t_1)| \rangle - 1/2 \end{bmatrix}. \quad (6.15)$$

The solution of Eq. (6.13) with the initial condition (6.15) can be expressed via the Green's function  $2 \times 2$  matrix  $G(t|t_{\text{in}})$ , defined as

$$\partial G(t|t_{\text{in}})/\partial t = M(t) G(t|t_{\text{in}}), \quad G(t_{\text{in}}|t_{\text{in}}) = \mathbb{1}. \quad (6.16)$$

Thus, for  $\mathbf{K}$  (now expressed via  $K_{ff}$  and  $K_{ff^*}$ ) we obtain

$$\begin{bmatrix} K_{ff}(t_1, t_2) \\ K_{ff^*}(t_1, t_2) \end{bmatrix} = \kappa G(t_2|t_1) \begin{bmatrix} \langle \alpha^2(t_1) \rangle \\ \langle |\alpha^2(t_1)| \rangle - 1/2 \end{bmatrix}. \quad (6.17)$$

To complete the calculation of  $K_{ff}$  and  $K_{ff^*}$ , we need the second moments of the intracavity field fluctuations,  $\langle \alpha^2(t_1) \rangle$  and  $\langle |\alpha^2(t_1)| \rangle$ . Following the result of Ref. [80], they can be obtained as a solution of a system of four first-order differential equations.

Alternatively, they can be obtained from Eq. (6.6) as (see [199])

$$\begin{aligned} & \begin{bmatrix} \langle |\alpha^2(t_1)| \rangle & \langle \alpha^2(t_1) \rangle \\ \langle \alpha^{*2}(t_1) \rangle & \langle |\alpha^2(t_1)| \rangle \end{bmatrix} = \frac{\kappa}{2} \int_{t_0}^{t_1} G(t_1|t') G^\dagger(t_1|t') dt' \\ & + G(t_1|t_0) \begin{bmatrix} \langle |\alpha^2(t_0)| \rangle & \langle \alpha^2(t_0) \rangle \\ \langle \alpha^{*2}(t_0) \rangle & \langle |\alpha^2(t_0)| \rangle \end{bmatrix} G^\dagger(t_1|t_0), \end{aligned} \quad (6.18)$$

where  $\langle \alpha^2(t_0) \rangle = \text{Tr}[a^2 \rho(t_0)]$ ,  $\langle |\alpha^2(t_0)| \rangle = \text{Tr}[a^\dagger a \rho(t_0)] + 1/2$ , and  $\rho(t_0)$  is a given intracavity state at an initial time  $t_0$  (for  $t_0 \rightarrow -\infty$ , the initial state is irrelevant).

Equations (6.16)–(6.18) are the main result of this chapter. Using these equations with  $M(t)$  defined in Eq. (6.14), we can find the correlators  $K_{ff}$  and  $K_{ff^*}$ , which can then be used to obtain the main correlator of interest  $K_{\varphi_1 \varphi_2}(t_1, t_2)$  via Eq. (6.8). As mentioned above, in the case of a non-zero bath temperature, the correlators should be multiplied by  $1 + 2\bar{n}_b$ .

At  $t_2 = t_1$ , the correlator  $K_{ff^*}$  contains the singular contribution  $(\bar{n}_b + 1/2) \delta(t_2 - t_1)$ , as follows from Eqs. (6.4) and (6.5), while  $K_{ff}$  does not have a singularity. Since in this case  $\varphi_1 = \varphi_2$ , the correlator  $K_{\varphi_1\varphi_2}(t_1, t_2)$  has the singular contribution  $(1/4)(1 + 2\bar{n}_b) \delta(t_2 - t_1)$ . In a real experiment, at  $t_2 \approx t_1$  there is also a contribution from the additional noise of a not-quantum-limited amplifier.

In the derivation we assumed that energy decay in the resonator is only due to coupling with the outgoing transmission line, i.e.  $\kappa = \kappa_{\text{out}}$ . If this is not the case, the correlators  $K_{\varphi_1\varphi_2}$ ,  $K_{ff}$ , and  $K_{ff^*}$  for  $t_1 \neq t_2$  should be simply multiplied by the factor  $\kappa_{\text{out}}/\kappa$ . This can be shown by repeating the derivation with Eq. (6.4) replaced by  $f = -v + \sqrt{\kappa_{\text{out}}}\alpha$  and Eq. (6.6) replaced by  $\dot{\alpha} = -(\kappa/2 + i\Omega)\alpha - (\varepsilon/2)\alpha^* + \sqrt{\kappa_{\text{out}}}v + \sqrt{\kappa - \kappa_{\text{out}}}v_{\text{add}}$ , where the additional uncorrelated noise  $v_{\text{add}}(t)$  satisfies Eq. (6.5) with the same temperature. Alternatively, the multiplication of the correlators by  $\kappa_{\text{out}}/\kappa$  is rather obvious because the system is then equivalent to adding a beamsplitter with transmission amplitude  $\sqrt{\kappa_{\text{out}}/\kappa}$  to the outgoing transmission line (after the circulator) in Fig. 6.1(a). Note that the singularity of correlators at  $t_2 = t_1$  does not change when  $\kappa_{\text{out}} \neq \kappa$ , because of the additional noise.

Even though our results have been derived for the case of a linear parametrically-driven resonator (6.1), we emphasize that they remain practically the same if a weak non-linearity is added to the resonator, as well as a coherent drive (see [258]). In this case the evolution of fluctuations should be linearized in the vicinity of the classical evolution (this modifies the matrix  $M$ ) and we need to use the Gaussian approximation.

## 6.4 Steady-state regime

In the steady state we can assume that the parametric drive amplitude  $\varepsilon$  does not depend on time (as well as parameters  $\Omega$  and  $\kappa$ ). This is the case considered in the literature (e.g., [88, 89, 261]). Using our formalism (with  $\bar{n}_b = 0$ ), we can easily find the Green's function  $G(t|t_{\text{in}})$  by finding eigenvalues and eigenvectors of the matrix  $M$ . Then from Eqs. (6.17) and (6.18) we obtain

$$K_{ff}(0, \tau) = -\frac{\kappa\varepsilon}{4} \left[ \left(1 - \frac{2i\Omega}{\varepsilon}\right) \frac{e^{-\kappa_-|\tau|/2}}{\kappa_-} + \left(1 + \frac{2i\Omega}{\varepsilon}\right) \frac{e^{-\kappa_+|\tau|/2}}{\kappa_+} \right], \quad (6.19)$$

$$K_{ff^*}(0, \tau) = \frac{\delta(\tau)}{2} + \frac{\kappa|\varepsilon|^2}{4\varepsilon} \left( \frac{e^{-\kappa_-|\tau|/2}}{\kappa_-} - \frac{e^{-\kappa_+|\tau|/2}}{\kappa_+} \right), \quad (6.20)$$

where  $\kappa_{\pm} = \kappa \pm \varepsilon$  and  $\varepsilon = \sqrt{|\varepsilon|^2 - 4\Omega^2}$  if  $|\Omega| < |\varepsilon|/2$  (overdamped case) or  $\varepsilon = i\sqrt{4\Omega^2 - |\varepsilon|^2}$  if  $|\Omega| > |\varepsilon|/2$  (underdamped case). The condition of stability is obviously  $|\varepsilon|^2 < \kappa^2 + 4\Omega^2$ . The singular contribution  $\delta(\tau)/2$  added into Eq. (6.20) follows from Eqs. (6.4) and (6.5).

We see that in the steady state,  $K_{ff^*}(0, \tau)$  is always real. Therefore, the squeezing is determined by three real parameters (which depend on  $\tau$ ), in contrast to four parameters in the general (transient) case.

A convenient way of introducing the four real parameters ( $A$ ,  $B$ ,  $\phi$  and  $\psi$ ) is by rewriting Eq. (6.8) as

$$K_{\varphi_1\varphi_2}(t_1, t_2) = A \cos(\varphi_1 - \phi) \cos(\varphi_2 - \psi) + B \sin(\varphi_1 - \phi) \sin(\varphi_2 - \psi) + \delta(t_2 - t_1)/4, \quad (6.21)$$

where we explicitly added the singular term (note that  $\varphi_1 = \varphi_2$  when  $t_1 = t_2$ ) and the

parameters  $A$ ,  $B$ ,  $\phi$  and  $\psi$  (all depending on  $t_1$  and  $t_2$ ) can be obtained from equations  $(A - B) e^{i(\phi+\psi)} = K_{ff}(t_1, t_2)$  and  $(A + B) e^{i(\phi-\psi)} = K_{ff^*}(t_1, t_2) - \delta(t_2 - t_1)/2$ . As discussed above, in the steady state  $K_{ff^*}$  is real, and therefore  $\phi = \psi$ , thus again leaving only three independent real parameters.

Note that in the case when  $\varphi_1 = \varphi_2$ , the correlator  $K_{\varphi\varphi}(t_1, t_2)$  drawn in the phase space as a function of the polar angle  $\varphi$  is always an ellipse (even in the transient regime), as follows from Eq. (6.21). In the steady state, from the measured three parameters of this ellipse it is possible to find all parameters in Eq. (6.21) ( $A$ ,  $B$ , and  $\phi = \psi$ ), thus predicting the correlator for  $\varphi_1 \neq \varphi_2$  as well. However, in the general (transient) case this is impossible because of one extra parameter.

## 6.5 Example of transient evolution

To observe experimentally the discussed features of the squeezing in transients, the simplest case is to use no detuning ( $\Omega = 0$ ) and to change abruptly the parametric drive amplitude  $|\varepsilon(t)| e^{i\theta(t)}$  (with a reasonably long cycle to accumulate ensemble statistics). If only  $|\varepsilon(t)|$  is changing [254], then the dynamics is still not very interesting (squeezing is still characterized by only three parameters). Therefore, the natural choice is to keep  $|\varepsilon|$  constant, but to change abruptly the phase  $\theta(t)$ , as shown in Fig. 6.1(b). Let us assume that  $\theta(t) = 0$  for  $t < 0$  and  $\theta(t) = \tilde{\theta}$  for  $t > 0$ . Then solving Eqs. (6.16)–(6.18) we obtain

$$K_{ff}(t_1, t_1 + \tau) = \kappa[P_- + P_+] e^{i\tilde{\theta}}, \quad (6.22)$$

$$K_{ff^*}(t_1, t_1 + \tau) = \kappa[P_+ - P_-], \quad (6.23)$$

$$P_{\pm} = \left\{ \frac{\kappa|\varepsilon|}{4(\kappa^2 - |\varepsilon|^2)} [(1 - \cos \tilde{\theta}) e^{-\kappa_{\pm} t_1} + i \sin \tilde{\theta} e^{-\kappa t_1}] - \frac{|\varepsilon|}{4\kappa_{\pm}} \right\} e^{-\kappa_{\pm} \tau / 2}, \quad (6.24)$$

where  $\kappa_{\pm} = \kappa \pm |\varepsilon|$  and  $\tau > 0$ . Figure 6.2 shows the corresponding parameters  $A$ ,  $B$ ,  $\phi$  and  $\psi$  in Eq. (6.21) as functions of  $\tau$  for several values of  $t_1$ . As expected, we see that  $\phi \neq \psi$ , except in the steady state ( $t_1 \rightarrow \infty$ ).

Thus, in this example the steady-state squeezing is described by three parameters;  $A(\tau)$ ,  $B(\tau)$ , and  $\phi$  (not depending on  $\tau$ ), while the transient squeezing is described by four parameters:  $A$ ,  $B$ ,  $\phi$ , and  $\psi$ , which all depend on both  $\tau$  and  $t_1$ . The same conclusion of three versus four parameters remains true if the correlator  $K_{\varphi_1 \varphi_2}(t_1, t_1 + \tau)$  is integrated over  $\tau$  or if we apply the Fourier transform over  $\tau$  (as in the squeezing spectrum).

Note that to check our results experimentally, it is easier to use a phase-preserving amplifier instead of the assumed phase-sensitive amplifier with time-varying amplified quadrature. All our results remain the same for a phase-preserving amplifier, except the singular contribution to  $K_{ff^*}$  becomes twice as large (in a real experiment the singular contribution broadens because of the finite bandwidth of the amplifier).

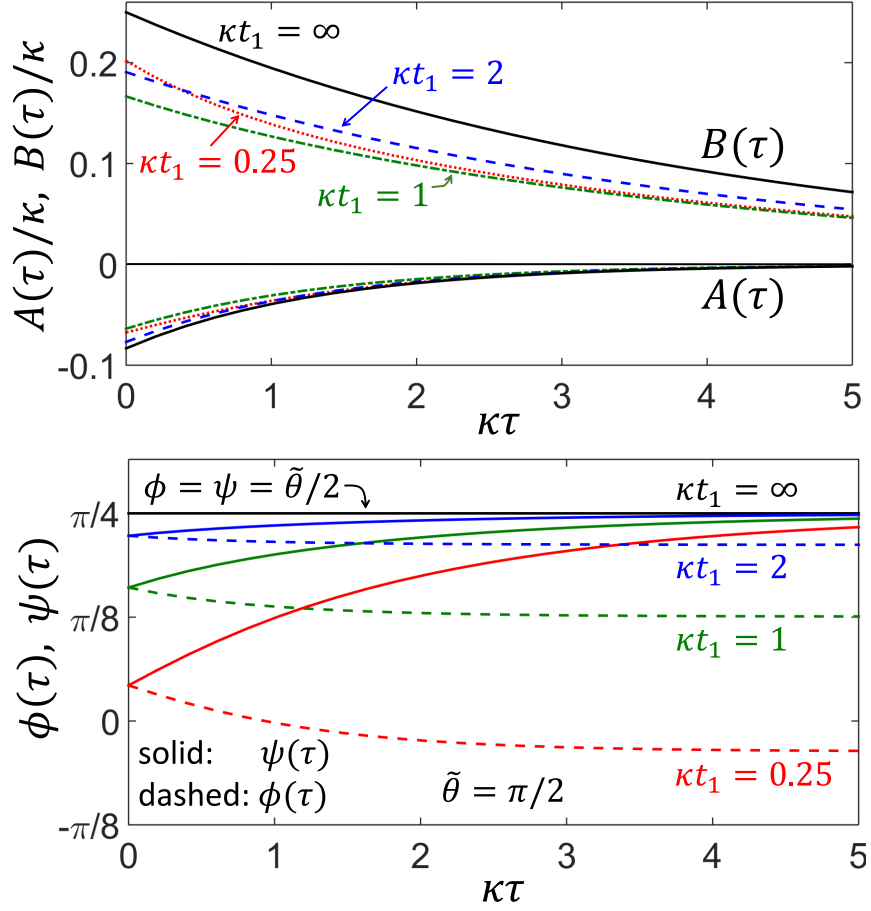


Figure 6.2: Parameters  $A$  and  $B$  (top panel) and  $\phi$  and  $\psi$  (bottom panel) as functions of  $\tau = t_2 - t_1$  for several values of time  $t_1$  passed after the abrupt change of the parametric drive shown in Fig. 6.1(b),  $\kappa t_1 = 0.25, 1, 2, \infty$ . In the steady state,  $\phi = \psi$ . We use  $\tilde{\theta} = \pi/2$ ,  $|\varepsilon|/\kappa = 0.5$ , and  $\Omega = 0$ .

## 6.6 Summary

In this chapter we have developed the theory for analyzing the squeezing of a propagating microwave field in the transient regime. The most natural way to characterize squeezing in this case is via the two-time correlators  $K_{\varphi_1\varphi_2}(t_1, t_2)$  of the detector output with different quadrature angles  $\varphi_1$  and  $\varphi_2$ , since in experiments these correlators are directly related to the fluctuations of the integrated signal. In our theory the correlators  $K_{\varphi_1\varphi_2}$

are expressed via the field fluctuation correlators  $K_{ff}$  and  $K_{ff^*}$ , for which the differential equations have been derived using the semiclassical model. Our theory is equally applicable to squeezing in optics, though it is more challenging to realize transients of optical squeezing experimentally.

## Chapter 7

# Conclusion

In this dissertation, we have investigated various aspects of the dispersive measurement of superconducting qubits, and have introduced models and tools that can be used to analyze these systems. The main message of this dissertation is that the driven qubit-resonator system, and in general more complicated joint systems in circuit QED setups, should be treated in the joint eigenbasis in contrast to the bare basis. In other words, the eigenbasis picture is the proper way of thinking and studying these systems. This way of thinking is evident throughout the chapters of this dissertation, and has contributed significantly to the theory and results.

In Chapter 2 we studied the dispersive measurement in the presence of neighboring qubits, as is common in circuit QED setups with arrays of qubits. We showed that for typical experimental parameters, the system is actually measured in the basis of joint eigenstates of the qubits, in contrast to what is expected from the textbook collapse postulate. However, the qubit excitation can jump between these eigenstates. By using a semiclassical model

for the fluctuating ac Stark shift, we derived an expression for the rate of these jumps, and confirmed it by numerically simulating the master equation for the system. These jumps contribute to the readout error in a manner similar to energy decay processes. We calculated analytical formulas for the minimum error that is achievable in the presence of such switching events, and found good agreement when comparing them with quantum trajectory simulations.

Chapter 3 studied the joint state of the qubit-resonator system during the measurement. In this chapter we showed that by pumping the readout resonator, a squeezed state forms by itself in the joint eigenbasis of the qubit-resonator system. We derived approximate equations to describe the qubit population leakage out of its initial state, and showed that within RWA the qubit mostly remains in its initial eigenladder, with negligible leakage to other eigenladders for typical experimental parameters. We also showed that the interaction with transmon induces nonlinearity in the resonator that squeezes its state, and introduced a numerically efficient hybrid approach that is capable of describing this self-developed squeezing of the readout resonator state during the ring-up process.

In Chapter 4 we developed analysis of the qubit-resonator system beyond the Jaynes-Cummings model, and identified built-in energy resonances that occur in the system when the photon number in the resonator increases. We found that the coupling between the resonant states is provided by the non-RWA terms that are usually neglected in the theory of the dispersive readout, and through these resonances the qubit can become excited out of the computational subspace. This theory of non-RWA level crossing was confirmed experimentally by the Google/USCB team, therefore describing the underlying mechanism

responsible for sudden deterioration of the measurement at large photon numbers. We also found that some energy resonances occur due to a broken symmetry in the transmon potential; this broken symmetry was experimentally observed and confirmed as well.

In Chapter 5 we introduced the hybrid phase-space-Fock-space approach to evolution of a driven and leaky nonlinear resonator. Study of such systems is important for the measurement of superconducting qubits, because as mentioned before, the qubit induces nonlinearity in the readout resonator that can squeeze the resonator state, therefore affecting the measurement fidelity. We separated the evolution into two parts: the evolution due to pump and energy decay which is naturally described in the phase space, and the evolution due to nonlinearity that can be easily described in the Fock space. By showing that Gaussian states in the phase space and Fock space are approximately equivalent, we combined the two parts of the evolution to write hybrid phase-space-Fock-space equations capable of describing the intracavity evolution of weakly nonlinear resonators. Our equations are very efficient for numerical analysis compared to master equation simulations, yet accurate within the Gaussian approximation.

In Chapter 6 we studied the evolution of the propagating output field of a parametrically driven resonator, which is practically equivalent to studying a coherently driven nonlinear resonator (as in the case of dispersive measurement of the qubit). We used a semiclassical model to derive evolution equations for two-time correlators of the propagating field, which are equivalent to the full quantum analysis for the parametrically driven linear resonator, and are valid within the Gaussian approximation for the nonlinear resonator case. These evolution equations are easy to simulate numerically, and can describe

the squeezing of the propagating field during the transients, which in turn can be used to optimize the fidelity and speed of the qubit measurement in dispersive readout schemes. We also showed that the transient squeezing is characterized by four parameters, in contrast to only three parameters needed in a steady state.

We hope that the results and tools presented in this dissertation will be useful in studying superconducting qubits and advancing our understanding of the dispersive readout in circuit QED systems.

## Appendix A

# Perturbative treatment of transmon states and circuit QED parameters

In this Appendix, by assuming an anharmonic oscillator model for the transmon and using perturbation theory, we calculate the energy spectrum of the transmon up to the second order in anharmonicity. For that, we need to go beyond quartic anharmonic approximation for the transmon potential. We also calculate the circuit QED (cQED) coupling energies between neighboring states up to the first order in anharmonicity, which is the first perturbative correction beyond the harmonic oscillator model. We finish by using the perturbative results to calculate the dispersive shift of the readout resonator in a cQED setup. Note that when the perturbative calculations of this appendix become inaccurate, we use the numerical methods discussed in [Appendix C](#).

## A.1 Hamiltonian

Transmon Hamiltonian can be written as [44]

$$H = 4E_C(\hat{n} - n_g)^2 - E_J \cos \hat{\varphi}, \quad (\text{A.1})$$

where  $\hat{n}$  is the number of Cooper pairs transferred through the Josephson junction,  $\hat{\varphi}$  is the superconducting phase across the junction,  $E_C = e^2/2C$  is the charging energy,  $n_g$  is the offset charge,  $E_J = I_c \frac{\Phi_0}{2\pi}$  is the Josephson energy,  $\Phi_0 = h/2e$  is the magnetic flux quantum, and  $[\hat{\varphi}, \hat{n}] = i$  (similar to  $\hat{x}$  and  $\hat{p}$ ). We now expand the cosine potential around  $\varphi = 0$  which corresponds to the bottom of the well. This expansion is allowed, since for the transmon we have  $E_J/E_C \gg 1$  (typically between 50 and 100), and therefore  $\varphi$  is near zero. Expanding up to  $\varphi^6$  gives

$$\begin{aligned} H &= 4E_C(\hat{n} - n_g)^2 - E_J \left( 1 - \frac{\hat{\varphi}^2}{2} + \frac{\hat{\varphi}^4}{24} - \frac{\hat{\varphi}^6}{720} \right) \\ &= -E_J + 4E_C(\hat{n} - n_g)^2 + \frac{E_J}{2}\hat{\varphi}^2 - \frac{E_J}{24}\hat{\varphi}^4 + \frac{E_J}{720}\hat{\varphi}^6. \end{aligned} \quad (\text{A.2})$$

The first term is a constant offset in energy, and we omit it in the rest of this appendix. By neglecting  $n_g$  (assuming  $n_g = 0$ ) and recognizing the canonical relation between  $\hat{n}$  and  $\hat{\varphi}$ , we can write

$$\hat{\varphi} = \left( \frac{8E_C}{E_J} \right)^{\frac{1}{4}} \frac{b + b^\dagger}{\sqrt{2}}, \quad (\text{A.3})$$

$$\hat{n} = \left( \frac{8E_C}{E_J} \right)^{-\frac{1}{4}} \frac{b - b^\dagger}{\sqrt{2}i}, \quad (\text{A.4})$$

where  $b$  and  $b^\dagger$  are lowering and raising operators in the space of eigenstates of quantum *harmonic* oscillator  $|i\rangle$  with usual properties

$$[b, b^\dagger] = 1, \quad (\text{A.5})$$

$$b|i\rangle = \sqrt{i} |i-1\rangle, \quad (\text{A.6})$$

$$b^\dagger|i\rangle = \sqrt{i+1} |i+1\rangle. \quad (\text{A.7})$$

Rewriting the Hamiltonian in terms of these lowering and raising operators yields

( $\hbar = 1$ )

$$\frac{H}{\omega_p} = \underbrace{b^\dagger b + \frac{1}{2}}_{H_0/\omega_p} - \lambda \overbrace{\left( \frac{b + b^\dagger}{\sqrt{2}} \right)^4 + \frac{4\lambda^2}{5} \left( \frac{b + b^\dagger}{\sqrt{2}} \right)^6}_{V/\omega_p}, \quad (\text{A.8})$$

where  $H_0$  is the unperturbed Hamiltonian of the harmonic oscillator, and  $V$  is the perturbation (anharmonic) part. The “plasma frequency”  $\omega_p$  and the perturbation parameter  $\lambda$  are

$$\omega_p = \sqrt{8E_J E_C}, \quad (\text{A.9})$$

$$\lambda = \frac{E_C}{3\omega_p} = \frac{1}{3} \sqrt{\frac{E_C}{8E_J}}. \quad (\text{A.10})$$

The “number of levels” in the cosine potential well can be defined as

$$N \equiv \frac{2E_J}{\omega_p} = \frac{1}{12\lambda}. \quad (\text{A.11})$$

## A.2 Perturbative Energies

Having  $\lambda \ll 1$ , which is true for typical transmon designs, we use the second order perturbation theory and keep terms of up to second order in  $\lambda$  to approximately find the

eigenstates of the Hamiltonian. From perturbation theory we know that for the  $n^{\text{th}}$  energy level  $E_n$  we have

$$E_n = E_n^{(0)} + \langle n|V|n\rangle + \sum_{j \neq n} \frac{|\langle j|V|n\rangle|^2}{E_n^{(0)} - E_j^{(0)}}, \quad (\text{A.12})$$

where  $E_n^{(0)} = \langle n|H_0|n\rangle = \omega_p(n + 1/2)$  is the zeroth-order energy level ( $n = 0, 1, \dots$ ) of the harmonic oscillator. Note that we use  $n$  for both the level number and the operator  $\hat{n}$  of number of Cooper pairs.

Having  $V$  in terms of lowering and raising operators and knowing its effect on the states  $|n\rangle$ , we can calculate the relevant matrix elements in Eq. (A.12). Keeping the terms up to *second* order in  $\lambda$ , the matrix elements of perturbation  $V$  are

$$\begin{aligned} \frac{1}{\omega_p} \langle n|V|n\rangle = & -\frac{\lambda}{4}(6n^2 + 6n + 3) \\ & + \frac{\lambda^2}{10}(20n^3 + 30n^2 + 40n + 15), \end{aligned} \quad (\text{A.13})$$

where we have used  $\varphi^4$  and  $\varphi^6$  terms in  $V$ , and

$$\begin{aligned} \frac{|\frac{1}{\omega_p} \langle j|V|n\rangle|^2}{E_n^{(0)} - E_j^{(0)}} = & \frac{\lambda^2}{16\omega_p(n-j)} \left| \sqrt{n(n-1)(n-2)(n-3)} \delta_{j,n-4} \right. \\ & + \sqrt{(n+1)(n+2)(n+3)(n+4)} \delta_{j,n+4} \\ & + 2(n+j+1) \sqrt{n(n-1)} \delta_{j,n-2} \\ & \left. + 2(n+j+1) \sqrt{(n+1)(n+2)} \delta_{j,n+2} \right|^2, \end{aligned} \quad (\text{A.14})$$

where we have only used the  $\varphi^4$  term in  $V$  to keep the terms up to second order in  $\lambda$ . Using these matrix elements in Eq. (A.12) and rearranging the answer in increasing orders of  $\lambda$  yields

$$\frac{E_n}{\omega_p} = n + \frac{1}{2} - \frac{\lambda}{4}(6n^2 + 6n + 3) - \frac{9\lambda^2}{8}(2n^3 + 3n^2 + 3n + 1). \quad (\text{A.15})$$

Level	Analytics	Numerics
0	1.125	1.125
1	10.125	10.125
2	39.375	39.37±0.01
3	102.375	102.37±0.01

Table A.1: Comparison of the analytical coefficients of the second order correction to the energy, with numerical results for exact eigenstates using Mathieu functions. The numerics column is calculated by finding the coefficient of  $\lambda^2$  when  $\lambda \rightarrow 0$  in exact eigenenergies.

Below, we have calculated  $E_n$  for the first four transmon energy levels

$$E_0 = \omega_p \left( \frac{1}{2} - \frac{3}{4}\lambda - \frac{9}{8}\lambda^2 \right), \quad (\text{A.16})$$

$$E_1 = \omega_p \left( \frac{3}{2} - \frac{15}{4}\lambda - \frac{81}{8}\lambda^2 \right), \quad (\text{A.17})$$

$$E_2 = \omega_p \left( \frac{5}{2} - \frac{39}{4}\lambda - \frac{315}{8}\lambda^2 \right), \quad (\text{A.18})$$

$$E_3 = \omega_p \left( \frac{7}{2} - \frac{75}{4}\lambda - \frac{819}{8}\lambda^2 \right). \quad (\text{A.19})$$

We have also compared the coefficient of the second-order correction (the  $\lambda^2$  terms) with the numerical coefficient derived by looking at the exact eigenenergies of the transmon using Mathieu functions (see Appendix C), and the analytical coefficients derived here match the numerical ones very well. The result of this comparison is presented in Table A.1.

Note that the term  $E_J\varphi^6/720$  in Eq. (A.2) is important for these results, and it produces the term  $\lambda^2(20n^3 + 30n^2 + 40n + 15)/10$  in Eq. (A.13). Without this term (i.e. in quartic approximation) the second order correction to the energy levels in Eq. (A.16)–(A.19) would have been incorrect.

Let us introduce the qubit frequency as ( $\omega_{kl} \equiv E_k - E_l$ )

$$\omega_q \equiv \omega_{10} = \omega_p (1 - 3\lambda - 9\lambda^2), \quad (\text{A.20})$$

and the frequency of the third and fourth level with respect to the ground state

$$\omega_{20} = \omega_p \left( 2 - 9\lambda - \frac{306}{8}\lambda^2 \right), \quad (\text{A.21})$$

$$\omega_{30} = \omega_p \left( 3 - 18\lambda - \frac{810}{8}\lambda^2 \right). \quad (\text{A.22})$$

Now let us define the anharmonicity as  $\eta \equiv \omega_{10} - \omega_{21}$ , which yields

$$\eta = 2\omega_q - \omega_{20} = \omega_p \left( 3\lambda + \frac{162}{8}\lambda^2 \right). \quad (\text{A.23})$$

We can then write the transmon energies (counting from  $E_0$ ) up to second order in  $\eta/\omega_q$

$$E_n - E_0 = \omega_q \left[ n - \frac{n(n-1)}{2} \frac{\eta}{\omega_q} - \frac{n(n-1)(n-2)}{4} \left( \frac{\eta}{\omega_q} \right)^2 \right], \quad (\text{A.24})$$

and similarly transmon frequencies

$$\omega_{n+1,n} = \omega_q \left[ 1 - n \frac{\eta}{\omega_q} - \frac{3n(n-1)}{4} \left( \frac{\eta}{\omega_q} \right)^2 \right]. \quad (\text{A.25})$$

### A.3 Perturbative Couplings

In typical cQED schemes for transmon readout where a detuned resonator is coupled to the qubit, the effective Hamiltonian of the system is [44, 78]

$$H = 4E_C(\hat{n} - n_g)^2 - E_J \cos \hat{\varphi} + \omega_r a^\dagger a + E_{\text{cpl}} \hat{n}(a + a^\dagger). \quad (\text{A.26})$$

Here,  $\omega_r$  is the readout resonator frequency,  $a$  and  $a^\dagger$  annihilate and create one photon in the resonator, and  $E_{\text{cpl}}$  is a constant depending on circuit parameters [see Eq. (3.1) in Ref. [44]]. Note that  $\hat{n} \neq a^\dagger a$  in Eq. (A.26); here  $\hat{n}$  is the number of Cooper pairs, not the number of photons.

If we rewrite this Hamiltonian in the basis of exact transmon eigenstates  $|\psi_n\rangle$  (i.e., Mathieu functions), then we obtain

$$H = \sum_n E_n |\psi_n\rangle \langle \psi_n| + \omega_r a^\dagger a + \sum_{n,m} g_{n,m} |\psi_n\rangle \langle \psi_m| (a + a^\dagger), \quad (\text{A.27})$$

where  $E_n$  is the energy of the  $n^{\text{th}}$  transmon state [derived perturbatively in Eq. (A.15)] and coupling energies are

$$g_{n,m} = E_{\text{cpl}} \langle \psi_n | \hat{n} | \psi_m \rangle. \quad (\text{A.28})$$

Expressing  $\hat{n}$  in terms of  $b$  and  $b^\dagger$  [see Eq. (A.4)] and neglecting  $n_g$ , we can rewrite the coupling energy as

$$g_{n,m} = \frac{E_{\text{cpl}}}{\sqrt{2}i} \sqrt[4]{\frac{E_J}{8E_C}} \langle \psi_n | (b - b^\dagger) | \psi_m \rangle. \quad (\text{A.29})$$

Note that  $g_{m,n} = g_{n,m}^*$  since anti-Hermitian  $b - b^\dagger$  is compensated by the imaginary unit.

We now calculate the coupling energies by examining the matrix elements of  $\langle \psi_n | (b - b^\dagger) | \psi_m \rangle$  in a first order perturbative approach. Recalling the transmon Hamiltonian in Eq. (A.8), we write the perturbative eigenstates of the transmon as follows

$$|\psi_n\rangle = |\psi_n^{(0)}\rangle + \sum_{j \neq n} \frac{\langle \psi_j^{(0)} | V | \psi_n^{(0)} \rangle}{E_n^{(0)} - E_j^{(0)}} |\psi_j^{(0)}\rangle, \quad (\text{A.30})$$

where  $|\psi_n^{(0)}\rangle = |n\rangle$  and  $E_n^{(0)} = \omega_p(n + 1/2)$  are zeroth order (harmonic oscillator) eigenstates and eigenenergies respectively. Using only the quartic anharmonic term  $\varphi^4$  in perturbation

$V$  [see Eq. (A.8)], up to *first* order in  $\lambda$  we get

$$\begin{aligned}
|\psi_n\rangle = & |n\rangle - \frac{\lambda}{4} \left[ \frac{\sqrt{n(n-1)(n-2)(n-3)}}{4} |n-4\rangle \right. \\
& - \frac{\sqrt{(n+1)(n+2)(n+3)(n+4)}}{4} |n+4\rangle \\
& + (2n-1)\sqrt{n(n-1)} |n-2\rangle \\
& \left. - (2n+3)\sqrt{(n+1)(n+2)} |n+2\rangle \right]. \tag{A.31}
\end{aligned}$$

Finally, after some algebra we find

$$\begin{aligned}
g_{n,m} = & \frac{E_{\text{cpl}}}{\sqrt{2}i} \sqrt[4]{\frac{E_J}{8E_C}} \left\{ \left[ \sqrt{n+1} - \frac{3\lambda}{2}(n+1)^{\frac{3}{2}} \right] \delta_{n,m-1} - \left[ \sqrt{n} - \frac{3\lambda}{2}n^{\frac{3}{2}} \right] \delta_{n,m+1} \right. \\
& - \frac{3\lambda}{4} \left( \sqrt{(n+1)(n+2)(n+3)} \delta_{n,m-3} \right. \\
& \left. \left. - \sqrt{n(n-1)(n-2)} \delta_{n,m+3} \right) \right\}, \tag{A.32}
\end{aligned}$$

where we have only kept the terms of up to first order in  $\lambda$ . Note that because of the selection rule (symmetry of the cosine potential), the charge matrix elements between transmon states that are separated by even numbers (e.g.,  $g_{n,n+2}$ ) are exactly zero. Also note that the  $\delta_{n,m\pm 5}$  terms are zero in the first order approximation and will only appear in the second order in  $\lambda$ .

Below we have calculated the nearest neighbor couplings  $g_{i,i+1}$  for first three neighbors

$$g_{0,1} = \frac{E_{\text{cpl}}}{\sqrt{2}i} \sqrt[4]{\frac{E_J}{8E_C}} \left( 1 - \frac{3}{2}\lambda \right), \tag{A.33}$$

$$g_{1,2} = \frac{E_{\text{cpl}}}{\sqrt{2}i} \sqrt[4]{\frac{E_J}{8E_C}} \left( \sqrt{2} - 3\sqrt{2}\lambda \right), \tag{A.34}$$

$$g_{2,3} = \frac{E_{\text{cpl}}}{\sqrt{2}i} \sqrt[4]{\frac{E_J}{8E_C}} \left( \sqrt{3} - \frac{9\sqrt{3}}{2}\lambda \right). \tag{A.35}$$

We can also rewrite these couplings in terms of  $g \equiv g_{0,1}$ , only keeping terms in *first* order of  $\eta/\omega_q$

$$g_{1,2} = g\sqrt{2}\left(1 - \frac{3}{2}\lambda\right) = g\sqrt{2}\left(1 - \frac{1}{2}\frac{\eta}{\omega_q}\right), \quad (\text{A.36})$$

$$g_{2,3} = g\sqrt{3}\left(1 - 3\lambda\right) = g\sqrt{3}\left(1 - \frac{\eta}{\omega_q}\right). \quad (\text{A.37})$$

More generally, for  $k \geq 0$  we have

$$g_{k,k+1} = g\sqrt{k+1}\left(1 - \frac{k}{2}\frac{\eta}{\omega_q}\right). \quad (\text{A.38})$$

The lowest non-nearest neighbor couplings are

$$g_{0,3} = -g\frac{3\sqrt{6}}{4}\lambda = -g\frac{\sqrt{6}}{4}\frac{\eta}{\omega_q}, \quad (\text{A.39})$$

$$g_{1,4} = -g\frac{3\sqrt{6}}{2}\lambda = -g\frac{\sqrt{6}}{2}\frac{\eta}{\omega_q}, \quad (\text{A.40})$$

$$g_{2,5} = -g\frac{3\sqrt{15}}{2}\lambda = -g\frac{\sqrt{15}}{2}\frac{\eta}{\omega_q}. \quad (\text{A.41})$$

More generally, for  $k \geq 0$  we have

$$g_{k,k+3} = -g\frac{\eta}{4\omega_q}\sqrt{(k+1)(k+2)(k+3)}. \quad (\text{A.42})$$

As mentioned above, only the couplings  $g_{k,k+1}$  and  $g_{k,k+3}$  are linear in  $\lambda$ . Other couplings of the form  $g_{k,k+2l+1}$  are of the higher orders in  $\lambda$ , while  $g_{k,k+2l} = 0$  because of the symmetry of the cosine potential. Note that in our results  $g_{n,m} = g_{m,n}^*$ , but  $g$  is imaginary. This is because of the asymmetric form of the interaction  $[(b - b^\dagger)/i](a + a^\dagger)$  assumed in Eq. (A.26) and (A.27) [it would be more natural to use  $(a - a^\dagger)/i$  for the resonator]. However, usually it is OK to assume that  $g$  is real, while keeping the interaction form (A.27).

## A.4 Perturbative derivation of dispersive shift

As an application of the perturbative results discussed above, we derive the dispersive shift of a coupled and detuned readout resonator, used in circuit QED measurement setup [78]. With the ket notation  $|\text{qubit, resonator}\rangle$ , and within the rotating wave approximation (RWA) that only keeps the excitation-preserving coupling terms, we can rewrite the Hamiltonian in Eq. (A.27) as

$$H = \sum_{k,n} (E_k + n\omega_r) |k, n\rangle\langle k, n| + \left( \sum_{k,n} g_{k,k+1} \sqrt{n} |k+1, n-1\rangle\langle k, n| + \text{H.c.} \right), \quad (\text{A.43})$$

where the first term is the bare energy of the qubit-resonator system, and the next terms are the RWA interactions. Note the different notation compared to the previous sections: here  $n$  is used for the resonator state and  $k$  for the transmon state (previously  $n$  was used for the transmon state). The Hamiltonian of Eq. (A.43) is illustrated in the Jaynes-Cummings ladder of energies in Fig. A.1.

Let us use notations  $\omega_r^{(0)}$  and  $\omega_r^{(1)}$  for the resonator frequency when the qubit is in the ground state and excited state respectively<sup>1</sup>. Since dispersive measurement schemes typically operate in the regime where  $|g| \ll |\Delta|$  ( $\Delta = \omega_r - \omega_q$  is the detuning between the resonator and the qubit), we use a second-order perturbation in  $g/\Delta$  to find the eigenenergies of the system. For simplicity we assume real  $g$ . Note that any pair of energy levels that are detuned by  $\tilde{\Delta}$  and coupled by  $\tilde{g}$  are each repelled by  $\tilde{g}^2/\tilde{\Delta}$  in the second order of  $\tilde{g}/\tilde{\Delta} \ll 1$ . By calculating level repulsions between all the pairs of energy levels, we can find

<sup>1</sup>These resonator frequencies are defined for the case when there are no photons in the resonator.

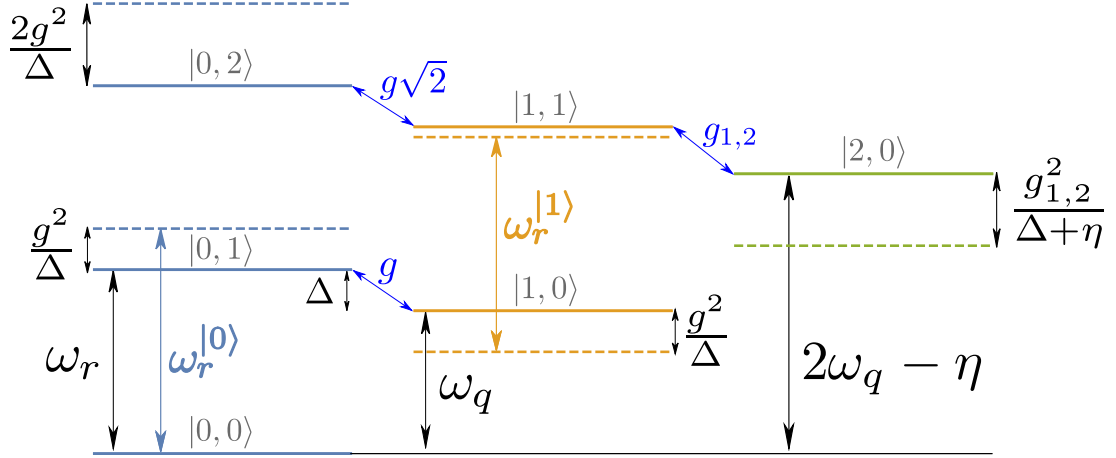


Figure A.1: Bottom levels in the Jaynes-Cummings ladder of the qubit and the readout resonator states. Solid horizontal lines show bare energy levels  $E_k + n\omega_r$  of the system, marked with the corresponding states  $|k, n\rangle$  with ket notation of  $|\text{qubit}, \text{resonator}\rangle$ , and dashed horizontal lines indicate repelled (perturbative) eigenenergies  $E_{\overline{|k, n\rangle}}$ . Each color-coded ladder corresponds to a different qubit state. Blue slanted arrows show excitation-preserving RWA couplings. Vertical arrows show energy differences in the system. Resonator frequencies when the qubit is in the ground state ( $\omega_r^{(0)}$ ) and when it is in the excited state ( $\omega_r^{(1)}$ ) are color coded and bold. Here  $\Delta = \omega_r - \omega_q$  is the detuning between the resonator and the qubit.

the resonator eigenfrequencies (see Fig. A.1)

$$\omega_r^{(0)} = E_{\overline{|0,1\rangle}} - E_{\overline{|0,0\rangle}} \approx \omega_r + \frac{g^2}{\Delta}, \quad (\text{A.44})$$

$$\omega_r^{(1)} = E_{\overline{|1,1\rangle}} - E_{\overline{|1,0\rangle}} \approx \omega_r - \frac{g^2}{\Delta} + \frac{g_{1,2}^2}{\Delta + \eta}, \quad (\text{A.45})$$

$$\Delta = \omega_r - \omega_q, \quad \eta = \omega_{10} - \omega_{21}, \quad (\text{A.46})$$

where  $g_{1,2} = g\sqrt{2}[1 - \eta/(2\omega_q)]$  is the perturbative transmon charge matrix element that was derived in Section A.3. Here  $E_{\overline{|k, n\rangle}}$  is the energy of the eigenstate  $\overline{|k, n\rangle}$  corresponding to bare state  $|k, n\rangle$ .

We can now calculate the total dispersive shift as

$$2\chi \equiv \omega_r^{(0)} - \omega_r^{(1)} \approx \frac{2g^2}{\Delta} - \frac{g_{1,2}^2}{\Delta + \eta} \approx 2 \frac{g^2}{\Delta} \frac{\eta}{\Delta + \eta} \frac{\omega_r}{\omega_q}. \quad (\text{A.47})$$

Note that the factor  $\omega_r/\omega_q$  comes from the first order perturbative correction to  $g_{1,2}$  [see Eq. (A.36)]. This correction is important for practical use in the lab, where typically  $2\chi$  is measured directly, and is used to extract the unknown coupling  $g$  using

$$g \approx \sqrt{2\chi \frac{\Delta(\Delta + \eta)}{2\eta} \frac{\omega_q}{\omega_r}}. \quad (\text{A.48})$$

Here the correction term  $\omega_q/\omega_r$  can change the extracted  $g$  by  $\sim 15\%$  for typical experimental parameters.

## Appendix B

# Transmon with addition of an inductor

In this Appendix, we consider the circuit for transmon and add an inductor in series with the Josephson junction. We perturbatively find the qubit frequency and anharmonicity, and show that this model can explain experimental observations for the dependence of anharmonicity on the qubit frequency. The model of transmon with addition of an inductor in series can also be used for study of Gmon qubits [48, 263].

### B.1 Derivation of Hamiltonian

Let us consider the usual transmon [44] with addition of a series inductor (Fig. B.1). We write the potential energy of the Josephson junction, potential energy of the inductor, and the kinetic energy of the capacitor for this circuit. We use these results to derive the

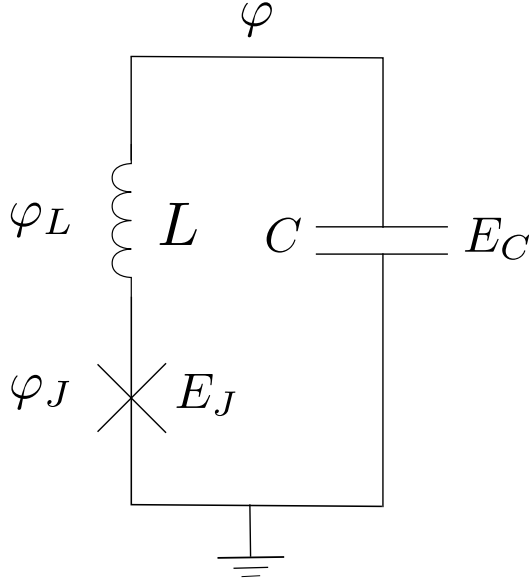


Figure B.1: A transmon with addition of an inductor. The superconducting phase difference across the Josephson junction is  $\varphi_J$  and across the inductor is  $\varphi_L$ , so that the total phase difference is  $\varphi = \varphi_J + \varphi_L$ . The Josephson energy is  $E_J$  (critical current  $I_c$ ), the charging energy is  $E_C$ , and the extra inductance is  $L$ .

Lagrangian of the circuit, which is then used to derive the circuit Hamiltonian.

With phase difference of  $\varphi_J$  across Josephson junction, the current passing through the junction is  $I_J = I_c \sin \varphi_J$ , which then leads (in the standard way) to the junction potential energy

$$U_{\text{junction}} = \frac{\Phi_0}{2\pi} \int I_J d\varphi_J = -\frac{\Phi_0}{2\pi} I_c \cos \varphi_J = -E_J \cos \varphi_J, \quad (\text{B.1})$$

where  $\Phi_0 = h/2e$  is the flux quantum, and  $E_J = \frac{\Phi_0}{2\pi} I_c$  is the Josephson energy.

The superconducting phase difference across the inductor,  $\varphi_L$ , and the current passing through it,  $I_L$ , are related via  $\frac{\Phi_0}{2\pi} \varphi_L = L I_L$ . Since the inductor is in series with the junction, the current that goes through both of them should be the same,  $I_L = I_J =$

$I_c \sin \varphi_J$ , which gives

$$\varphi_L = \frac{2\pi}{\Phi_0} L I_c \sin \varphi_J. \quad (\text{B.2})$$

We use this relation to write the potential energy of the inductor as a function of the Josephson junction phase  $\varphi_J$

$$U_{\text{inductor}} = \frac{\Phi_0}{2\pi} \int I_L d\varphi_L = \frac{1}{2L} \left( \frac{\varphi_L \Phi_0}{2\pi} \right)^2 = \frac{L I_c^2}{2} \sin^2 \varphi_J = E_L \sin^2 \varphi_J, \quad (\text{B.3})$$

with inductor energy scale

$$E_L = \frac{1}{2} L I_c^2 = \frac{1}{2} L E_J^2 \left( \frac{2\pi}{\Phi_0} \right)^2. \quad (\text{B.4})$$

Note that

$$\frac{E_L}{E_J} = \frac{L}{2L_J}, \quad (\text{B.5})$$

where  $L_J = (\Phi_0/2\pi)/I_c = (\Phi_0/2\pi)^2/E_J$  is the Josephson junction inductance.

To find the “kinetic energy” of the system, we need to find the voltage of the capacitor. The capacitor voltage is proportional to the time derivative of the phase across it as  $V_C = (\Phi_0/2\pi) d\varphi/dt$ , where

$$\varphi = \varphi_J + \varphi_L = \varphi_J + \frac{L}{L_J} \sin \varphi_J \quad (\text{B.6})$$

is the *total* phase across the capacitor, and  $L/L_J = \frac{2\pi}{\Phi_0} L I_c$ . The “kinetic energy” of the capacitor is then

$$T_{\text{capacitor}} = \frac{C \dot{\varphi}^2}{2} \left( \frac{\Phi_0}{2\pi} \right)^2 = \frac{\dot{\varphi}^2}{16E_C}, \quad (\text{B.7})$$

where  $C$  is the capacitance and  $E_C = e^2/(2C)$  is the charging energy [so that  $1/(16E_C) = (C/2) \left( \frac{\Phi_0}{2\pi} \right)^2$ ].

Noting the capacitive energy above, it is more convenient to choose the total phase  $\varphi$  as the generalized coordinate (unlike the usual choice of the Josephson phase  $\varphi_J$ ) for the Lagrangian of the circuit. With the total potential energy  $U = U_{\text{junction}} + U_{\text{inductor}}$ , we can write

$$\mathcal{L} = T - U = \frac{\dot{\varphi}^2}{16E_C} + E_J \cos[\varphi_J(\varphi)] - E_L \sin^2[\varphi_J(\varphi)], \quad (\text{B.8})$$

where  $\varphi_J(\varphi)$  is the Josephson junction phase expressed in terms of the total phase  $\varphi$ , which can be calculated by solving Eq. (B.6). It is straightforward to check that this Lagrangian gives correct equation of motion (i.e., classical current equation) for this circuit.

From the Lagrangian, we can find the canonical conjugate momentum to  $\varphi$  as

$$p_\varphi = \partial\mathcal{L}/\partial\dot{\varphi} = \frac{\dot{\varphi}}{8E_C}, \quad (\text{B.9})$$

which is related to the capacitor charge  $Q$  as  $p_\varphi = (\Phi_0/2\pi)Q$ . We then use  $\mathcal{H} = p_\varphi \dot{\varphi} - \mathcal{L}$  to write the Hamiltonian of the circuit as a function of the total phase  $\varphi$  across both the Josephson junction and inductor, and its conjugate momentum  $p_\varphi$ :

$$\mathcal{H} = 4E_C \hat{p}_\varphi^2 - E_J \cos[\varphi_J(\hat{\varphi})] + E_L \sin^2[\varphi_J(\hat{\varphi})], \quad (\text{B.10})$$

with

$$E_L = \frac{L}{2L_J} E_J, \quad (\text{B.11})$$

where  $\hat{\varphi}$  and  $\hat{p}_\varphi$  are canonical conjugate operators,  $[\hat{\varphi}, \hat{p}_\varphi] = i\hbar$ .

## B.2 Perturbative Treatment

In this section we calculate the perturbative eigenenergies of the circuit described by the Hamiltonian (B.10). To do so, we first need to write the Hamiltonian of (B.10)

in terms of the total phase  $\varphi$  only. For that, let us assume  $L/L_J \ll 1$ , then  $\varphi_J$  is only slightly different from  $\varphi$ . Using iteration in Eq. (B.6) and keeping terms up to first order in  $L/L_J \ll 1$ , we can find an approximate solution to the Josephson junction phase as

$$\varphi_J(\varphi) \approx \frac{\varphi + (L/6L_J)\varphi^3}{1 + (L/L_J)}. \quad (\text{B.12})$$

Inserting this solution into the Hamiltonian (B.10) and expanding up to 4th order in  $\varphi \ll 1$ , we get

$$H \approx 4E_C \hat{p}_\varphi^2 + \frac{E_J}{2} \frac{\hat{\varphi}^2}{1 + L/L_J} - \frac{E_J}{24} \frac{\hat{\varphi}^4}{(1 + L/L_J)^4} f(L/L_J), \quad (\text{B.13})$$

where  $f(x) = 1 - 12x^2 - 12x^3 - 4x^4$  is a polynomial. Since we have already thrown away second order terms in  $L/L_J \ll 1$  when solving Eq. (B.6), we ignore higher order terms in this polynomial and use  $f(L/L_J) \approx 1$ . [In this case  $(1 + L/L_J)^4 \approx 1 + 4L/L_J$ , but it is more convenient to use powers of  $1 + L/L_J$ .] Note that having Eq. (B.12) in third order of  $\varphi$  is enough to expand the Hamiltonian up to fourth order in  $\varphi$ , because the next term in (B.12) is fifth order in  $\varphi$ .

The first two terms in Eq. (B.13) make a quantum harmonic oscillator, therefore we can define

$$\hat{\varphi} = \left( \frac{8E_C}{E_J} (1 + L/L_J) \right)^{\frac{1}{4}} \frac{b + b^\dagger}{\sqrt{2}}, \quad (\text{B.14})$$

$$\hat{p}_\varphi = \left( \frac{8E_C}{E_J} (1 + L/L_J) \right)^{-\frac{1}{4}} \frac{b - b^\dagger}{\sqrt{2}i}, \quad (\text{B.15})$$

where  $b$  and  $b^\dagger$  are usual lowering and raising operators of the quantum harmonic oscillator. Rewriting the Hamiltonian (B.13) in terms of these lowering and raising operators yields ( $\hbar = 1$ )

$$\frac{H}{\tilde{\omega}_p} = bb^\dagger + \frac{1}{2} - \tilde{\lambda} \left( \frac{b + b^\dagger}{\sqrt{2}} \right)^4, \quad (\text{B.16})$$

where the “plasma frequency”  $\tilde{\omega}_p$  and perturbation parameter  $\tilde{\lambda}$  are defined as

$$\tilde{\omega}_p = \sqrt{8E_J E_C / (1 + L/L_J)}, \quad (\text{B.17})$$

$$\tilde{\lambda} = \frac{1}{3} \sqrt{\frac{E_C}{8E_J} \frac{1}{(1 + L/L_J)^5}}. \quad (\text{B.18})$$

Note that the above plasma frequency and perturbation parameter agree with Eqs. (A.9) and (A.10) in Appendix A when the inductor is absent ( $L = 0$ ).

Following the procedure in Appendix A and perturbatively writing the eigenenergies of the Hamiltonian in Eq. (B.16), we can find the qubit frequency  $\omega_q$  and anharmonicity  $\eta \equiv 2\omega_q - \omega_{20}$  to first order in  $\tilde{\lambda}$  as

$$\omega_q \approx \tilde{\omega}_p (1 - 3\tilde{\lambda}) = \sqrt{\frac{8E_C E_J}{(1 + L/L_J)}} - \frac{E_C}{(1 + L/L_J)^3}, \quad (\text{B.19})$$

$$\eta \approx 3\tilde{\lambda}\tilde{\omega}_p = \frac{E_C}{(1 + L/L_J)^3}. \quad (\text{B.20})$$

We note that Eq. (B.20) coincides with the anharmonicity calculation in Ref. [48]. Furthermore, we can add the  $\varphi^6$  term to Eq. (B.13) and calculate the anharmonicity with better accuracy as (neglecting terms of the order  $L/L_J \sqrt{E_C/E_J}$ )

$$\eta \approx E_C \left( \frac{1}{(1 + L/L_J)^3} + \frac{9}{4} \sqrt{\frac{E_C}{8E_J}} \right). \quad (\text{B.21})$$

One of our goals is to see how the anharmonicity of the qubit changes with the qubit frequency, which is tuned by varying the effective value of  $E_J$ . Since  $L/L_J \propto E_J$ , let us define  $L/L_J = (E_J/E_{J_0})r_0$ , where  $E_{J_0}$  is the value of  $E_J$  at some chosen point and  $r_0$  is the ratio of  $L/L_J$  at that point ( $r_0 \ll 1$ ). Then, rewriting the anharmonicity (B.21) as a function of  $E_J$  gives

$$\eta \approx E_C \left( \frac{1}{[1 + (E_J/E_{J_0})r_0]^3} + \frac{9}{4} \sqrt{\frac{E_C}{8E_J}} \right). \quad (\text{B.22})$$

Equation (B.22) shows that the anharmonicity  $\eta$  decreases when  $E_J$  increases, and we also know that the qubit frequency  $\omega_q$  increases with  $E_J$  [see Eq. (B.19)]. This observation explains decrease of  $\eta$  with increasing  $\omega_q$  in experimental observations (see Fig. B.2 and its discussion). For  $r_0 = 0$ , anharmonicity in (B.22) coincides with Eq. (A.23) in Appendix A.

### B.3 Comparison with experimental observations

The experiment was performed by Zijun (Jimmy) Chen at UCSB as part of the Google/UCSB team effort, using a flux-tunable transmon (Xmon [46]) qubit. The qubit anharmonicity  $\eta$  was experimentally measured at different qubit frequencies  $\omega_q$ , and the result is shown by black dots in Fig. B.2(a). The surprising experimental observation was that the anharmonicity  $\eta(\omega_q)$  decreases roughly 4 times faster than it was expected for a typical transmon [see Eqs. (A.9), (A.10), (A.20), (A.23), and black dash-dotted line in Fig. B.2(b); in the simple theory with  $L = 0$  it should be  $\partial\eta/\partial\omega_q \approx -(9/4)(\eta/\omega_q)^2$ ]. However, since the Xmon is physically large, its geometrical inductance becomes important and should be taken into account when modeling the qubit. Therefore, the model of the previous section with addition of an extra inductor in series with the junction can be used to explain the experimental observation for dependence of anharmonicity on the qubit frequency, as detailed below.

We use  $r_0 = L/L_{J0}$  as a fitting parameter to fit the *linear slope* of the experimental dependence  $\eta(\omega_q)$  [see upper blue line in Fig. B.2(a) and its discussion]. The fitting gives  $r_0 = 0.032$ , which corresponds to the series inductance  $L \approx 0.3$  nH. This value of  $L$  seems

to be reasonable for the experimental geometry used by Google/UCSB team, although few times higher than expected. Therefore, the addition of the series inductor can crudely explain the surprisingly fast decrease of  $\eta$  with qubit frequency in experimental observations.

However, the results of the previous section cannot explain the significant curving down of the experimental data in Fig. B.2(a) at larger qubit frequencies close to 6 GHz. As we found, this is due to a different effect: eigenstate formation between the transmon and its readout resonator. Coupling to the readout resonator slightly shifts the transmon energy levels, which additionally decreases the measured anharmonicity. We can calculate the anharmonicity of the qubit in presence of the coupled readout resonator by calculating the eigenenergies in the Jaynes-Cummings (JC) ladder of the qubit and the resonator. The qubit eigenfrequencies are (see Fig. A.1)

$$\bar{\omega}_{10} = E_{\overline{|1,0\rangle}} - E_{\overline{|0,0\rangle}} \approx \omega_q - \frac{g^2}{\Delta}, \quad (\text{B.23})$$

$$\bar{\omega}_{21} = E_{\overline{|2,0\rangle}} - E_{\overline{|1,0\rangle}} \approx \omega_q - \eta + \frac{g^2}{\Delta} - \frac{g_{1,2}^2}{\Delta + \eta}, \quad (\text{B.24})$$

where  $\bar{\omega}_{kl}$  denotes the eigenfrequency in the JC ladder,  $E_{\overline{|k,n\rangle}}$  denotes the JC eigenenergy for the eigenstate  $\overline{|k,n\rangle}$ , and we use the ket notation  $|\text{qubit}, \text{resonator}\rangle$ . The approximate formulas in (B.23)–(B.24) are derived perturbatively using two-level energy repulsions, similar to the calculations in Sec. A.4 and with the same notations as there. The experimentally measured anharmonicity is then

$$\eta_{\text{exp}} = \bar{\omega}_{10} - \bar{\omega}_{21} \approx \eta - 2\chi, \quad (\text{B.25})$$

where  $2\chi = \omega_r^{(0)} - \omega_r^{(1)} = 2g^2/\Delta - g_{1,2}^2/(\Delta + \eta)$  is the total dispersive shift of the readout resonator frequency when the qubit state changes from excited to ground state [see Eq. (A.47) and its derivation in Sec. A.4].

When the qubit frequency increases, the detuning between the qubit and the resonator decreases<sup>1</sup> and consequently the dispersive shift  $2\chi$  increases [see Eq. (A.47)]. Moreover, the dispersive shift does not linearly increase with the qubit frequency, therefore its effect on  $\eta_{\text{exp}}$  can produce the curving observed in the experimental data [see Fig. B.2(a)]. For the experimental results presented here, the value of  $2\chi$  at qubit frequency of 5 GHz and 5.9 GHz is 1.7 MHz and 6.6 MHz respectively, producing a significant change in the experimentally observed  $\eta_{\text{exp}}$  compared to  $\eta$ .

The lower solid green line in Fig. B.2(a) shows the anharmonicity obtained from numerical simulation for the Hamiltonian (B.10) [based on numerical solution for  $\varphi_J(\varphi)$ ] assuming  $r_0 = 0.032$ , with the additional decrease by  $2\chi$  (obtained from experiment). As we see, the green line matches the experimental data quite well (except for two points below 4.9 GHz, which are possibly shifted by some other reason, e.g., a defect). The upper solid blue line shows the same numerical results without the additional decrease by  $2\chi$ . Figure B.2(b) shows the same blue line as in the panel (a), along with the dashed orange line corresponding to the analytical formula (B.22) with the same parameters (see the caption). As we see, the slope of the dependence  $\eta(\omega_q)$  given by the analytics is close to the numerically calculated slope, though there is still a noticeable difference between them (the vertical shift between the analytics and numerics is not important here because  $E_C$  is an overall fitting parameter anyway). The black dash-dotted line in Fig. B.2(b) is the anharmonicity of the transmon in the absence of the series inductor and coupling to the resonator [calculated numerically using Eq. (C.2)]; it decreases roughly four times slower than the experimental observation.

---

<sup>1</sup>In this experiment the qubit frequency is smaller than the resonator frequency.

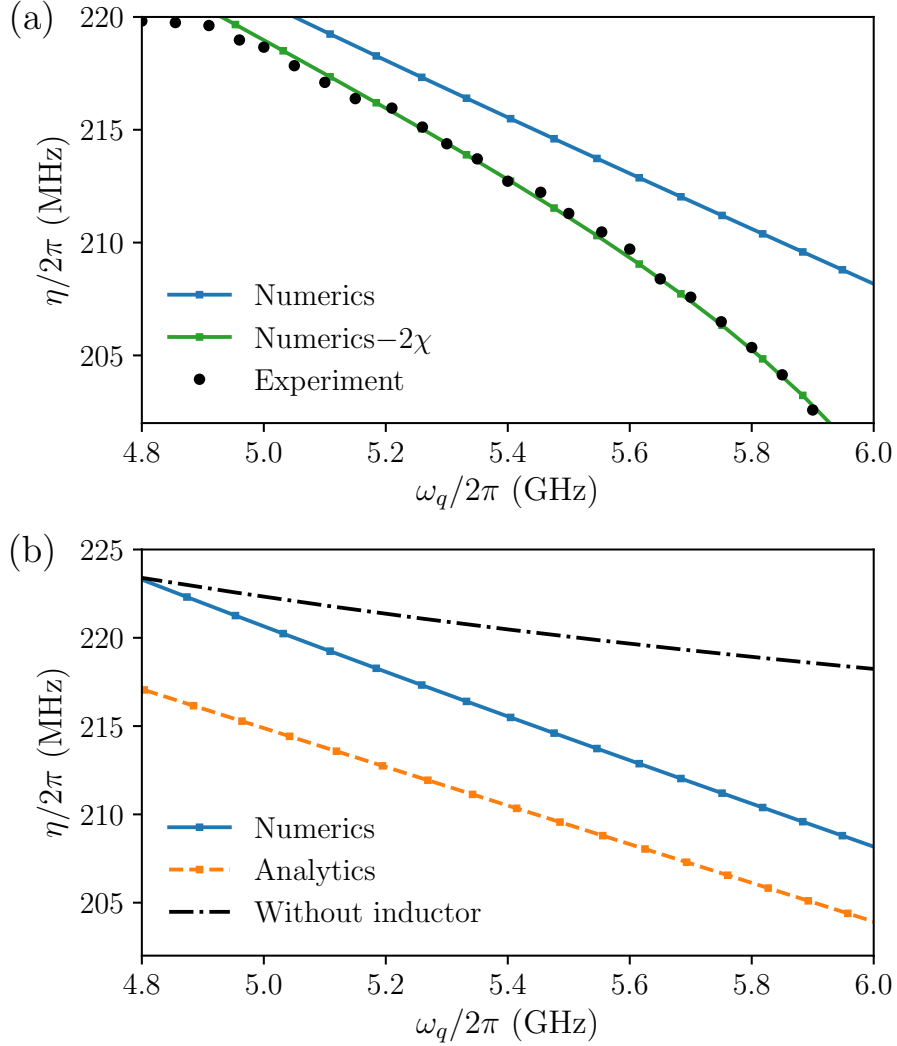


Figure B.2: Anahrmonicity  $\eta$  of the transmon vs qubit frequency  $\omega_q$ . Black circles are Google/UCSB experimental data, solid blue line (in both panels) is the numerical simulation of the Hamiltonian in Eq. (B.10), lower solid green line in panel (a) is the numerical simulation with the additional decrease by  $2\chi$  (the values of  $2\chi$  are obtained from experiment and are frequency dependent), and dashed orange line in panel (b) is the analytical formula (B.22). Black dash-dotted line in panel (b) is the anharmonicity of the transmon in the absence of the series inductor [calculated numerically using Eq. (C.2)], which decreases roughly four times slower than the experimental observation. Here  $E_C/2\pi = 214$  MHz and  $r_0 = 0.032$ , so that  $L/L_J = 0.032$  for the qubit frequency of 5 GHz (at this frequency  $E_{J_0}/2\pi = 16.31$  GHz) and  $L/L_J \approx 0.046$  for the qubit frequency of 6 GHz. The resonator frequency is 6.63 GHz. Experimental data is courtesy of Zijun (Jimmy) Chen.

We conclude that the model which takes into account an inductor in series with the Josephson junction and also additional contribution of  $-2\chi$ , can explain well the experimental observations for dependence of anharmonicity on qubit frequency. Note that the model of transmon with addition of a series inductor is applicable to Gmon qubits [48, 263], and that similar equations also arise when modeling inductive couplers [264].

## Appendix C

# Numerical methods for studying readout of qubits

In this appendix we briefly explain how the numerical analysis of the dispersive measurement of a qubit is done throughout this dissertation. We start by reviewing eigenenergies and eigenstates of transmon, and then show how the Jaynes-Cummings (JC) ladder of the qubit-resonator system can be numerically diagonalized to calculate useful quantities related to dispersive measurement.

### C.1 Transmon

Transmon in its simplest form consists of a Josephson junction that is shunted by a relatively large capacitor. The Hamiltonian for this qubit can be written as [44]:

$$H = 4E_C(\hat{n} - n_g)^2 - E_J \cos \hat{\varphi}, \quad (\text{C.1})$$

where  $\hat{\varphi}$  is the superconducting phase difference across the Josephson junction,  $\hat{n}$  is the number of Cooper pairs transferred through the junction,  $E_C = e^2/2C$  is the charging energy,  $n_g$  is the (dimensionless) offset charge, and  $E_J = I_c\Phi_0/2\pi$  is the Josephson energy, with commutation relation  $[\hat{\varphi}, \hat{n}] = i$  (similar to  $\hat{x}$  and  $\hat{p}$ ). Transmons operate in the regime where  $E_J/E_C \gg 1$  (typically between 50 to 100), which enabled us to perturbatively solve for lowest eigenenergies and eigenstates in Appendix A. Below, we discuss exact solutions for the eigenenergies and eigenstates of the Hamiltonian (C.1).

The time-independent Schrodinger equation for the cosine potential of transmon can be analytically solved using Mathieu functions [265, 266]. Since the transmon states with the phase  $\varphi$  shifted by  $2\pi$  are physically equivalent, the wave function should be  $2\pi$ -periodic in  $\varphi$ . Imposing this periodic boundary condition on the Mathieu solutions yields the discrete set of eigenenergies of transmon

$$E_k = E_C \mathcal{M}_A(r_k, -\frac{E_J}{2E_C}), \quad (\text{C.2})$$

where  $\mathcal{M}_A(r, q)$  is the characteristic value for even Mathieu function, and

$$r_k = k + 1 - (k + 1)(\text{mod } 2) + 2n_g(-1)^{k - [\text{Sign}(n_g) - 1]/2}, \quad k = 0, 1, \dots \quad (\text{C.3})$$

Here  $(k + 1)(\text{mod } 2)$  denotes  $k + 1$  modulo 2, which can be either 0 or 1, and  $\text{Sign}(n_g) = \pm 1$ . Note that  $\mathcal{M}_A(r, q)$  is a monotonously increasing function of  $r$ ; therefore for  $E_k$  increasing with  $k$ , we need  $r_k$  increasing with  $k$ . Equation (C.3) shows monotonous increase with  $k$  only when  $n_g$  belongs to the exclusive range  $(-1/2, 1/2)$ . Because the eigenenergies and the eigenfunctions are periodic in  $n_g$  with period of 1, values of  $n_g$  that are outside of the range  $(-1/2, 1/2)$  should be moved to this range by adding an integer. Also note that the

procedure may not work well for integer  $r_k$ , therefore for integer or half-integer  $n_g$  we should sometimes shift  $n_g$  by a negligible amount to avoid an exact integer  $r_k$ .

The eigenstates of transmon are

$$\langle \varphi | k \rangle = \psi_k(\varphi) = \frac{e^{in_g\varphi}}{\sqrt{2\pi}} \left[ \mathcal{M}_C \left( \frac{E_k}{E_C}, \frac{-E_J}{2E_C}, \frac{\varphi}{2} \right) + i(-1)^{k+1} \mathcal{M}_S \left( \frac{E_k}{E_C}, \frac{-E_J}{2E_C}, \frac{\varphi}{2} \right) \right], \quad (\text{C.4})$$

where  $\mathcal{M}_C(a, q, \theta)$  and  $\mathcal{M}_S(a, q, \theta)$  are even and odd Mathieu functions respectively (also called Mathieu cosine and Mathieu sine functions). Mathieu functions  $\mathcal{M}_C$  and  $\mathcal{M}_S$  and Mathieu characteristic value  $\mathcal{M}_A$  can be evaluated to arbitrary precision using numerical packages and softwares. For example, Wolfram Mathematica includes them as the functions `MathieuC`, `MathieuS`, and `MathieuCharacteristicA`.

The eigenstates can be used to calculate charge matrix elements of the transmon

$$\langle l | \hat{n} | k \rangle = \int_{-\pi}^{\pi} \psi_l^*(\varphi) \frac{\partial}{i\partial\varphi} \psi_k(\varphi) d\varphi. \quad (\text{C.5})$$

The derivatives of the Mathieu functions are also included in numerical packages.

The eigenenergies and charge matrix elements calculated here can be used to model the dispersive measurement of the qubit, as detailed in the next section.

## C.2 JC ladder of qubit and resonator

In circuit QED (cQED) setups, the transmon is typically measured via a detuned readout resonator that is coupled to it [78]. The frequency of the resonator changes depending on the state of the qubit, and this change of the resonator frequency (also called dispersive shift of the resonator frequency, hence the name dispersive readout) is used to measure the state of the qubit. Here we focus on numerical approaches for modeling the

dispersive measurement.

With the ket convention  $|\text{qubit, resonator}\rangle$ , we write the bare Hamiltonian of the qubit and resonator ( $\hbar = 1$ ) as

$$H_b = \sum_{k,n} (E_k + n\omega_r) |k, n\rangle \langle k, n|, \quad (\text{C.6})$$

where  $\omega_r$  is the bare resonator frequency, and  $E_k$  is the transmon eigenenergy for level  $k$ , with qubit bare frequency  $\omega_q = E_1 - E_0$ . The transmon eigenenergies can be calculated using numerical methods in Sec. C.1, or via perturbative formulas in Appendix A, depending on the accuracy required. The bare Hamiltonian of (C.6) produces the Jaynes-Cummings ladder of energy levels, as depicted in Fig. C.1.

Typically the qubit and the readout resonator are capacitively coupled, therefore there is a charge-charge interaction between them. In the rotating wave approximation (RWA), this interaction has the form

$$H_{\text{RWA}} = \sum_{k,n} g_{k,k+1} \sqrt{n} |k+1, n-1\rangle \langle k, n| + \text{H.c.}, \quad (\text{C.7})$$

where  $g_{k,k+1} \equiv g \langle k|\hat{n}|k+1\rangle / \langle 0|\hat{n}|1\rangle$  are the normalized charge matrix elements of the transmon<sup>1</sup>. Again, these matrix elements can be calculated either numerically as discussed in Sec. C.1, or via perturbative formulas of Appendix A, depending on the accuracy required. The RWA couplings are shown as black curved arrows in Fig. C.1.

Our goal is to numerically diagonalize the total Hamiltonian  $H = H_b + H_{\text{RWA}}$  to find the eigenenergies and eigenstates of the system, and also to correctly identify (label) these eigenstates such that they correspond to their bare states. The idea for labeling is

---

<sup>1</sup>Note that coefficients  $\sqrt{n}$  in Eq. (C.7) are the charge matrix elements of the readout resonator (harmonic oscillator).

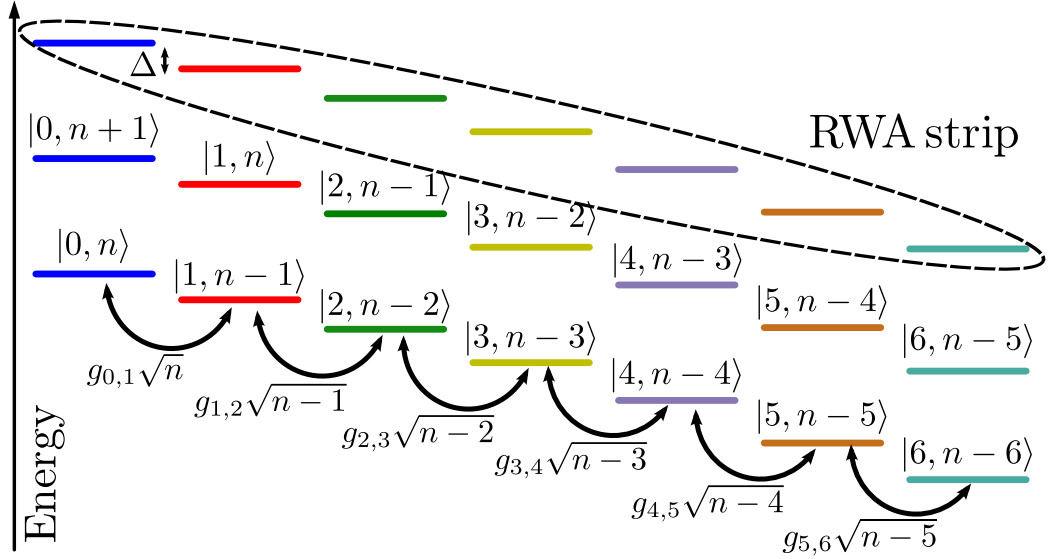


Figure C.1: JC ladder of the qubit and the resonator. Bare states are shown as horizontal lines and labeled with the ket convention  $|qubit, resonator\rangle$ , black curved arrows indicate coupling within an RWA strip, with corresponding RWA coupling strengths written below them. An RWA strip is enclosed by dashed line.

to use the fact that the RWA interaction preserves total number of excitations. This forms subspaces in the JC ladder, where the excitation number is fixed and states within that subspace couple *only* to each other as a linear chain. We call these subspaces “RWA strips”, one of which is marked in Fig. C.1.

Within each RWA strip, the energy levels repel from each other. In the most practical case when qubit frequency is smaller than the resonator frequency, the bare energies within one RWA strip decrease monotonously with  $k$ ; then the repelled eigenenergies do not cross each other with increasing  $n$ . Therefore, the order of the eigenenergies within an RWA strip is the same as for bare energies, and this fact can be used to correctly identify and label the numerically calculated eigenenergies.

The numerical procedure in the case  $\omega_q < \omega_r$  is as follows. We first construct the

Hamiltonian for an RWA strip with a given total excitation number  $n_\Sigma$ , with bare energies  $E_{|k,n\rangle} = E_k + n\omega_r$  and bare states  $|k,n\rangle$ , where  $n = n_\Sigma - k$ . Note that the bare energies within an RWA strip are ordered (i.e., from largest to smallest) by construction. Next, this RWA strip Hamiltonian is numerically diagonalized, giving *unlabeled* pairs of eigenenergies and eigenstates. We then sort (e.g., in increasing order) these eigenenergies and match them for labeling with the bare energies that were ordered by construction in the RWA strip. This procedure yields the correctly labeled eigenenergies  $E_{\overline{|k,n\rangle}}$  and corresponding eigenstates  $\overline{|k,n\rangle}$  (overline indicates eigenstate). This procedure is repeated for all the RWA strips in the JC ladder.

In the less common case when the qubit frequency is larger than the resonator frequency, the RWA strips can bend on themselves. In this configuration, the bare energies inside a strip are not ordered anymore, and furthermore there can be energy level crossings *within* an RWA strip as the photon number increases and states repel from each other. Therefore the labeling scheme discussed above will not always work; however, one can in principle keep track of these level crossings as the photon number increases and update the labels accordingly. Even without more complicated labeling schemes, the simple numerical method discussed above can be used for studying the JC ladder when the qubit frequency is larger than for the resonator, with good agreement between the numerical model and experimental results [179].

With addition of nonRWA terms, the labeling method discussed above will no longer work, because nonRWA terms couple different RWA strips to each other (see chapter 4). However, for typical cQED parameter regimes, these nonRWA terms are far more

off-resonant compared to the RWA terms. This means that, although they do change the eigenenergies and eigenstates of the system, this change is relatively small. The fact that the change in the eigenstates is relatively small can be used to label nonRWA eigenenergies. The idea is to use the same label as the one belonging to the closest RWA eigenstate to it. This way we can label eigenenergies and eigenstates of the system with inclusion of nonRWA terms as follows (note that this labeling may jump at the level crossings). We first calculate and label the RWA eigenenergies and eigenstates of the Hamiltonian  $H_b + H_{\text{RWA}}$  to find  $E_{|k,n\rangle}^{(\text{RWA})}$  and  $|\overline{k,n}\rangle^{(\text{RWA})}$ . We also diagonalize the Hamiltonian  $H_b + H_{\text{RWA}} + H_{\text{nonRWA}}$  to get the *unlabeled* eigenenergies  $E_{|\overline{j}\rangle}$  and corresponding eigenstates  $|\overline{j}\rangle$ . For each nonRWA eigenstate/eigenenergy pair, we search through the RWA eigenstates to maximize the absolute value of the inner product between  $|\overline{j}\rangle$  and  $|\overline{k,n}\rangle^{(\text{RWA})}$ , which we then use to label the pairs.

Another numerical detail that should be noted is the problem with the overall sign of the eigenstates. When numerical codes diagonalize a matrix, the overall sign of the eigenstates will be ambiguous and may change for different parameters and in different conditions. We fix this by setting the overall sign of each eigenstate such that it does not flip with changing  $n$ . In other words, we make sure that the overall sign of  $|\overline{k,n}\rangle$  is the same as for  $|\overline{k,n+1}\rangle$ .

With eigenenergies and eigenstates correctly labeled, we can calculate a variety of useful quantities related to the dispersive measurement of qubits. For example, the qubit frequency when the resonator is populated with  $n$  photons is

$$\omega_q(n) = E_{|\overline{1,n}\rangle} - E_{|\overline{0,n}\rangle}, \quad (\text{C.8})$$

which can be used to find the ac Stark shift  $\omega_q(n) - \omega_q(0)$ , e.g., for photon number calibration in an experiment [151, 179]. The resonator frequency when the qubit is in the state  $|k\rangle$  is

$$\omega_r^{(k)}(n) = E_{|k,n+1\rangle} - E_{|k,n\rangle}, \quad (\text{C.9})$$

which can be used to calculate the dispersive shift  $2\chi(n) = \omega_r^{(0)}(n) - \omega_r^{(1)}(n)$ . Finally, the “fan diagram” frequencies (see Chapter 4 and Ref. [151]) are calculated as

$$\bar{\omega}_k(n) \equiv E_{|k,n-k\rangle} - n\omega_r, \quad (\text{C.10})$$

which can be used to calculate the photon number at which the readout induced nonRWA transitions occur (see chapter 4).

A Python implementation of these numerical methods is available at <https://github.com/MostafaKhezri/JC-ladder>.

## Appendix D

# Derivation of the measurement error in presence of a neighboring qubit

This appendix is related to Chapter 2 and uses the same notations as in that chapter. Here we provide a more complete derivation of the measurement error, assuming the regime with  $\Gamma_m \ll \Delta$ , where the two-qubit eigenstates are the optimal logical states. Our derivation will consist of two parts. First, neglecting transients for the resonator and assuming abrupt switching events, we will calculate the histograms  $P(\bar{I} | 00)$  and  $P(\bar{I} | \bar{1}\bar{0})$  for the integrated measurement output  $\bar{I} = \int_0^t I(t') dt'/t$ , corresponding to the initial states  $|00\rangle$  and  $|\bar{1}\bar{0}\rangle$ , respectively (we use the word “histogram” instead of “probability distribution” as a shorter term). Second, we will impose a discrimination threshold  $I_{\text{th}}$  on these histograms to compute the probability of error according to our definition in Eq. (2.34).

## D.1 Readout histograms

Our primary assumption for obtaining the readout histograms is that we can separate the integrated normalized measurement output  $\bar{I}$  into two approximately uncorrelated terms (signal and noise)

$$\bar{I}(t) = \bar{z}_{\text{tot}}(t) + \bar{\xi}(t). \quad (\text{D.1})$$

The first term,  $\bar{z}_{\text{tot}} \equiv \bar{z} + \bar{Z}$ , is the total integrated bare-population difference between the ground and excited states of the main qubit, which includes a part  $\bar{z}$  in the single-excitation subspace, as well as a part  $\bar{Z}$  outside this subspace,

$$\bar{z}(t) \equiv \frac{1}{t} \int_0^t [P_{10}(t') - P_{01}(t')] dt', \quad (\text{D.2})$$

$$\bar{Z}(t) \equiv \frac{1}{t} \int_0^t [P_{11}(t') - P_{00}(t')] dt'. \quad (\text{D.3})$$

The second term of Eq. (D.1) is integrated zero-mean white noise, which is randomly sampled from a Gaussian distribution of variance  $\tau/t$ ,

$$P_{\xi}(\bar{\xi}) = \sqrt{\frac{t}{2\pi\tau}} \exp\left(-\frac{\bar{\xi}^2 t}{2\tau}\right). \quad (\text{D.4})$$

We note that the assumption of an uncorrelated dynamics of  $\xi(t)$  and  $z(t)$  is in general not good in the quantum Bayesian approach. For example, for single-qubit Rabi oscillations, the correlation between  $\xi(t)$  and  $z(t)$  is as strong as autocorrelation for  $z(t)$  [267]. However, for the dynamics with rare switching events this assumption should be sufficiently good because the correlation between  $\xi(t)$  and  $z(t)$  is most important only in the vicinity of switching events, which occupy a small fraction of the total integration time. The approximation (D.1) also neglects transients of duration  $\sim \kappa^{-1}$  at the start of the measurement and near switching events, implying  $t \gg \kappa^{-1}$ .

The approximation of Eq. (D.1) permits us to calculate each histogram for  $\bar{I}$  in a simple way as a convolution between a histogram for the population difference  $\bar{z}_{\text{tot}}$  and the Gaussian white noise distribution for  $\bar{\xi}$ . If we additionally assume that in the single-excitation subspace the state is always pinned to an eigenstate, with abrupt jumps between the eigenstates (in particular, this implies  $\rho_{\bar{0}\bar{1},\bar{1}\bar{0}} = 0$ ), then the histogram for  $\bar{z}$  is determined by the histogram for the *eigenstate* population difference  $\bar{z}_e$ ,

$$\bar{z} = \cos(2\theta) \bar{z}_e, \quad \bar{z}_e \equiv \frac{1}{t} \int_0^t [P_{\bar{1}\bar{0}}(t') - P_{\bar{0}\bar{1}}(t')] dt', \quad (\text{D.5})$$

via the conversion factor  $\cos(2\theta)$  with rotation angle  $2\theta = \arctan(2g/\Delta)$ . We will now calculate the histograms corresponding to the specific initial populations  $P_{00}(0) = 1$  or  $P_{\bar{1}\bar{0}}(0) = 1$ , which are the optimal logical states for discrimination.

### D.1.1 Ground-state histogram

An initial ground state  $|00\rangle$  remains  $|00\rangle$  for an arbitrarily long time, and the corresponding output signal also does not change in time, since we assumed the steady state for the resonator. Therefore, an initial population  $P_{00}(0) = 1$  produces the stationary integrated coordinate  $\bar{Z} = -1$  (with  $\bar{z} = 0$ ) and the stationary integrated total population difference  $\bar{z}_{\text{tot}} = -1$ , which implies a delta-function histogram  $P_z[\bar{z}_{\text{tot}}(t) | 00] = \delta(\bar{z}_{\text{tot}} + 1)$ . Convoluting this histogram with the Gaussian white noise in Eq. (D.4) produces the histogram for the integrated measurement result,

$$P(\bar{I} | 00) = \sqrt{\frac{t}{2\pi\tau}} \exp\left[-\frac{(\bar{I} + 1)^2 t}{2\tau}\right], \quad (\text{D.6})$$

which is the expected Gaussian distribution of the same width as the noise that is centered at the ground state normalized signal of  $I_0 = -1$ .

### D.1.2 Excited-state histogram

An initially excited eigenstate  $|\bar{10}\rangle$  will randomly jump to the eigenstate  $|\bar{01}\rangle$  at the rate  $\Gamma_{\text{sw}}^-$ , as discussed in Section 2.4, and may then randomly jump back to the original eigenstate at the rate  $\Gamma_{\text{sw}}^+$ . We assume that these jumps can be treated as instantaneous compared to the integration time  $t$ , and that we can treat the eigenstates as stationary between these jumps. We also assume that the jumps obey Poissonian statistics and that the average time between the jumps is long compared to typical integration times,  $\Gamma_{\text{sw}}^\pm t \ll 1$ ; therefore it will be sufficient to consider only zero, one, or two possible jumps per integration duration  $t$ . The total histogram for the excited state will then be a weighted contribution of histograms with a definite number of jumps

$$P(\bar{I} | \bar{10}) = p_0 P^{(0)}(\bar{I} | \bar{10}) + p_1 P^{(1)}(\bar{I} | \bar{10}) + p_2 P^{(2)}(\bar{I} | \bar{10}). \quad (\text{D.7})$$

We compute each of these histograms and their weights separately. The derivation is significantly easier for the case when  $\Gamma_{\text{sw}}^+ = \Gamma_{\text{sw}}^- \equiv \Gamma_{\text{sw}}$ , so we will be starting the discussion with this case and then discussing more approximate results for unequal switching rates.

For Poissonian jump statistics with equal switching rates, the probability of having  $k$  jumps within the measurement duration  $t$  is  $p_k = e^{-\Gamma_{\text{sw}} t} (\Gamma_{\text{sw}} t)^k / k!$ . Since we consider only  $k \leq 2$ , we will use

$$p_0 = e^{-\Gamma_{\text{sw}} t}, \quad p_2 = \frac{(\Gamma_{\text{sw}} t)^2}{2} e^{-\Gamma_{\text{sw}} t}, \quad p_1 = 1 - p_0 - p_2, \quad (\text{D.8})$$

where  $p_1$  is chosen to adjust normalization because the largest neglected contribution,  $k = 3$ , also has an odd number of jumps, and such choice slightly improves the accuracy for the calculation of the measurement error (though this is not really important).

In the case of unequal switching rates the exact formulas for  $p_k$  are quite lengthy,  $p_0 = e^{-\Gamma_{\text{sw}}^- t}$ ,  $p_1 = \Gamma_{\text{sw}}^- (e^{-\Gamma_{\text{sw}}^- t} - e^{-\Gamma_{\text{sw}}^+ t}) / (\Gamma_{\text{sw}}^+ - \Gamma_{\text{sw}}^-)$ ,  $p_2 = \Gamma_{\text{sw}}^- \Gamma_{\text{sw}}^+ [e^{-\Gamma_{\text{sw}}^+ t} + e^{-\Gamma_{\text{sw}}^- t} (\Gamma_{\text{sw}}^+ t - \Gamma_{\text{sw}}^- t - 1)] / (\Gamma_{\text{sw}}^+ - \Gamma_{\text{sw}}^-)^2$ , so we will use the approximation

$$p_0 = e^{-\Gamma_{\text{sw}}^- t}, \quad p_2 \approx \frac{\Gamma_{\text{sw}}^- \Gamma_{\text{sw}}^+ t^2}{2}, \quad p_1 = 1 - p_0 - p_2, \quad (\text{D.9})$$

Note that the next-order approximation for  $p_2$  is  $p_2 \approx \frac{1}{2} \Gamma_{\text{sw}}^- \Gamma_{\text{sw}}^+ t^2 [1 - (2\Gamma_{\text{sw}}^- + \Gamma_{\text{sw}}^+) t / 3]$ . Also note that to linear order in  $t$  (then fully neglecting  $p_2$ , as in the main text)

$$p_1 \approx \Gamma_{\text{sw}}^- t. \quad (\text{D.10})$$

The excited-state histogram with zero jumps is similar to the ground-state histogram in Eq. (D.6). The initial eigenpopulation remains stationary in this case, corresponding to a stationary eigenpopulation difference  $\bar{z}_e = 1$ , and thus a bare population difference of  $\bar{z} = \cos(2\theta)$  and a histogram of

$$P_z^{(0)}(\bar{z}_{\text{tot}} | \bar{10}) = \delta[\bar{z}_{\text{tot}} - \cos(2\theta)]. \quad (\text{D.11})$$

Convolving this histogram with the Gaussian noise in Eq. (D.4) yields the measurement histogram

$$P^{(0)}(\bar{I} | \bar{10}) = \sqrt{\frac{t}{2\pi\tau}} \exp\left[-\frac{[\bar{I} - \cos(2\theta)]^2 t}{2\tau}\right], \quad (\text{D.12})$$

which is a Gaussian distribution similar to the ground-state histogram, but centered at  $\cos(2\theta) \approx 1 - 2(g/\Delta)^2$  that is slightly shifted from the otherwise expected mean of  $I_1 = +1$  by the coupling to the neighboring qubit. This slight shift was neglected in the main text as small.

Now let us calculate the histogram with a *single jump*. If the jump occurs at time moment  $t_1$ , then the signal of  $\cos(2\theta)$  is integrated for time  $t_1$  and the signal of  $-\cos(2\theta)$  is integrated for time  $t - t_1$ , resulting in the average

$$\bar{z}^{(1)} = \frac{2t_1 - t}{t} \cos(2\theta). \quad (\text{D.13})$$

In the case  $\Gamma_{\text{sw}}^- = \Gamma_{\text{sw}}^+$ , the jump time  $t_1$  is equally likely at any time in the interval  $[0, t]$ . Then  $\bar{z}_{\text{tot}}^{(1)}$  has a uniform histogram  $P_z^{(1)}(\bar{z}_{\text{tot}} | \bar{10}) = [2 \cos(2\theta)]^{-1}$  in the corresponding interval  $[-\cos(2\theta), \cos(2\theta)]$ , illustrated in Fig. D.1(a). Convoluting this uniform distribution with the Gaussian white noise in Eq. (D.4) yields the measurement histogram

$$P^{(1)}(\bar{I} | \bar{10}) = \frac{\text{erf} \frac{\bar{I} + \cos(2\theta)}{\sqrt{2\tau/t}} - \text{erf} \frac{\bar{I} - \cos(2\theta)}{\sqrt{2\tau/t}}}{4 \cos(2\theta)}, \quad (\text{D.14})$$

which is a smoothed box distribution [in Fig. D.1(a) the smoothing is shown for  $t/\tau = 10$ ]. This addition to the excited-state histogram is the dominant effect of the quantum jumps on the readout. Note that for  $t/\tau \gtrsim 4$  the smoothing appreciably affects only the edges of the rectangular distribution  $P_z^{(1)}(\bar{z}_{\text{tot}} | \bar{10})$ , so that for  $\cos(2\theta) - |\bar{I}| \gtrsim 2\sqrt{\tau/t}$  we can use  $P^{(1)}(\bar{I} | \bar{10}) \approx P_z^{(1)}(\bar{I} | \bar{10})$ .

In the case of unequal switching rates,  $\Gamma_{\text{sw}}^- \neq \Gamma_{\text{sw}}^+$ , the jump time  $t_1$  is no longer equally distributed within  $t$ ; instead, it has the (normalized) probability distribution  $e^{-\Gamma_{\text{sw}}^- t_1} e^{-\Gamma_{\text{sw}}^+ (t-t_1)} (\Gamma_{\text{sw}}^+ - \Gamma_{\text{sw}}^-) / (e^{-\Gamma_{\text{sw}}^- t} - e^{-\Gamma_{\text{sw}}^+ t})$ . Then the probability distribution for  $\bar{z}^{(1)}$  within the interval  $[-\cos(2\theta), \cos(2\theta)]$  is given by the same formula, with  $t_1$  replaced by  $[1 + \bar{z}^{(1)} / \cos(2\theta)] t / 2$  and extra normalization factor  $t / [2 \cos(2\theta)]$ . This probability distribution for  $\bar{z}^{(1)}$  should then be convolved with the Gaussian noise to obtain  $P^{(1)}(\bar{I} | \bar{10})$ . The

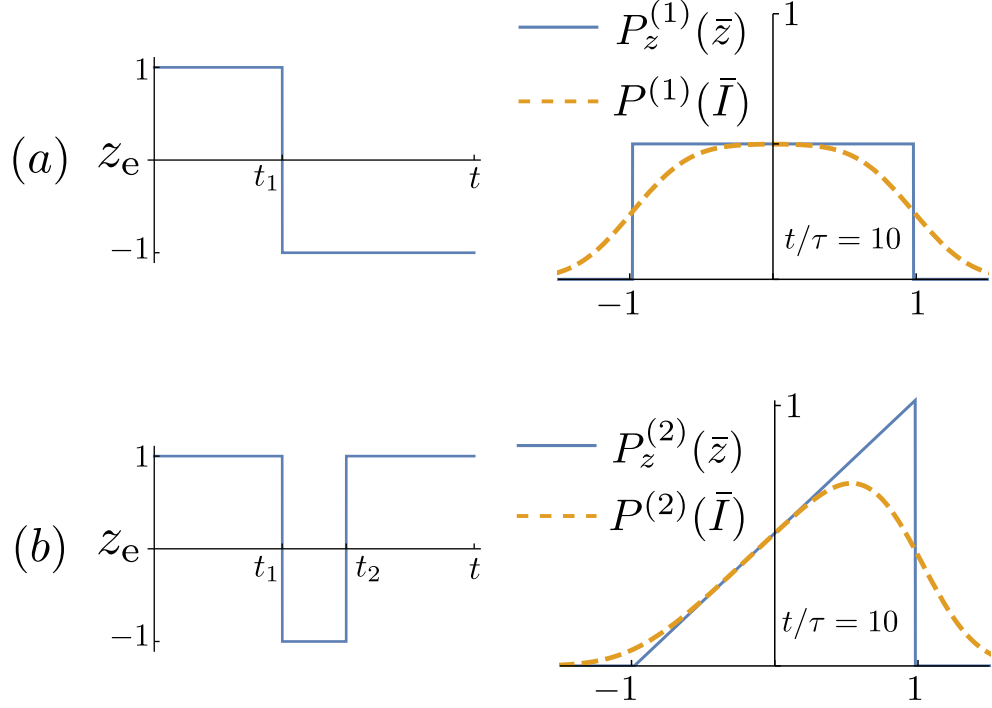


Figure D.1: (a) Left panel: schematic evolution of the eigenbasis population difference  $z_e$  with a jump from 1 to  $-1$  at  $t_1$ . Right panel: the histogram  $P_z^{(1)}(\bar{z}_{\text{tot}}|\bar{1}\bar{0})$  for time-averaged bare-basis population difference in the one-jump scenario (solid line) and the corresponding histogram  $P^{(1)}(\bar{I}|\bar{1}\bar{0})$ , which includes Gaussian noise (dashed line). (b) Similar schematic and histograms for the two-jump scenario. We assume  $t/\tau = 10$ ,  $g/\Delta = 1/10$ , and  $\Gamma_{\text{sw}}^+ = \Gamma_{\text{sw}}^-$ .

resulting formula is very long, so for simplicity we can use

$$P_z^{(1)}(\bar{z}_{\text{tot}}|\bar{1}\bar{0}) \approx \frac{1 + \frac{(\Gamma_{\text{sw}}^+ - \Gamma_{\text{sw}}^-)t}{2 \cos(2\theta)} \bar{z}_{\text{tot}}}{2 \cos(2\theta)}, \quad |\bar{z}_{\text{tot}}| \leq \cos(2\theta), \quad (\text{D.15})$$

and since the convolution of a linear function with the Gaussian noise affects mostly the vicinity of edges, we can use  $P^{(1)}(\bar{I}|\bar{1}\bar{0}) \approx P_z^{(1)}(\bar{I}|\bar{1}\bar{0})$  for  $\cos(2\theta) - |\bar{I}| \gtrsim 2\sqrt{\tau/t}$ . A little better approximation is to use Eq. (D.14) with added term  $\bar{I}(\Gamma_{\text{sw}}^+ - \Gamma_{\text{sw}}^-)t/4 \cos^2(2\theta)$  at  $|\bar{I}| \leq \cos(2\theta)$ .

Note that if we also want to take into account the energy relaxation with the

rate  $T_1^{-1}$ , then for the energy relaxation event occurring at time  $t_1$  we have  $\bar{z}_{\text{tot}}^{(1)} = [1 + \cos(2\theta)]t_1/t - 1$ . Then using approximation of uniformly distributed  $t_1$  (applicable for  $t/T_1 \ll 1$ ) we obtain the uniform distribution for  $\bar{z}_{\text{tot}}^{(1)}$  within the interval  $[-1, \cos(2\theta)]$ . Convolution with the Gaussian noise will then lead to a slightly asymmetric probability distribution  $P^{(1)}(\bar{I}|\bar{10})$ .

Now let us calculate the histogram with *two jumps*. If the first jump occurs at time moment  $t_1$  and the return jump occurs at  $t_2$ , then the system spends duration  $\Delta t = t_2 - t_1$  in the “wrong” state  $|\bar{01}\rangle$ , so that

$$\bar{z}^{(2)} = \frac{t - 2\Delta t}{t} \cos(2\theta). \quad (\text{D.16})$$

In the case  $\Gamma_{\text{sw}}^- = \Gamma_{\text{sw}}^+$  the probability distribution of time moments  $t_1$  and  $t_2$  is uniform within the range  $0 \leq t_1 \leq t_2 \leq t$ , and therefore the normalized probability distribution for  $\Delta t$  is linearly decreasing,  $P_{\Delta t}(\Delta t) = (2/t)[1 - (\Delta t)/t]$ . This produces the linearly increasing probability distribution for the integrated signal,

$$P_z^{(2)}(\bar{z}_{\text{tot}}|\bar{10}) = \frac{\cos(2\theta) + \bar{z}_{\text{tot}}}{2 \cos^2(2\theta)}, \quad |\bar{z}_{\text{tot}}| \leq \cos(2\theta), \quad (\text{D.17})$$

which is illustrated in Fig. D.1(b). The convolution with the Gaussian white noise in Eq. (D.4) yields the measurement histogram

$$P^{(2)}(\bar{I}|\bar{10}) = \int_{-\cos(2\theta)}^{\cos(2\theta)} \frac{e^{-t(\bar{I}-\bar{z})^2/2\tau}}{\sqrt{2\pi\tau/t}} \frac{\cos(2\theta) + \bar{z}}{2 \cos^2(2\theta)} d\bar{z}, \quad (\text{D.18})$$

which we leave unevaluated here for brevity. As above, we can use approximation  $P^{(2)}(\bar{I}|\bar{10}) \approx P_z^{(2)}(\bar{I}|\bar{10})$  sufficiently far from the edges,  $\cos(2\theta) - |\bar{I}| \gtrsim 2\sqrt{\tau/t}$  [see Fig. D.1(b)].

In the case when  $\Gamma_{\text{sw}}^- \neq \Gamma_{\text{sw}}^+$ , the exact formulas are much lengthier because the probability distribution for the jump moments  $t_1$  and  $t_2$  [which is proportional to

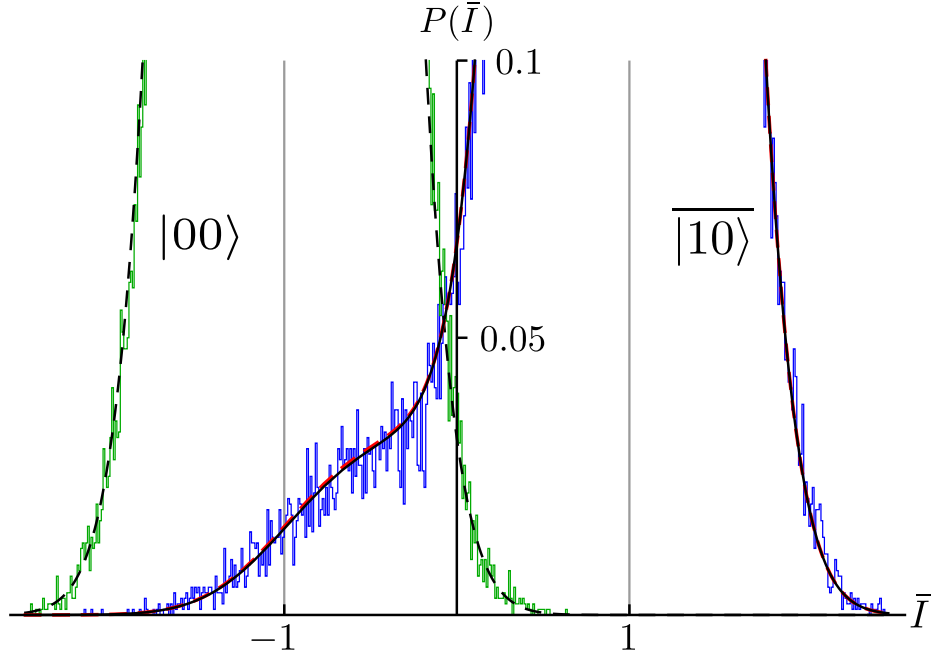


Figure D.2: Comparison between analytical and numerical results for the measurement histograms  $P(\bar{I}|00)$  and  $P(\bar{I}|\bar{10})$ . The green and blue lines show the same numerical results as in Fig. 2.6, but on an enlarged scale. The solid black line shows the analytical result [Eq. (D.7)] for  $P(\bar{I}|\bar{10})$ , taking into account up to two jumps. The almost coinciding red dashed line shows the result with up to one jump. The black dashed line shows Eq. (D.6) for  $P(\bar{I}|00)$ .

$e^{-(\Gamma_{\text{sw}}^+ - \Gamma_{\text{sw}}^-)(t_2 - t_1)}$  is no longer uniform. However, since  $|\Gamma_{\text{sw}}^+ - \Gamma_{\text{sw}}^-|t \ll 1$ , we can still approximate it as a uniform distribution, and then Eqs. (D.17) and (D.18) are still approximately valid. Since the two-jump histogram brings a very small contribution to the total histogram (D.7), any crude approximation should be sufficient. Note that if the first jump was due to the energy relaxation event, then the return jump is impossible.

Thus, the no-jump contribution to the total excited-state histogram (D.7) produces the main Gaussian shape, the single-jump contribution adds an extended nearly uniform tail, and the two-jump contribution produces a very small linearly increasing correction.

Figure D.2 shows on an enlarged scale the numerical (quantum trajectory) histograms presented in Fig. 2.6 (green and blue lines) and also shows the analytical results derived in this section. The solid black line shows the result for  $P(\bar{I}|\bar{10})$  using Eq. (D.7) taking into account up to two jumps, with  $\Gamma_{\text{sw}}^- = \Gamma_{\text{sw}}^+ = 2\Gamma_{\text{m}}g^2/(\Delta^2 + 4g^2)$  for parameters of Fig. 2.6 (so that  $\Gamma_{\text{sw}}^\pm\tau = 9.6 \times 10^{-3}$  and  $t/\tau = 7$ ). The dashed red line shows a similar result using a simplified one-jump approach, in which  $p_0 = e^{-\Gamma_{\text{sw}}^-t}$  and  $p_1 = 1 - p_0$ . We see that the difference between the results for the one-jump and two-jump approaches is very small, but the two-jump approach still agrees slightly better with the numerical results (blue line) for the tail of the distribution. It is interesting to note that the tail looks almost linearly increasing, in contrast to the horizontal shape expected from the uniform distribution of  $P_z^{(1)}(\bar{z}_{\text{tot}}|\bar{10})$ . This is because near its edge,  $\bar{I} = -\cos(2\theta) \approx -1$ , the Gaussian averaging plays the major role [see Fig. D.1(a)]. The black dashed line shows Eq. (D.6) for  $P(\bar{I}|00)$ ; its agreement with the numerical results (green line) is rather trivial because in this case only noise is simulated numerically.

The evolution of the tail of the excited-state distribution  $P(\bar{I}|\bar{10})$  is illustrated in Fig. D.3 (we do not show the ground-state histogram for clarity). We assume  $\Gamma_{\text{sw}}^\pm\tau = 10^{-3}$  and show the histogram at four equally spaced time points,  $t/\tau = 5, 10, 15, 20$ . At short integration times the Gaussian noise dominates, and the jump events contribute only a small bump distortion in the tail of the Gaussian. However, as the integration time increases, this bump grows to a flattened tail that becomes significant compared to the otherwise shrinking Gaussian noise. The overlap between  $P(\bar{I}|\bar{10})$  and  $P(\bar{I}|00)$  produces measurement error, which we discuss next.

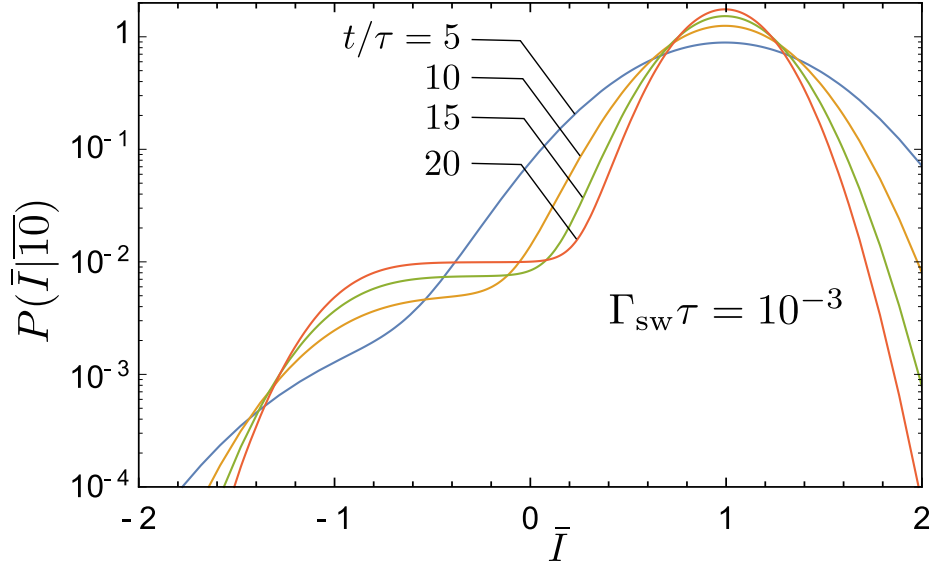


Figure D.3: Time evolution of the integrated signal histogram for an initially excited eigenstate  $|\bar{1}\bar{0}\rangle$ , shown on a semi-log scale, for times  $t/\tau = 5, 10, 15, 20$ , assuming  $\Gamma_{\text{sw}}^{\pm}\tau = 10^{-3}$ . The histogram width due to Gaussian noise decreases with increasing integration time, analogously to the ground state histogram (which is not shown). Also, a tail due to quantum jumps between the eigenstates appears at the left side of the histogram; this tail grows in amplitude and flattens with increasing integration time.

## D.2 Measurement error probability

We assume that the states  $|00\rangle$  and  $|\bar{1}\bar{0}\rangle$  are discriminated by integrating the normalized quadrature  $I(t)$  and comparing the result  $\bar{I}$  with a threshold value  $I_{\text{th}}$ . Slightly changing the notations used in the main text, we introduce the error probabilities for the two initial states as

$$P_{\text{err}}(t | 00) = \int_{I_{\text{th}}}^{\infty} P(\bar{I} | 00) d\bar{I}, \quad (\text{D.19})$$

$$P_{\text{err}}(t | \bar{1}\bar{0}) = \int_{-\infty}^{I_{\text{th}}} P(\bar{I} | \bar{1}\bar{0}) d\bar{I}, \quad (\text{D.20})$$

where in the notations of the main text  $P_{\text{err}}(t|00) \equiv P_{\text{err}}^{(0)}$  and  $P_{\text{err}}(t|\bar{10}) \equiv P_{\text{err}}^{(1)}$ , so that the overall error is

$$P_{\text{err}}(t) = \frac{1}{2} [P_{\text{err}}(t|00) + P_{\text{err}}(t|\bar{10})]. \quad (\text{D.21})$$

The error for the ground state  $|00\rangle$  has a simple form,

$$P_{\text{err}}(t|00) = \frac{1}{2} \left[ 1 - \text{erf} \frac{1 + I_{\text{th}}}{\sqrt{2\tau/t}} \right], \quad (\text{D.22})$$

which follows from Eq. (D.6). The error for the state  $|\bar{10}\rangle$  can be calculated as a weighted sum of contributions from zero, one, and two jumps, following Eq. (D.7),

$$P_{\text{err}}(t|\bar{10}) = p_0 P_{\text{err}}^{(0)}(t|\bar{10}) + p_1 P_{\text{err}}^{(1)}(t|\bar{10}) + p_2 P_{\text{err}}^{(2)}(t|\bar{10}), \quad (\text{D.23})$$

with the probabilities  $p_k$  of  $k$  jumps given by Eqs. (D.8) and (D.9), and the partial error probabilities,

$$P_{\text{err}}^{(k)}(t|\bar{10}) = \int_{-\infty}^{I_{\text{th}}} P^{(k)}(\bar{I}|\bar{10}) d\bar{I}, \quad (\text{D.24})$$

obtained from the partial histograms  $P^{(k)}(\bar{I}|\bar{10})$  discussed above.

The zero-jump error is then similar to the ground-state error,

$$P_{\text{err}}^{(0)}(t|\bar{10}) = \frac{1}{2} \left[ 1 - \text{erf} \frac{\cos(2\theta) - I_{\text{th}}}{\sqrt{2\tau/t}} \right], \quad (\text{D.25})$$

and similarly to Eq. (D.22), it steadily decreases with increasing  $t$ . The exact formula for the single-jump error  $P_{\text{err}}^{(1)}(t|\bar{10})$  is very lengthy, but for practical purposes it can be significantly simplified. First, let us note that in the case  $\Gamma_{\text{sw}}^- = \Gamma_{\text{sw}}^+$ , the distribution (D.14) for  $P^{(1)}(\bar{I}|\bar{10})$  is symmetric (since it is a convolution of a symmetric distribution  $P_z^{(1)}(\bar{z}_{\text{tot}}|\bar{10})$  and Gaussian noise). Therefore, for the symmetric threshold,  $I_{\text{th}} = 0$ , we have  $P_{\text{err}}^{(1)}(t|\bar{10}) = 1/2$ . Second, for  $t/\tau \gtrsim 4$ , the distribution  $P^{(1)}(\bar{I}|\bar{10}) \approx [2 \cos(2\theta)]^{-1}$

is practically flat for  $I_{\text{th}}$  close to zero,  $\cos(2\theta) - |I_{\text{th}}| \gtrsim \sqrt{4\tau/t}$ . Therefore, in this case  $dP_{\text{err}}^{(1)}(t|\bar{10})/dI_{\text{th}} \approx [2\cos(2\theta)]^{-1}$ , which gives

$$P_{\text{err}}^{(1)}(t|\bar{10}) \approx \frac{1}{2} + \frac{I_{\text{th}}}{2\cos(2\theta)}. \quad (\text{D.26})$$

Very near the symmetric threshold,  $|I_{\text{th}}| \lesssim \tau/3t$ , a better approximation is possible,

$$P_{\text{err}}^{(1)}(t|\bar{10}) \approx \frac{1}{2} + \frac{I_{\text{th}}}{2\cos(2\theta)} \operatorname{erf} \frac{\cos(2\theta)}{\sqrt{2\tau/t}}, \quad (\text{D.27})$$

which corresponds to the exact derivative at  $I_{\text{th}} = 0$ ,  $P^{(1)}(\bar{I} = 0|\bar{10}) = [2\cos(2\theta)]^{-1} \times \operatorname{erf}[\cos(2\theta)/\sqrt{2\tau/t}]$ . Note that very good accuracy for  $P_{\text{err}}^{(1)}(t|\bar{10})$  is not really needed since its weight  $p_1$  in Eq. (D.23) is small. In the case  $\Gamma_{\text{sw}}^- \neq \Gamma_{\text{sw}}^+$  we can use approximation (D.15) and neglect the Gaussian averaging, assuming  $\cos(2\theta) - |I_{\text{th}}| \gtrsim \sqrt{4\tau/t}$ . Then Eq. (D.26) generalizes as

$$P_{\text{err}}^{(1)}(t|\bar{10}) \approx \frac{1}{2} + \frac{I_{\text{th}}}{2\cos(2\theta)} - \frac{(\Gamma_{\text{sw}}^+ - \Gamma_{\text{sw}}^-)t}{8} \left(1 - \frac{I_{\text{th}}^2}{\cos^2(2\theta)}\right). \quad (\text{D.28})$$

Note that for  $|\Gamma_{\text{sw}}^+ - \Gamma_{\text{sw}}^-|t \ll 1$  and  $I_{\text{th}} = 0$  we have  $P_{\text{err}}^{(1)}(t|\bar{10}) \approx 1/2$ , which stems from the property that a nearly symmetric distribution (D.15) for  $\bar{z}_{\text{tot}}^{(1)}$  remains nearly symmetric after convolution with the Gaussian noise. This explain the factor 1/2 in Eq. (2.38) of the main text, which follows from Eq. (D.23) with  $p_0 \approx 1$ ,  $p_1 \approx \Gamma_{\text{sw}}^- t$ , and  $p_2 \approx 0$ . Similar approximations have been used in Eq. (2.43), in which we also assumed  $\cos(2\theta) \approx 1$ .

The double-jump contribution to the total error (D.23) is very small because of small probability  $p_2$ . Therefore, it is sufficient to use a crude estimate for  $P_{\text{err}}^{(2)}(t|\bar{10})$ . In particular, using Eq. (D.17) and assuming  $P^{(2)}(\bar{I}|\bar{10}) \approx P_z^{(2)}(\bar{I}|\bar{10})$ , we find

$$P_{\text{err}}^{(2)}(t|\bar{10}) \approx \frac{1}{4} + \frac{I_{\text{th}}}{2\cos(2\theta)} + \frac{I_{\text{th}}^2}{4\cos^2(2\theta)}. \quad (\text{D.29})$$

Even though we neglect the three-jump processes, we actually take into account the main contribution from them automatically, by combining their probability  $p_3$  with  $p_1$  in Eqs. (D.8) and (D.9). This is because  $P_{\text{err}}^{(3)}(t|\overline{10}) \approx 1/2$  for  $I_{\text{th}} = 0$  (following from the symmetry of three-jump processes), which is the same as  $P_{\text{err}}^{(1)}(t|\overline{10})$ . However, the dependence on  $I_{\text{th}}$  for the one-jump and three-jump terms is different.

The blue dot-dashed line in Fig. 2.8 in the main text shows the error  $P_{\text{err}}(t|\overline{10})$  calculated using Eq. (D.23) with the probabilities  $p_k$  given by Eq. (D.8), the term  $P_{\text{err}}^{(0)}(t|\overline{10})$  given by Eq. (D.25), the term  $P_{\text{err}}^{(1)}(t|\overline{10})$  equal to  $1/2$  (because in Fig. 2.8 we use symmetric threshold,  $I_{\text{th}} = 0$ ), and the term  $P_{\text{err}}^{(2)}(t|\overline{10})$  obtained by integration of the histogram (D.18). This analytics fits the numerical result (red solid line in Fig. 2.8) significantly better than the simple analytics (dashed green line) discussed in the main text. Actually, for the two-jump processes it is sufficient to use  $P_{\text{err}}^{(2)}(t|\overline{10}) = 1/4$  [see Eq. (D.29)] instead of numerical integration; the result is almost indistinguishable. Note that this is practically equivalent to using  $p_0 = e^{-\Gamma_{\text{sw}}^- t}$ ,  $p_1 = \Gamma_{\text{sw}}^- t [1 - (3/4)\Gamma_{\text{sw}}^- t]$ ,  $p_2 = 0$ .

Finally, we emphasize that we have used the initial eigenstate  $|\overline{10}\rangle$  in the definition for measurement error in Eq. (D.20), since this is the optimal choice of logical encoding for the regime with  $\Gamma_{\text{m}} \ll \Delta$ . If instead we use the bare state  $|10\rangle$ , then it will additionally collapse to a mixture of the eigenstates  $|\overline{10}\rangle$  and  $|\overline{01}\rangle$ , which will increase the error,

$$\begin{aligned} P_{\text{err}}(t|10) &= \cos^2(\theta) P_{\text{err}}(t|\overline{10}) + \sin^2(\theta)[1 - P_{\text{err}}(t|\overline{10})], \\ &= \cos(2\theta) P_{\text{err}}(t|\overline{10}) + \sin^2 \theta. \end{aligned} \tag{D.30}$$

Thus, for the total error (D.21), we will have a nearly constant amount of additional error when distinguishing bare qubit states,  $P_{\text{err,bare}} \approx P_{\text{err}} + (g/\Delta)^2/2$  for  $g \ll \Delta$ .

## Appendix E

# Vanishing entanglement in dressed coherent and squeezed states

This appendix is related to Chapter 3, and uses the same notations as in that chapter. Here we show that dressed coherent states and dressed squeezed states are practically unentangled for large average numbers of photons  $\bar{n}$ . For a dressed coherent state we can anticipate this result because coherent states with large  $\bar{n}$  are practically classical. Thus, the transmon is essentially driven by a classical field, and should therefore produce an unentangled state. However, this result is rather paradoxical because the dressed coherent state (3.10) is constructed out of highly entangled eigenstates of the transmon-resonator system, so significant entanglement could be naively expected. The derivation below resolves this paradox. A similar result also applies to a dressed squeezed state.

Let us consider a general dressed state

$$|\psi\rangle = \sum_n c_n \overline{|n, k\rangle}, \quad (\text{E.1})$$

where  $|\overline{n, k}\rangle$  are the eigenstates of the transmon-resonator system for the transmon nominally in the state  $|k\rangle_{\text{q}}$ , and the coefficients  $c_n$  describe the nominal resonator state  $\sum_n c_n |n\rangle_{\text{r}}$ ,  $\sum_n |c_n|^2 = 1$ . Our first goal is to derive a condition for which this dressed state can be approximately represented as a direct product of the resonator state  $\sum_n c_n |n\rangle_{\text{r}}$  and some transmon state (which will be generally different from the nominal state  $|k\rangle_{\text{q}}$ ).

The eigenstate  $|\overline{n, k}\rangle$  can be expanded in the bare basis (within the RWA strip) as

$$|\overline{n, k}\rangle = \sum_l d_l^{(n, k)} |n - l, k + l\rangle, \quad (\text{E.2})$$

where the summation involves a few transmon levels,  $-k \leq l \leq k_{\text{max}} - k$ ,  $k < k_{\text{max}} \simeq 7$ . The coefficients  $d_l^{(n, k)}$  depend on  $n$  because the coupling (3.4) between neighboring bare levels  $|n - l, k + l\rangle$  and  $|n - l - 1, k + l + 1\rangle$  is proportional to  $\sqrt{n - l}$ . However, this dependence can be neglected,  $\sqrt{n - l} \approx \sqrt{\bar{n} - l}$  if

$$\sigma_n \ll \bar{n}, \quad k_{\text{max}} \ll \bar{n}, \quad (\text{E.3})$$

where by the standard deviation  $\sigma_n$  we characterize the spread of  $n$  in the state (E.1). In this case we can use approximation with  $n$ -independent coefficients  $d_l^{(k)}$  (which may still depend on  $\bar{n}$ ),

$$|\overline{n, k}\rangle \approx \sum_l d_l^{(k)} |n - l, k + l\rangle. \quad (\text{E.4})$$

Substituting Eq. (E.4) into Eq. (E.1), shifting the indices,  $n - l \rightarrow n$ , and changing the order of summation, we obtain

$$\begin{aligned} |\psi\rangle &\approx \sum_l d_l^{(k)} \sum_n c_{n+l} |n, k + l\rangle \\ &= \sum_l d_l^{(k)} |k + l\rangle_{\text{q}} |\phi_l\rangle, \end{aligned} \quad (\text{E.5})$$

$$|\phi_l\rangle = \sum_n c_{n+l} |n\rangle_{\text{r}}, \quad (\text{E.6})$$

where  $|k + l\rangle_{\text{q}}$  is the transmon level and  $|\phi_l\rangle$  is the resonator state, which depends on transmon index  $l$ . Note that  $|\phi_l\rangle$  are (practically) normalized, since the coefficients  $c_{n+l}$  are the same as in the normalized state (E.1) and the shift of indices by  $l$  is not important when the condition (E.3) is satisfied.

The dependence of  $|\phi_l\rangle$  on the transmon index  $l$  indicates the entanglement between the transmon and resonator. If  $|\phi_l\rangle$  were not dependent on  $l$ , then  $|\psi\rangle$  in Eq. (E.5) is an (unentangled) direct product of the transmon and resonator states. Moreover, any  $l$ -dependent phase factor,  $|\phi_l\rangle = e^{i\varphi_l}|\phi_0\rangle$ , may be absorbed into the transmon state, still yielding a direct product. This gives us a *condition* for the approximate absence of entanglement:  $|\langle\phi_0|\phi_l\rangle| \approx 1$  for all transmon indices  $l$ .

Thus, we have shown that if

$$\left| \sum_n c_n^* c_{n+l} \right| \approx 1 \quad (\text{E.7})$$

for any  $l$  within the relevant range,  $|l| \leq k_{\text{max}} \simeq 7$ , then the dressed state (E.1) is approximately a direct product,

$$\sum_n c_n \overline{|n, k\rangle} \approx \sum_n c_n |n\rangle_{\text{r}} \otimes \sum_l e^{i\varphi_l} d_l^{(k)} |k + l\rangle_{\text{q}}, \quad (\text{E.8})$$

where  $\varphi_l = \arg(\sum_n c_n^* c_{n+l})$  and  $d_l^{(k)}$  are the coefficients in the eigenstate (E.4).

Now let us show that the condition (E.7) is satisfied for a *dressed coherent state*  $|\alpha\rangle_k$  given by Eq. (3.10). Since in this case  $c_n = \exp(-|\alpha|^2/2) \alpha^n / \sqrt{n!}$ , we find

$$\begin{aligned} \sum_n c_n^* c_{n+l} &= \sum_n e^{-|\alpha|^2} \frac{|\alpha|^{2n}}{n!} \frac{|\alpha|^l e^{il \arg(\alpha)}}{\sqrt{(n+1)(n+2)\cdots(n+l)}} \\ &\approx e^{i\varphi_l}, \quad \varphi_l = l \arg(\alpha), \end{aligned} \quad (\text{E.9})$$

where we approximated  $\sqrt{(n+1)(n+2)\cdots(n+l)} \approx n^{l/2} \approx |\alpha|^l$ . This approximation requires  $|\alpha|^2 \gg l^2$ . Thus, the dressed coherent state  $|\alpha\rangle_k$  is practically unentangled if  $|\alpha|^2 \gg k_{\max}^2$ .

The solid lines in Fig. E.1(a) show the inaccuracy of the direct-product approximation (E.8) for the dressed coherent state  $|\alpha\rangle_0$  as a function of  $|\alpha|^2$  for typical parameters:  $(\omega_r - \omega_q)/2\pi = 1$  GHz,  $\eta/2\pi = 200$  MHz, and  $g/2\pi = 100$  MHz (lower blue line,  $n_c = 25$ ) or  $g/2\pi = 141.4$  MHz (upper orange line,  $n_c = 12.5$ ). As a measure of inaccuracy we use  $1 - |\langle\psi_{\text{dp}}|\alpha\rangle_0|^2$ , where the direct-product state  $|\psi_{\text{dp}}\rangle$  is given by Eq. (E.8). Note that for small  $\alpha$  we average coefficients  $d_l^{(n,k)}$  in Eq. (E.2) to obtain  $d_l^{(k)}$ . We see that the solid lines in Fig. E.1(a) significantly increase with  $\bar{n} \approx |\alpha|^2$  until  $\bar{n}$  becomes much larger than  $n_c$ . This behavior is due to a competition between the continuously increasing entanglement of eigenstates (E.2) and the decrease of entanglement due to the increasingly satisfied condition (E.7). However, we see that even at large  $\bar{n}$ , the dressed coherent state  $|\alpha\rangle_0$  is very close to the direct-product state (E.8). For comparison, we show with blue and orange dots the much larger inaccuracy when we try to approximate the corresponding eigenstates  $|\bar{n}, 0\rangle$  (i.e., the dressed Fock states) with similar direct-product wavefunctions. It is easy to prove that the best such approximation is the bare state with the largest coefficient in the expansion (E.2); the visible kinks in Fig. E.1(a) are due to the change of this best bare state. Figure E.1(b) is similar to Fig. E.1(a), except it shows the entanglement of formation [268] (equal to the entropy of entanglement for pure states) for the same dressed coherent states  $|\alpha\rangle_0$  and dressed Fock states  $|\bar{n}, 0\rangle$ . With this measure we again confirm that the dressed coherent states are practically unentangled, in contrast to the strongly entangled

dressed Fock states [note an overall similarity between Figs. E.1(a) and E.1(b)].

Even though a dressed coherent state is practically unentangled, there is a strong classical correlation between the resonator and transmon dynamics. This can be seen by adding explicit time dependence into Eq. (E.8), thus going from the rotating frame into the lab frame. Replacing coefficients  $c_n$  for the coherent state with  $c_n(t) = e^{-in\omega_r t} c_n(0)$  (the remaining factor  $e^{-iE(k, \bar{n})t}$  is an overall phase and therefore not important), we find  $\alpha(t) = e^{-i\omega_r t} \alpha(0)$ . As a result,  $\phi_l = l \arg[\alpha(0)] - l\omega_r t$ , and therefore the dressed coherent state evolves in time as

$$|\alpha\rangle_k = |e^{-i\omega_r t} \alpha(0)\rangle_r \otimes \sum_l e^{-il\omega_r t} e^{il \arg[\alpha(0)]} d_l^{(k)} |k+l\rangle_q. \quad (\text{E.10})$$

We see that both resonator and transmon states are evolving with the period  $2\pi/\omega_r$  in a phase-synchronized way; the resonator state evolution is a simple oscillation, but the transmon evolution within the period is quite non-trivial. This is exactly what we would expect classically for a non-linear oscillator that is harmonically driven with frequency  $\omega_r$ . We have performed numerical simulations for the transmon state evolution in Eq. (E.10) using the  $x$ -representation (where  $x$  in this case is the superconducting phase difference) and confirmed such non-trivial evolution within one period of oscillations when  $\bar{n}$  is significantly larger than  $n_c$ .

To check the direct-product condition (E.7) for a *dressed squeezed state*, let us use its approximate sheared Gaussian representation in Eq. (3.22). Then we find

$$\sum_n c_n^* c_{n+l} \approx e^{il \arg(\beta)} \left[ 1 - \frac{l^2}{2W\bar{n}} - \frac{2K^2W}{\bar{n}} l^2 \right], \quad (\text{E.11})$$

assuming large  $\bar{n} = |\beta|^2$ . We see that the condition (E.7) is satisfied if

$$\bar{n} \gg k_{\max}^2 \max(1/2W, 2K^2W). \quad (\text{E.12})$$

In this case the dressed squeezed state is practically unentangled. For the dressed coherent state ( $W = 1, K = 0$ ) this inequality reduces to  $\bar{n} \gg k_{\max}^2$ , as expected.

Note that in the case when the dressed sheared state is practically unentangled, the phase  $\varphi_l = l \arg(\beta)$  in Eq. (E.8) is still the same as for the dressed coherent state (except for the notation change,  $\alpha \rightarrow \beta$ ). Therefore, the transmon state and its evolution within the period of  $\omega_r$  is still the same as for the dressed coherent state with  $\alpha = \beta$ . In other words, for sufficiently large  $\bar{n}$  there is no difference for the transmon if it is driven by a coherent or a squeezed field from the resonator.

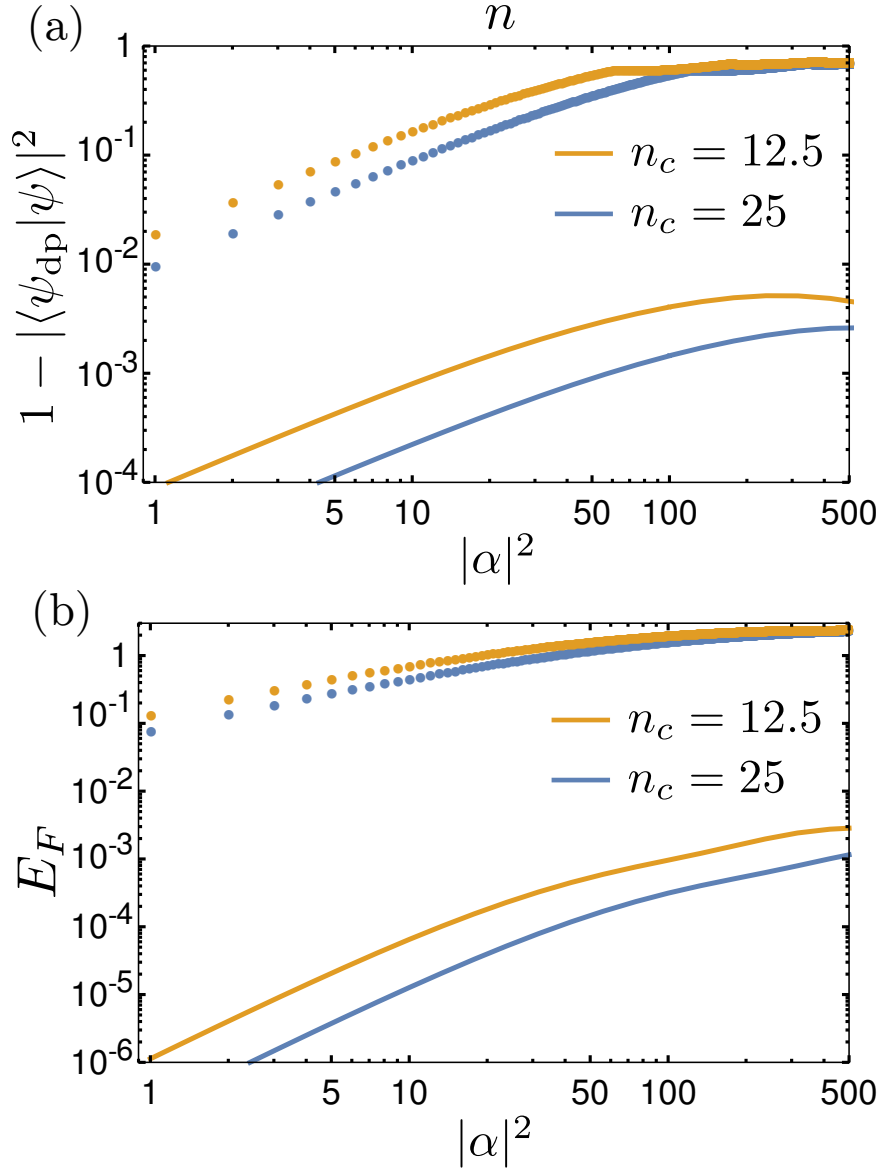


Figure E.1: (a) Solid lines: infidelity  $1 - |\langle \psi_{\text{dp}} | \alpha \rangle_0|^2$  of approximating the dressed coherent state  $|\alpha\rangle_0$  with a direct-product state  $|\psi_{\text{dp}}\rangle$  given by Eq. (E.8), as a function of  $|\alpha|^2$ . For comparison, the dots show similar infidelity for the eigenstates  $|n, 0\rangle$ , i.e., dressed Fock states, as a function of  $n$  (axes of  $n$  and  $|\alpha|^2$  coincide). We assume  $(\omega_r - \omega_q)/2\pi = 1$  GHz,  $\eta/2\pi = 200$  MHz, and  $g/2\pi = 100$  MHz (lower blue line/dots,  $n_c = 25$ ) or  $g/2\pi = 141.4$  MHz (upper orange line/dots,  $n_c = 12.5$ ). (b) Entanglement of formation  $E_F$  (coinciding with entropy of entanglement) for the dressed coherent states  $|\alpha\rangle_0$  (lines) and dressed Fock states (dots) with the same parameters as in (a).

## Appendix F

# Rotating-frame evolution of a linear-resonator state

This appendix is related to Chapter 5, and uses the same notations as in that chapter. Here we discuss derivation of the rotating-frame equations (5.38)–(5.41) for evolution of the Gaussian-state parameters  $\beta$ ,  $D_0$ ,  $b$ , and  $\theta$  from the laboratory-frame equations (5.32)–(5.36), using the rotating wave approximation (RWA).

Let us start with introducing the rotating frame based on the drive frequency  $\omega_d$ , by defining the dimensionless rotating-frame position and momentum operators  $\hat{x}$  and  $\hat{p}$  as

$$\hat{x} + i\hat{p} = (\hat{x} + i\hat{p}) e^{i\omega_d t}. \quad (\text{F.1})$$

This is equivalent to introducing a new lowering operator  $\hat{a} = \hat{a} e^{i\omega_d t}$ . From Eq. (F.1) we

obtain the canonical transformation

$$\hat{x} = \hat{x} \cos \omega_d t + \hat{p} \sin \omega_d t, \quad (\text{F.2})$$

$$\hat{p} = \hat{p} \cos \omega_d t - \hat{x} \sin \omega_d t. \quad (\text{F.3})$$

To find the rotating-frame evolution equation for the Gaussian state center, we use Eqs. (5.32) and (5.33) for the evolution of  $x_c = \langle \hat{x} \rangle$  and  $p_c = \langle \hat{p} \rangle$ , and convert them into equations for  $\tilde{x}_c = \langle \hat{x} \rangle$  and  $\tilde{p}_c = \langle \hat{p} \rangle$ , thus obtaining

$$\begin{aligned} \frac{d}{dt}(\tilde{x}_c + i\tilde{p}_c) &= -i(\omega_r - \omega_d)(\tilde{x}_c + i\tilde{p}_c) - i\varepsilon - i\varepsilon^* e^{i2\omega_d t} \\ &\quad - i\kappa \left( \tilde{p}_c \frac{1 + e^{i2\omega_d t}}{2} + \tilde{x}_c \frac{1 - e^{i2\omega_d t}}{2i} \right). \end{aligned} \quad (\text{F.4})$$

This equation is still exact. Now using RWA, we neglect the terms oscillating with frequency  $2\omega_d$ , thus obtaining slow evolution of the Gaussian state center,

$$\dot{\beta} = -i(\omega_r - \omega_d)\beta - \frac{\kappa}{2}\beta - i\varepsilon, \quad \beta \equiv \tilde{x}_c + i\tilde{p}_c, \quad (\text{F.5})$$

which is Eq. (5.38).

To derive Eqs. (5.39) and (5.40) for  $\dot{D}_0$  and  $\dot{b}$ , let us start with expressing  $D_x$ ,  $D_p$ , and  $D_{xp}$  via the corresponding rotating-frame quantities  $D_{\tilde{x}}$ ,  $D_{\tilde{p}}$ , and  $D_{\tilde{x}\tilde{p}}$  (with obvious definitions)

$$D_x = D_{\tilde{x}} \cos^2(\omega_d t) + D_{\tilde{p}} \sin^2(\omega_d t) + D_{\tilde{x}\tilde{p}} \sin(2\omega_d t), \quad (\text{F.6})$$

$$D_p = D_{\tilde{x}} \sin^2(\omega_d t) + D_{\tilde{p}} \cos^2(\omega_d t) - D_{\tilde{x}\tilde{p}} \sin(2\omega_d t), \quad (\text{F.7})$$

$$D_{xp} = D_{\tilde{x}\tilde{p}} \cos(2\omega_d t) + (1/2)(D_{\tilde{p}} - D_{\tilde{x}}) \sin(2\omega_d t). \quad (\text{F.8})$$

Note that  $D_0 \equiv (D_x + D_p)/2$  has the same expression in the rotating frame,  $D_0 = (D_{\tilde{x}} + D_{\tilde{p}})/2$ ; similarly,  $b^2 \equiv (D_p - D_x)^2/4 + D_{xp}^2$  can also be expressed as  $b^2 = (D_{\tilde{p}} - D_{\tilde{x}})^2/4 + D_{\tilde{x}\tilde{p}}^2$ .

For the evolution of  $D_0$ , from Eqs. (5.34) and (5.35) we find  $\dot{D}_0 = -\kappa D_p + (\kappa/4) \coth(\omega_r/2T_b)$ . Then using Eq. (F.7), we obtain

$$\begin{aligned} \dot{D}_0 = & -\kappa[D_{\tilde{x}} \sin^2(\omega_d t) + D_{\tilde{p}} \cos^2(\omega_d t) - D_{\tilde{x}\tilde{p}} \sin(2\omega_d t)] \\ & + (\kappa/4) \coth(\omega_r/2T_b). \end{aligned} \quad (\text{F.9})$$

Now using RWA, we neglect the terms oscillating with frequency  $2\omega_d$ , so that  $\sin^2(\omega_d t) \rightarrow 1/2$ ,  $\cos^2(\omega_d t) \rightarrow 1/2$ , and  $\sin(2\omega_d t) \rightarrow 0$ . This gives us

$$\dot{D}_0 = -\kappa D_0 + (\kappa/4) \coth(\omega_r/2T_b), \quad (\text{F.10})$$

which is Eq. (5.39).

For the evolution of  $b$ , from Eqs. (5.34)–(5.36) we obtain

$$\begin{aligned} d(b^2)/dt = & (\kappa/4)(D_p - D_x) \coth(\omega_r/2T_b) \\ & - \kappa(D_p - D_x)D_p - 2\kappa D_{xp}^2. \end{aligned} \quad (\text{F.11})$$

Within RWA, the first term on the right-hand side is zero because  $D_p - D_x$  oscillates with frequency  $2\omega_d$  [see Eqs. (F.6) and (F.7)]. The second term is not zero because  $D_p$  has also a part oscillating with  $2\omega_d$ ; averaging over these oscillations we obtain  $-\kappa[D_{\tilde{x}\tilde{p}}^2 + (D_{\tilde{p}} - D_{\tilde{x}})^2/4]$ , which equals  $-\kappa b^2$ . Similarly, for the third term we use Eq. (F.8) and averaging over the oscillations obtain  $-\kappa[D_{\tilde{x}\tilde{p}}^2 + (D_{\tilde{p}} - D_{\tilde{x}})^2/4]$ , which is again  $-\kappa b^2$ . Thus, within RWA

$$d(b^2)/dt = -2\kappa b^2. \quad (\text{F.12})$$

Equivalently,  $\dot{b} = -\kappa b$ , which is Eq. (5.40).

To derive Eq. (5.41) for  $\dot{\theta}$ , we start with Eqs. (5.14) and (5.31), which give

$$\begin{aligned} \theta &= \arctan\left(\frac{2D_{xp}}{D_x - D_p}\right) + 2\omega_d t \\ &+ (\pi/2)[1 + \text{sign}(D_x - D_p)]. \end{aligned} \quad (\text{F.13})$$

Neglecting the last term, the time derivative is

$$\dot{\theta} = \frac{\dot{D}_{xp}(D_x - D_p) - D_{xp}(\dot{D}_x - \dot{D}_p)}{2b^2} + 2\omega_d. \quad (\text{F.14})$$

Using Eqs. (5.34)–(5.36), we find that the numerator here is  $-4\omega_r b^2 - 2\kappa D_{xp} D_0 + (\kappa/2) D_{xp} \times \coth(\omega_r/2T_b)$ , in which the only non-oscillating term is  $-4\omega_r b^2$ . Dividing it by  $2b^2$  and adding  $2\omega_d$ , from Eq. (F.14) we obtain  $\dot{\theta} = -2(\omega_r - \omega_d)$ , which is Eq. (5.41).

## Appendix G

# Equivalence between Gaussian and Fock-space Gaussian states

This appendix is related to Chapter 5, and uses the same notations as in that chapter. Here we show that the Fock-space Gaussian state introduced in Eq. (5.42) is approximately the same as the standard Gaussian state [Eq. (5.9)] in the limit of large photon number,  $|\beta| \gg 1$ , and derive the conversion relations (5.44)–(5.47). This is done by comparing the Husimi  $Q$ -functions of the Gaussian and Fock-space Gaussian states. We use the rotating frame and characterize the Gaussian state by the complex parameter  $\beta$  (center) and three real parameters:  $D_0$ ,  $b$ , and  $\theta$  – see Eqs. (5.12)–(5.14). The Fock-space Gaussian state is characterized by the complex parameter  $e^{i\phi_\beta}|\beta|$  (which is chosen to be the same as  $\beta$ ) and three real parameters:  $W_1$ ,  $W_2$ , and  $K$  – see Eq. (5.42).

The Husimi  $Q$ -function  $Q(\alpha)$  of a state with density matrix  $\rho$  is defined via its

overlap with the coherent state  $|\alpha\rangle$ ,

$$Q(\alpha) = \frac{1}{\pi} \langle \alpha | \rho | \alpha \rangle, \quad |\alpha\rangle = e^{-\frac{1}{2}|\alpha|^2} \sum_{n=0}^{\infty} \frac{\alpha^n}{\sqrt{n!}} |n\rangle, \quad (\text{G.1})$$

where  $\alpha = \tilde{x} + i\tilde{p}$  assumes the rotating frame, in contrast to the notation  $\alpha$  used in Sec. 5.3.1. The function  $Q(\alpha)$  can be calculated from the Wigner function  $W(\alpha)$  (here in the rotating frame; note a slightly different notation used in Sec. 5.3.1),

$$Q(\alpha) = \frac{2}{\pi} \int W(\alpha') e^{-2|\alpha-\alpha'|^2} d\text{Re}(\alpha') d\text{Im}(\alpha'). \quad (\text{G.2})$$

For the Gaussian state (5.9) it is equal

$$\begin{aligned} Q(\alpha) &= \pi^{-1} [4(D_0 - b + 1/4)(D_0 + b + 1/4)]^{-1/2} \\ &\times \exp \left\{ -\frac{(D_0 + b \cos \theta + 1/4) [\text{Re}(\alpha - \beta)]^2}{2(D_0 - b + 1/4)(D_0 + b + 1/4)} \right. \\ &\quad - \frac{(D_0 - b \cos \theta + 1/4) [\text{Im}(\alpha - \beta)]^2}{2(D_0 - b + 1/4)(D_0 + b + 1/4)} \\ &\quad \left. - \frac{(2b \sin \theta) \text{Re}(\alpha - \beta) \text{Im}(\alpha - \beta)}{2(D_0 - b + 1/4)(D_0 + b + 1/4)} \right\}. \end{aligned} \quad (\text{G.3})$$

Recall that  $\beta$  is the Gaussian state center,  $D_0 + b$  is the maximum quadrature variance,  $D_0 - b$  is the minimum quadrature variance, and  $\theta/2$  is the angle between the minimum quadrature direction and  $\tilde{x}$ -axis (see Fig. 5.1). Note that in the diagonal basis, Eq. (G.3) reduces to Eq. (5.17), up to a slight change of notations.

Now let us calculate the  $Q$ -function for the Fock-space Gaussian state, Eq. (5.42), and compare it with Eq. (G.3). We will use a series of approximations to calculate  $Q(\alpha)$ . First, for  $|\beta| \gg 1$  we can also assume  $|\alpha| \gg 1$ ; then the coherent state  $|\alpha\rangle$  in Eq. (G.1) can be approximated as  $|\alpha\rangle \approx (2\pi|\alpha|^2)^{-1/4} \sum_n \exp[-(n - |\alpha|^2)^2/4|\alpha|^2] \exp[in\phi_\alpha]$ , where

$\phi_\alpha = \arg(\alpha)$ , so that the  $Q$ -function is approximately

$$Q(\alpha) = \frac{1}{\pi\sqrt{2\pi|\alpha|^2}} \sum_{n,m=0}^{\infty} \rho_{nm} \exp \left[ -\frac{(n-|\alpha|^2)^2}{4|\alpha|^2} - \frac{(m-|\alpha|^2)^2}{4|\alpha|^2} - i\phi_\alpha(n-m) \right]. \quad (\text{G.4})$$

Substituting  $\rho_{nm}$  from Eq. (5.42), we obtain

$$Q(\alpha) = N \sum_{n,m} \exp[-An^2 - \tilde{A}m^2 - B(m)n - \tilde{B}m - C], \quad (\text{G.5})$$

$$N = \pi^{-1}(4\pi^2W_1|\beta|^2|\alpha|^2)^{-1/2}, \quad (\text{G.6})$$

$$A = \frac{1}{4|\alpha|^2} + \frac{1}{8W_1|\beta|^2} + \frac{1}{8W_2|\beta|^2} + i\frac{K}{|\beta|^2}, \quad (\text{G.7})$$

$$\tilde{A} = \frac{1}{4|\alpha|^2} + \frac{1}{8W_1|\beta|^2} + \frac{1}{8W_2|\beta|^2} - i\frac{K}{|\beta|^2}, \quad (\text{G.8})$$

$$B(m) = -\frac{1}{2} + i(\phi_\alpha - \phi_\beta) + \frac{m}{4W_1|\beta|^2} - \frac{1}{2W_1} - \frac{m}{4W_2|\beta|^2} - 2iK, \quad (\text{G.9})$$

$$\tilde{B} = -\frac{1}{2} - i(\phi_\alpha - \phi_\beta) - \frac{1}{2W_1} + 2iK, \quad (\text{G.10})$$

$$C = \frac{|\alpha|^2}{2} + \frac{|\beta|^2}{2W_1}. \quad (\text{G.11})$$

Then replacing summation over  $n$  and  $m$  by integration within infinite limits (assuming  $|\beta| \gg 1$ ) and calculating the integral over  $n$ , we find

$$Q(\alpha) = N \frac{\sqrt{\pi}e^{-C}}{\sqrt{A}} \int_{-\infty}^{\infty} \exp \left[ \frac{[B(m)]^2}{4A} - \tilde{A}m^2 - \tilde{B}m \right] dm. \quad (\text{G.12})$$

Using Eq. (G.9), we then represent  $[B(m)]^2/4A$  as

$$[B(m)]^2/4A = \bar{A}m^2 + \bar{B}m + \bar{C}, \quad (\text{G.13})$$

$$\bar{A} = \frac{1}{4A} \left( \frac{1}{4W_1|\beta|^2} \right)^2 \left( 1 - \frac{W_1}{W_2} \right)^2, \quad (\text{G.14})$$

$$\bar{B} = \frac{1}{4A} \frac{1}{2W_1|\beta|^2} \left( 1 - \frac{W_1}{W_2} \right) \left[ -\frac{1}{2} - \frac{1}{2W_1} + i(\phi_\alpha - \phi_\beta) - 2iK \right], \quad (\text{G.15})$$

$$\bar{C} = \frac{1}{4A} \left( -\frac{1}{2} - \frac{1}{2W_1} + i(\phi_\alpha - \phi_\beta) - 2iK \right)^2. \quad (\text{G.16})$$

Then the exponent in Eq. (G.12) is  $\exp[-(\tilde{A} - \bar{A})m^2 - (\tilde{B} - \bar{B})m]$  and its integral over  $dm$  can be easily calculated,

$$Q(\alpha) = (2\pi\sqrt{W_1}|\beta||\alpha|)^{-1} [A(\tilde{A} - \bar{A})]^{-1/2} \times \exp\{(\tilde{B} - \bar{B})^2/[4(\tilde{A} - \bar{A})] - C - \bar{C}\}. \quad (\text{G.17})$$

Since we want to compare this result with Eq. (G.3), we need to find its dependence on the difference  $\alpha - \beta$ . Assuming  $|\beta| \gg 1$ , we expand Eq. (G.17) up to second order in  $\text{Re}(\alpha - \beta)$  and  $\text{Im}(\alpha - \beta)$ . Let us consider first the special case when  $\beta$  is real ( $\beta > 0$ ), so that  $\phi_\beta = 0$ . Then expansion of Eq. (G.17) produces (after some algebra) the result

$$Q(\alpha) \approx \frac{1}{\pi} \left( \frac{1}{4} + \frac{W_1}{4W_2} + \frac{1}{4W_2} + \frac{W_1}{4} + 4K^2W_1 \right)^{-1/2} \times \exp \left\{ -\frac{2(1 + W_2 + 16W_1W_2K^2) [\text{Re}(\alpha - \beta)]^2}{1 + W_1 + W_2 + W_1W_2(1 + 16K^2)} - \frac{2W_2(1 + W_1) [\text{Im}(\alpha - \beta)]^2}{1 + W_1 + W_2 + W_1W_2(1 + 16K^2)} - \frac{16W_1W_2K \text{Re}(\alpha - \beta) \text{Im}(\alpha - \beta)}{1 + W_1 + W_2 + W_1W_2(1 + 16K^2)} \right\}. \quad (\text{G.18})$$

Comparing this formula with Eq. (G.3) for the Gaussian state, we see that the formulas

coincide if

$$D_0 = \frac{1}{8W_2} + \frac{W_1}{8} + 2K^2W_1, \quad (\text{G.19})$$

$$b = \frac{1}{4} \sqrt{\left(\frac{1}{2W_2} + \frac{W_1}{2} + 8K^2W\right)^2 - \frac{W_1}{W_2}}, \quad (\text{G.20})$$

$$\begin{aligned} \theta_0 = \arctan\left(\frac{8KW_1W_2}{1 - W_1W_2 + 16K^2W_1W_2}\right) \\ + (\pi/2)[1 - \text{sign}(1 - W_1W_2 + 16K^2W_1W_2)], \end{aligned} \quad (\text{G.21})$$

where we use notation  $\theta_0$  instead of  $\theta$  to remind that we consider the special case of a real positive  $\beta$ . Note that Eqs. (G.19)–(G.21) coincide with Eqs. (5.45)–(5.47) in the case of a real positive  $\beta$ .

For a complex  $\beta$ , it is also possible to use the second-order expansion of Eq. (G.17); however, it is easier to use the fact that dependence of  $Q(\alpha)$  on the complex phase  $\phi_\beta$  in Eqs. (G.5)–(G.11) comes only from the combination  $\phi_\alpha - \phi_\beta$ . Therefore, the  $Q$ -function of the Fock-space Gaussian state does not change in the transformation  $\beta \rightarrow |\beta|$ ,  $\alpha \rightarrow e^{-i\phi_\beta}\alpha$ , so for a complex  $\beta$  we can still use Eq. (G.18) with the substitution  $(\alpha - \beta) \rightarrow e^{-i\phi_\beta}(\alpha - \beta)$ . Using this substitution in the equivalent Eq. (G.3), we easily find that it results in replacing the angle  $\theta_0$  (for real  $\beta$ ) with

$$\theta = \theta_0 + 2\phi_\beta, \quad (\text{G.22})$$

while the parameters  $D_0$  and  $b$  do not change. Another way to obtain Eq. (G.22) is to note that the parameters  $W_1$ ,  $W_2$ , and  $K$  of the Fock-space Gaussian state do not change when the phase space is rotated (i.e.,  $\beta \rightarrow e^{i\Delta\phi}\beta$ ,  $\alpha \rightarrow e^{i\Delta\phi}\alpha$ ), while for the Gaussian state this results in the change  $\theta \rightarrow \theta + 2\Delta\phi$  with unchanged parameters  $D_0$  and  $b$  (see Fig. 5.1). Therefore, we can first rotate the phase space clockwise by the angle  $\phi_\beta$  (to make  $\beta$  real),

then convert parameters  $W_1$ ,  $W_2$ , and  $K$ , into  $D_0$ ,  $b$ , and  $\theta_0$  using Eqs. (G.19)–(G.21), and then move the phase space back by counterclockwise rotation with the same angle  $\phi_\beta$ , which results in  $\theta$  change (G.22).

Thus we have derived the conversion relations (5.45)–(5.47) between the Gaussian and Fock-space Gaussian states ( $\beta$  does not change). Note that our derivation relied on the fact that the Husimi  $Q$ -function uniquely defines a quantum state [173]. Since Eq. (G.18) is only an approximation, a Fock-space Gaussian state is not exactly equal to a Gaussian state. However, the accuracy of the conversion improves at larger  $|\beta|$ , approaching exact equivalence in the limit  $|\beta| \rightarrow \infty$ . Numerical results in Sec. 5.5.1 show that infidelity of the conversion scales as  $|\beta|^{-2}$ .

## Appendix H

# Steady-state squeezing and heating of a driven nonlinear resonator

This appendix is related to Chapter 5, and uses the same notations as in that chapter. Here we derive results for  $D_0$ ,  $b$ , and  $\theta$  in the steady state. The parameters  $r$  and  $n_{\text{th}}$  can be then calculated using Eq. (5.30). The squeezing factor is  $[4(D_0 - b)]^{-1}$ , the effective temperature  $T_{\text{eff}}$  is given by  $\coth(\omega_{\text{r0}}/2T_{\text{eff}}) = 4\sqrt{(D_0 + b)(D_0 - b)}$ . All variables discussed in this appendix are only for the steady state.

The steady-state value of  $\beta$  can be calculated from Eq. (5.63); in general it does not have an analytical expression. Note that

$$\varepsilon/\beta = \omega_{\text{d}} - \omega_{\text{r}}(|\beta|^2) + i\kappa/2, \quad (\text{H.1})$$

so  $\text{Re}(\varepsilon/\beta)$  can be positive or negative, depending on detuning.

From Eqs. (5.67) and (5.68) in the steady state we find

$$D_0 = \frac{\coth(\omega_{r0}/2T_b)}{4} \frac{1}{1 - [2\eta_\beta|\beta|^2 \sin(\Delta\theta)/\kappa]^2}, \quad (\text{H.2})$$

$$b = \frac{\coth(\omega_{r0}/2T_b)}{4} \frac{2\eta_\beta|\beta|^2 \sin(\Delta\theta)/\kappa}{1 - [2\eta_\beta|\beta|^2 \sin(\Delta\theta)/\kappa]^2}, \quad (\text{H.3})$$

where  $\eta_\beta = d\omega_r(n)/dn|_{n=|\beta|^2}$  is the steady-state nonlinearity. To obtain explicit analytics for  $D_0$  and  $b$ , we still need to find  $\sin(\Delta\theta)$ . For that we can substitute the ratio  $b/D_0 = 2\eta_\beta|\beta|^2 \sin(\Delta\theta)/\kappa$  into Eq. (5.69) in the steady state, thus obtaining

$$\tan(\Delta\theta) = \frac{\kappa/2}{\eta_\beta|\beta|^2 - \text{Re}(\varepsilon/\beta)}. \quad (\text{H.4})$$

Since  $\eta_\beta \sin(\Delta\theta) \geq 0$  (because  $b \geq 0$ ), we can use

$$\sin(\Delta\theta) = \text{sign}(\eta_\beta) \sqrt{\frac{(\kappa/2)^2}{(\kappa/2)^2 + [\eta_\beta|\beta|^2 - \text{Re}(\varepsilon/\beta)]^2}} \quad (\text{H.5})$$

in Eqs. (H.2) and (H.3).

The angle  $\theta$  can be calculated as

$$\begin{aligned} \theta &= 2 \arg(\beta) + \arctan\left(\frac{\kappa/2}{\eta_\beta|\beta|^2 - \text{Re}(\varepsilon/\beta)}\right) \\ &+ (\pi/2)\{1 - \text{sign}[|\beta|^2 - \eta_\beta^{-1}\text{Re}(\varepsilon/\beta)]\}. \end{aligned} \quad (\text{H.6})$$

These results can be compared with results of Ref. [186] in the case of Kerr nonlinearity (Duffing oscillator),  $H_r^{\text{lf}} = \omega_{r0}a^\dagger a + (\eta/2)(a^\dagger)^2 a^2$ , which is equivalent to our Hamiltonian when  $\omega_r = \omega_{r0} + n\eta$  [see Eq. (5.73)], so that  $\eta_\beta = \eta = \text{const}$ . In this case Eq. (4.4)

of Ref. [186] (converted into our notations) gives

$$\langle a^2 \rangle - \beta^2 = -\frac{\eta\beta^2(\omega_{r0} + 2\eta|\beta|^2 - \omega_d + i\kappa/2)(1 + 2n_b)}{2\lambda}, \quad (\text{H.7})$$

$$\langle a^\dagger a \rangle - |\beta|^2 = \frac{\eta^2|\beta|^4(1 + 2n_b)}{2\lambda} + n_b, \quad (\text{H.8})$$

$$\lambda = (\omega_{r0} + 2\eta|\beta|^2 - \omega_d)^2 + \kappa^2/4 - \eta^2|\beta|^4. \quad (\text{H.9})$$

From these values,  $D_0$ ,  $b$ , and  $\theta$  can be obtained using Eqs. (5.18)–(5.20) [also, Eq. (5.26) gives  $\langle a^\dagger a \rangle - |\beta|^2 = 2D_0 - 1/2$ ].

We have numerically compared these results with our Eqs. (H.2), (H.3), and (H.6) and found that they coincide for all parameters, which we checked. Thus, for the steady state in the case of Kerr nonlinearity, our results for squeezing and heating agree with results of Ref. [186] (note that the terminology of squeezing and/or heating was not used in Ref. [186]).

Our steady-state results for a Duffing oscillator in the limit of small dissipation ( $\kappa \rightarrow 0$ ) can also be directly compared with the analytical results presented in Secs. 2.1 and 2.5 of Ref. [196]. In this case the squeezing and heating are determined only by the parameter combination  $\varepsilon^2\eta/(\omega_d - \omega_{r0})^3$  (which was called  $\beta$  in Ref. [196]). Results of Ref. [196] show that the squeezing parameter  $\xi = re^{i\theta}$  is real and equals

$$\xi = \frac{1}{4} \ln \frac{3Q^2 - 1}{Q^2 - 1}, \quad (\text{H.10})$$

where  $Q$  satisfies equation

$$Q(Q^2 - 1) = \sqrt{\varepsilon^2\eta/(\omega_d - \omega_{r0})^3}. \quad (\text{H.11})$$

Here in the case  $\varepsilon^2\eta/(\omega_d - \omega_{r0})^3 > 4/27$ , there is only one real solution for  $Q$ . The range  $0 < \varepsilon^2\eta/(\omega_d - \omega_{r0})^3 < 4/27$  corresponds to bistability, and there are three real solutions

for  $Q$ , with the largest value corresponding to the upper bistability branch and the middle value for the lower branch. In the case  $\varepsilon^2\eta/(\omega_d - \omega_{r0})^3 < 0$ , we need to use the purely imaginary solution for  $Q$ .

The angle  $\theta$  in this limit is zero (squeezing is in phase with the drive), except  $\theta = \pi$  for the lower bistability branch (then  $\xi < 0$ ). The number of thermal photons is [196]

$$n_{\text{th}} = n_{\text{b}} + (2n_{\text{b}} + 1) \sinh^2 r. \quad (\text{H.12})$$

We have numerically compared Eqs. (H.10) and (H.12) for  $\xi$  and  $n_{\text{th}}$  with our results following from Eqs. (H.2), (H.3), and (H.6). As expected, we have found that they coincide in the limit  $\kappa \rightarrow 0$  for a fixed value of  $\varepsilon^2\eta/(\omega_d - \omega_{r0})^3$ . Thus, our results agree with the results of Ref. [196].

# Bibliography

- [1] R. Feynman, “There’s plenty of room at the bottom,” (1959), American Physical Society meeting at Caltech.
- [2] Y. Manin, *Computable and uncomputable* (Sovetskoye Radio, Moscow, 1980).
- [3] R. P. Feynman, “Simulating physics with computers,” *Int. J. Theor. Phys.* **21**, 467 (1982).
- [4] C. H. Bennett and G. Brassard, “Quantum cryptography: Public key distribution and coin tossing,” in *Proceedings of IEEE International Conference on Computers, Systems and Signal Processing*, Vol. 175 (1984) p. 175.
- [5] D. Deutsch, “Quantum theory, the ChurchTuring principle and the universal quantum computer,” *Proc. R. Soc. Lond. A* **400**, 97 (1985).
- [6] D. Deutsch and R. Jozsa, “Rapid solution of problems by quantum computation,” *Proc. R. Soc. Lond. A* **439**, 553 (1992).
- [7] P. W. Shor, “Algorithms for quantum computation: discrete logarithms and factoring,” in *Proceedings 35th Annual Symposium on Foundations of Computer Science* (1994) p. 124.
- [8] P. Shor, “Polynomial-Time Algorithms for Prime Factorization and Discrete Logarithms on a Quantum Computer,” *SIAM J. Comput.* **26**, 1484 (1997), [arXiv:quant-ph/9508027](https://arxiv.org/abs/quant-ph/9508027).
- [9] A. Y. Kitaev, “Quantum measurements and the Abelian Stabilizer Problem,” [arXiv:quant-ph/9511026](https://arxiv.org/abs/quant-ph/9511026) .
- [10] L. K. Grover, “A fast quantum mechanical algorithm for database search,” in *Annual ACM symposium on theory of computing* (ACM, 1996) p. 212.
- [11] P. W. Shor, “Scheme for reducing decoherence in quantum computer memory,” *Phys. Rev. A* **52**, 2493(R) (1995).
- [12] A. Steane, “Multiple-particle interference and quantum error correction,” *Proc. R.*

- Soc. Lond. A **452**, 2551 (1996).
- [13] A. R. Calderbank and P. W. Shor, “Good quantum error-correcting codes exist,” *Phys. Rev. A* **54**, 1098 (1996).
  - [14] S. Lloyd, “Universal Quantum Simulators,” *Science* **273**, 1073 (1996).
  - [15] E. Bernstein and U. Vazirani, “Quantum Complexity Theory,” *SIAM J. Comput.* **26**, 1411 (1997).
  - [16] A. Y. Kitaev, “Fault-tolerant quantum computation by anyons,” *Ann. Phys.* **303**, 2 (2003).
  - [17] A. Montanaro, “Quantum algorithms: an overview,” *npj Quantum Inf.* **2**, 15023 (2016).
  - [18] M. W. Johnson, M. H. S. Amin, S. Gildert, T. Lanting, F. Hamze, N. Dickson, R. Harris, A. J. Berkley, J. Johansson, P. Bunyk, E. M. Chapple, C. Enderud, J. P. Hilton, K. Karimi, E. Ladizinsky, N. Ladizinsky, T. Oh, I. Perminov, C. Rich, M. C. Thom, E. Tolkacheva, C. J. S. Truncik, S. Uchaikin, J. Wang, B. Wilson, and G. Rose, “Quantum annealing with manufactured spins,” *Nature* **473**, 194 (2011).
  - [19] T. Albash and D. A. Lidar, “Adiabatic quantum computation,” *Rev. Mod. Phys.* **90**, 015002 (2018).
  - [20] J. R. McClean, J. Romero, R. Babbush, and A. Aspuru-Guzik, “The theory of variational hybrid quantum-classical algorithms,” *New J. Phys.* **18**, 023023 (2016).
  - [21] A. Aspuru-Guzik, A. D. Dutoi, P. J. Love, and M. Head-Gordon, “Simulated Quantum Computation of Molecular Energies,” *Science* **309**, 1704 (2005).
  - [22] J. Biamonte, P. Wittek, N. Pancotti, P. Rebentrost, N. Wiebe, and S. Lloyd, “Quantum machine learning,” *Nature* **549**, 195 (2017).
  - [23] D. P. DiVincenzo, “The Physical Implementation of Quantum Computation,” *Fortschr. Phys.* **48**, 771 (2000).
  - [24] D. J. Wineland, M. Barrett, J. Britton, J. Chiaverini, B. DeMarco, W. M. Itano, B. Jelenković, C. Langer, D. Leibfried, V. Meyer, T. Rosenband, and T. Schätz, “Quantum information processing with trapped ions,” *Phil. Trans. R. Soc. Lond. A* **361**, 1349 (2003).
  - [25] H. Häffner, C. F. Roos, and R. Blatt, “Quantum computing with trapped ions,” *Phys. Rep.* **469**, 155 (2008).
  - [26] R. Blatt and C. F. Roos, “Quantum simulations with trapped ions,” *Nat. Phys.* **8**,

277 (2012).

- [27] M. H. Devoret, A. Wallraff, and J. M. Martinis, “Superconducting Qubits: A Short Review,” [arXiv:cond-mat/0411174](#) .
- [28] J. Clarke and F. K. Wilhelm, “Superconducting quantum bits,” *Nature* **453**, 1031 (2008).
- [29] R. J. Schoelkopf and S. M. Girvin, “Wiring up quantum systems,” *Nature* **451**, 664 (2008).
- [30] G. Wendin, “Quantum information processing with superconducting circuits: a review,” *Rep. Prog. Phys.* **80**, 106001 (2017).
- [31] D. Loss and D. P. DiVincenzo, “Quantum computation with quantum dots,” *Phys. Rev. A* **57**, 120 (1998).
- [32] C. Kloeffel and D. Loss, “Prospects for Spin-Based Quantum Computing in Quantum Dots,” *Annu. Rev. Condens. Matter Phys.* **4**, 51 (2013).
- [33] F. A. Zwanenburg, A. S. Dzurak, A. Morello, M. Y. Simmons, L. C. L. Hollenberg, G. Klimeck, S. Rogge, S. N. Coppersmith, and M. A. Eriksson, “Silicon quantum electronics,” *Rev. Mod. Phys.* **85**, 961 (2013).
- [34] M. Veldhorst, J. C. C. Hwang, C. H. Yang, A. W. Leenstra, B. d. Ronde, J. P. Dehollain, J. T. Muhonen, F. E. Hudson, K. M. Itoh, A. Morello, and A. S. Dzurak, “An addressable quantum dot qubit with fault-tolerant control-fidelity,” *Nat. Nanotech.* **9**, 981 (2014).
- [35] P. Bonderson, A. Kitaev, and K. Shtengel, “Detecting Non-Abelian Statistics in the  $\nu = 5/2$  Fractional Quantum Hall State,” *Phys. Rev. Lett.* **96**, 016803 (2006).
- [36] C. Nayak, S. H. Simon, A. Stern, M. Freedman, and S. Das Sarma, “Non-Abelian anyons and topological quantum computation,” *Rev. Mod. Phys.* **80**, 1083 (2008).
- [37] T. Karzig, C. Knapp, R. M. Lutchyn, P. Bonderson, M. B. Hastings, C. Nayak, J. Alicea, K. Flensberg, S. Plugge, Y. Oreg, C. M. Marcus, and M. H. Freedman, “Scalable designs for quasiparticle-poisoning-protected topological quantum computation with Majorana zero modes,” *Phys. Rev. B* **95**, 235305 (2017).
- [38] K. K. Likharev, *Dynamics of Josephson Junctions and Circuits* (CRC Press, New York, 1986).
- [39] Y. Nakamura, Y. A. Pashkin, and J. S. Tsai, “Coherent control of macroscopic quantum states in a single-Cooper-pair box,” *Nature* **398**, 786 (1999).

- [40] J. E. Mooij, T. P. Orlando, L. Levitov, L. Tian, C. H. v. d. Wal, and S. Lloyd, “Josephson Persistent-Current Qubit,” *Science* **285**, 1036 (1999).
- [41] I. Chiorescu, Y. Nakamura, C. J. P. M. Harmans, and J. E. Mooij, “Coherent Quantum Dynamics of a Superconducting Flux Qubit,” *Science* **299**, 1869 (2003).
- [42] J. M. Martinis, S. Nam, J. Aumentado, and C. Urbina, “Rabi Oscillations in a Large Josephson-Junction Qubit,” *Phys. Rev. Lett.* **89**, 117901 (2002).
- [43] M. Steffen, M. Ansmann, R. McDermott, N. Katz, R. C. Bialczak, E. Lucero, M. Neeley, E. M. Weig, A. N. Cleland, and J. M. Martinis, “State Tomography of Capacitively Shunted Phase Qubits with High Fidelity,” *Phys. Rev. Lett.* **97**, 050502 (2006).
- [44] J. Koch, T. M. Yu, J. Gambetta, A. A. Houck, D. I. Schuster, J. Majer, A. Blais, M. H. Devoret, S. M. Girvin, and R. J. Schoelkopf, “Charge-insensitive qubit design derived from the Cooper pair box,” *Phys. Rev. A* **76**, 042319 (2007).
- [45] J. Majer, J. M. Chow, J. M. Gambetta, J. Koch, B. R. Johnson, J. A. Schreier, L. Frunzio, D. I. Schuster, A. A. Houck, A. Wallraff, A. Blais, M. H. Devoret, S. M. Girvin, and R. J. Schoelkopf, “Coupling superconducting qubits via a cavity bus,” *Nature* **449**, 443 (2007).
- [46] R. Barends, J. Kelly, A. Megrant, D. Sank, E. Jeffrey, Y. Chen, Y. Yin, B. Chiaro, J. Mutus, C. Neill, P. O’Malley, P. Roushan, J. Wenner, T. C. White, A. N. Cleland, and J. M. Martinis, “Coherent Josephson Qubit Suitable for Scalable Quantum Integrated Circuits,” *Phys. Rev. Lett.* **111**, 080502 (2013).
- [47] F. R. Ong, M. Boissonneault, F. Mallet, A. C. Doherty, A. Blais, D. Vion, D. Esteve, and P. Bertet, “Quantum Heating of a Nonlinear Resonator Probed by a Superconducting Qubit,” *Phys. Rev. Lett.* **110**, 047001 (2013).
- [48] Y. Chen, C. Neill, P. Roushan, N. Leung, M. Fang, R. Barends, J. Kelly, B. Campbell, Z. Chen, B. Chiaro, A. Dunsworth, E. Jeffrey, A. Megrant, J. Mutus, P. OMalley, C. Quintana, D. Sank, A. Vainsencher, J. Wenner, T. White, M. R. Geller, A. Cleland, and J. M. Martinis, “Qubit Architecture with High Coherence and Fast Tunable Coupling,” *Phys. Rev. Lett.* **113**, 220502 (2014).
- [49] J. M. Chow, J. M. Gambetta, E. Magesan, D. W. Abraham, A. W. Cross, B. R. Johnson, N. A. Masluk, C. A. Ryan, J. A. Smolin, S. J. Srinivasan, and M. Steffen, “Implementing a strand of a scalable fault-tolerant quantum computing fabric,” *Nat. Commun.* **5**, 4015 (2014).
- [50] D. Ristè, S. Poletto, M.-Z. Huang, A. Bruno, V. Vesterinen, O.-P. Saira, and L. DiCarlo, “Detecting bit-flip errors in a logical qubit using stabilizer measurements,” *Nat. Commun.* **6**, 6983 (2015).

- [51] Y. Tabuchi, S. Ishino, A. Noguchi, T. Ishikawa, R. Yamazaki, K. Usami, and Y. Nakamura, “Coherent coupling between a ferromagnetic magnon and a superconducting qubit,” *Science* **349**, 405 (2015).
- [52] S. Hacothen-Gourgy, L. S. Martin, E. Flurin, V. V. Ramasesh, K. B. Whaley, and I. Siddiqi, “Quantum dynamics of simultaneously measured non-commuting observables,” *Nature* **538**, 491 (2016).
- [53] M. Hutchings, J. Hertzberg, Y. Liu, N. Bronn, G. Keefe, M. Brink, J. M. Chow, and B. Plourde, “Tunable Superconducting Qubits with Flux-Independent Coherence,” *Phys. Rev. Appl.* **8**, 044003 (2017).
- [54] R. W. Heeres, P. Reinhold, N. Ofek, L. Frunzio, L. Jiang, M. H. Devoret, and R. J. Schoelkopf, “Implementing a universal gate set on a logical qubit encoded in an oscillator,” *Nat. Commun.* **8**, 94 (2017).
- [55] E. A. Sete, M. J. Reagor, N. Didier, and C. T. Rigetti, “Charge- and Flux-Insensitive Tunable Superconducting Qubit,” *Phys. Rev. Appl.* **8**, 024004 (2017).
- [56] F. Luthi, T. Stavenga, O. Enzing, A. Bruno, C. Dickel, N. Langford, M. Rol, T. Jespersen, J. Nygård, P. Krogstrup, and L. DiCarlo, “Evolution of Nanowire Transmon Qubits and Their Coherence in a Magnetic Field,” *Phys. Rev. Lett.* **120**, 100502 (2018).
- [57] A. Opremcak, I. V. Pechenezhskiy, C. Howington, B. G. Christensen, M. A. Beck, E. Leonard Jr., J. Suttle, C. Wilen, K. N. Nesterov, G. J. Ribeill, T. Thorbeck, F. Schlenker, M. G. Vavilov, B. L. T. Plourde, and R. McDermott, “Measurement of a Superconducting Qubit with a Microwave Photon Counter,” [arXiv:1803.01014](https://arxiv.org/abs/1803.01014) .
- [58] M. A. Nielsen and I. L. Chuang, *Quantum computation and quantum information* (Cambridge University Press, Cambridge, UK, 2000).
- [59] D. C. McKay, C. J. Wood, S. Sheldon, J. M. Chow, and J. M. Gambetta, “Efficient Z gates for quantum computing,” *Phys. Rev. A* **96**, 022330 (2017).
- [60] E. Lucero, J. Kelly, R. C. Bialczak, M. Lenander, M. Mariantoni, M. Neeley, A. D. OConnell, D. Sank, H. Wang, M. Weides, J. Wenner, T. Yamamoto, A. N. Cleland, and J. M. Martinis, “Reduced phase error through optimized control of a superconducting qubit,” *Phys. Rev. A* **82**, 042339 (2010).
- [61] B. R. Johnson, M. P. d. Silva, C. A. Ryan, S. Kimmel, J. M. Chow, and T. A. Ohki, “Demonstration of robust quantum gate tomography via randomized benchmarking,” *New J. Phys.* **17**, 113019 (2015).
- [62] J. Kelly, R. Barends, A. G. Fowler, A. Megrant, E. Jeffrey, T. C. White, D. Sank, J. Y. Mutus, B. Campbell, Y. Chen, Z. Chen, B. Chiaro, A. Dunsworth, I. C. Hoi,

- C. Neill, P. J. J. O'Malley, C. Quintana, P. Roushan, A. Vainsencher, J. Wenner, A. N. Cleland, and J. M. Martinis, "State preservation by repetitive error detection in a superconducting quantum circuit," *Nature* **519**, 66 (2015).
- [63] M. Rol, C. Bultink, T. O'Brien, S. de Jong, L. Theis, X. Fu, F. Luthi, R. Vermeulen, J. de Sterke, A. Bruno, D. Deurloo, R. Schouten, F. Wilhelm, and L. DiCarlo, "Restless Tuneup of High-Fidelity Qubit Gates," *Phys. Rev. Appl.* **7**, 041001 (2017).
- [64] F. W. Strauch, P. R. Johnson, A. J. Dragt, C. J. Lobb, J. R. Anderson, and F. C. Wellstood, "Quantum Logic Gates for Coupled Superconducting Phase Qubits," *Phys. Rev. Lett.* **91**, 167005 (2003).
- [65] J. Ghosh, A. Galiutdinov, Z. Zhou, A. N. Korotkov, J. M. Martinis, and M. R. Geller, "High-fidelity controlled- $\sigma_z$  gate for resonator-based superconducting quantum computers," *Phys. Rev. A* **87**, 022309 (2013).
- [66] J. M. Martinis and M. R. Geller, "Fast adiabatic qubit gates using only  $\sigma_z$  control," *Phys. Rev. A* **90**, 022307 (2014).
- [67] L. DiCarlo, J. M. Chow, J. M. Gambetta, L. S. Bishop, B. R. Johnson, D. I. Schuster, J. Majer, A. Blais, L. Frunzio, S. M. Girvin, and R. J. Schoelkopf, "Demonstration of two-qubit algorithms with a superconducting quantum processor," *Nature* **460**, 240 (2009).
- [68] R. Barends, J. Kelly, A. Megrant, A. Veitia, D. Sank, E. Jeffrey, T. C. White, J. Mutus, A. G. Fowler, B. Campbell, Y. Chen, Z. Chen, B. Chiaro, A. Dunsworth, C. Neil, P. O'Malley, P. Roushan, A. Vainsencher, J. Wenner, A. N. Korotkov, A. N. Cleland, and J. M. Martinis, "Superconducting quantum circuits at the surface code threshold for fault tolerance," *Nature* **508**, 500 (2014).
- [69] C. Rigetti and M. Devoret, "Fully microwave-tunable universal gates in superconducting qubits with linear couplings and fixed transition frequencies," *Phys. Rev. B* **81**, 134507 (2010).
- [70] E. Magesan and J. M. Gambetta, "Effective Hamiltonian models of the cross-resonance gate," [arXiv:1804.04073](https://arxiv.org/abs/1804.04073) .
- [71] S. Sheldon, E. Magesan, J. M. Chow, and J. M. Gambetta, "Procedure for systematically tuning up cross-talk in the cross-resonance gate," *Phys. Rev. A* **93**, 060302 (2016).
- [72] A. Dewes, F. R. Ong, V. Schmitt, R. Lauro, N. Boulant, P. Bertet, D. Vion, and D. Esteve, "Characterization of a Two-Transmon Processor with Individual Single-Shot Qubit Readout," *Phys. Rev. Lett.* **108**, 057002 (2012).
- [73] M. Reagor, C. B. Osborn, N. Tezak, A. Staley, G. Prawiroatmodjo, M. Scheer, N. Ali-

- doust, E. A. Sete, N. Didier, M. P. d. Silva, E. Acala, J. Angeles, A. Bestwick, M. Block, B. Bloom, A. Bradley, C. Bui, S. Caldwell, L. Capelluto, R. Chilcott, J. Cordova, G. Crossman, M. Curtis, S. Deshpande, T. E. Bouayadi, D. Girshovich, S. Hong, A. Hudson, P. Karalekas, K. Kuang, M. Lenihan, R. Manenti, T. Manning, J. Marshall, Y. Mohan, W. O'Brien, J. Otterbach, A. Papageorge, J.-P. Paquette, M. Pelstring, A. Polloreno, V. Rawat, C. A. Ryan, R. Renzas, N. Rubin, D. Russel, M. Rust, D. Scarabelli, M. Selvanayagam, R. Sinclair, R. Smith, M. Suska, T.-W. To, M. Vahidpour, N. Vodrahalli, T. Whyland, K. Yadav, W. Zeng, and C. T. Rigetti, "Demonstration of universal parametric entangling gates on a multi-qubit lattice," *Sci. Adv.* **4**, eaao3603 (2018).
- [74] P. J. Leek, S. Filipp, P. Maurer, M. Baur, R. Bianchetti, J. M. Fink, M. Gppl, L. Steffen, and A. Wallraff, "Using sideband transitions for two-qubit operations in superconducting circuits," *Phys. Rev. B* **79**, 180511 (2009).
- [75] S. Poletto, J. M. Gambetta, S. T. Merkel, J. A. Smolin, J. M. Chow, A. D. Crocoles, G. A. Keefe, M. B. Rothwell, J. R. Rozen, D. W. Abraham, C. Rigetti, and M. Steffen, "Entanglement of Two Superconducting Qubits in a Waveguide Cavity via Monochromatic Two-Photon Excitation," *Phys. Rev. Lett.* **109**, 240505 (2012).
- [76] J. M. Chow, J. M. Gambetta, A. W. Cross, S. T. Merkel, C. Rigetti, and M. Steffen, "Microwave-activated conditional-phase gate for superconducting qubits," *New J. Phys.* **15**, 115012 (2013).
- [77] A. W. Cross and J. M. Gambetta, "Optimized pulse shapes for a resonator-induced phase gate," *Phys. Rev. A* **91**, 032325 (2015).
- [78] A. Blais, R.-S. Huang, A. Wallraff, S. M. Girvin, and R. J. Schoelkopf, "Cavity quantum electrodynamics for superconducting electrical circuits: An architecture for quantum computation," *Phys. Rev. A* **69**, 062320 (2004).
- [79] M. Khezri, E. Mlinar, J. Dressel, and A. N. Korotkov, "Measuring a transmon qubit in circuit QED: Dressed squeezed states," *Phys. Rev. A* **94**, 012347 (2016).
- [80] M. Khezri and A. N. Korotkov, "Hybrid phase-space–Fock-space approach to evolution of a driven nonlinear resonator," *Phys. Rev. A* **96**, 043839 (2017).
- [81] M. A. Castellanos-Beltran, K. D. Irwin, G. C. Hilton, L. R. Vale, and K. W. Lehnert, "Amplification and squeezing of quantum noise with a tunable Josephson metamaterial," *Nat. Phys.* **4**, 929 (2008).
- [82] N. Bergeal, F. Schackert, M. Metcalfe, R. Vijay, V. E. Manucharyan, L. Frunzio, D. E. Prober, R. J. Schoelkopf, S. M. Girvin, and M. H. Devoret, "Phase-preserving amplification near the quantum limit with a Josephson ring modulator," *Nature* **465**, 64 (2010).

- [83] C. Eichler, D. Bozyigit, C. Lang, M. Baur, L. Steffen, J. M. Fink, S. Filipp, and A. Wallraff, “Observation of two-mode squeezing in the microwave frequency domain,” *Phys. Rev. Lett.* **107**, 113601 (2011).
- [84] F. Mallet, M. A. Castellanos-Beltran, H. S. Ku, S. Glancy, E. Knill, K. D. Irwin, G. C. Hilton, L. R. Vale, and K. W. Lehnert, “Quantum state tomography of an itinerant squeezed microwave field,” *Phys. Rev. Lett.* **106**, 220502 (2011).
- [85] R. Vijay, D. H. Slichter, and I. Siddiqi, “Observation of quantum jumps in a superconducting artificial atom,” *Phys. Rev. Lett.* **106**, 110502 (2011).
- [86] T. C. White, J. Y. Mutus, I.-C. Hoi, R. Barends, B. Campbell, Y. Chen, Z. Chen, B. Chiaro, A. Dunsworth, E. Jeffrey, J. Kelly, A. Megrant, C. Neill, P. J. J. O’Malley, P. Roushan, D. Sank, A. Vainsencher, J. Wenner, S. Chaudhuri, J. Gao, and J. M. Martinis, “Traveling wave parametric amplifier with Josephson junctions using minimal resonator phase matching,” *Appl. Phys. Lett.* **106**, 242601 (2015).
- [87] C. Macklin, K. O’Brien, D. Hover, M. E. Schwartz, V. Bolkhovskiy, X. Zhang, W. D. Oliver, and I. Siddiqi, “A nearquantum-limited Josephson traveling-wave parametric amplifier,” *Science* **350**, 307 (2015).
- [88] C. W. Gardiner and P. Zoller, *Quantum Noise*, 3rd ed. (Springer, Berlin, 2004).
- [89] D. F. Walls and G. J. Milburn, *Quantum Optics* (Springer, Berlin, 2008).
- [90] A. A. Clerk, M. H. Devoret, S. M. Girvin, F. Marquardt, and R. J. Schoelkopf, “Introduction to quantum noise, measurement, and amplification,” *Rev. Mod. Phys.* **82**, 1155 (2010).
- [91] E. M. Purcell, “Proceedings of the American Physical Society, Minutes of the Spring meeting at Cambridge,” *Phys. Rev.* **69**, 681 (1946).
- [92] M. D. Reed, B. R. Johnson, A. A. Houck, L. DiCarlo, J. M. Chow, D. I. Schuster, L. Frunzio, and R. J. Schoelkopf, “Fast reset and suppressing spontaneous emission of a superconducting qubit,” *Appl. Phys. Lett.* **96**, 203110 (2010).
- [93] E. Jeffrey, D. Sank, J. Y. Mutus, T. C. White, J. Kelly, R. Barends, Y. Chen, Z. Chen, B. Chiaro, A. Dunsworth, A. Megrant, P. J. J. O’Malley, C. Neill, P. Roushan, A. Vainsencher, J. Wenner, A. N. Cleland, and J. M. Martinis, “Fast Accurate State Measurement with Superconducting Qubits,” *Phys. Rev. Lett.* **112**, 190504 (2014).
- [94] N. T. Bronn, Y. Liu, J. B. Hertzberg, A. D. Croles, A. A. Houck, J. M. Gambetta, and J. M. Chow, “Broadband filters for abatement of spontaneous emission in circuit quantum electrodynamics,” *Appl. Phys. Lett.* **107**, 172601 (2015).
- [95] E. A. Sete, J. M. Martinis, and A. N. Korotkov, “Quantum theory of a bandpass

- Purcell filter for qubit readout,” *Phys. Rev. A* **92**, 012325 (2015).
- [96] J. Heinsoo, C. K. Andersen, A. Remm, S. Krinner, T. Walter, Y. Salath, S. Gasparinetti, J.-C. Besse, A. Potočnik, C. Eichler, and A. Wallraff, “Rapid high-fidelity multiplexed readout of superconducting qubits,” [arXiv:1801.07904](#) .
- [97] D. Bacon, “Operator quantum error-correcting subsystems for self-correcting quantum memories,” *Phys. Rev. A* **73**, 012340 (2006).
- [98] A. G. Fowler, M. Mariantoni, J. M. Martinis, and A. N. Cleland, “Surface codes: Towards practical large-scale quantum computation,” *Phys. Rev. A* **86**, 032324 (2012).
- [99] A. A. Kovalev and L. P. Pryadko, “Fault tolerance of quantum low-density parity check codes with sublinear distance scaling,” *Phys. Rev. A* **87**, 020304(R) (2013).
- [100] D. T. McClure, H. Paik, L. S. Bishop, M. Steffen, J. M. Chow, and J. M. Gambetta, “Rapid Driven Reset of a Qubit Readout Resonator,” *Phys. Rev. Applied* **5**, 011001 (2016).
- [101] S. Boutin, C. K. Andersen, J. Venkatraman, A. J. Ferris, and A. Blais, “Resonator reset in circuit QED by optimal control for large open quantum systems,” *Phys. Rev. A* **96**, 042315 (2017).
- [102] E. Magesan, J. M. Gambetta, A. Crcoles, and J. M. Chow, “Machine Learning for Discriminating Quantum Measurement Trajectories and Improving Readout,” *Phys. Rev. Lett.* **114**, 200501 (2015).
- [103] T. Walter, P. Kurpiers, S. Gasparinetti, P. Magnard, A. Potočnik, Y. Salathé, M. Pechal, M. Mondal, M. Oppliger, C. Eichler, and A. Wallraff, “Rapid High-Fidelity Single-Shot Dispersive Readout of Superconducting Qubits,” *Phys. Rev. Appl.* **7**, 054020 (2017).
- [104] A. Wallraff, D. I. Schuster, A. Blais, L. Frunzio, R.-S. Huang, J. Majer, S. Kumar, S. M. Girvin, and R. J. Schoelkopf, “Strong coupling of a single photon to a superconducting qubit using circuit quantum electrodynamics,” *Nature* **431**, 162 (2004).
- [105] L. Sun, A. Petrenko, Z. Leghtas, B. Vlastakis, G. Kirchmair, K. M. Sliwa, A. Narla, M. Hatridge, S. Shankar, J. Blumoff, L. Frunzio, M. Mirrahimi, M. H. Devoret, and R. J. Schoelkopf, “Tracking photon jumps with repeated quantum non-demolition parity measurements,” *Nature* **511**, 444 (2014).
- [106] S. J. Weber, A. Chantasri, J. Dressel, A. N. Jordan, K. W. Murch, and I. Siddiqi, “Mapping the optimal route between two quantum states,” *Nature* **511**, 570 (2014).
- [107] D. Ristè, M. Dukalski, C. A. Watson, G. de Lange, M. J. Tiggelman, Y. M. Blanter, K. W. Lehnert, R. N. Schouten, and L. DiCarlo, “Deterministic entanglement of su-

- perconducting qubits by parity measurement and feedback,” *Nature* **502**, 350 (2013).
- [108] Z. R. Lin, K. Inomata, K. Koshino, W. D. Oliver, Y. Nakamura, J. S. Tsai, and T. Yamamoto, “Josephson parametric phase-locked oscillator and its application to dispersive readout of superconducting qubits,” *Nat. Commun.* **5**, 4480 (2014).
- [109] J. Q. You and F. Nori, “Atomic physics and quantum optics using superconducting circuits,” *Nature* **474**, 589–597 (2011).
- [110] M. H. Devoret and R. J. Schoelkopf, “Superconducting Circuits for Quantum Information: An Outlook,” *Science* **339**, 1169 (2013).
- [111] A. Y. Kitaev, “Quantum computations: algorithms and error correction,” *Russian Math. Surveys* **52**, 1191 (1997).
- [112] M. D. Reed, L. DiCarlo, S. E. Nigg, L. Sun, L. Frunzio, S. M. Girvin, and R. J. Schoelkopf, “Realization of three-qubit quantum error correction with superconducting circuits,” *Nature* **482**, 382 (2012).
- [113] A. D. Córcoles, E. Magesan, S. J. Srinivasan, A. W. Cross, M. Steffen, J. M. Gambetta, and J. M. Chow, “Demonstration of a quantum error detection code using a square lattice of four superconducting qubits,” *Nat. Commun.* **6**, 6979 (2015).
- [114] A. Galiutdinov, A. N. Korotkov, and J. M. Martinis, “Resonator-zero-qubit architecture for superconducting qubits,” *Phys. Rev. A* **85**, 042321 (2012).
- [115] J. M. Gambetta, W. A. Braff, A. Wallraff, S. M. Girvin, and R. J. Schoelkopf, “Protocols for optimal readout of qubits using a continuous quantum nondemolition measurement,” *Phys. Rev. A* **76**, 012325 (2007).
- [116] D. Esteve, M. H. Devoret, and J. M. Martinis, “Effect of an arbitrary dissipative circuit on the quantum energy levels and tunneling of a Josephson junction,” *Phys. Rev. B* **34**, 158 (1986).
- [117] A. A. Houck, J. A. Schreier, B. R. Johnson, J. M. Chow, J. Koch, J. M. Gambetta, D. I. Schuster, L. Frunzio, M. H. Devoret, S. M. Girvin, and R. J. Schoelkopf, “Controlling the spontaneous emission of a superconducting Transmon qubit,” *Phys. Rev. Lett.* **101**, 080502 (2008).
- [118] J. Gambetta, A. Blais, D. I. Schuster, A. Wallraff, L. Frunzio, J. Majer, M. H. Devoret, S. M. Girvin, and R. J. Schoelkopf, “Qubit-photon interactions in a cavity: Measurement-induced dephasing and number splitting,” *Phys. Rev. A* **74**, 042318 (2006).
- [119] J. Gambetta, A. Blais, M. Boissonneault, A. A. Houck, D. I. Schuster, and S. M. Girvin, “Quantum trajectory approach to circuit QED: Quantum jumps and the Zeno

- effect,” *Phys. Rev. A* **77**, 012112 (2008).
- [120] A. N. Korotkov, “Quantum Bayesian approach to circuit QED measurement,” in *Quantum machines, Lecture notes of the Les Houches Summer School (Session 96, July 2011)*, edited by M. Devoret et al. (Oxford University Press, Oxford, 2014) Chap. 17, p. 533, [arXiv:1111.4016](#) .
- [121] M. Mariantoni, H. Wang, T. Yamamoto, M. Neeley, R. C. Bialczak, Y. Chen, M. Lenander, E. Lucero, A. D. O’Connell, D. Sank, M. Weides, J. Wenner, Y. Yin, J. Zhao, A. N. Korotkov, A. N. Cleland, and J. M. Martinis, “Implementing the quantum von Neumann architecture with superconducting circuits,” *Science* **334**, 61–65 (2011).
- [122] S. Haroche and J.-M. Raimond, *Exploring the Quantum: Atoms, Cavities, and Photons* (Oxford University Press, New York, 2013).
- [123] A. Fragner, M. Göppl, J. M. Fink, M. Baur, R. Bianchetti, P. J. Leek, A. Blais, and A. Wallraff, “Resolving Vacuum Fluctuations in an Electrical Circuit by Measuring the Lamb Shift,” *Science* **322**, 1357–1360 (2008).
- [124] A. N. Korotkov, “Error matrices in quantum process tomography,” [arXiv:1309.6405](#) Appendix B.
- [125] P. Stoica and R. L. Moses, *Introduction to spectral analysis* (Prentice Hall, New Jersey, 1997).
- [126] M. Boissonneault, J. M. Gambetta, and A. Blais, “Nonlinear dispersive regime of cavity QED: The dressed dephasing model,” *Phys. Rev. A* **77**, 060305 (2008).
- [127] M. Boissonneault, J. M. Gambetta, and A. Blais, “Dispersive regime of circuit QED: Photon-dependent qubit dephasing and relaxation rates,” *Phys. Rev. A* **79**, 013819 (2009).
- [128] H. Carmichael, *An open systems approach to quantum optics: lectures presented at the Université Libre de Bruxelles, October 28 to November 4, 1991*, Vol. 18 (Springer, Berlin, 1993).
- [129] H. M. Wiseman and G. J. Milburn, “Quantum theory of field-quadrature measurements,” *Phys. Rev. A* **47**, 642–662 (1993).
- [130] A. N. Korotkov, “Continuous quantum measurement of a double dot,” *Phys. Rev. B* **60**, 5737–5742 (1999).
- [131] H. M. Wiseman and G. J. Milburn, *Quantum measurement and control* (Cambridge University Press, Cambridge, UK, 2010).

- [132] K. W. Murch, S. J. Weber, C. Macklin, and I. Siddiqi, “Observing single quantum trajectories of a superconducting quantum bit,” *Nature* **502**, 211 (2013).
- [133] M. Hatridge, S. Shankar, M. Mirrahimi, F. Schackert, K. Geerlings, T. Brecht, K. M. Sliwa, B. Abdo, L. Frunzio, S. M. Girvin, R. J. Schoelkopf, and M. H. Devoret, “Quantum back-action of an individual variable-strength measurement,” *Science* **339**, 178 (2013).
- [134] G. de Lange, D. Ristè, M. J. Tiggelman, C. Eichler, L. Tornberg, G. Johansson, A. Wallraff, R. N. Schouten, and L. DiCarlo, “Reversing quantum trajectories with analog feedback,” *Phys. Rev. Lett.* **112**, 080501 (2014).
- [135] N. Roch, M. E. Schwartz, F. Motzoi, C. Macklin, R. Vijay, A. W. Eddins, A. N. Korotkov, K. B. Whaley, M. Sarovar, and I. Siddiqi, “Observation of measurement-induced entanglement and quantum trajectories of remote superconducting qubits,” *Phys. Rev. Lett.* **112**, 170501 (2014).
- [136] A. N. Korotkov, “Selective quantum evolution of a qubit state due to continuous measurement,” *Phys. Rev. B* **63**, 115403 (2001).
- [137] W. K. Wootters and W. H. Zurek, “A single quantum cannot be cloned,” *Nature* **299**, 802–803 (1982).
- [138] D. Dieks, “Communication by EPR devices,” *Phys. Lett. A* **92**, 271–272 (1982).
- [139] A. N. Korotkov, “Quantum Bayesian approach to circuit QED measurement with moderate bandwidth,” *Phys. Rev. A* **94**, 042326 (2016).
- [140] E. Mlinar, *Measurement and Quantum State Transfer in Superconducting Qubits*, Ph.D. thesis, University of California, Riverside (2017).
- [141] J. A. Schreier, A. A. Houck, J. Koch, D. I. Schuster, B. R. Johnson, J. M. Chow, J. M. Gambetta, J. Majer, L. Frunzio, M. H. Devoret, S. M. Girvin, and R. J. Schoelkopf, “Suppressing charge noise decoherence in superconducting charge qubits,” *Phys. Rev. B* **77**, 180502 (2008).
- [142] H. Paik, D. I. Schuster, L. S. Bishop, G. Kirchmair, G. Catelani, A. P. Sears, B. R. Johnson, M. J. Reagor, L. Frunzio, L. I. Glazman, S. M. Girvin, M. H. Devoret, and R. J. Schoelkopf, “Observation of High Coherence in Josephson Junction Qubits Measured in a Three-Dimensional Circuit QED Architecture,” *Phys. Rev. Lett.* **107**, 240501 (2011).
- [143] G. de Lange, B. van Heck, A. Bruno, D. J. van Woerkom, A. Geresdi, S. R. Plissard, E. P. A. M. Bakkers, A. R. Akhmerov, and L. DiCarlo, “Realization of Microwave Quantum Circuits Using Hybrid Superconducting-Semiconducting Nanowire Josephson Elements,” *Phys. Rev. Lett.* **115**, 127002 (2015).

- [144] T. W. Larsen, K. D. Petersson, F. Kuemmeth, T. S. Jespersen, P. Krogstrup, J. Nygård, and C. M. Marcus, “Semiconductor-nanowire-based superconducting qubit,” *Phys. Rev. Lett.* **115**, 127001 (2015).
- [145] J. M. Chow, J. M. Gambetta, A. D. Córcoles, S. T. Merkel, J. A. Smolin, C. Rigetti, S. Poletto, G. A. Keefe, M. B. Rothwell, J. R. Rozen, M. B. Ketchen, and M. Steffen, “Universal Quantum Gate Set Approaching Fault-Tolerant Thresholds with Superconducting Qubits,” *Phys. Rev. Lett.* **109**, 060501 (2012).
- [146] D. Ristè, J. G. van Leeuwen, H.-S. Ku, K. W. Lehnert, and L. DiCarlo, “Initialization by measurement of a superconducting quantum bit circuit,” *Phys. Rev. Lett.* **109**, 050507 (2012).
- [147] V. Braginsky and F. Khalili, *Quantum Measurement* (Cambridge University Press, Cambridge, UK, 1995).
- [148] M. Boissonneault, J. M. Gambetta, and A. Blais, “Improved superconducting qubit readout by qubit-induced nonlinearities,” *Phys. Rev. Lett.* **105**, 100504 (2010).
- [149] D. H. Slichter, C. Müller, R. Vijay, S. J. Weber, A. Blais, and I. Siddiqi, “Quantum Zeno effect in the strong measurement regime of circuit quantum electrodynamics,” *New J. Phys.* **18**, 053031 (2016).
- [150] C. C. Bultink, M. A. Rol, T. E. O’Brien, X. Fu, B. C. S. Dikken, C. Dickel, R. F. L. Vermeulen, J. C. de Sterke, A. Bruno, R. N. Schouten, and L. DiCarlo, “Active resonator reset in the nonlinear dispersive regime of circuit QED,” *Phys. Rev. Applied* **6**, 034008 (2016).
- [151] D. Sank, Z. Chen, M. Khezri, J. Kelly, R. Barends, B. Campbell, Y. Chen, B. Chiaro, A. Dunsworth, A. Fowler, E. Jeffrey, E. Lucero, A. Megrant, J. Mutus, M. Neeley, C. Neill, P. J. J. O’Malley, C. Quintana, P. Roushan, A. Vainsencher, T. White, J. Wenner, A. N. Korotkov, and J. M. Martinis, “Measurement-induced state transitions in a superconducting qubit: Beyond the rotating wave approximation,” *Phys. Rev. Lett.* **117**, 190503 (2016).
- [152] E. A. Sete, A. Galiutdinov, E. Mlinar, J. M. Martinis, and A. N. Korotkov, “Catch-Disperse-Release readout for superconducting qubits,” *Phys. Rev. Lett.* **110**, 210501 (2013).
- [153] E. A. Sete, J. M. Gambetta, and A. N. Korotkov, “Purcell effect with microwave drive: Suppression of qubit relaxation rate,” *Phys. Rev. B* **89**, 104516 (2014).
- [154] L. C. G. Govia and F. K. Wilhelm, “Entanglement generated by the dispersive interaction: The dressed coherent state,” *Phys. Rev. A* **93**, 012316 (2016).
- [155] L. C. G. Govia, E. J. Pritchett, C. Xu, B. L. T. Plourde, M. G. Vavilov, F. K.

- Wilhelm, and R. McDermott, “High-fidelity qubit measurement with a microwave-photon counter,” *Phys. Rev. A* **90**, 062307 (2014).
- [156] Y.-F. Chen, D. Hover, S. Sendelbach, L. Maurer, S. T. Merkel, E. J. Pritchett, F. K. Wilhelm, and R. McDermott, “Microwave Photon Counter Based on Josephson Junctions,” *Phys. Rev. Lett.* **107**, 217401 (2011).
- [157] F. Mallet, F. R. Ong, A. Palacios-Laloy, F. Nguyen, P. Bertet, D. Vion, and D. Esteve, “Single-shot qubit readout in circuit quantum electrodynamics,” *Nat. Phys.* **5**, 791 (2009).
- [158] P. Krantz, A. Bengtsson, M. Simoen, S. Gustavsson, V. Shumeiko, W. D. Oliver, C. M. Wilson, P. Delsing, and J. Bylander, “Single-shot read-out of a superconducting qubit using a Josephson parametric oscillator,” *Nat. Commun.* **7**, 11417 (2016).
- [159] G. Kirchmair, B. Vlastakis, Z. Leghtas, S. E. Nigg, H. Paik, E. Ginossar, M. Mirrahimi, L. Frunzio, S. M. Girvin, and R. J. Schoelkopf, “Observation of quantum state collapse and revival due to the single-photon Kerr effect,” *Nature* **495**, 205 (2013).
- [160] S. Barzanjeh, D. P. DiVincenzo, and B. M. Terhal, “Dispersive qubit measurement by interferometry with parametric amplifiers,” *Phys. Rev. B* **90**, 134515 (2014).
- [161] N. Didier, A. Kamal, W. D. Oliver, A. Blais, and A. A. Clerk, “Heisenberg-limited qubit read-out with two-mode squeezed light,” *Phys. Rev. Lett.* **115**, 093604 (2015).
- [162] L. C. G. Govia, E. J. Pritchett, and F. K. Wilhelm, “Generating nonclassical states from classical radiation by subtraction measurements,” *New J. Phys.* **16**, 045011 (2014).
- [163] S. Puri and A. Blais, “High-Fidelity Resonator-Induced Phase Gate with Single-Mode Squeezing,” *Phys. Rev. Lett.* **116**, 180501 (2016).
- [164] E. Flurin, N. Roch, F. Mallet, M. H. Devoret, and B. Huard, “Generating entangled microwave radiation over two transmission lines,” *Phys. Rev. Lett.* **109**, 183901 (2012).
- [165] K. W. Murch, S. J. Weber, K. M. Beck, E. Ginossar, and I. Siddiqi, “Reduction of the radiative decay of atomic coherence in squeezed vacuum,” *Nature* **499**, 62 (2013).
- [166] D. M. Toyli, A. W. Eddins, S. Boutin, S. Puri, D. Hover, V. Bolkhovskiy, W. D. Oliver, A. Blais, and I. Siddiqi, “Resonance fluorescence from an artificial atom in squeezed vacuum,” *Phys. Rev. X* **6**, 031004 (2016).
- [167] E. T. Jaynes and F. W. Cummings, “Comparison of quantum and semiclassical radiation theories with application to the beam maser,” *IEEE Proc.* **51**, 89 (1963).

- [168] R. Tanaś, “Squeezed states of an anharmonic oscillator,” in *Coherence and Quantum Optics V*, Proceedings of the fifth Rochester conference on coherence and quantum optics, edited by L. Mandel and E. Wolf (Plenum Press, New York, 1984) p. 645.
- [169] R. Tanaś, “Squeezing from an anharmonic oscillator model:  $(a^\dagger)^2 a^2$  versus  $(a^\dagger a)^2$  interaction Hamiltonians,” *Phys. Lett. A* **141**, 217 (1989).
- [170] G. J. Milburn, “Quantum and classical Liouville dynamics of the anharmonic oscillator,” *Phys. Rev. A* **33**, 674 (1986).
- [171] M. Kitagawa and Y. Yamamoto, “Number-phase minimum-uncertainty state with reduced number uncertainty in a Kerr nonlinear interferometer,” *Phys. Rev. A* **34**, 3974 (1986).
- [172] H. P. Yuen, “Two-photon coherent states of the radiation field,” *Phys. Rev. A* **13**, 2226 (1976).
- [173] C. C. Gerry and P. Knight, *Introductory Quantum Optics* (Cambridge University Press, Cambridge, UK, 2005).
- [174] M. Tavis and F. W. Cummings, “Exact solution for an  $n$ -molecule-radiation-field hamiltonian,” *Phys. Rev.* **170**, 379 (1968).
- [175] F. Yan, J. Bylander, S. Gustavsson, F. Yoshihara, K. Harrabi, D. G. Cory, T. P. Orlando, Y. Nakamura, J.-S. Tsai, and W. D. Oliver, “Spectroscopy of low-frequency noise and its temperature dependence in a superconducting qubit,” *Phys. Rev. B* **85**, 174521 (2012).
- [176] M. D. Reed, L. DiCarlo, B. R. Johnson, L. Sun, D. I. Schuster, L. Frunzio, and R. J. Schoelkopf, “High-fidelity readout in circuit quantum electrodynamics using the Jaynes-Cummings nonlinearity,” *Phys. Rev. Lett.* **105**, 173601 (2010).
- [177] J. E. Johnson, C. Macklin, D. H. Slichter, R. Vijay, E. B. Weingarten, J. Clarke, and I. Siddiqi, “Heralded State Preparation in a Superconducting Qubit,” *Phys. Rev. Lett.* **109**, 050506 (2012).
- [178] D. Sank, *Fast, Accurate State Measurement in Superconducting Qubits*, Ph.D. thesis, University of California, Santa Barbara (2014).
- [179] Z. Chen, *Metrology of Quantum Control and Measurement in Superconducting Qubits*, Ph.D. thesis, University of California, Santa Barbara (2018).
- [180] D. H. Slichter, R. Vijay, S. J. Weber, S. Boutin, M. Boissonneault, J. M. Gambetta, A. Blais, and I. Siddiqi, “Measurement-induced qubit state mixing in circuit qed from up-converted dephasing noise,” *Phys. Rev. Lett.* **109**, 153601 (2012).

- [181] D. I. Schuster, A. Wallraff, A. Blais, L. Frunzio, R.-S. Huang, J. Majer, S. M. Girvin, and R. J. Schoelkopf, “ac Stark Shift and Dephasing of a Superconducting Qubit Strongly Coupled to a Cavity Field,” *Phys. Rev. Lett.* **94**, 123602 (2005).
- [182] É. Dumur, B. Küng, A. Feofanov, T. Weißl, Y. Krupko, N. Roch, C. Naud, W. Guichard, and O. Buisson, “Unexpectedly allowed transition in two inductively coupled transmons,” *IEEE Trans. Appl. Supercond.* **26**, 1700304 (2016).
- [183] J. M. Martinis, K. B. Cooper, R. McDermott, M. Steffen, M. Ansmann, K. D. Osborn, K. Cicak, S. Oh, D. P. Pappas, R. W. Simmonds, and C. C. Yu, “Decoherence in Josephson Qubits from Dielectric Loss,” *Phys. Rev. Lett.* **95**, 210503 (2005).
- [184] M. Khezri, J. Dressel, and A. N. Korotkov, “Qubit measurement error from coupling with a detuned neighbor in circuit QED,” *Phys. Rev. A* **92**, 052306 (2015).
- [185] M. I. Dykman and M. A. Krivoglaz, “Quantum theory of nonlinear oscillators interacting with the medium,” *Sov. Phys. JETP* **37**, 506 (1973).
- [186] P. D. Drummond and D. F. Walls, “Quantum theory of optical bistability. I. Nonlinear polarisability model,” *J. Phys. A: Math. Gen.* **13**, 725 (1980).
- [187] L. A. Lugiato, “Theory of optical bistability,” *Prog. Opt.* **21**, 69 (1984).
- [188] *Fluctuating nonlinear oscillators*, edited by M. I. Dykman (Oxford University Press, Oxford, 2012).
- [189] I. Siddiqi, R. Vijay, F. Pierre, C. M. Wilson, L. Frunzio, M. Metcalfe, C. Rigetti, R. J. Schoelkopf, M. H. Devoret, D. Vion, and D. Esteve, “Direct observation of dynamical bifurcation between two driven oscillation states of a Josephson junction,” *Phys. Rev. Lett.* **94**, 027005 (2005).
- [190] M. Blencowe, “Quantum electromechanical systems,” *Phys. Rep.* **395**, 159 (2004).
- [191] K. C. Schwab and M. L. Roukes, “Putting mechanics into quantum mechanics,” *Phys. Today* **58**, 36 (2005).
- [192] A. D. O’Connell, M. Hofheinz, M. Ansmann, R. C. Bialczak, M. Lenander, E. Lucero, M. Neeley, D. Sank, H. Wang, M. Weides, J. Wenner, J. M. Martinis, and A. N. Cleland, “Quantum ground state and single-phonon control of a mechanical resonator,” *Nature* **464**, 697 (2010).
- [193] E. E. Wollman, C. U. Lei, A. J. Weinstein, J. Suh, A. Kronwald, F. Marquardt, A. A. Clerk, and K. C. Schwab, “Quantum squeezing of motion in a mechanical resonator,” *Science* **349**, 952 (2015).
- [194] O.-P. Saira, P. Groen, J., J. Cramer, M. Meretska, G. de Lange, and L. DiCarlo,

- “Entanglement Genesis by Ancilla-Based Parity Measurement in 2D Circuit QED,” *Phys. Rev. Lett.* **112**, 070502 (2014).
- [195] R. Vijay, *Josephson bifurcation amplifier: Amplifying quantum signals using a dynamical bifurcation*, Ph.D. thesis, Yale University (2008).
- [196] M. I. Dykman, “Periodically modulated quantum nonlinear oscillators,” in *Fluctuating nonlinear oscillators* (Oxford University Press, Oxford, 2012) p. 165, [arXiv:1112.2407](#).
- [197] K. Tomita and H. Tomita, “Irreversible circulation of fluctuation,” *Prog. Theor. Phys.* **51**, 1731 (1974).
- [198] M. I. Dykman and M. A. Krivoglaz, “Theory of fluctuational transitions between the stable states of a non-linear oscillator,” *Sov. Phys. JETP* **50**, 30 (1979).
- [199] D. Ludwig, “Persistence of Dynamical Systems under Random Perturbations,” *SIAM Rev.* **17**, 605 (1975).
- [200] *Quantum squeezing*, edited by P. D. Drummond and Z. Ficek (Springer-Verlag, Berlin, 2004).
- [201] M. I. Dykman, “Critical exponents in metastable decay via quantum activation,” *Phys. Rev. E* **75**, 011101 (2007).
- [202] C. Laflamme and A. A. Clerk, “Quantum-limited amplification with a nonlinear cavity detector,” *Phys. Rev. A* **83**, 033803 (2011).
- [203] C. M. Caves, “Quantum-mechanical noise in an interferometer,” *Phys. Rev. D* **23**, 1693 (1981).
- [204] V. Giovannetti, S. Lloyd, and L. Maccone, “Quantum-enhanced measurements: Beating the standard quantum limit,” *Science* **306**, 1330 (2004).
- [205] L. S. Collaboration, “Enhanced sensitivity of the LIGO gravitational wave detector by using squeezed states of light,” *Nat. Photon.* **7**, 613 (2013).
- [206] N. Didier, J. Bourassa, and A. Blais, “Fast quantum nondemolition readout by parametric modulation of longitudinal qubit-oscillator interaction,” *Phys. Rev. Lett.* **115**, 203601 (2015).
- [207] L. C. G. Govia and A. A. Clerk, “Enhanced qubit readout using locally generated squeezing and inbuilt Purcell-decay suppression,” *New J. Phys.* **19**, 023044 (2017).
- [208] A. Eddins, S. Schreppler, D. Toyli, L. Martin, S. Hacoheh-Gourgy, L. Govia, H. Ribeiro, A. Clerk, and I. Siddiqi, “Stroboscopic Qubit Measurement with Squeezed Illumination,” *Phys. Rev. Lett.* **120**, 040505 (2018).

- [209] R. Ruskov, K. Schwab, and A. N. Korotkov, “Squeezing of a nanomechanical resonator by quantum nondemolition measurement and feedback,” *Phys. Rev. B* **71**, 235407 (2005).
- [210] V. Peano, H. G. L. Schwefel, C. Marquardt, and F. Marquardt, “Intracavity squeezing can enhance quantum-limited optomechanical position detection through deamplification,” *Phys. Rev. Lett.* **115**, 243603 (2015).
- [211] R. Movshovich, B. Yurke, P. G. Kaminsky, A. D. Smith, A. H. Silver, R. W. Simon, and M. V. Schneider, “Observation of zero-point noise squeezing via a Josephson-parametric amplifier,” *Phys. Rev. Lett.* **65**, 1419 (1990).
- [212] G. Milburn and D. F. Walls, “Production of squeezed states in a degenerate parametric amplifier,” *Opt. Commun.* **39**, 401 (1981).
- [213] M. J. Collett and C. W. Gardiner, “Squeezing of intracavity and traveling-wave light fields produced in parametric amplification,” *Phys. Rev. A* **30**, 1386 (1984).
- [214] D. Rugar and P. Grütter, “Mechanical parametric amplification and thermomechanical noise squeezing,” *Phys. Rev. Lett.* **67**, 699 (1991).
- [215] B. Yurke, “Use of cavities in squeezed-state generation,” *Phys. Rev. A* **29**, 408 (1984).
- [216] P. Rabl, A. Shnirman, and P. Zoller, “Generation of squeezed states of nanomechanical resonators by reservoir engineering,” *Phys. Rev. B* **70**, 205304 (2004).
- [217] A. Kronwald, F. Marquardt, and A. A. Clerk, “Arbitrarily large steady-state bosonic squeezing via dissipation,” *Phys. Rev. A* **88**, 063833 (2013).
- [218] A. Szorkovszky, A. C. Doherty, G. I. Harris, and W. P. Bowen, “Mechanical squeezing via parametric amplification and weak measurement,” *Phys. Rev. Lett.* **107**, 213603 (2011).
- [219] K. Jähne, C. Genes, K. Hammerer, M. Wallquist, E. S. Polzik, and P. Zoller, “Cavity-assisted squeezing of a mechanical oscillator,” *Phys. Rev. A* **79**, 063819 (2009).
- [220] M. R. Vanner, I. Pikovski, G. D. Cole, M. S. Kim, Č. Brukner, K. Hammerer, G. J. Milburn, and M. Aspelmeyer, “Pulsed quantum optomechanics,” *Proc. Natl. Acad. Sci.* **108**, 16182 (2011).
- [221] C. U. Lei, A. J. Weinstein, J. Suh, E. E. Wollman, A. Kronwald, F. Marquardt, A. A. Clerk, and K. C. Schwab, “Quantum nondemolition measurement of a quantum squeezed state beyond the 3 dB limit,” *Phys. Rev. Lett.* **117**, 100801 (2016).
- [222] M. I. Dykman, D. G. Luchinsky, R. Mannella, P. V. E. McClintock, N. D. Stein, and N. G. Stocks, “Supernarrow spectral peaks and high-frequency stochastic resonance

- in systems with coexisting periodic attractors,” *Phys. Rev. E* **49**, 1198 (1994).
- [223] E. Buks and B. Yurke, “Mass detection with a nonlinear nanomechanical resonator,” *Phys. Rev. E* **74**, 046619 (2006).
- [224] R. Almog, S. Zaitsev, O. Shtempluck, and E. Buks, “Noise squeezing in a nanomechanical Duffing resonator,” *Phys. Rev. Lett.* **98**, 078103 (2007).
- [225] I. Serban, M. I. Dykman, and F. K. Wilhelm, “Relaxation of a qubit measured by a driven Duffing oscillator,” *Phys. Rev. A* **81**, 022305 (2010).
- [226] A. N. Cleland, *Foundations of nanomechanics: from solid-state theory to device applications* (Springer, Berlin, 2003).
- [227] B. Y. Zel’dovich, A. M. Perelomov, and V. S. Popov, “Relaxation of a quantum oscillator,” *Sov. Phys. JETP* **28**, 308 (1969).
- [228] U. Weiss, *Quantum dissipative systems* (World Scientific, London, 2012).
- [229] A. N. Korotkov, “Error matrices in quantum process tomography”, [arXiv:1309.6405](https://arxiv.org/abs/1309.6405).
- [230] J. Halliwell and A. Zoupas, “Quantum state diffusion, density matrix diagonalization, and decoherent histories: A model,” *Phys. Rev. D* **52**, 7294 (1995).
- [231] W. H. Zurek, S. Habib, and J. P. Paz, “Coherent states via decoherence,” *Phys. Rev. Lett.* **70**, 1187 (1993).
- [232] C. Weedbrook, S. Pirandola, R. García-Patrón, N. J. Cerf, T. C. Ralph, J. H. Shapiro, and S. Lloyd, “Gaussian quantum information,” *Rev. Mod. Phys.* **84**, 621 (2012).
- [233] S. L. Braunstein and P. van Loock, “Quantum information with continuous variables,” *Rev. of Mod. Phys.* **77**, 513 (2005).
- [234] A. Ferraro, S. Olivares, and M. G. A. Paris, *Gaussian states in quantum information* (Bibliopolis, Napoli, 2005); [arXiv:quant-ph/0503237](https://arxiv.org/abs/quant-ph/0503237).
- [235] P. Marian and T. A. Marian, “Squeezed states with thermal noise. I. Photon-number statistics,” *Phys. Rev. A* **47**, 4474 (1993).
- [236] H. Fearn and M. J. Collett, “Representations of squeezed states with thermal noise,” *J. Mod. Opt.* **35**, 553 (1988).
- [237] M. S. Kim, F. A. M. de Oliveira, and P. L. Knight, “Properties of squeezed number states and squeezed thermal states,” *Phys. Rev. A* **40**, 2494 (1989).
- [238] A. C. Doherty and K. Jacobs, “Feedback control of quantum systems using continuous

- state estimation,” *Phys. Rev. A* **60**, 2700 (1999).
- [239] A. Hopkins, K. Jacobs, S. Habib, and K. Schwab, “Feedback cooling of a nanomechanical resonator,” *Phys. Rev. B* **68**, 235328 (2003).
- [240] M. G. A. Paris, F. Illuminati, A. Serafini, and S. De Siena, “Purity of Gaussian states: Measurement schemes and time evolution in noisy channels,” *Phys. Rev. A* **68**, 012314 (2003).
- [241] A. Serafini, M. G. A. Paris, F. Illuminati, and S. De Siena, “Quantifying decoherence in continuous variable systems,” *J. Opt. B: Quantum Semiclass. Opt.* **7**, R19 (2005).
- [242] K. E. Cahill and R. J. Glauber, “Density operators and quasiprobability distributions,” *Phys. Rev.* **177**, 1882 (1969).
- [243] S. Haroche and J.-M. Raimond, *Exploring the quantum: Atoms, cavities, and photons* (Oxford University Press, New York, 2006).
- [244] L. D. Landau and E. M. Lifshitz, *Mechanics* (Butterworth-Heinemann, Amsterdam, 1976), Sec. 29.
- [245] A. H. Nayfeh and D. T. Mook, *Nonlinear oscillations* (Wiley-VCH, New York, 1995), Chap. 4.
- [246] A. Szorkovszky, G. A. Brawley, A. C. Doherty, and W. P. Bowen, “Strong Thermo-mechanical Squeezing via Weak Measurement,” *Phys. Rev. Lett.* **110**, 184301 (2013).
- [247] T. Yamamoto, K. Inomata, M. Watanabe, K. Matsuba, T. Miyazaki, W. D. Oliver, Y. Nakamura, and J. S. Tsai, “Flux-driven Josephson parametric amplifier,” *Appl. Phys. Lett.* **93**, 042510 (2008).
- [248] J. Y. Mutus, T. C. White, R. Barends, Y. Chen, Z. Chen, B. Chiaro, A. Dunsworth, E. Jeffrey, J. Kelly, A. Megrant, C. Neill, P. J. J. O’Malley, P. Roushan, D. Sank, A. Vainsencher, J. Wenner, K. M. Sundqvist, A. N. Cleland, and J. M. Martinis, “Strong environmental coupling in a Josephson parametric amplifier,” *Appl. Phys. Lett.* **104**, 263513 (2014).
- [249] H. Zheng, M. Silveri, R. T. Brierley, S. M. Girvin, and K. W. Lehnert, “Accelerating dark-matter axion searches with quantum measurement technology,” [arXiv:1607.02529](https://arxiv.org/abs/1607.02529).
- [250] A. Bienfait, P. Campagne-Ibarcq, A. Kiilerich, X. Zhou, S. Probst, J. Pla, T. Schenkel, D. Vion, D. Esteve, J. Morton, K. Moelmer, and P. Bertet, “Magnetic Resonance with Squeezed Microwaves,” *Phys. Rev. X* **7**, 041011 (2017).
- [251] C. M. Wilson, G. Johansson, A. Pourkabirian, M. Simoen, J. R. Johansson, T. Duty,

- F. Nori, and P. Delsing, “Observation of the dynamical Casimir effect in a superconducting circuit,” *Nature* **479**, 376 (2011).
- [252] P. Lähteenmäki, G. S. Paraoanu, J. Hassel, and P. J. Hakonen, “Dynamical Casimir effect in a Josephson metamaterial,” *Proc. Natl. Acad. Sci. USA* **110**, 4234 (2013).
- [253] J. B. Clark, F. Lecocq, R. W. Simmonds, J. Aumentado, and J. D. Teufel, “Observation of strong radiation pressure forces from squeezed light on a mechanical oscillator,” *Nat. Phys.* **12**, 683 (2016).
- [254] A. Ekert and P. L. Knight, “Non-stationary squeezing in a parametric amplifier,” *Opt. Commun.* **71**, 107 (1989).
- [255] B. Yurke, P. Grangier, R. E. Slusher, and M. J. Potasek, “Generating and detecting short-duration pulses of squeezed light,” *Phys. Rev. A* **35**, 3586 (1987).
- [256] Z. Ficek, R. Tanaś, and S. Kielich, “Squeezed states in the transient regime of resonance fluorescence,” *J. Opt. Soc. Am. B* **1**, 882 (1984).
- [257] R. Stassi, S. Savasta, L. Garziano, B. Spagnolo, and F. Nori, “Output field-quadrature measurements and squeezing in ultrastrong cavity-QED,” *New J. Phys.* **18**, 123005 (2016).
- [258] J. Atalaya, M. Khezri, and A. N. Korotkov, “Two-time correlators for propagating squeezed microwave in transients,” [arXiv:1804.08789](https://arxiv.org/abs/1804.08789) .
- [259] M. I. Dykman, “Theory of nonlinear nonequilibrium oscillators interacting with a medium,” *Sov. Phys. JETP* **41**, 1042 (1975).
- [260] D. Bozyigit, C. Lang, L. Steffen, J. M. Fink, C. Eichler, M. Baur, R. Bianchetti, P. J. Leek, S. Filipp, M. P. d. Silva, A. Blais, and A. Wallraff, “Antibunching of microwave-frequency photons observed in correlation measurements using linear detectors,” *Nat. Phys.* **7**, 154 (2011).
- [261] H. J. Carmichael, *Statistical Methods in Quantum Optics 2: Non-Classical Fields* (Springer-Verlag, Berlin, 2008).
- [262] Z. Y. Ou, C. K. Hong, and L. Mandel, “Coherence properties of squeezed light and the degree of squeezing,” *J. Opt. Soc. Am. B* **4**, 1574 (1987).
- [263] C. Neill, P. Roushan, K. Kechedzhi, S. Boixo, S. V. Isakov, V. Smelyanskiy, A. Megrant, B. Chiaro, A. Dunsworth, K. Arya, R. Barends, B. Burkett, Y. Chen, Z. Chen, A. Fowler, B. Foxen, M. Giustina, R. Graff, E. Jeffrey, T. Huang, J. Kelly, P. Klimov, E. Lucero, J. Mutus, M. Neeley, C. Quintana, D. Sank, A. Vainsencher, J. Wenner, T. C. White, H. Neven, and J. M. Martinis, “A blueprint for demonstrating quantum supremacy with superconducting qubits,” *Science* **360**, 195 (2018).

- [264] D. Kafri, C. Quintana, Y. Chen, A. Shabani, J. M. Martinis, and H. Neven, “Tunable inductive coupling of superconducting qubits in the strongly nonlinear regime,” [Phys. Rev. A \*\*95\*\*, 052333 \(2017\)](#).
- [265] M. Abramowitz and I. A. Stegun, eds., *Handbook of Mathematical Functions: with Formulas, Graphs, and Mathematical Tables* (Dover Publications, New York, 1965).
- [266] A. Cottet, *Implementation of a quantum bit in a superconducting circuit*, [Ph.D. thesis](#), Universite Paris (2002).
- [267] A. N. Korotkov, “Output spectrum of a detector measuring quantum oscillations,” [Phys. Rev. B \*\*63\*\*, 085312 \(2001\)](#).
- [268] M. B. Plenio and S. S. Virmani, “An Introduction to Entanglement Theory,” in *Quantum Information and Coherence*, Scottish Graduate Series, edited by E. Andersson and P. Öhberg (Springer, New York, 2014) p. 173, [arXiv:quant-ph/0504163](#) .